AD-A286 298

WL-TR-94-3134

DAMAGE TOLERANT REPAIR TECHNIQUES
FOR PRESSURIZED AIRCRAFT FUSELAGES

CAPT ROBERT S. FREDELL

HQ USAFA/DFEM
2354 FAIRCHILD DRIVE SUITE 6112
USAF ACADEMY CO 80840-6240

JUNE 1994

FINAL REPORT FOR 06/15/91-11/15/93

APPROVED FOR PUBLIC RELEASE; DISTRIBUTION IS UNLIMITED.

94-35469

FLIGHT DYNAMICS DIRECTORATE
WRIGHT LABORATORY
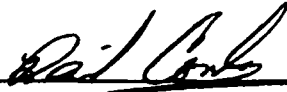AIR FORCE MATERIEL COMMAND
WRIGHT PATTERSON AFB OH 45433-7562

94 11 16 089

NOTICE

When Government drawings, specifications, or other data are used for any purpose other than in connection with a definitely Government-related procurement, the United States Government incurs no responsibility or any obligation whatsoever. The fact that the government may have formulated or in any way supplied the said drawings, specifications, or other data, is not to be regarded by implication, or otherwise in any manner construed, as licensing the holder, or any other person or corporation; or as conveying any rights or permission to manufacture, use, or sell any patented invention that may in any way be related thereto.

This report is released to the National Technical Information Service (NTIS). At NTIS, it will be available to the general public, including foreign nations.
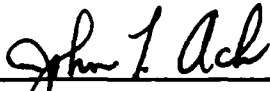
This technical report has been reviewed and is approved for publication.

David Conley
Structural Integrity Engineer
Fatigue, Fracture & Reliability Sect

Anthony S. Lizza, Technical Mgr
Fatigue, Fracture & Reliability Sect
Structural Integrity Branch

John T. Ach, Acting Chief
Structures Division
Flight Dynamics Directorate

REPORT DOCUMENTATION PAGE

Public reporting burden for this collection of information is estimated to average 1 hour per response, including the time for reviewing instructions, searching existing data sources, gathering and maintaining the data needed, and completing and reviewing the collection of information. Send comments regarding this burden estimate or any other aspect of this collection of information, including suggestions for reducing this burden, to Washington Headquarters Services, Directorate for Information Operations and Reports, 1215 Jefferson Davis Highway, Suite 1204, Arlington, VA 22202-4302, and to the Office of Management and Budget, Paperwork Reduction Project (0704-0188), Washington, DC 20503.

1. AGENCY USE ONLY (Leave blank)	2. REPORT DATE	3. REPORT TYPE AND DATES COVERED
	6 Jun 94	Final, 3 Jan 91 – 27 Nov 93

4. TITLE AND SUBTITLE

Damage Tolerant Repair Techniques for Pressurized
Aircraft Fuselages

6. AUTHOR(S)

Capt Robert S. Fredell

5. FUNDING NUMBERS

C
PE 62201
PR 2401
TA LE
WU 00

7. PERFORMING ORGANIZATION NAME(S) AND ADDRESS(ES)

Capt Robert S. Fredell
HQ USAFA/DFEM
2354 Fairchild Drive Suite 6112
USAF Academy CO 80840-6240

8. PERFORMING ORGANIZATION REPORT NUMBER

9. SPONSORING/MONITORING AGENCY NAME(S) AND ADDRESS(ES)

WL/FIBEC   FLIGHT DYNAMICS DIRECTORATE
Building 45
2130 Eighth St Suite 1
Wright-Patterson AFB OH 45433-7542

10. SPONSORING/MONITORING AGENCY REPORT NUMBER

WL-TR-94-3134

11. SUPPLEMENTARY NOTES

12a. DISTRIBUTION/AVAILABILITY STATEMENT

APPROVED FOR PUBLIC RELEASE; DISTRIBUTION IS UNLIMITED

12b. DISTRIBUTION CODE

13. ABSTRACT (Maximum 200 words) Concerns over the safety of the continued use of aging transport aircraft have been voiced in the industry. A key component in the structural integrity of aging aircraft is the damage tolerance of fuselage structural repairs. The investigation focuses on the analysis and testing of contemporary repair methods and develops two improvements. The first technique, known as "soft patching," is appropriate for damage tolerant riveted repairs to incidental fuselage damage. Soft patching involves the use of high strength, moderate elastic modulus GLARE 3 fiber metal laminate patches. They extend the fatigue life of riveted repairs to monolithic aluminum fuselages while reducing life cycle costs. The second technique involves bonded crack patching of intact fatigue cracks in fuselage skins. An easy to use analysis program is presented along with analytical and test results of a low cost, high performance patch material known as GLARE 2. The findings demonstrate that GLARE 2 can replace the expensive boron/epoxy composites used in fuselage crack patching applications.

14. SUBJECT TERMS Repair, fatigue, damage tolerance, fuselage structures, crack patching, adhesive bonding, surface pretreatment, riveting, advanced composite materials, fiber metal laminates, GLARE, coefficient of thermal expansion, finite element analysis, continuum analysis.

15. NUMBER OF PAGES

282

16. PRICE CODE

17. SECURITY CLASSIFICATION OF REPORT	18. SECURITY CLASSIFICATION OF THIS PAGE	19. SECURITY CLASSIFICATION OF ABSTRACT	20. LIMITATION OF ABSTRACT
Unclassified	Unclassified	Unclassified	Unlimited

Table of Contents

List of Figures

v

List of Tables

Acknowledgments

My three years of Ph.D. work would have been impossible without the sponsorship of the United States Air Force. Thanks are due especially to Col Cary Fisher, head of the Engineering Mechanics Department at USAFA, for sponsoring my study. Thanks go also to my program managers LtCol James Waller and Major Jim Hogan at the Air Force Institute of Technology for their flexibility and support. Ted Reinhart of Wright Labs deserves a nod for first introducing me to Delft and fiber metal laminates in 1986.

I want to thank my promoter, Professor Doctor Ingenieur Jacobus Schijve, for his interest in and support of this project. His constructive criticism was appreciated. Special thanks are due to my co-promoter Professor Ingenieur Boud Vogelesang, whose unquenchable enthusiasm and strong support was and continues to be a welcome daily inspiration. Thanks, too, for the invitation to do research in a special place. The B2 group reflects your personality and "can-do" spirit.

My students who were the "repair project" deserve special notice. Thanks to Henri Vander Stichele for his excellent work on adhesives and pretreatments, to Walter van Barneveld for the exceptional effort on crack patching analysis, to Cees Borsboom for the ground-breaking eddy current and damage tolerance work, and to Rob Hoens for the clever adhesive bonding and laminate failure mechanism work.

Certain colleagues rate special mention. Richard Müller has been a great friend and sounding board throughout this investigation. My running partner and "coach" Ad Vlot provided guidance and support to make a three-year program a reality. Mart Heerschap's guiding hand made the finite element work much easier.

The technical and support staff of the laboratory are what really make it a special and productive place. Thanks go to Jan Snijder, Berthil Grashof, Arie Burgers, Kees Paalvast, Frans Oostrum, Berthis van der Stok and his talented machinists, Hans Vonk and Hannie van Deventer for their friendly help. I wish also to acknowledge the financial and technical support of Structural Laminates bv.

Finally, none of this would have been possible without the strong emotional support of my wife Kris. Sweetie, I couldn't have done it without you, and I wouldn't have wanted to.

List of Symbols

symbol	description	dimensions
A	area	m^2
A_i	$E_i / (1 - \nu_{ij} \nu_{ji})$	GPa
a	patch half-length	m
a_c	crack half-length	m
B_i	thermal constant (i = 1-5)	m/N
b	patch half-width	m
b_i	constant	
C	boundary curve of D	..
C	constants	
C_i	constants (i = 1-5)	
D	area covered by reinforcement (patch)	m^2
D_i	thermal stress constant (i = 1,2)	
d_x	heat blanket half-length	m
d_y	heat blanket half-width	m
Det	determinant	..
E	elastic modulus	GPa
EA	extensional stiffness	N
EI	flexural stiffness	Nm^2
F(x,y)	shear traction per unit area exerted by adhesive at (x,y)	MPa
F_i	thermal stress constant (i = 1-3)	N/m
f	cross-sectional area	m^2
G	crack extension force	N/m
G_A	adhesive shear modulus	MPa
G_{ij}	elastic shear modulus	MPa
H_1	thermal stress constant	m/N
h	heat transfer coefficient	$W/m^2 K$
K	stress intensity factor	MPa $\sqrt{m}$
K	absolute temperature (Kelvin)	degrees
K_0	thermal stress constant	..
K_1	thermal stress constant	N/m
k	thermal conductivity	W/m K

M	portion of plate complementary to $D+C$	m^2
M_i	moment (i = 1,2, ...)	Nm
m	heat transfer term = $\sqrt{(hu)/(kf)}$	m^{-1}
n	(number of dimensions) - 1	--
n	normal to C	--
P	remote stress in x-direction	MPa
P	load per unit length	N/m
P_i	loads per unit length (i = 1,2)	N/m
p	additional x-stress in inclusion	MPa
Q	remote stress in y-direction	MPa
Q	heat transfer rate	WK^2
q	additional y-stress in inclusion	MPa
Rx	double stringer spacing	m
Ry	frame spacing	m
r	root of differential equation	
r	single space coordinate	m
r	radius	m
T	tractions acting on boundary C	MPa
T	temperature	ºC
t	thickness	m
$T(x,y)$	temperature distribution	ºC
T_∞	temperature of coolant	ºC
u	displacement	m
u	circumference	m
u	displacement in x-direction	m
v	displacement in y-direction	m
W	work expended by allowing the stress $\sigma_\bullet$ to relax to zero	Nm
W_i	constant	
w	deflection	m
x	x-coordinate	m
y	y-coordinate	m
z	z-coordinate	m
z_0	neutral axis	

α	coefficient of thermal expansion	$°C^{-1}$
α, β	roots of the characteristic equation	--
Δ	increase or change	--
δ	increase or change	--
δ	displacement	m
ε	strain	--
Λ^{-1}	bonded lap joint load transfer length	m
Λ^{-1}	root of characteristic equation	--
ν_{ij}	Poisson's ratio	--
σ	normal stress	MPa
$\sigma_{\bullet}$	normal stress in the reinforced plate (from Stage I analysis)	MPa

sub- and superscripts

A	of the adhesive
amb	ambient
c	cure
c	crack
cr	cruise
D	of the doubled region in the bending model
e	edge
eff	effective
I	in the inclusion
M	in the matrix
max	maximum
min	minimum
P	of the base plate (aircraft skin)
R	in the reinforcing patch
r	radial coordinate
r	repaired value
rel	relative
t	taper
th	thermal
u	short cracks

x	x-direction
y	y-direction
α,β	x- or y- coordinate
γ	shear
ϴ	tangential coordinate
+,-	direction of approach
∞	infinity
	referring to coolant
	long cracks
•	corrected for elastic modulus
	additional contributions
	length of crack outside of intact patch

1

Introduction

"No one sews a piece of new, unshrunk cloth on an old garment; if he does, the patch tears away from it, the new from the old, and a worse tear is made. And no one puts new wine into old wineskins; if he does, the wine will burst the skins, and the wine is lost, and so are the skins; but new wine is for fresh skins."

Mark 2: 21-22

1.1 Historical Background

"By the afternoon of December 12, 1903, the machine was again ready.   Orville Wright recorded in his diary that day:

'Got machine outside in afternoon with intention of making a trial . . . . In starting one time the frames supporting the tail were caught on the end of the track and broken.'"

The Wrights spent the morning of December 14th "making repairs to the damaged tail of the Flyer." Later that day, Wilbur made the first real trial of the Flyer with only partial success.   The gravity-assisted (and thus unofficial) flight covered only 32 meters, and on landing, the front landing skids and part of the front rudder were broken.   "Repairs to the damaged machine occupied the next couple of days," leading up to the historic first powered flight on December 17th [1].

The need for good repair techniques predates powered flight and continues to be an integral part of flying today. Structural repairs to commercial airliners are most typically required for fatigue cracking, corrosion and incidental damage such as impact [2]. For military aircraft, battle damage joins the above list.

Investigators traced the cause of the largest-ever loss of life from a single aircraft accident to an improperly performed structural repair. In August 1985, 520 persons perished when the aft pressure bulkhead of a Japan Air Lines Boeing 747 failed.   In the crash investigation, Boeing stated "its engineering team had carried out the bulkhead repair incorrectly, and that the mistake led to a weakening of the structure which caused the bulkhead to fail along the repair line."   Figure 1.1 shows the repaired area.
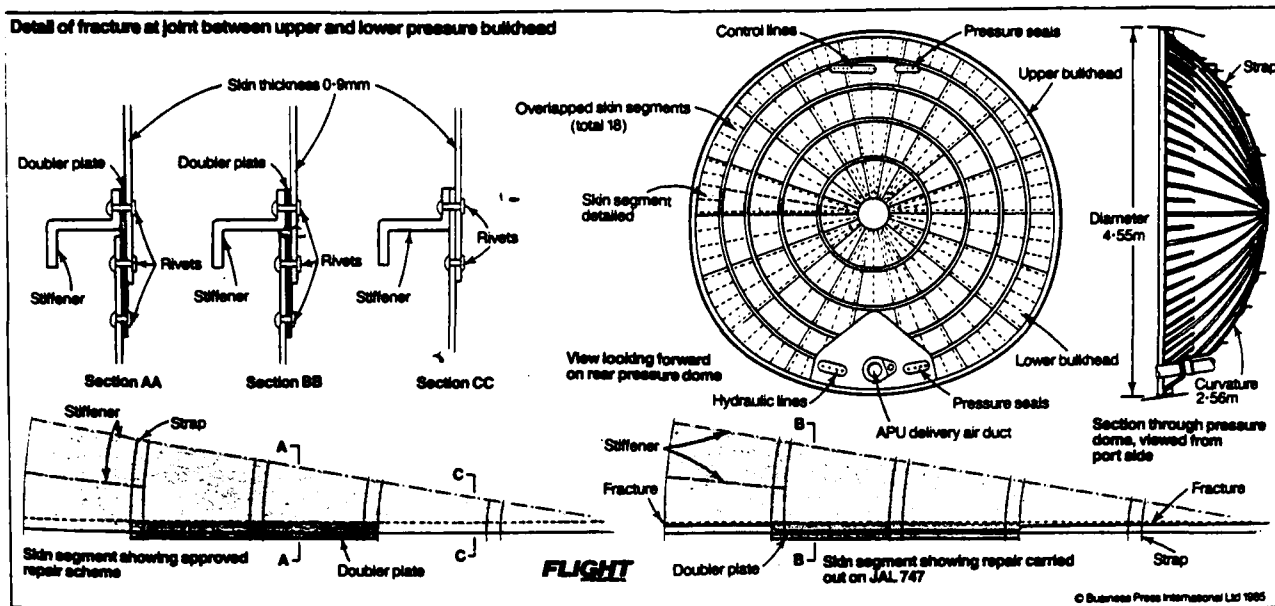
Figure 1.1. Sketch shows improper bulkhead repair that led to the loss of JAL 747 [3].

Another well-known structural failure called into question the long-term integrity and safety of structural repairs. Aloha Airlines' flight 243, an early model Boeing 737, suffered catastrophic failure of its forward fuselage in April 1988, as shown in figure 1.2. Although one flight attendant died in the uncontrolled decompression, remarkably, the aircraft landed safely with 94 people on board.

Figure 1.2. Photo of Aloha Airlines' flight 243 after cabin pressure failure [4].

Post-failure investigation of the aircraft and the airline by the U.S. National Transportation Safety Board (NTSB) revealed the cause of the mishap. "The failure mechanism was a result of multiple site fatigue cracking of the skin adjacent to rivet holes along the lap joint upper rivet row and tear strap disbond which negated the fail-safe characteristics of the fuselage [4]."

NTSB investigators found at least 25 separate fuselage skin repairs on the aircraft. Two of these repairs occurred on the only portion of the failed section recovered. Inspectors discovered a small section of a right side lap joint lodged in the right wing after the explosive decompression. Investigators found "extensive fatigue cracking in the upper row rivet holes both under and between the patches." The longest crack found in this piece was about 7 mm long.

Some writers have speculated whether the lap joint failure (which initiated on the left side of the fuselage) was due to fatigue damage at another previous repair location. The answer lies at the bottom of the Pacific Ocean. Regardless, the discovery of hidden fatigue cracks in the failed section points out that repairs can often impair the inspectability of a structure. The NTSB report concluded that the mishap was primarily the fault of Aloha Airlines. The air carrier "should have followed a maintenance program to detect and repair cracking before it reached a critical condition [4]." In the words of an NTSB member, "one of the lessons learned by the whole industry from this accident is the criticality of maintenance and inspection programs [5]."

Several factors combine to make fuselage skins one of the most severe problem areas for structural durability and maintenance. First, any corrosion damage to fuselage skins will probably remove a significant percentage of the skin thickness. Second, taxiing and frequent ground handling cause a significant amount of incidental impact damage to thin fuselage skins [2]. Finally, the relatively uniform stress level over a large part of the fuselage makes the occurrence of multiple site fatigue damage likely at lap joints.

Following the Aloha incident, the U.S. Federal Aviation Administration (FAA) began several corrective actions to assure the quality of airline structural maintenance. One action taken by the FAA has been to increase the number of field inspectors from 2,100 in 1988 to more than 3,000 in 1991. The FAA assigned these field inspectors "the task of assuring maintenance compliance by airlines and independent repair operators [6]."

1.2 The Damage Tolerance Concept

In 1978, the FAA amended the Federal Aviation Requirements (FAR 25.571) to include the damage tolerance philosophy for new transport category aircraft. Damage tolerance replaced the older "fail-safe" and "safe-life" concepts. The damage tolerance philosophy states "engineering evaluation of the structure under typical load environmental spectra must show that catastrophic failure due to fatigue, accidental damage or corrosion will be avoided throughout the operational life of the aircraft." In 1981, the FAA extended damage tolerance requirements to transport aircraft types already certified. rule change included any repair affecting "threshold, frequency and type of inspection of principal structural elements [7, 8]." (*Threshold* refers to the first major structural inspection performed on an aircraft, usually at about half the design life. Thereafter, inspections are done with increased *frequency*.)

The threshold inspection is the first major structural inspection performed on an aircraft. It is usually performed at about the middle of the planned economic life of an aircraft. The threshold is based on experience, calculations and full-scale fatigue testing, which establish a conservative estimate of the minimum time required for detectable cracks to occur. The threshold inspection is then followed by periodic inspections spaced at shorter intervals. These intervals are based on the amount of flights a detectable crack takes to grow to a critical size. This number is divided by a safety factor, usually about three, to give greater probability of detecting a crack before it causes a failure.

The Aloha incident and further study of the phenomenon of multiple site damage led the FAA to change its philosophy in dealing with chronic structural problems. "In the past, the agency has relied upon repeated inspection to detect damage in an aircraft structure." This process can add significantly to maintenance workloads. The FAA now places new emphasis on developing a permanent modification to solve the problem without increasing inspection requirements [6]. Airlines typically perform these so-called "terminating actions" during a heavy overhaul known as a D-check.

This new philosophy resulted in a flood of FAA airworthiness directives (ADs) aimed at repairing up to 2,600 aging transport aircraft operated by U.S. carriers. A report issued by the U.S. General Accounting Office said "these ADs represent the largest structural maintenance requirement ever placed on U.S. airlines." The deep recession of this decade

has ended doubts whether enough capacity exists to perform the work by the FAA-
mandated 1994 deadline [9]. Earlier, however, writers expressed fears that by 1993
several hundred airliners would "be queuing outside the hangars for new skins and joints
[10]." In fact, hundreds of aircraft now sit mothballed around the world, awaiting
customers. Figure 1.3 shows just such an aging 737 in storage at Mojave, California. A
large number of riveted fuselage repairs are visible.

Figure 1.3. Boeing 737 in long-term storage in the Mojave desert, California [11].

These actions in the commercial airline fleet follow a decade of improvements in aircraft
reliability and maintainability (R & M) by the U.S. Air Force. As an example, the so-called
"R & M 2000" initiative targets increased combat capability through greater structural
reliability. Further, the initiative targets reduced work requirements (through more durable
airframes and shorter repair times when maintenance is required) and decreased life cycle
cost (by making long-lasting repairs with inexpensive materials and processes). However,
R & M 2000 considers more than aircraft under development; it also applies to existing
aircraft. Substitution of more reliable subcomponents and adoption of better materials and
processes to maintenance techniques are two examples.

1.3 Application of Advanced Materials and Processes

In 1905, with two years of powered flight experience behind them, the Wright Brothers exchanged a series of letters with the Army Board of Ordnance and Fortification. The Army "wanted to see if the machine, provided it could fly, could be adapted for military use. For all anyone knew, the Wright machine might be some weird agglomeration of fragile parts, unusable in rough circumstances, unable to stand up to continuous operation [12]." The War Department finally accepted the Wrights' bid to furnish a flying machine for $25,000 three years later [13].

In today's world of advanced aerospace materials and processes, purchasers are equally reluctant to try something new. A new material can take 20 years or more to make the jump from the laboratory to the flight line. Japan's development of an advanced carbon fiber composite wing for the FS-X fighter is an example. "As engineers start to consider the aircraft's real operational requirements, worries are being expressed about how to maintain the plastic wing's quality during manufacture and when in service, and how to repair it after damage in combat [14]."

Any new material or process must strike a balance between damage tolerance, structural efficiency and life cycle cost. As Jurgen Weber, Chairman of Lufthansa Airlines said, "Air carriers do not support innovative design changes for the sake of flying the latest state-of-the-art technology, but for the economic benefits they offer [15]."

The United States Air Force (USAF) has explained the process for the successful transition of advanced materials to aircraft under design development. Lincoln [16] listed five criteria "essential to the successful completion of the tasks of the USAF Aircraft Structural Integrity Program. Those five factors are:

    --stabilized material and material processes,
    --producibility,
    --characterized mechanical properties,
    --predictability of structural performance, and
    --supportability."

According to Lincoln, the supportability of new materials is "a major consideration because of accidental and battle damage." Before a new material is mature enough for use on an aircraft, it must first have a viable, economic inspection and repair concept. This

maintenance concept must consider both the working environment and the existing maintenance system.

One way to ease the transition of new structural materials and processes into flying service is to demonstrate them first in small, controlled flying demonstrations on conventional aircraft. This method has been moderately successful in the past.

1.4 Outline

This dissertation will concentrate on the application of advanced materials and processes to the damage tolerant repair of existing transport category airplanes. The paper will show that small changes in analysis and repair techniques can result in significant improvements to the durability and damage tolerance of pressurized fuselages at substantial life cycle cost savings over current techniques. The aims of the study in general terms are:

- to develop simple repair techniques that satisfy damage tolerance requirements (safety and durability) without imposing impractical requirements on maintainers, and

- to prove by analysis and experiments that the proposed repair techniques will be satisfactory.

For these purposes, this thesis presents the following:

- Chapter 2: current practices for riveted repairs, analysis of improved techniques

- Chapter 3: results of static and fatigue testing of these improvements

- Chapter 4: developments in materials and processes that simplify and improve the quality of bonded repairs

- Chapter 5: analysis of bonded "crack patching" repairs, including a user-friendly computer program to simplify the process and a parametric study of several advanced composite patch materials

- Chapter 6: results of fatigue and damage tolerance testing of low-cost material advances in crack patching

- Chapter 7: summary and conclusions

References, Chapter 1

1. Wescott, L., and P. Degen, "Wind and Sand." New York: H. N. Abrams Inc., 1983.

2. Vlot, A., "Low Velocity Impact Loading on Fibre Reinforced Aluminium Laminates, Ph.D. thesis, Faculty of Aerospace Engineering, Delft University, Delft, The Netherlands, 1991.

3. "The Bulkhead That Failed," *Flight International*, 5 October 1985, p. 7.

4. "Aircraft Accident Report: Aloha Airlines, Flight 243, Boeing 737-200, N73711, near Maui, Hawaii, April 28, 1988. Washington: U.S. National Transportation Safety Board, 1989.

5. "NTSB Raps Aloha, Aviation System for Fuselage Failure," *Aviation Week and Space Technology*, 29 May 1989, p. 24.

6. "FAA Hiring Field Inspectors to Monitor Aging Aircraft," *Aviation Week and Space Technology*, 24 April 1989, p.110.

7. Swift, T., "Repairs to Damage Tolerant Aircraft," *Proc. Int'l Symp. on Structural Integrity of Aging Airplanes*, Atlanta, Georgia, 20-22 March 1990.

8. "Airframe Makers Use Aging Aircraft Experience to Refine Design Practices," *Aviation Week and Space Technology*, 24 July 1989, pp. 94-95.

9. Wilson, J.R. and J. Keller, "Overhaul Trends Buck Predictions," *Interavia Aero. Review*, March 1992, pp. 59-62.

10. "Ageing Aircraft Face Tough Deadline," *Interavia Aero. Review*, August 1991, pp. 64-65.

11. Claasen, H., "Development of Maintenance Programs for Airplane Structures From the Initial Phase to the Present Time Considering Aging Aircraft Problems," *Proc. 5th Int'l Symp. on Structural Integrity of Aging Airplanes*, Hamburg, 16-18 June, 1993, p.46.

12. Walsh, J.E, "First Flight: The Untold Story of the Wright Brothers." London: George Allen & Unwin Ltd., 1976.

13. Renstrom, A.G., "Wilbur & Orville Wright: A Chronology Commemorating the Hundredth Anniversary of the Birth of Orville Wright, August 19, 1871." Washington: Library of Congress, 1975.

14. "Wings of Desire," *The Economist*, 24 August 1991, p. 54.

15. Weber, J., presentation to the Second International Conference on Bonded Aircraft Structures Technology Application and Repair Techniques, Lubeck, Germany, 1987.

16. Lincoln, J.W., "Structural Technology Transition to New Aircraft," *Proc. 14th Symp. Int'l Comm. on Aeronautical Fatigue*, Ottawa, 8-12 June 1987.

2

Analysis of Riveted Repairs

"Although it is generally rash to cut holes in existing structure, some people seem unable to resist the temptation to do so."

J.E. Gordon, *Structures* or Why Things Don't Fall Down (1978)

2.1 Introduction

Riveted repairs make up the single largest type of repairs performed on metal-skinned aircraft structures. Riveted repairs possess many advantages over other techniques: They are quick and easy to carry out on the aircraft and require little support equipment. Maintenance personnel often install riveted repairs with little or no engineering analysis.

Though commonly used, riveted repairs are not without their disadvantages. Swift said "riveted repairs can substantially degrade fatigue life if extreme care in detail design is not taken." [1] Most riveted repairs provide only for the restoration of equal or better static strength to the structure. Typically, repairers ignore fatigue, although the damage tolerance requirements mandate its consideration.

The problem of properly repairing an aircraft structure is complicated. Usually, the repairer has no access to the original structural loads and stress calculations of the designer. Instead, one must rely on the Structural Repair Manual (SRM) provided by the manufacturer. The SRM typically shows only "approved" methods and maximum repairable damage sizes.

This chapter discusses current practices for riveted repairs, highlighting some pitfalls in the accepted methods. Improvements based on modified design improvements made to new structures are discussed, and a new approach to repair known as "soft patches" is introduced. A detailed finite element analysis of some typical riveted repairs is presented, supported by extensive static and fatigue testing of concepts for damage tolerant riveted repairs.

2.2 Current Practice: Design for Static Strength

The literature covering five decades of aircraft maintenance is consistent in discussing general requirements for riveted repairs to aluminum structures [2-4]. Writers heavily emphasize the restoration of equal or better static strength to the structure. Figure 2.1, from [3], shows an example of a riveted repair of a small (51 mm) skin crack in a 0.64 mm thick 2024-T3 aluminum skin.
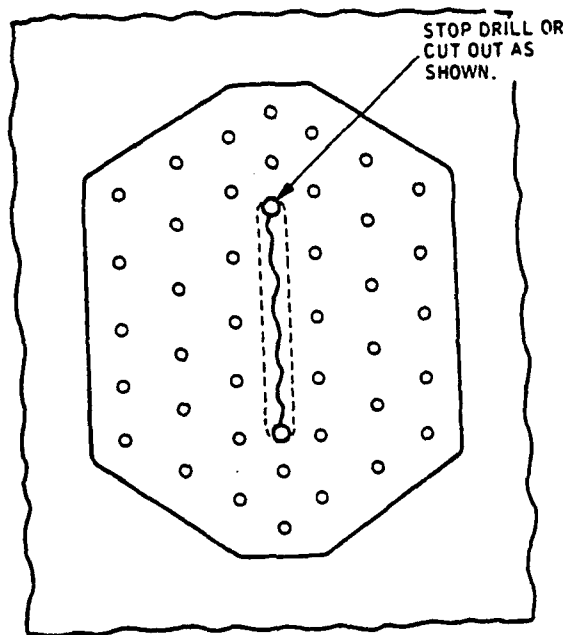
Figure 2.1. Example of a riveted repair performed on a cracked aluminum sheet [3].

General guidelines for such a repair can be summarized as follows:

- Stop-drill the ends of the cracks with a 3 mm diameter hole to prevent the crack from spreading [2-4].

- Select patch materials of the same gage (thickness) or one gage thicker than the original skin. Use material of the same type [2,4].

- Choose a rivet diameter at least three times the thickness of the thickest sheet joined in the repair [2,3].

- Cut the patch so it overlaps the damaged area by eight times the diameter of the rivets (two rivet rows). Use 12 times the rivet diameter in case of three rivet rows [2].

- Use a rivet pitch (the space between rivet centers in the same row) of at least three times the rivet diameter [3].

- Select the number of rivets using rivet tables in the aircraft Structural Repair Manual or by a formula (adapted from [2]) which equates rivet shear strength with the tensile strength of the missing material:

$$N\tau\frac{\pi}{4}d^2 = Lt\sigma_{ult} \qquad (2\text{-}1)$$

simplifying, the required number of rivets is

$$N = \frac{4Lt\sigma_{ult}}{\pi d^2 \tau} \qquad (2\text{-}2)$$

A similar formula has been developed to set the bearing strength of the sheet equal to the tensile strength of the missing material:

$$N\sigma_b dt = Lt\sigma_{ult} \qquad (2\text{-}3)$$

solving for the number of rivets,

$$N = \frac{L\sigma_{ult}}{d\sigma_b} \qquad (2\text{-}4)$$

Where: N is the number of rivets per side of the patch,
L is the length of the crack,
t is the thickness of the original skin,
d is the rivet diameter,
σ_b is the skin bearing strength,
σ_{ult} is the skin ultimate strength and
τ is the rivet shear strength.

The repairer is to choose the larger result from equations 2-2 and 2-4.

- Use edge distances of at least twice the rivet diameters [3].

- Carefully drill and deburr (smooth) the rivet holes before riveting [3].

- Figure 2.2 shows typical rivet hole patterns for double and triple or multiple rows, respectively [2].

- When using countersunk rivets, avoid countersinks deeper than three-fourths the thickness of the countersunk sheet. This prevents the so-called "knife edge condition," which results in a high stress concentration. The knife-edge condition drastically reduces the fatigue life of a repair [5,6].
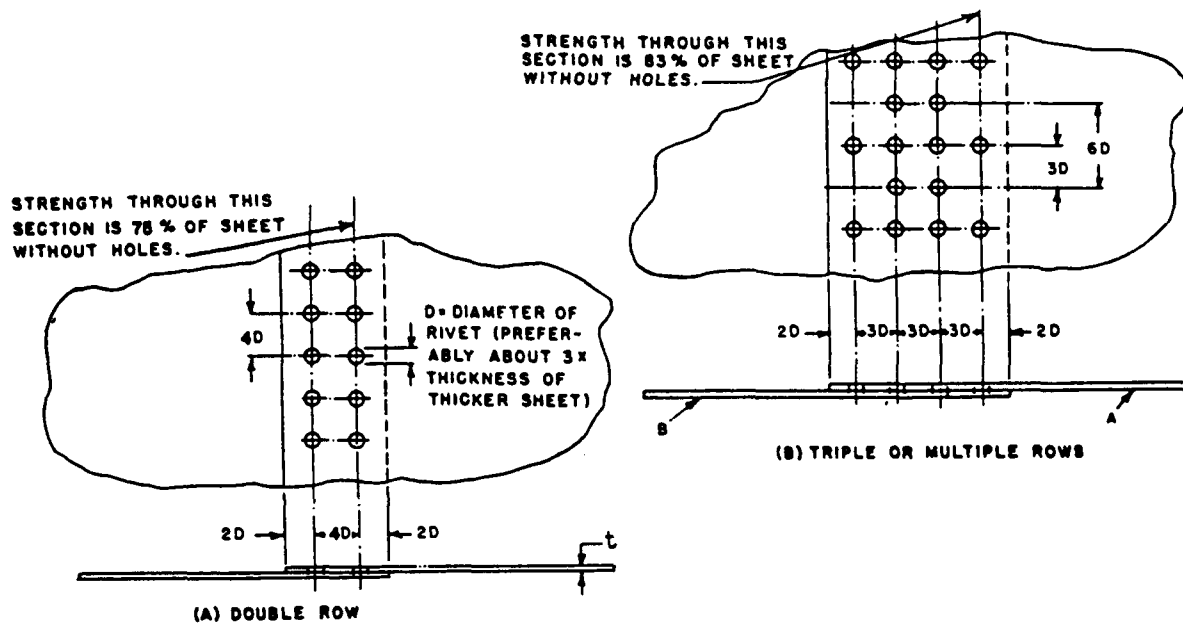
Figure 2.2. FAA-recommended rivet pattern for structural repair [2].

2.3 Improvements to the Current Practice

Most authors on the subject of airframe structural repair never explicitly mention fatigue. A repair mechanic could closely follow these guidelines to produce a riveted repair that is a fatigue "hot spot." Some examples follow.

- Simply stop-drilling a crack produces only a marginal retardation of crack growth. The stop-drilled crack behaves as a sharp notch with a high stress concentration. In the example shown in figure 2.1, the 51 mm crack stop-drilled with a 3 mm diameter hole gives a stress concentration factor (K_t) of 9.4. A better practice

would be to stop-drill the crack with a larger hole (4.8 mm, K_t = 7.7), then fill the hole with a cold-expanded rivet. This procedure increases the remaining fatigue life of the unrepaired sheet by up to two orders of magnitude [6]. If filling the hole is not possible, a larger hole should be made at the crack tip before patching. Otherwise, the crack will quickly re-initiate.

- The use of two rivet rows instead of three in attaching a patch to a pressure skin results in high bearing loads at each rivet. The fatigue life of the repair is drastically reduced compared with three rivet rows [5].

- Employment of rivet pitch values of three times the rivet diameter (3D) results in a peak stress concentration of more than three times the gross skin stress. A minimum rivet pitch of four times the rivet diameter reduces peak stresses, enhances fatigue life and improves residual strength in the presence of a crack [5].

- Figure 2.2 (from the FAA) advocates leaving out alternating rivets in the first and last rivet rows. This is not a good idea because they are already the fatigue-critical rows. Fewer rivets in the end rows simply increase the bearing load carried by each remaining rivet, reducing fatigue lives [7].

Figure 2.3. Sketch of repair made to Lockheed Electra lower wing skin.
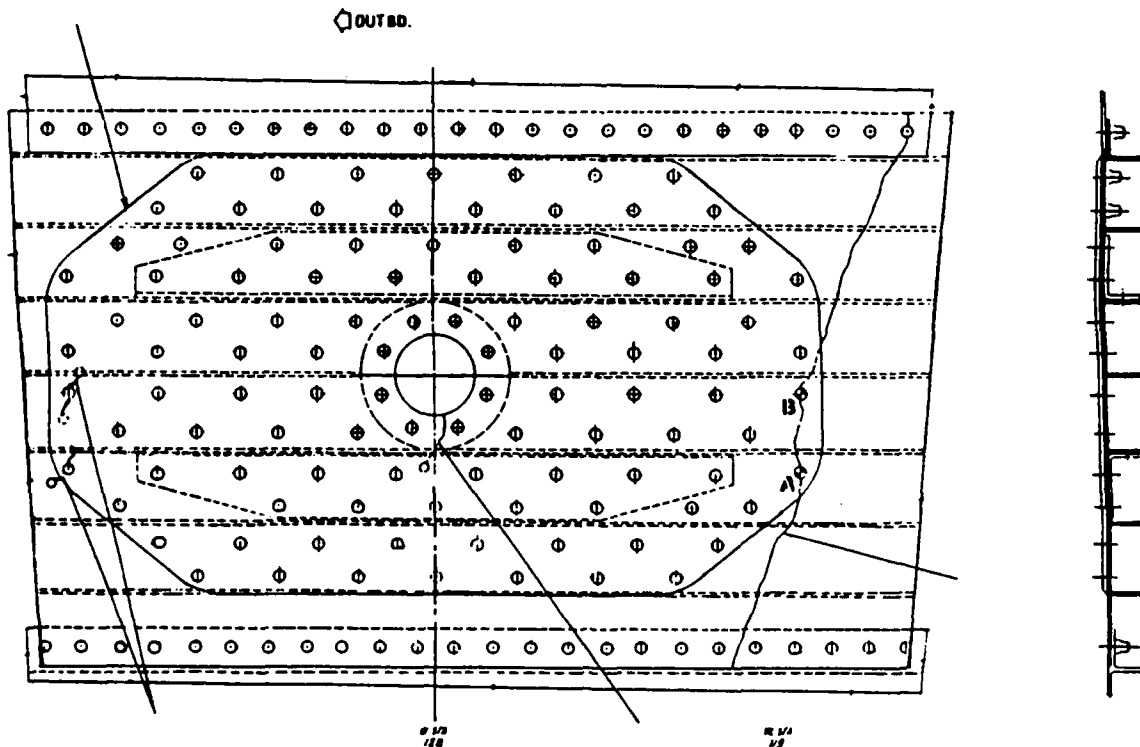
An example taken from airline service illustrates the previous point. A Lockheed Electra developed cracks in the lower wing skin next to an access cover. The resulting repair, shown in figure 2.3, was "designed" to reinforce the cracked portion by placing a doubler plate over the original blade-stiffened wing skin.

The wing was a "fail-safe" design with multiple span-wise planks. To provide additional strength in the repair, the designer specified two riveted angled triplers inside the blade stiffeners. These ran along the outer edges of the access hole. The outer two rivet rows used four rivets each, while the other (inner) rows all had six [8].

The consequences of placing an extremely stiff patch with a reduced number of rivets in the critical first and last rows can be easily understood. Approximately 10,000 flight hours after the repair was performed, new fatigue cracks initiated at the inboard critical rivet row (A and B in figure 2.3). The design obscured the inspector's view of any new cracks until the cracks joined up and grew to a complete fracture of the wing plank, when "moderate turbulence" caused a 450 kg fuel loss that forced the pilot to make an emergency landing. Upon further inspection, investigators found similar hidden cracks that developed from the outboard critical rivet row as well.

To improve the fatigue performance of riveted repairs, one should treat them as a structural modification involving (small) lap joints. This difference in treatment is primarily a matter of perspective. While maintainers approach riveted repairs as static strength-critical items, designers consider joints to be fatigue-critical. The detail design of a joint is "the most important single factor affecting the fatigue life [5]." The following apply:

- Use symmetrical joints whenever possible.

- Minimize local eccentricity.

- Avoid abrupt changes in cross-section.

- Relieve critical first fastener row loads by:
  - tapering the joint or patch (see figure 2.4),
  - employing a thin auxiliary doubler one extra row (figure 2.5), and
  - using a smaller or more flexible rivet in the critical row.

These recommendations are often easier to incorporate in a new design than in a repair. Lack of space or equipment may severely limit repair methods. The repairer may have

access to only one side of the structure. He may lack milling equipment or simply not have enough time available to perform such a complex repair.
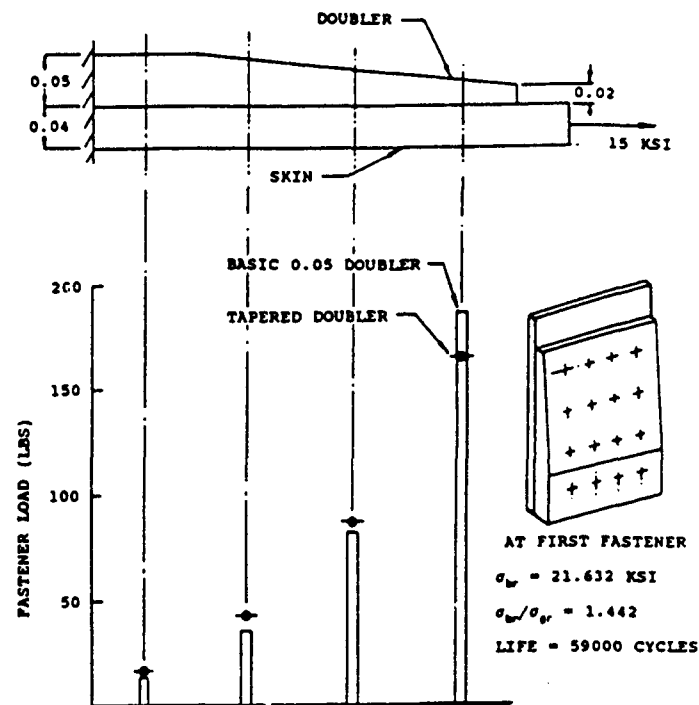
Figure 2.4. Tapered joint for reduction of critical first row fastener loads [1].
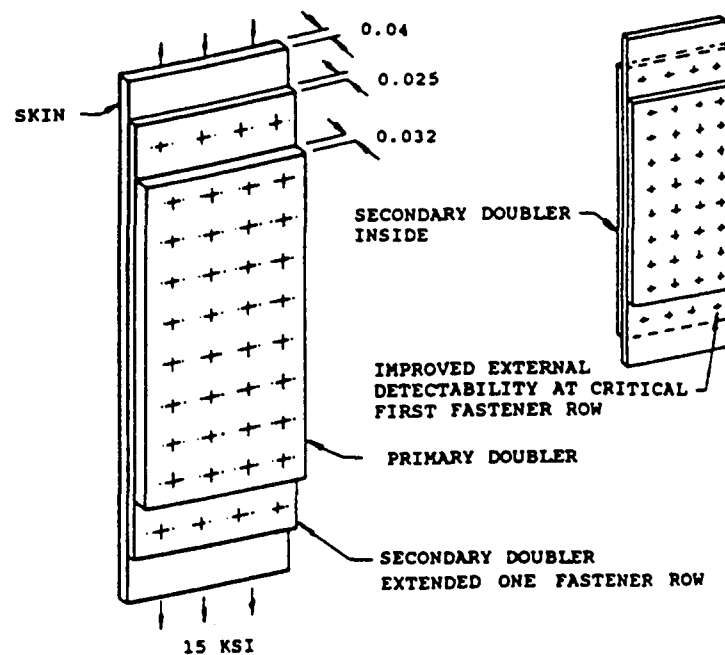
Figure 2.5. Example of a thin auxiliary doubler extended by one row
to improve fatigue life and inspectability [1].

16

The load transfer in and around a repair is sometimes even more complex than in joints. With a lap joint, all loads are transferred from one sheet to the next. The one-dimensional case shown in figure 2.6a illustrates the point. The patch repair, however, is a case of (at least) two-dimensional load transfer.

The patch must carry the loads of the (now-)removed skin. If the patch is too stiff (figure 2.6b), it also can attract loads from outside the patch area, resulting in high stresses in the load transfer areas. This causes fatigue problems in the skin area immediately next to the patch. If a patch is not stiff enough (figure 2.6c), the damage being repaired will have too high a stress. This could cause a fatigue crack to re-initiate from the original damage. (The latter case is uncommon.)
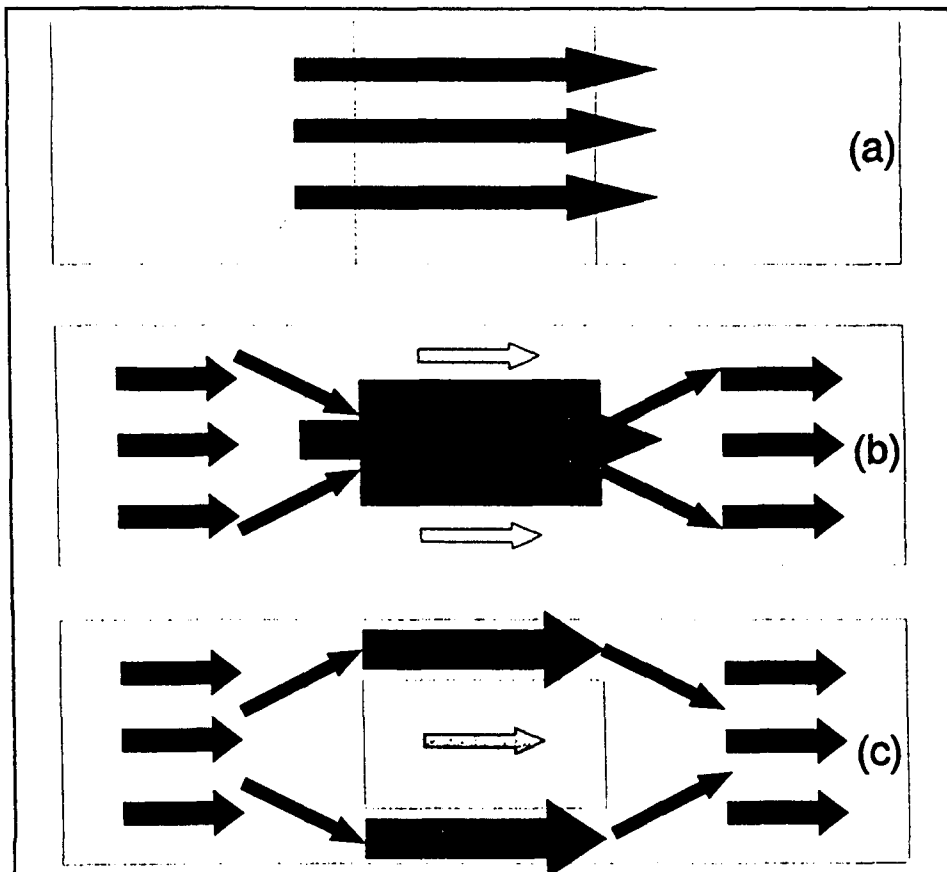
Figure 2.6. Schematic of load transfer in a) lap joint, b) stiff patch repair, c) flexible patch repair.

A patch needs to be just stiff enough to carry its share of the load without attracting the load from surrounding structure. Also, the patch must possess sufficient static strength and fatigue resistance so it does not become the weak link. This can be hard to achieve with conventional patch materials.

2.3.1 Fingers for Inspectability

The externally applied repair patch often hides any fatigue cracking in the critical first rivet row of the repaired skin. Cracks under externally applied repair patches are sometimes difficult to detect before they grow to critical size, as shown by the Aloha incident [9]. When the substructure allows, patches can be applied internally, leaving the outer skin visually inspectable. (This practice is also preferred from an aerodynamic point of view.)

Swift [1] attacks the problem of inspection in the detail design of fatigue resistant joints. His method combines long fatigue life (durability) with good damage tolerance (residual strength in the presence of cracks) and excellent external inspectability. The so-called "fingered" inner doubler shown in figure 2.7 "effectively reduces the inner doubler area between the first and second fastener rows, thus relieving the first fastener load. This results in [reduced] skin bearing stress and improves crack initiation life. This configuration offers the highest fatigue life coupled with excellent external inspectability."

The Douglas DC-10/MD-11 longitudinal fuselage joints employ this type of doubler on new structural joints [10]. Unfortunately, geometric (space), economic and time constraints sometimes rule out use of the fingered inner doubler in repair.
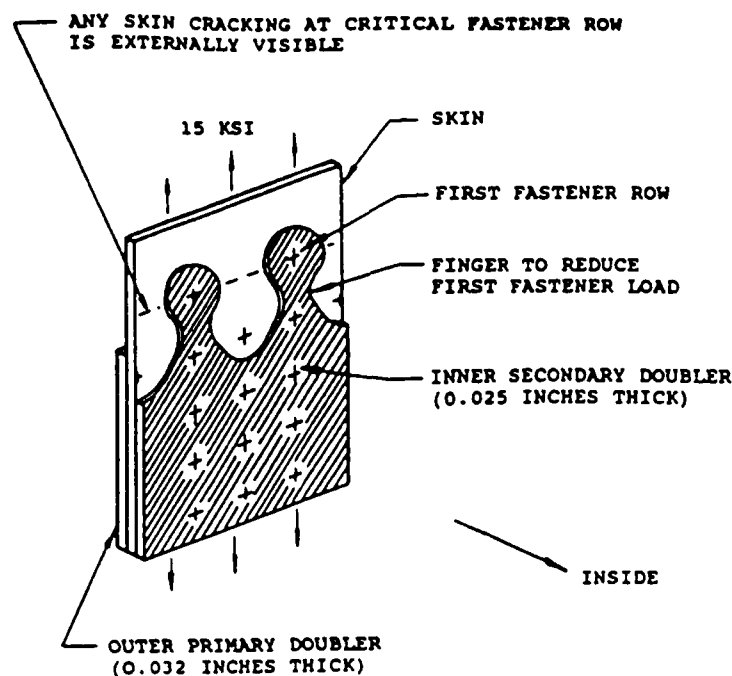
Figure 2.7. "Fingered" inner doubler for long joint fatigue life
and external visual inspection [1].

2.3.2 "Soft" Patches

A new approach to smoothing the load transfer into a riveted patch will be presented here. It involves the use of the high-strength, moderate modulus material GLARE 3 as a patch for monolithic aluminum skins.

GLARE 3 is a fiber metal laminate made up of thin sheets of aluminum alloy adhesively bonded to cross-plied glass/epoxy composite prepregs. It is one in a family of laminates designed to replace monolithic aluminum in fatigue-critical fuselage skin applications. One of its outstanding properties is an extremely slow fatigue crack growth rate, combined with high residual strength in the presence of damage. GLARE laminates are also about eight percent less dense than aluminum and are resistant to impact damage and burn-through. The laminates can be drilled, cut, formed, riveted and bonded much like monolithic aluminum alloys [11-18].

The mechanical properties of GLARE 3 are listed in comparison with 2024-T3 in table 2.1.

Table 2.1 Mechanical, Physical Properties of 2024-T3 and GLARE 3

Material	Lay-up	Thickness, mm	E_{11}, E_{22}, GPa	$\sigma_{0.2}$, MPa	σ_{ult}, MPa	$\sigma_{bluntnotch}$ MPa
2024-T3	monolithic	variable	72	359	455	440
GLARE 3	2/1-0.3	0.85	60	315	662	452
GLARE 3	3/2-0.2	1.1	57	295	804	469
GLARE 3	3/2-0.3	1.4	58	305	717	456

Using "soft" (i.e., low modulus) patches for the repair of aluminum fuselage structures was first discussed in [11]. The basic concept of using "soft" patches is to transfer the load previously carried by the removed or failed structure without attracting too much additional load into the repair area. It will be more fully developed in section 2.4.

2.4 Finite Element Analysis of Riveted Repairs

"Don't fight forces, use them."

R. Buckminster Fuller, *Shelter* (1932)

The finite element analysis method was chosen to complement traditional direct methods of strain measurement used in stress analysis. Strain gages, photoelastic coatings and thermoelastic measurements are practically limited to the outer surfaces of structural elements. In contrast, the finite element method gives one the ability to look inside the structure of interest. Because of the significant amount of bending involved in most riveted patch repairs, finite element analysis offers the best opportunity for analyzing and understanding their mechanical response to flight loads.

This section presents the results of extensive modeling done to understand the load transfer in rivet repairs. Supporting strain gage measurements provide confidence in the accuracy of the model.

2.4.1 Specimen Geometry

A typical riveted patch repair to a fuselage skin is shown in figure 2.8. The sketch shows a 50 mm diameter hole cut into a 600 by 300 mm sheet of 1.0 mm thick 2024-T3 aluminum. The hole simulates the removal of corrosion or impact damage. The repair must accomplish two primary purposes: It provides an alternate load path in place of the removed material, and it acts as a pressure seal for the fuselage skin. The configuration is not intended to represent an optimized repair. Rather, it serves as a typical baseline for comparison of various patch concepts and their influence on the overall load transfer picture in the structure. The dimensions of the modeled specimen, also used in the fatigue tests discussed in the following chapter, were set by the limits of the fatigue testing equipment.
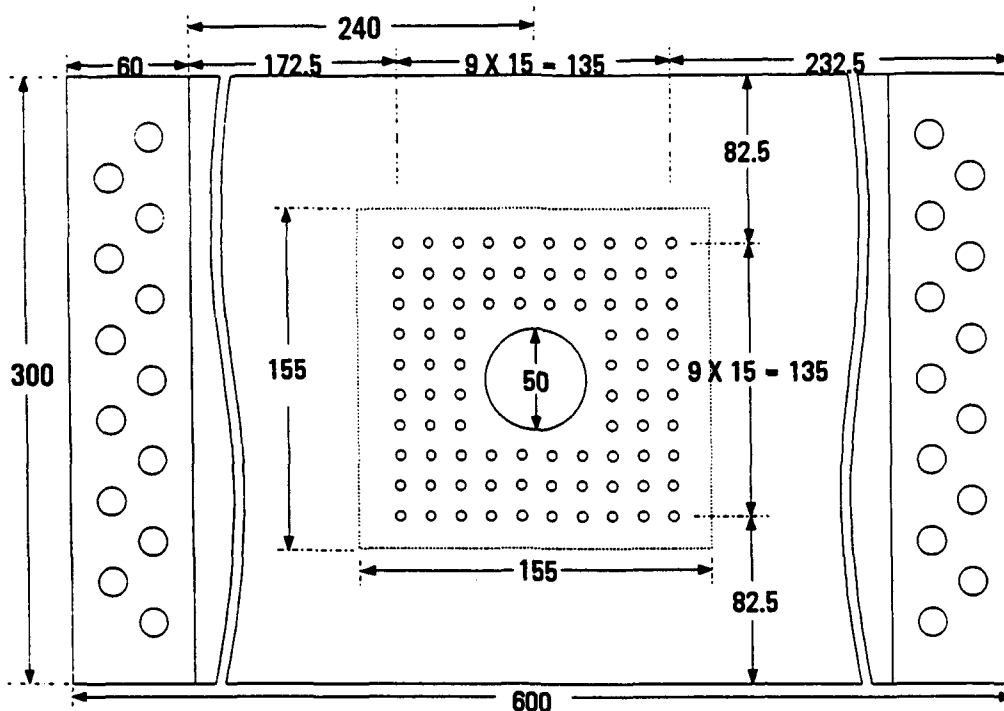
*Figure 2.8. Riveted repair specimen used in this study for
finite element analysis and fatigue testing.*

The four riveted patch types modeled in the analysis are summarized in table 2.2.

Table 2.2. Summary of riveted patch types modeled in this analysis.

Patch material	Patch thickness, mm	Patch extensional stiffness (Et), GPa-mm
2024-T3	1.0	72
2024-T3	1.3	94
2024-T3	1.3/0.7 tapered	72/50
GLARE 3, 2/1 layup	0.85	51

The thickness tapered 2024 patch is shown in figure 2.9. The monolithic patch thicknesses were chosen by the previously discussed "rules of thumb." The GLARE patch thickness was picked to match as closely as possible the blunt notch strength of the original 2024 skin. The ratio of the extensional stiffness (elastic modulus multiplied by thickness) of the GLARE 3 and the untapered 1.3 mm 2024 patches was approximately 0.54. All patches were attached with NAS1097AD countersunk rivets of 3.2 mm diameter.
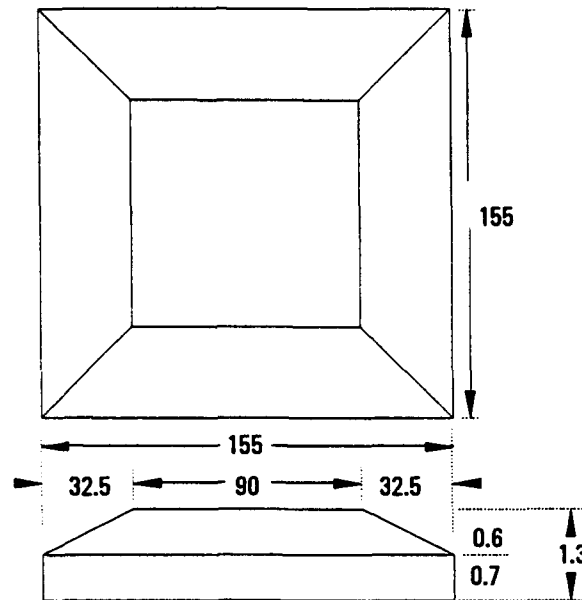
Figure 2.9. Tapered patch used in this study.

2.4.2 Finite Element Modeling

The point of the finite element modeling was to provide a clear picture of the role of patch selection in the load transfer into and around the repair joint. Model pre- and post-processing was accomplished with PATRAN; finite element calculations were performed using ABAQUS version 4-9.

The model was treated as a geometrically non-linear problem. In this sense, sheet rotation due to secondary bending was allowed. Shear and normal deflection and rotation of the rivets were also modeled. The material responses were treated as linear elastic. This is considered a valid assumption: The calculated stress levels remained below the yield point of 2024-T3. All materials were treated as isotropic, a slight inaccuracy with the GLARE 3 patch. Although E_{11} and E_{22} are equal in GLARE 3, the material is neither isotropic nor homogeneous. This simplification was considered to have minimal impact on the results.

2.4.2.1 Elements. The skin and patch were modeled as a series of 8-noded quadratic quadrilateral shell elements (PATRAN Quad/8/16, ABAQUS S8R). The rivets were modeled as quadratic three-noded beam elements (PATRAN Bar, ABAQUS B32). The

circular cross-section beam element used to represent the rivet allowed bending, shear and extensional loading of the rivet to be considered. The beam diameter was chosen to match the rivet diameter of 3.2 mm.

rivet (beam)

patch shell element

skin shell element
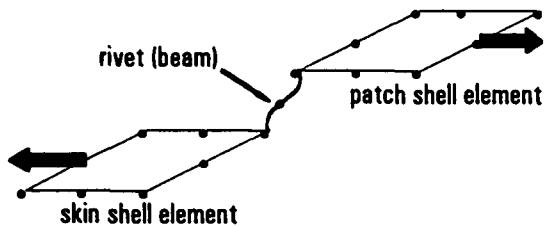
2.4.2.2 Rivet Attachment. Beams were used to model the skin-to-patch connection in the method discussed by Seegers [19] and Slagter [20]. Figure 2.10 at left shows the connection schematically. The rivet holes were not explicitly modeled.

This method of connecting beams to the eight-noded shell elements is effective for modeling concentrated shear loads such as rivets. It allows rivet flexibility and rotation to be analyzed accurately, although certain assumptions made in the modeling are inaccurate. The modeled beam length is only one-half of the actual rivet shank, which reduces rivet flexibility. On the other hand, the attachment of the beam at its end points means the modeled beam is more flexible than a real rivet, supported by the rivet hole over its entire length.

The use of beams avoided the stiff "hard points" of multi-point constraints or spot welds, which overestimate the magnitude of first rivet row loads. The connection of the beams at a single point in the shell element resulted in a stress singularity at that point. This in turn induced high local tensile stresses in the shell. (Real rivets cannot pull but only transmit load through bearing on a surface.) The rivet section forces are input into the model at the infinitely small nodal (attachment) point, resulting (locally) in very high stresses. These local disturbances damp out quickly, and overall model accuracy is good, as will be shown in the following section.

By not explicitly modeling the rivet holes, the output does not directly yield numerical values of the expected high stress concentrations of the rivet holes. Furthermore, no attempt was made to model the contact between rivet and hole, which involves plasticity and friction effects. For a more detailed look at these effects, the reader is referred to the work of Slagter [20] and Müller [21].

The alternative of using a solid modeling approach for each of the 21 rivets and 42 rivet holes in the present model was considered (briefly). It would have resulted in an untenably

large model that exceeds the scope of this work and the available computer facilities. On the other hand, reducing the size of the model to a simpler three-rivet lap joint was not seriously considered either. Such a simplification would have eliminated from consideration the complex biaxial load transfer around the cutout that was the primary goal of the modeling.

Because of the implicit hole modeling and the beam attachment method, stress and strain contours within approximately two rivet diameters of the attachment nodes are considered inaccurate. No direct comparisons of indicated stress levels can be made at the implicitly modeled rivet holes with levels shown at the explicitly modeled cut-out. Nonetheless, the effect of patch selection on the global load transfer picture is presented clearly within the previously discussed limits.

2.4.2.3 Boundary Conditions. Modeling took advantage of the specimen symmetry about the quarter axes to reduce computational times by modeling only one-fourth of the specimen. Additional boundary conditions for the models included displacement and in-plane rotation restraints parallel to the loaded edge(s), to simulate the load introduction clamps. Fixed displacements corresponding to a stress of 100 MPa in the equivalent undamaged, unrepaired sheet were imposed in the primary (hoop) load direction on the loaded edge. For the biaxial case, an additional fixed displacement corresponding to a stress of 50 MPa was imposed in the secondary (longitudinal) load direction. A schematic of the uniaxial load case boundary conditions is shown in figure 2.11.

Load cases representing both uniaxial and biaxial tension were analyzed. The uniaxial model was 500 mm long by 300 mm wide, with 155 mm square patches. This geometry matched exactly the unclamped dimensions of the static and fatigue specimens discussed in chapter 3. The biaxial model was modified to 500 mm square to give sufficient width for accurate distribution of secondary (transverse) loads. A biaxiality ratio of 0.5 was chosen representative of typical fuselage pressure loads.
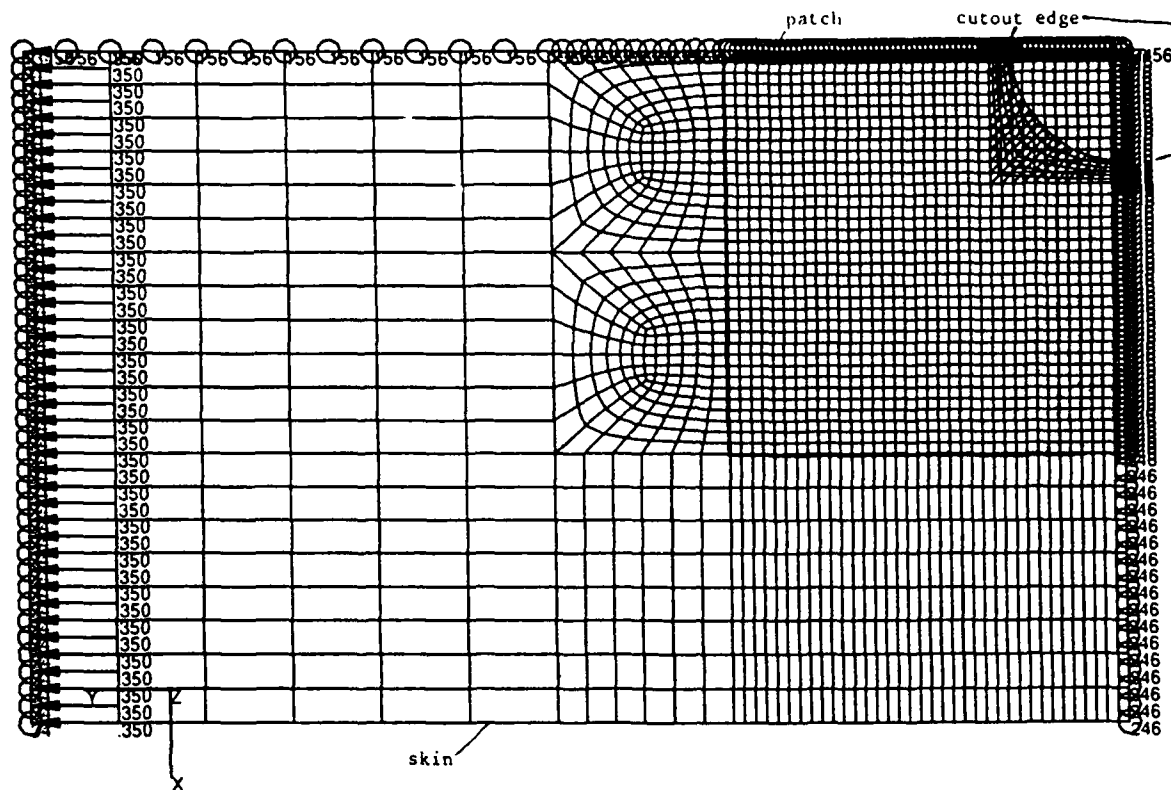
Figure 2.11. Uniaxially loaded model with boundary conditions shown.

2.4.3 Convergence Study

Before detailed calculations of the model began, a series of computer runs were made with increasing mesh densities to ensure the accuracy of the results. The critical areas were expected to be at the side of the cutout and in the rivet area. For the cutout area, an unpatched open hole model was used for refinement testing. Refinement continued until mesh densities resulted in a stress concentration factor of about 3.1, consistent with elastic theory [7] for a hole in a finite width plate. In the rivet load transfer area, a single 15 mm-wide strip with three 3.2 mm diameter "rivets" was used, as shown in figure 2.12. Mesh densities of four elements per rivet pitch gave good convergence. The mesh densities were relaxed in areas of low or no stress gradient.

25
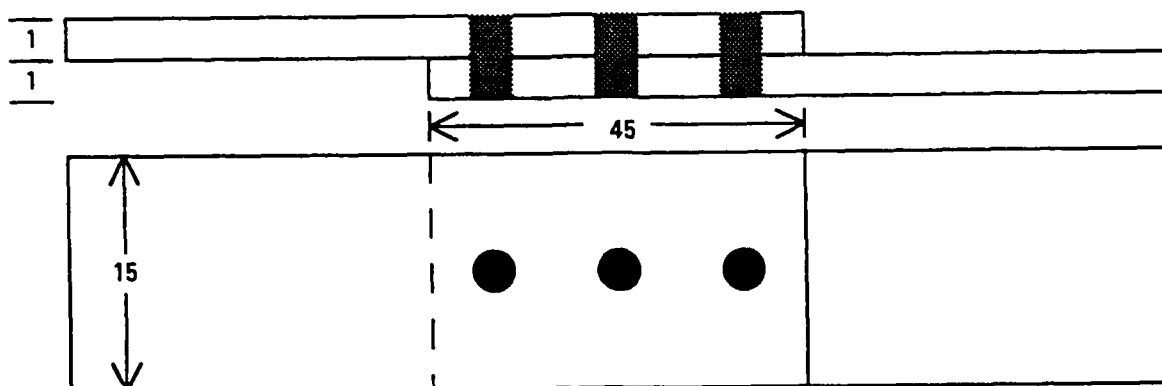
Figure 2.12. *Strip model used for convergence studies. All dimensions mm.*
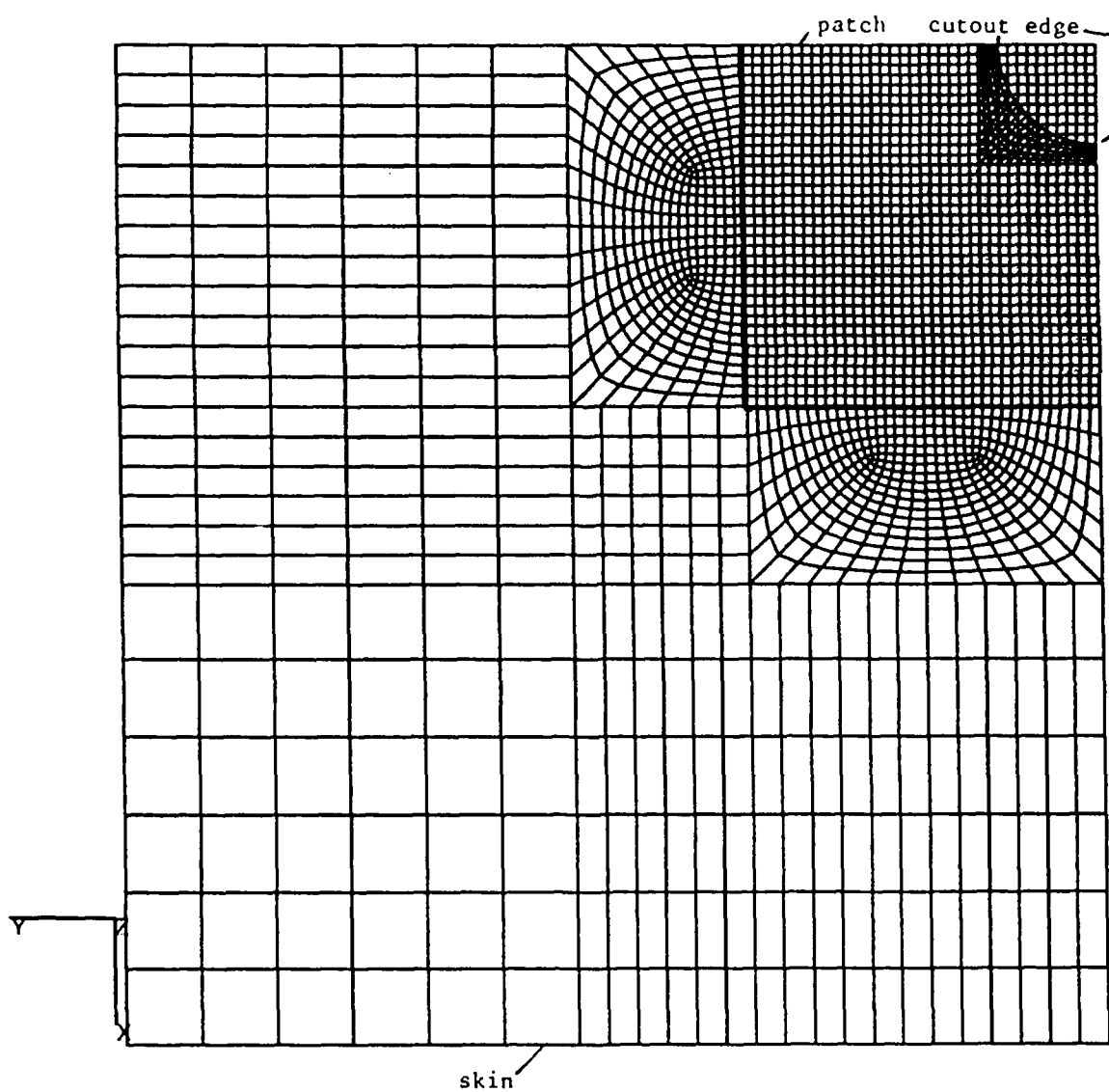
Figure 2.13 *Final arrangement of the biaxially loaded finite element model.*

Figure 2.13 shows the final arrangement of the biaxial case finite element model. The model contained approximately 3,000 shell elements, 21 bar elements and about 10,000 nodes, resulting in over 60,000 degrees of freedom. The uniaxial model was only slightly smaller, with 9,135 nodes and approximately 55,000 degrees of freedom.

2.4.4 Validity of the Model

The output of the convergent finite element calculations is compared in this section with measured and observed results from statically loaded specimens.

2.4.4.1 Displacements. Figure 2.14 shows the deformed shape of the uniaxial specimen (deformations exaggerated for clarity). As expected, the patched area experiences considerable bending deflections. The inner surface of skin experiences the maximum bending tension at the outer rivet row. However, realistic direct strain measurements are extremely difficult in this area, underscoring the utility of the finite element method. The deformed shapes were consistent with those observed during the tests.

UNIAXIAL 100 MPA 1 MM 2024 RIVETED PATCH
ABAQUS V4-9-1 5-MAY-93 14:24:31 2961 9135
PROCEDURE 1 TIME STEP 1 INCREMENT 3

Figure 2.14 Deformations of the uniaxially loaded model.

2.4.4.2 Rivet load distribution. The results of the ABAQUS calculations of first row rivet bearing forces are presented in figure 2.15 for the uniaxial case. Figure 2.16 shows the biaxial case. In both, the effect of the patch stiffness can be seen to have a large effect on the rivet forces. The stiffest patch attracts the highest rivet loads in the first row, which should have a negative influence on fatigue life. The GLARE patch, with the lowest stiffness, has the lightest first rivet row loads.

The major difference between the two load cases is primarily a function of the magnitude of the loads applied. The corner rivets (displayed on the left side of the graph) feel the highest resultant loads.
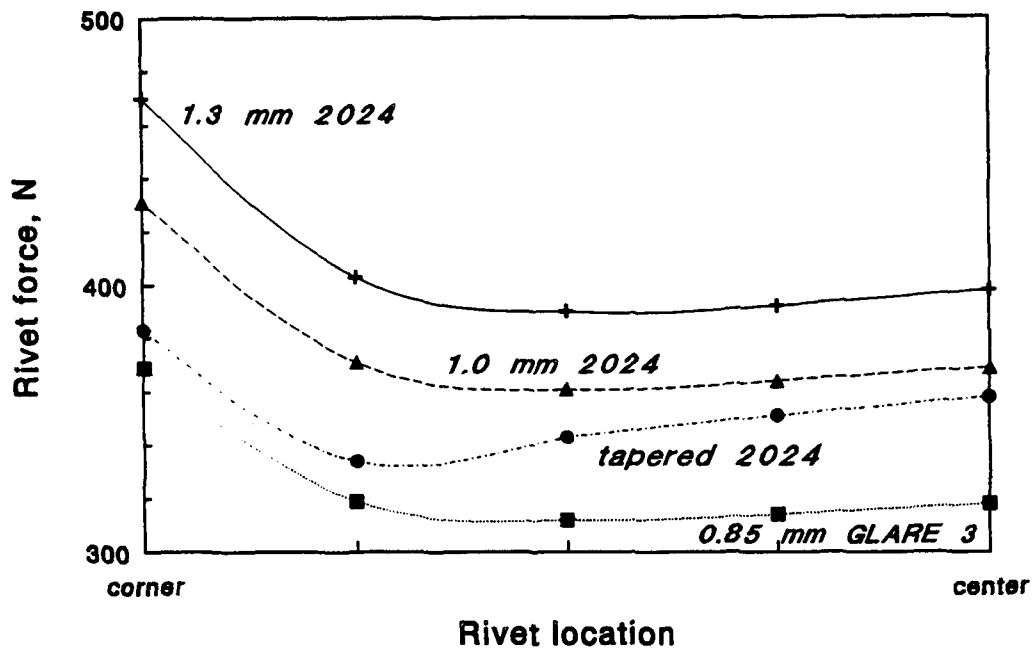
Figure 2.15 Beam section resultant forces for the first rivet row, uniaxially loaded model.

In the uniaxial case, this high shear loading of the corner rivet is primarily a Poisson effect. This is consistent with the results of Müller [21], who found the same behavior in unstiffened riveted single lap specimens. The longitudinal extension of the sheet causes lateral contraction, resisted by compressive loading on the patch. Most of this load is reacted with high transverse shear loads in the outer rivet columns, including the corner rivets.

In the biaxial specimens, the corner rivet can be considered as twice located in the first row: once for the longitudinal and again for the transverse load. In contrast with the uniaxial case, the biaxial loading places the patch in transverse tension.

The tapered patches in both load cases display a small dip in the section force carried by the rivet adjacent to the corner. This is possibly due to being located in an intermediate thickness zone (1.0 mm) compared with its neighbors.
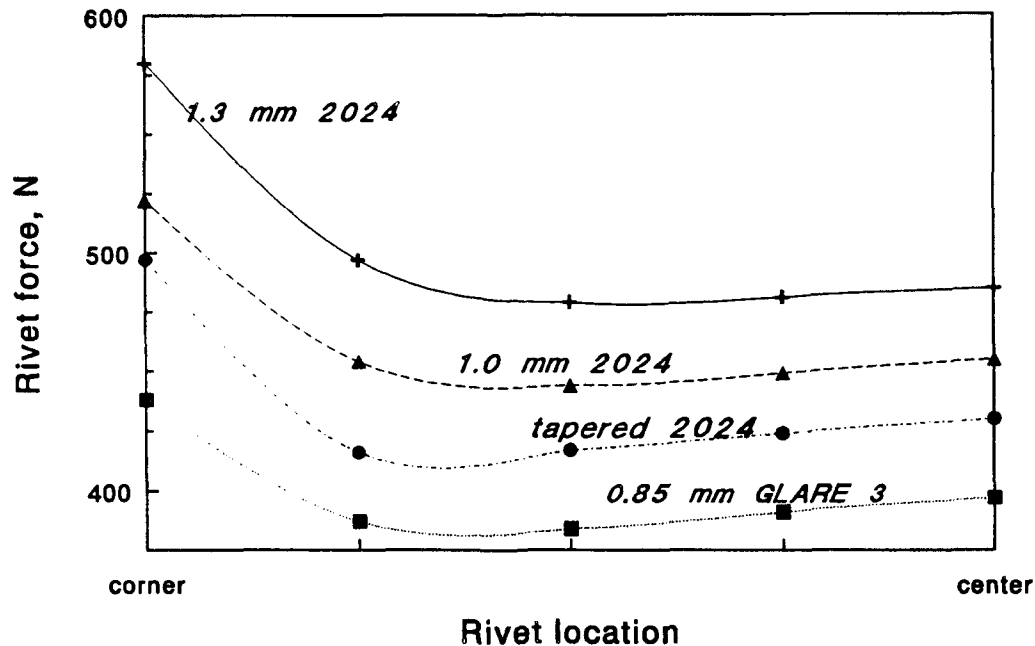
Figure 2.16 Beam section resultant forces for the first rivet row, biaxially loaded model.

Figure 2.17 compares the rivet bearing loads for the uniaxial and biaxial cases (1.3 mm monolithic patch). One can immediately see the increase in bearing magnitude in both directions for the biaxial case. Furthermore, the sense (direction) of the transverse bearing force is reversed. The Poisson force on the patch for the uniaxial case is compressive; the biaxial case puts the patch in transverse tension.
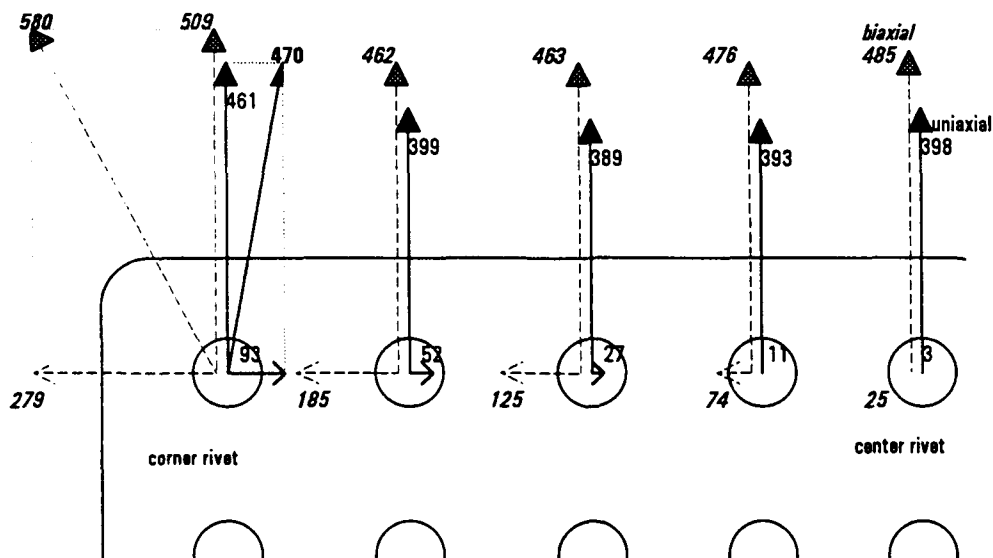
Figure 2.17. Comparison of first row rivet bearing forces, 1.27 mm aluminum patch, uniaxial and biaxial load cases. Forces are in Newtons.

30

2.4.4.3 Comparison with measured strains. Two riveted specimens identical to that shown in figure 2.8 were manufactured and instrumented with electrical resistance strain gages. The GLARE 3 and tapered 2024 patches were used. Strain gages were limited by practical considerations to the outside surfaces of the specimens. Thus, comparison of the model predictions on the inner, more highly loaded surfaces is not possible. However, if the predictions of the model are accurate on the outer surfaces, they can be considered equally accurate elsewhere. (Of course, the area around the rivet holes is excepted.)

Table 2.3 Comparison of measured and predicted strains in riveted patch specimens.

Location	measured strain	predicted strain	percent difference
GLARE 3 patch			
skin: 1. 12 mm beyond first rivet row, center	1077	1150	-6.8
2. between 1st/2nd rivet rows, corner	1335	1350	-1.1
3. adjacent to patch, mid-length	1420	1250	+12
4. adj. to patch, back side, mid-length	1040	1150	-11
5. cutout edge	2455	2350	+4.3
6. free edge, patch side, mid-length	1402	1400	+0.1
patch: 7. center, cut-out side	1155	1025	+11
Average difference (%)			**6.6**
tapered (1.3/0.7 mm) 2024 patch			
skin: 1. 12 mm beyond first rivet row, center	1593	1600	-0.44
2. between 1st/2nd rivet rows, corner	1478	1250	+15
3. adjacent to patch, mid-length	1274	1200	+5.8
4. adj. to patch, back side, mid-length	994	1100	-11
5. cut-out edge	1867	2100	-12
6. free edge, patch side	1382	1450	-4.9
patch: 7. center, cut-out side	813	750	+7.7
Average difference (%)			**8.1**

Test conditions: 100 MPa uniaxial tension
+ means measured strain magnitude exceeded predicted strain
- indicates predicted strain magnitude exceeded measured strain

Table 2.3 compares the results of the finite element model with the measured strains at selected locations of interest. Figure 2.18 shows the location of the gages. The average difference between measured and predicted was 6.6 percent for the GLARE 3 patch specimen. For the tapered 2024 piece, an average difference of 8.1 percent was

recorded. This slightly higher error in the tapered patch can be a result of the stepwise tapering done in modeling the patch. The test specimen had a smooth milled taper.

As expected, differences between the mathematical model and the measured strains were greatest in areas of high strain gradient. The measurements were especially suspect between rivets, where differences ranged up to 15 percent. This can be attributed to strain gage placement and the averaging function of a finite size strain gage. The agreement between measurements and calculations is satisfactory.
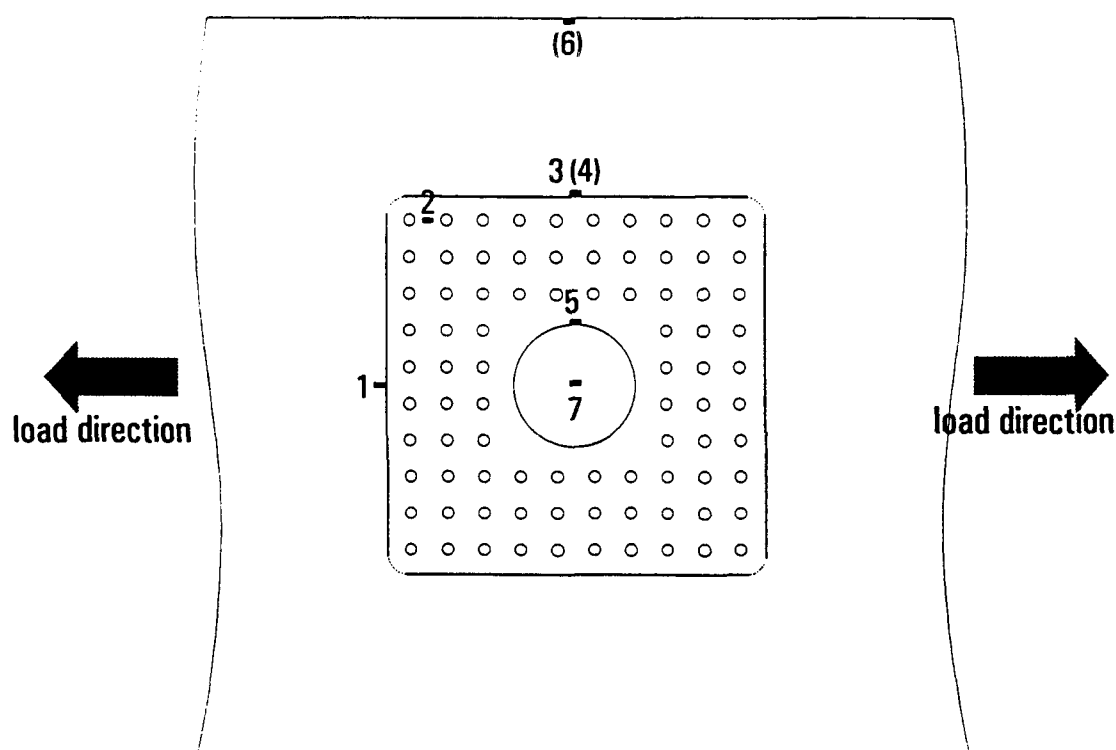
Figure 2.18. Location of strain gages referred to in Table 2.3. Parentheses indicate strain gages on the back (patch) side of the specimen.

Some details are worthy of mention. The less stiff GLARE patch is loaded to 42 percent higher strain than the thicker tapered 2024 patch. This is not anticipated to cause problems in the GLARE patch, stronger and more fatigue resistant than the monolithic material. However, the edge of the 2024 skin cut-out also has a higher strain with the soft patch: 2,455 microstrains with the GLARE patch (corresponding to 49 percent of the yield strain of 2024-T3) versus 1,867 for the tapered patch, an increase of 31 percent. The strain results are considered good enough to proceed with confidence in the model.

2.4.5 Finite Element Analysis Results

The results give a fuller appreciation of the role of patch selection on the load transfer into and around the patch. Two factors dominate the response. The first is the patch *extensional stiffness* (the product of elastic modulus and thickness or Et). Patch extensional stiffness determines bearing load transfer and overall load attraction of the patched area. The second is the patch *thickness* at the first rivet row, which sets the secondary bending stresses in the skin.

2.4.5.1 General. When one considers a single-sided riveted patch repair, it is conven-ient to divide the repair conceptually into three zones, as shown in figure 2.19.
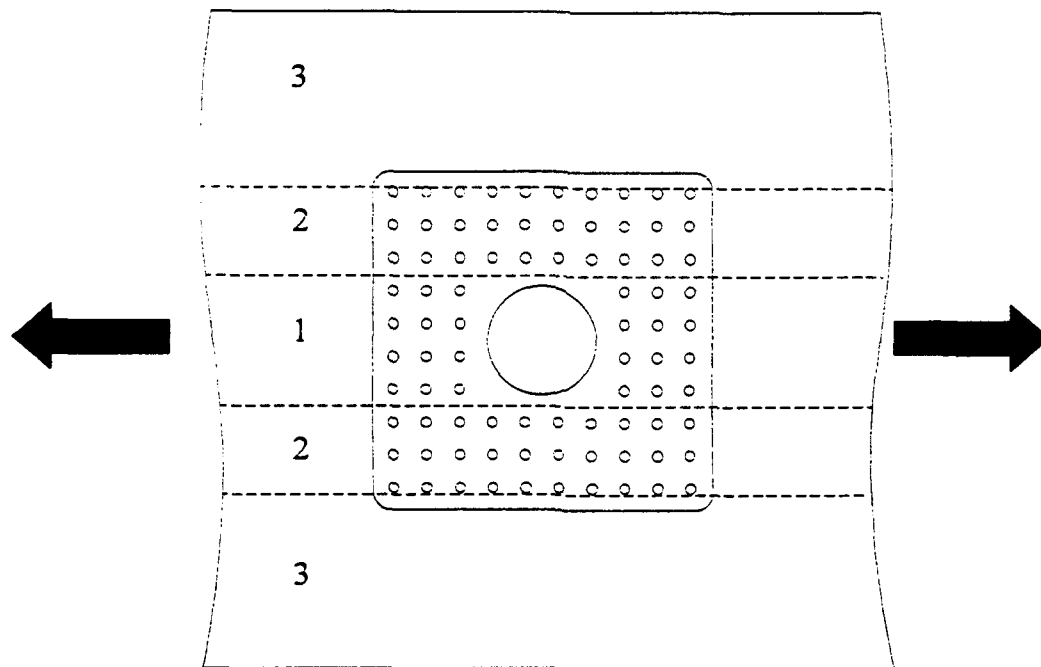
Figure 2.19. Conceptual model of three zones in a riveted repair.

Zone 1, the strip including the cut-out, may be considered as a special case of a single lap joint. On first examination, it must transfer *all* skin loads into the patch with only three rivet rows. Zone 2, by comparison, transfers only some of its load into the patch with five rivet rows. However, the load normally carried by the cut-out area actually has two potential load paths: into the patch and into the skin around the cut-out into zone 2. This contrasts with an ordinary lap joint, which must transfer all loads from the first sheet

to the second in one direction. As a result, zone 1 of the repair is expected to be the region of second highest load.

Zone 2 is a combination of a doubler strip and the underlying sheet to which it is riveted. This zone is the stiffest region of those under consideration here. Therefore, it attracts load from the less stiff areas on either side. The skin/doubler combination acts as an alternate load path for the material that has been removed from zone 1. Strain compatibility conditions mean high stresses occur in the skin just outside the patch. The step change in thickness induces bending, which has its highest tensile value on the inner surface of the skin along the first rivet row. In combination with the stress concentration of the rivet holes and the high bearing forces of the first row of rivets, this area should experience the highest stresses.

Zone 3 is the unstiffened area outside the repair patch. It sees the lowest stresses and experiences little bending. Depending on the relative stiffness of zones 1 and 2, zone 3 is *un*loaded slightly because of the load attraction of the stiffer zones.

2.4.5.2 Uniaxial Model. As mentioned previously, four patch types were modeled. Figure 2.20 presents plots of the first principal stress for the four patch cases under 100 MPa uniaxial tension. All plots show the inner surface of the repaired sheet that, due to bending effects, always experiences the highest stresses. The primary load direction is oriented along the y-axis in the figures. One can see the large influence of patch selection on the overall stress pattern of the repaired sheet. The results validated the decision to emphasize finite element modeling over surface strain measurement techniques (e.g., strain gages, photoelastic and thermoelastic methods). The outer surfaces were always loaded much less severely than the inner surfaces. This was primarily the effect of bending due to the step change in neutral axis at the outer rivet row.

A general impression can be gained by observing the size of the disturbed zone of the first principal stresses around the patches. From figure 2.20a (1.3 mm patch) to figure 2.20d (0.85 mm GLARE 3 patch), the disturbed area grows progressively smaller. A distinctive stress "hump" is visible around the doubler area (zone 2). This illustrates how the doubler attracts load; again, the stiffest patch shows the largest disturbed area. It is interesting to note the relative similarity of the overall patterns of the 1.0 mm and the tapered 1.3/0.7 mm aluminum patches (respectively, figures 2.19b and c).

Figure 2.21 shows the critical rivet areas in greater detail. (Recall that simplifying assumptions made during model construction render an area of approximately two rivet diameters around each rivet not meaningful. A circle of two diameters rings each rivet to indicate "off-limits" stress readings.) The differences between the various patches are subtle, but small differences in stress levels can translate to large differences in fatigue performance. As expected, the highest stresses again occur with the 1.3 mm patch (figure 2.21a). The 1.0 mm and tapered aluminum patches (2.21b and c, respectively) show approximately one fringe (5 MPa) lower stresses in the first rivet row. The GLARE patch (figure 2.21d) shows an additional reduction of one fringe.

In all uniaxial cases, the second rivet of the critical row was located in the most highly loaded region. For the tapered patch, the corner and second rivets were about equally critical. However, at distances more than several rivet diameters away, the larger disturbed zones centered on or nearest the second rivet. Beyond the first rivet row in the direction of the cut-out, the skin stresses decayed rapidly to below the nominal 100 MPa level.

The higher corner rivet loads have already been attributed to lateral (Poisson) contraction. Indeed, as shown previously in figure 2.15, the corner rivets consistently attracted about 15 percent higher bearing loads than the other rivets in the same row. However, the stress plots appear to indicate that the second rivet is located in the area of highest stress. As will be discussed in chapter 3, fatigue tests showed that cracks usually initiated from the second rivet in the critical outer rivet row. Although the corner rivet consistently feels the highest resultant section force, the second rivet usually shows the highest stresses and the largest disturbed zone in the contour plots.

The second rivet may feel the influence of neighboring rivets. The stress field of each rivet extends into the disturbed zone of the adjacent rivets. In a way, the second rivet "stands on the shoulders" of the two adjacent rivets and thus experiences the highest stresses. This superposition of stresses gives the second rivet the highest stress concentration in the uniaxial cases. The corner rivet has a slightly smaller disturbed area because it has interaction with only one highly loaded rivet.

The orientation of the first principal stress is almost parallel to the loading axis. Cracks occurring in the rivet rows should run roughly parallel to the rivet line, or roughly perpendicular to the loading axis.

A word of caution is in order regarding the stresses plotted at the edge of the cut-out. Recall that the rivet holes were not explicitly modeled. Hence, the stresses plotted in the region of the rivet holes are not directly comparable with the stresses shown at the explicitly modeled cut-out. Furthermore, stresses above 165 MPa were not differentiated for the sake of greater clarity in the area of interest.
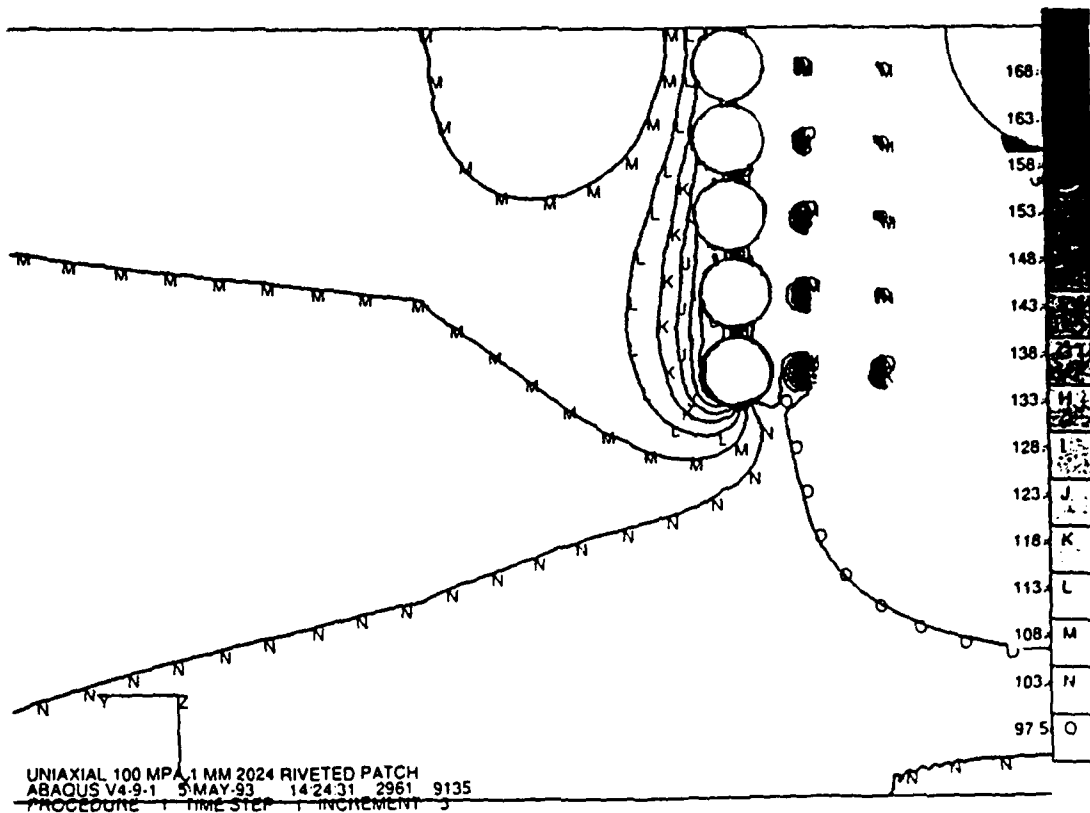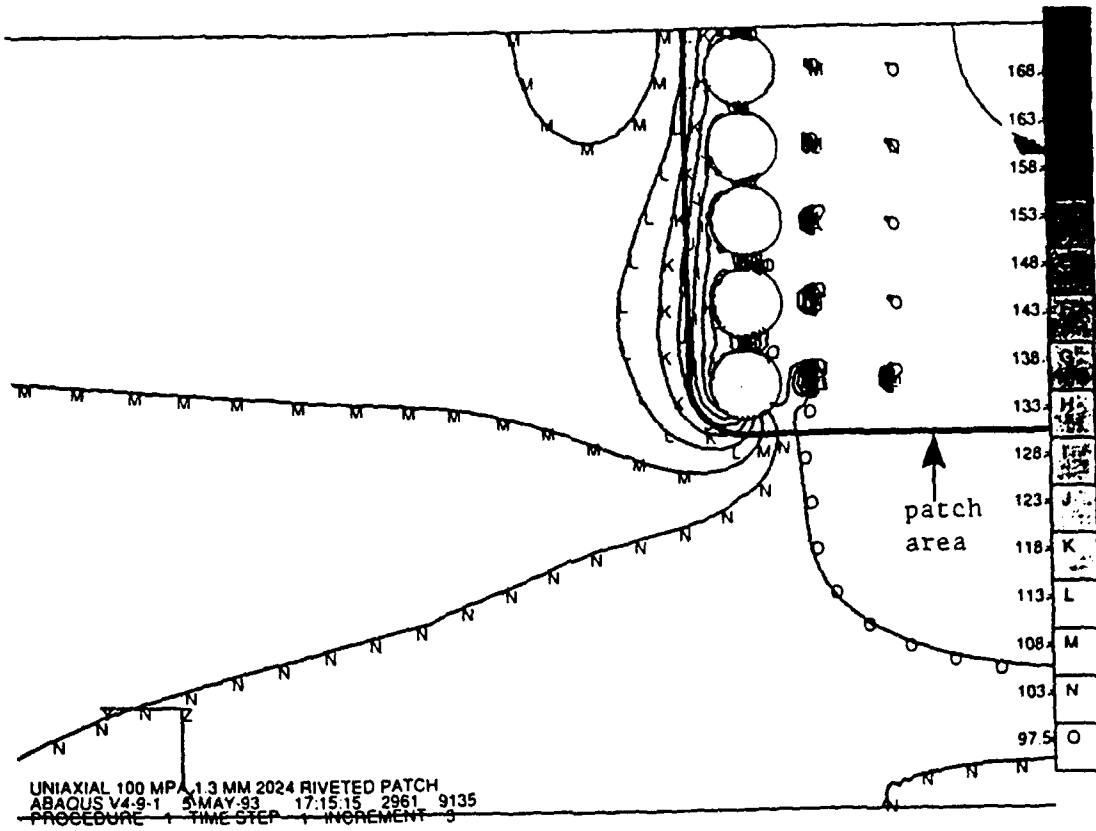
Figures 2.20a,b. First principal skin stresses of riveted patch designs, 100 MPa uniaxial tension. The circles indicate areas near rivets considered inaccurate.

UNIAXIAL 100 MPA 1.3/0.7 MM TAPERED PATCH
ABAQUS V4-9-1   1 JUN-93   17:33:43   2961   9135
PROCEDURE 1 TIME STEP 1 INCREMENT 3

UNIAXIAL 100 MPA 0.85 GLARE3 RIVETED PATCH
ABAQUS V4-9-1   1 JUN-93   16:24:55   2961   9135
PROCEDURE 1 TIME STEP 1 INCREMENT 3
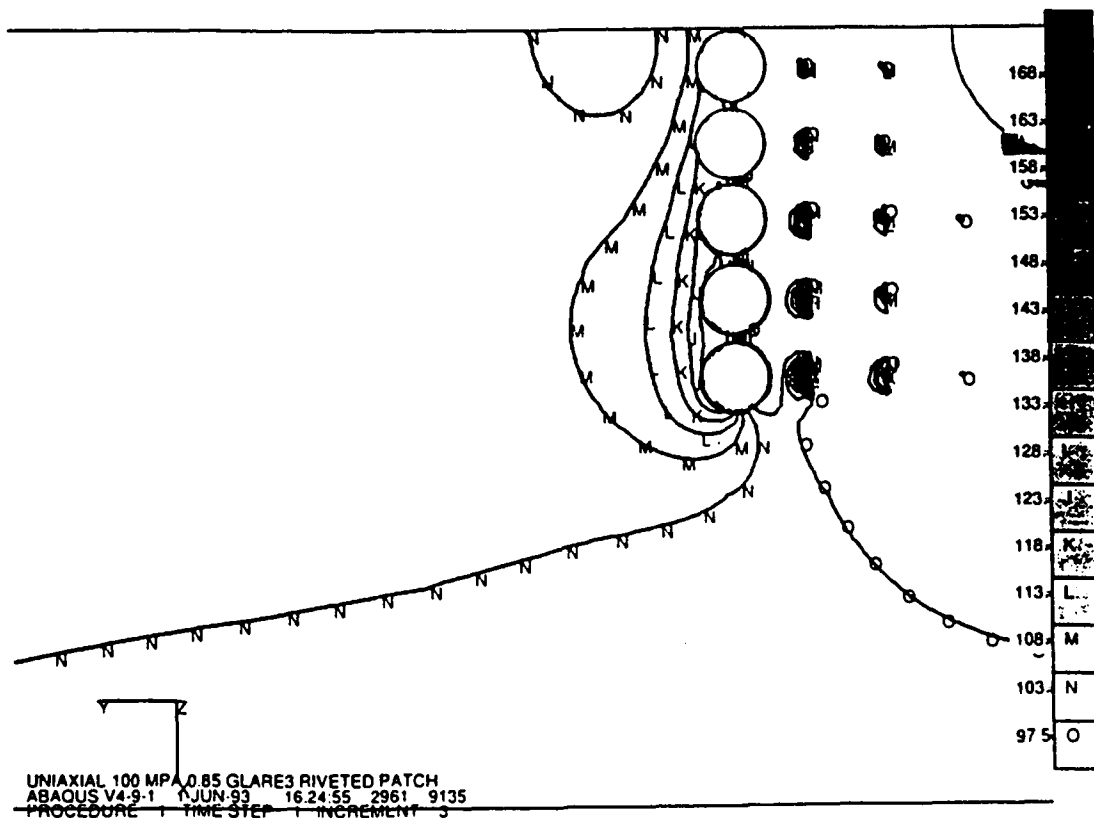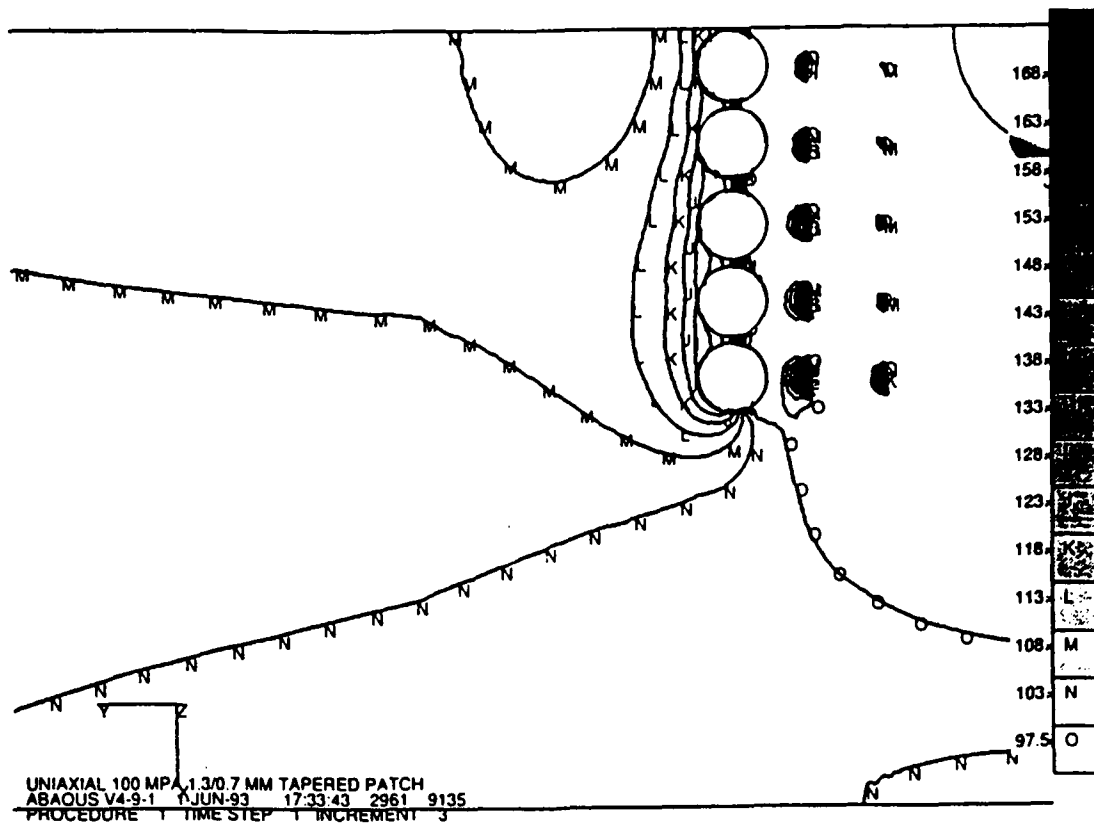
*Figures 2.20c,d.   First principal skin stresses of riveted patch designs, 100 MPa uniaxial tension.
The circles indicate areas near rivets considered inaccurate.*

38
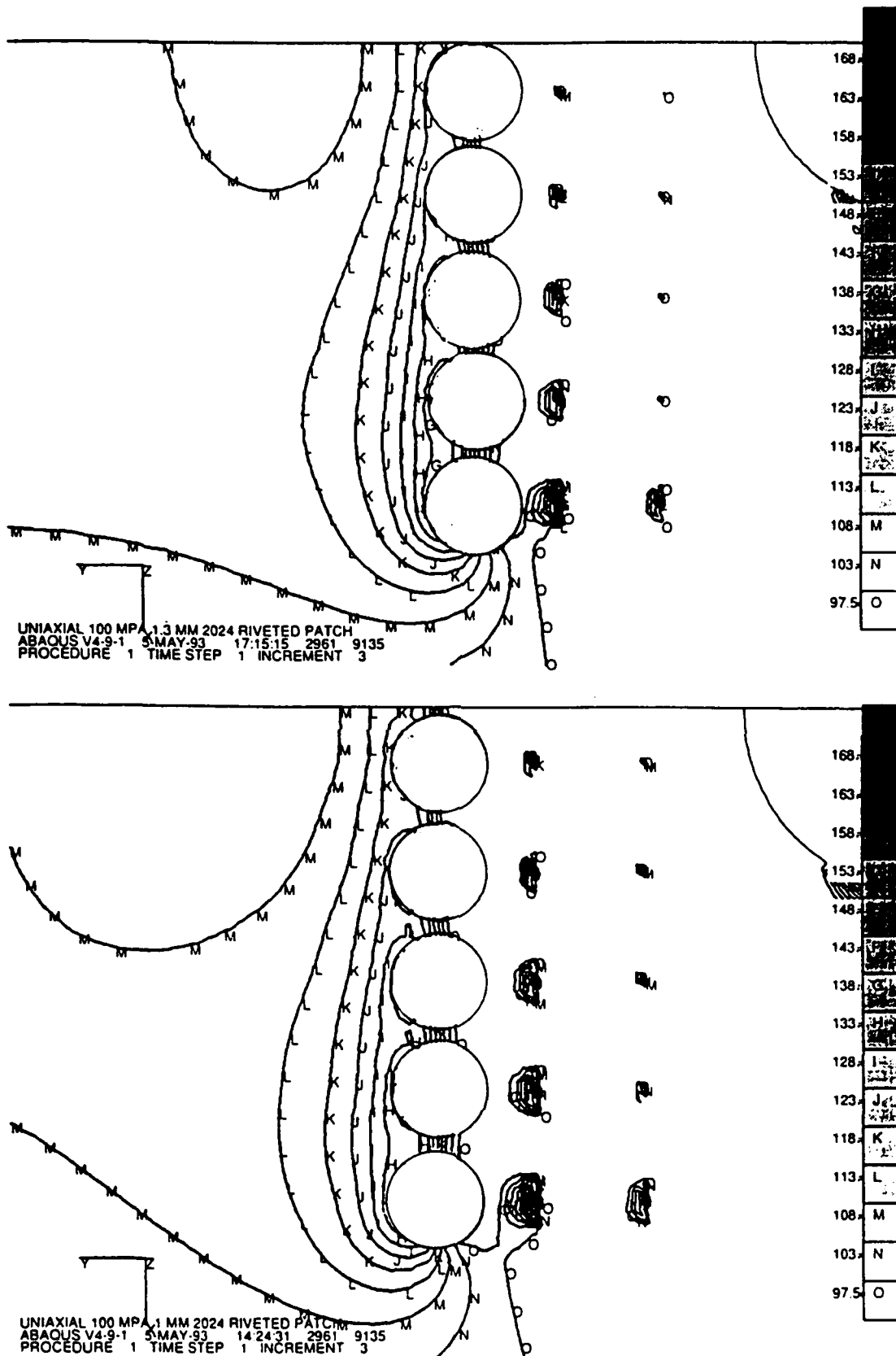
Figure 2.21a,b. *Detail of first principal stresses in critical rivet areas, repaired skin, 100 MPa uniaxial tension. Circles indicate areas near rivets considered inaccurate.*

UNIAXIAL 100 MPA 1.3/0.7 MM TAPERED PATCH
ABAQUS V4-9-1 5-MAY-93   15:20:42 2961 9135
PROCEDURE 1 TIME STEP 1 INCREMENT 3

UNIAXIAL 100 MPA 0.85 GLARE3 RIVETED PATCH
ABAQUS V4-9-1 5-MAY-93   16:19:02 2961 9135
PROCEDURE 1 TIME STEP 1 INCREMENT 3
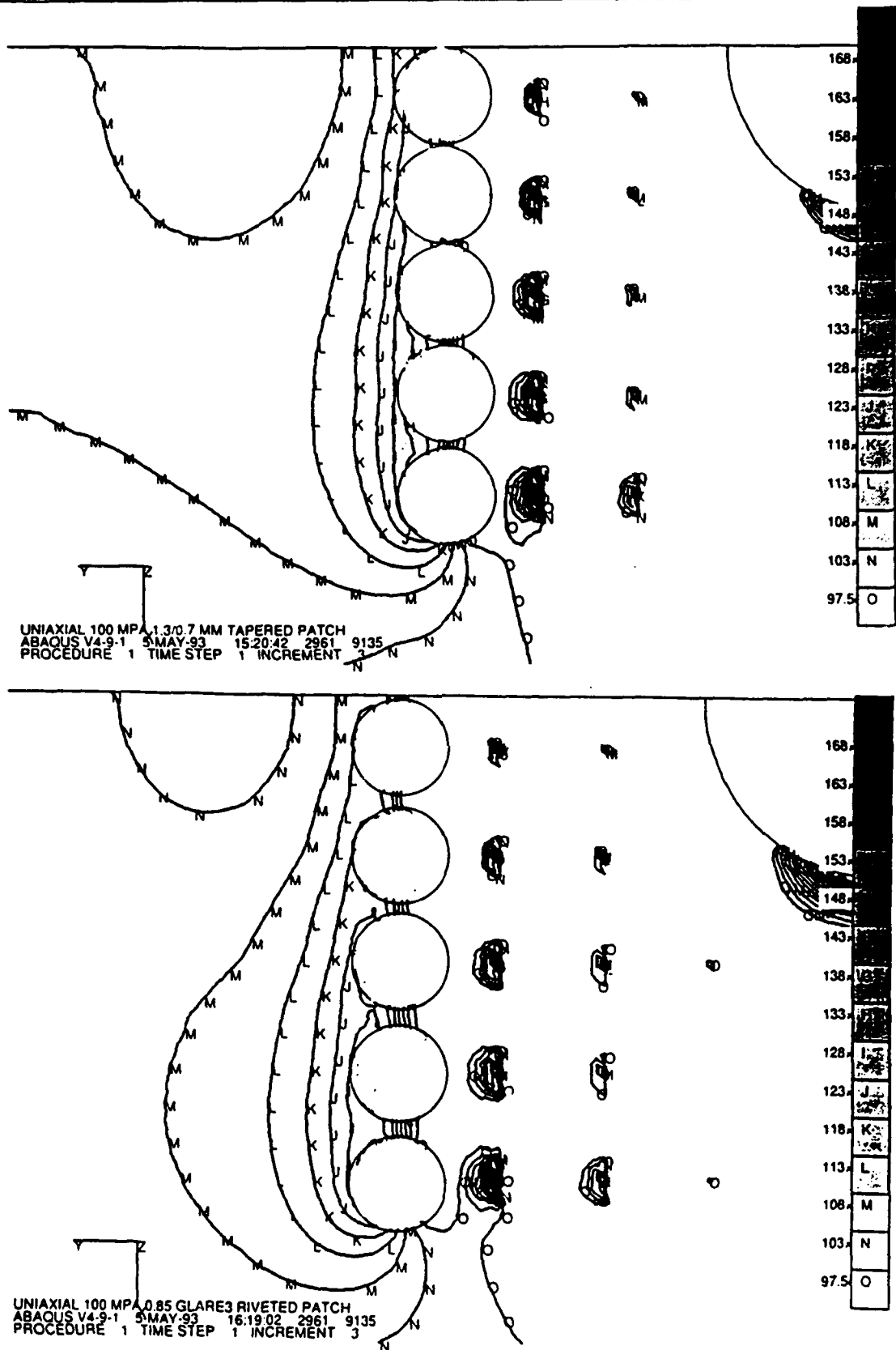
Figure 2.21c,d. Detail of first principal stresses in critical rivet areas, repaired skin, 100 MPa uniaxial tension. Circles indicate areas near rivets considered inaccurate.

2.4.5.4 Biaxial Model The principal stress results of the biaxially loaded model are presented in figure 2.22. The major differences in the output were caused by the addition of 50 MPa transverse tension (shown horizontally in the stress plots). The biaxiality resulted in a clear shift in the location of the most highly loaded rivet to the corner rivet. This was expected, as the corner rivet lies in both critical rows with respect to the two loading directions. The corner rivet is clearly the most highly loaded.

The relative rankings of the patches remained the same as with the uniaxial model: The skin panel with the GLARE patch again showed the lowest stress, although the magnitude of the differences increased.

The plots show the orientation of the principal stresses has rotated from the uniaxial cases. The lateral load in the biaxial case is a tensile load. This contrasts with a smaller compressive (Poisson contraction) load exerted on the patch in the uniaxial case. In combination with the change in critical rivet location to the corner, fatigue cracks that occur under biaxial loading should run out from under the patch very quickly. Depending on the actual biaxiality ratio encountered, crack orientation should be offset somewhat between the two principle load directions. In other words, fatigue cracks initiating in corner rivets should run skew from the first rivet row. This should make visual detection of a crack easier in case of an externally applied patch.

These results are consistent with the work of Miller and co-workers. They analyzed a riveted repair to a large rectangular cut-out adjacent to a stringer spanning two fuselage frames. The corner rivet holes in the skin were also found to be critical. Patch stresses were quite low [22].

It was unclear from the analysis where fatigue failure would occur in the biaxially loaded GLARE 3 specimen (at the cut-out or the corner rivet hole). Peak stresses recorded at the cut-out remained consistent with the uniaxial case. For example, with the GLARE 3 patch, the skin stress at the cut-out for the uniaxial case was 182 MPa. In the biaxial case, the stress level was 185 MPa. While appearing high, these stresses are about half the yield stress of 2024-T3.
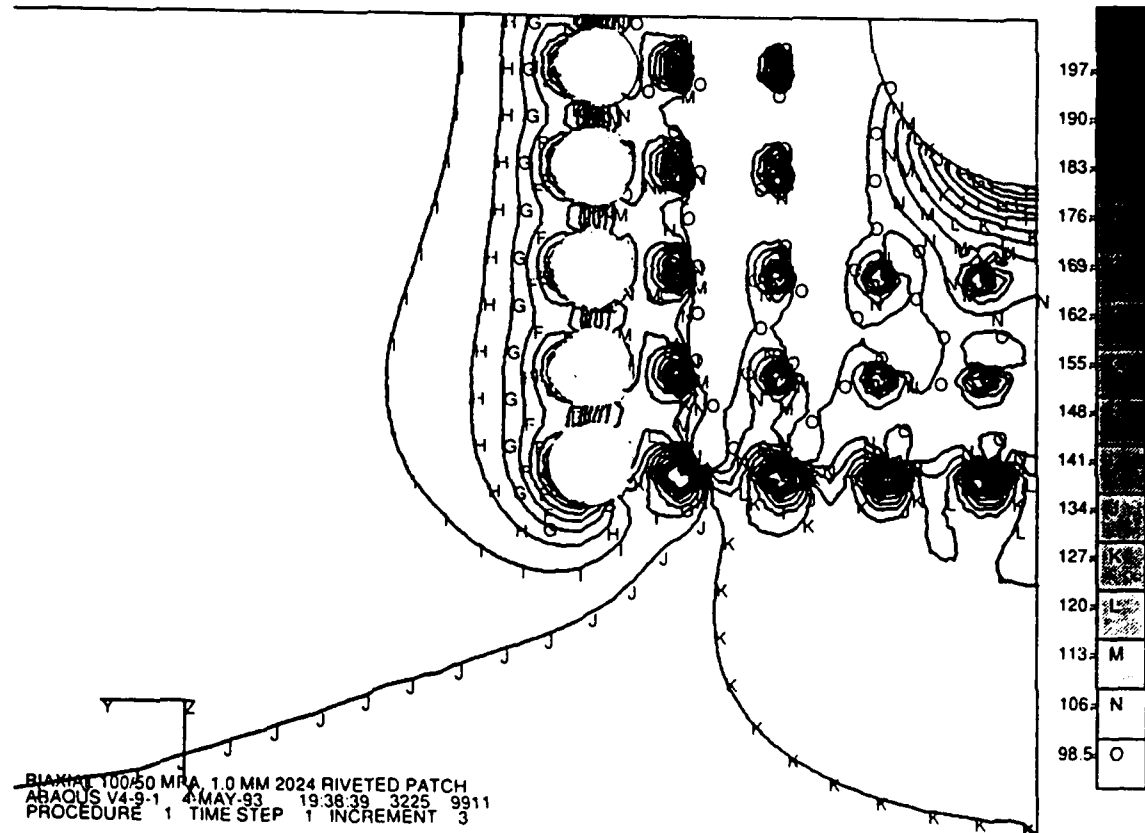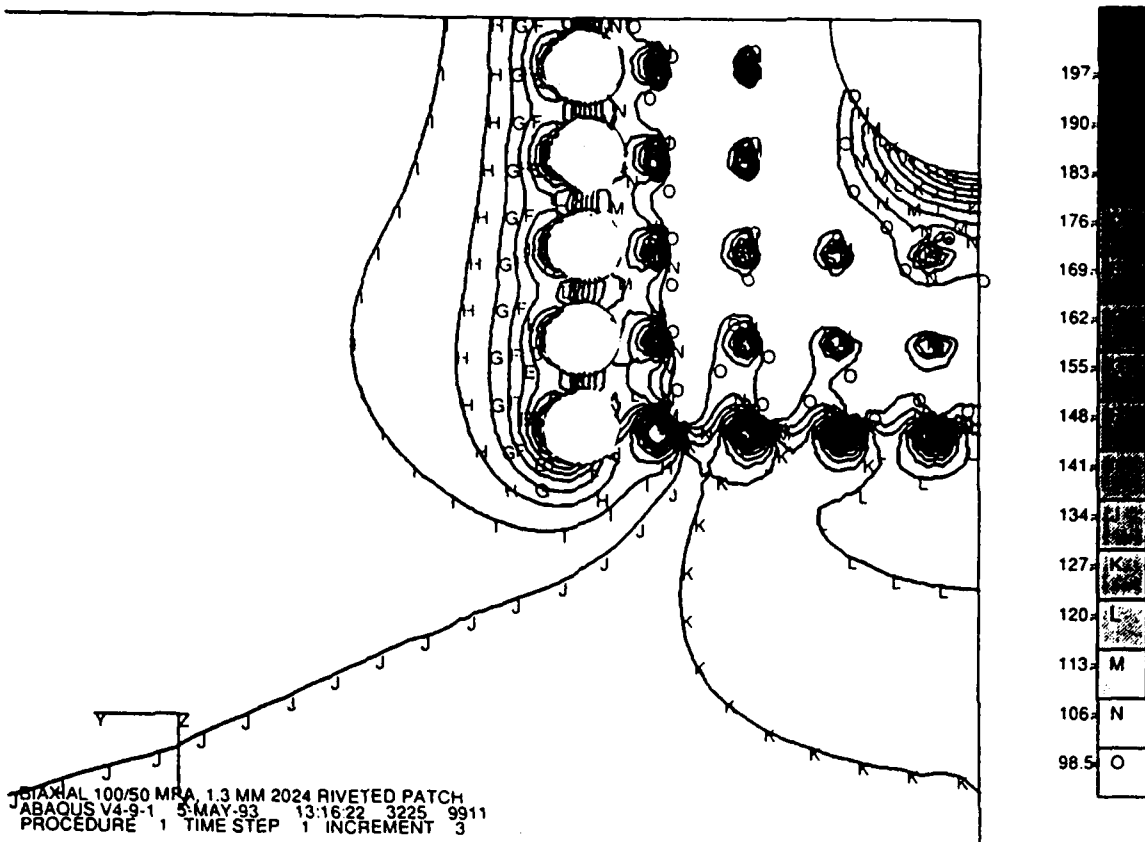
Figure 2.22a,b. Details of first principal stresses in area of first rivet row, biaxial tension.
Circles indicate areas near rivets considered inaccurate.

42

BIAXIAL 100/50 MPA, TAPERED 1 3/8 T MM 2024 PATCH
ABAQUS V4-9-1   4-MAY-93   20:56:05   3225   9911
PROCEDURE 1 TIME STEP 1 INCREMENT 3

BIAXIAL 100/50 MPA, 0.85 MM GLARE3 RIVETED PATCH
ABAQUS V4-9-1   5-MAY-93   12:04:27   3225   9911
PROCEDURE 1 TIME STEP 1 INCREMENT 3
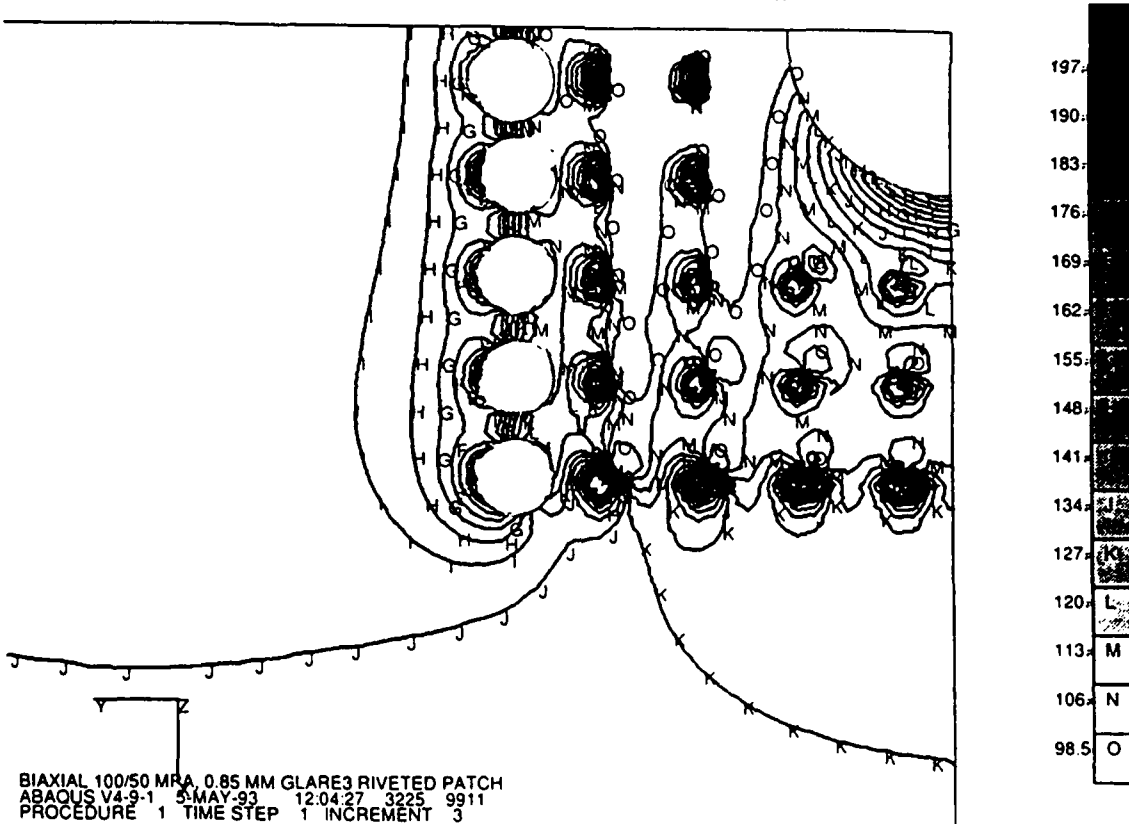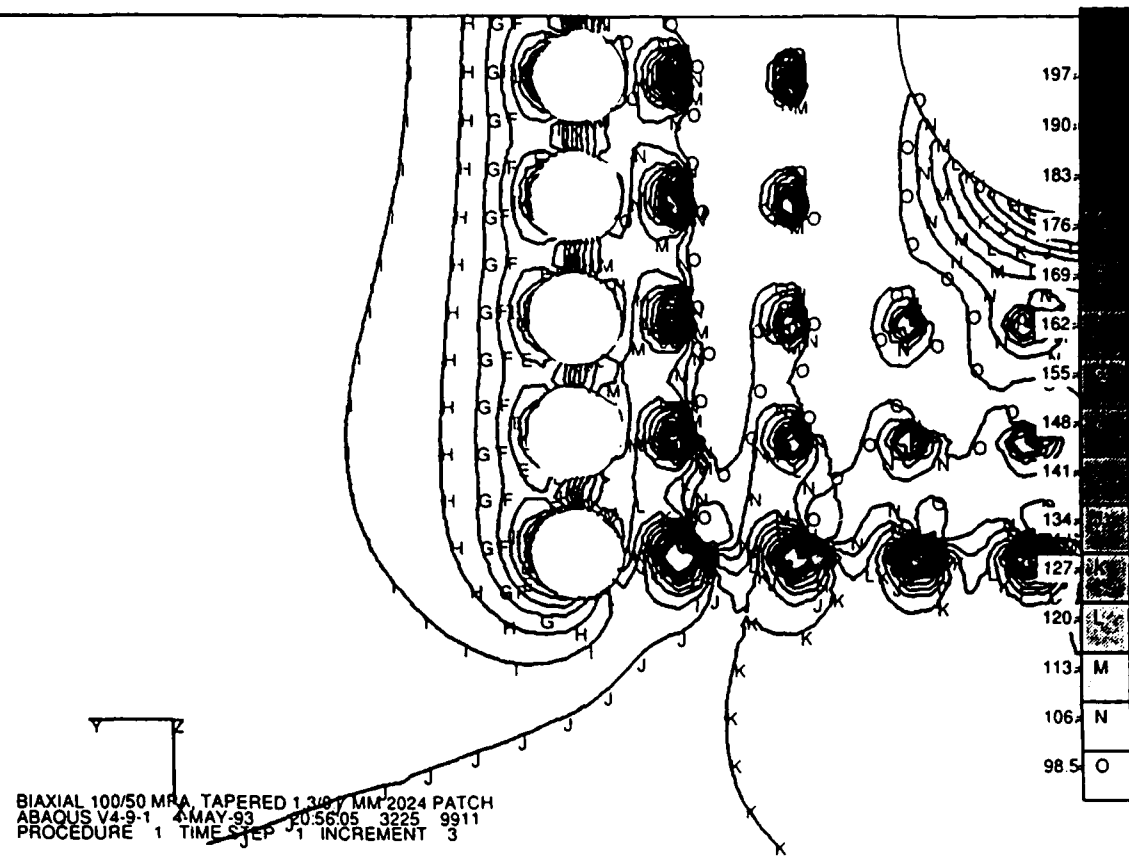
*Figure 2.22c,d. Details of first principal stresses in area of first rivet row, biaxial tension.
Circles indicate areas near rivets considered inaccurate.*

2.5 Discussion

The finite element results indicate that patch thickness and stiffness play dominant roles in the load redistribution around a typical repair configuration. Conventional aluminum alloy patches cause high stress concentrations at the first rivet row. These can lead to early cracking in the corner rivet (biaxial load case) or the adjacent rivet (uniaxial load case).

In the biaxial case, the high stresses at the corner rivet hole and the orientation of the first principal stress should make cracks easily visible. This predicted failure behavior involving riveted aluminum patch repairs casts doubt on the value of complex patch configurations like fingered patches to ease inspections. Thickness tapering or fingering of patches, while increasing the overall life of a riveted repair, do so at a high cost of time and labor. Furthermore, tapering only incrementally increases the amount of cycles during which a skin crack can be detected. This imposes a heavy inspection workload on the airlines.

High-strength, moderate-modulus patch materials like GLARE 3 give the lowest stresses at the critical rivet row, without the need for thickness tapering. The high-strength material allows a thinner patch to be used. This in turn reduces both secondary bending and first rivet row bearing loads, compared with a conventional aluminum patch. The low extensional stiffness of the patch attracts less load into the repair area.

2.6 Summary and Conclusions

Current methods of riveted repair of pressurized aluminum fuselage skins cause fatigue problems for operators. Besides their adverse affect on safety, conventional riveted repairs are accompanied by the unwanted economic burden of increased inspection requirements.

A new concept called "soft patching" has been analyzed for improving the load transfer and fatigue performance of riveted repairs to pressurized aluminum fuselage skins. Soft patching involves the use of thin, untapered patches of the high-strength, low-modulus fiber metal laminate GLARE 3 in place of thick tapered monolithic patches. This reduces load attraction to the repair zone, while diminishing bearing loads on the critical first rivet row and decreasing secondary bending.

References, Chapter 2

1. Swift, T., "Repairs to Damage Tolerant Aircraft," *Proc. 2nd Int'l Symp. on Structural Integrity of Aging Airplanes*, Atlanta, Georgia, 20-22 March 1990.

2. Advisory Circular 43.13-1A, "Acceptable Methods, Techniques, and Practices: Aircraft Inspection and Repair," U.S. Department of Transportation, Federal Aviation Administration, 1972.

3. Delp, F., R.D. Bent and J.L. McKinley, "Aircraft Maintenance and Repair, 5th edition." New York: McGraw-Hill Book Co., 1980.

4. Henshaw, J.T., "Airframe Construction and Repair (Metal Stressed-Skin Aircraft)." London: Sir Isaac Pitman and Sons, Ltd., 1943.

5. Niu, M. C-Y., "Airframe Structural Design." Hong Kong: Conmilit Press Ltd., 1988.

6. Landy, M.A., H. Armen and L.L. Eidinoff, "Enhanced Stop-Drill Repair Procedure for Cracked Structures," ASTM STP 927, J.M. Potter, ed. Philadelphia: American Society for Testing and Materials, 1986.

7. Schijve, J., "Fatigue, Static Tensile Strength and Stress Corrosion of Aircraft Materials and Structures," Report LR-630, Delft University of Technology, Department of Aerospace Engineering, Delft, The Netherlands, March 1990.

8. O'Brien, K.R.A. *et al.*, "The Impact of Long Service on the Fatigue of Transport Aircraft--Airworthiness Aspects," *Proc. 7th ICAF Symp.: Fail-Safe Aircraft Structures,* London, July 1973, pp. 3.3/10-25

9. "Aircraft Accident Report: Aloha Airlines, Flight 243, Boeing 737-200, N73711, Near Maui, Hawaii, April 28, 1988. Washington: U.S. National Trans. Safety Board, 1989.

10. Stone, M. "Fatigue and Fail-Safe Design Features of the DC-10 Airplane," *Proc. Sixth ICAF Symp: Advanced Approaches to Fatigue Evaluation,* Miami, 1971.

11. Fredell, R. and J.W. Gunnink, "Fiber Metal Laminates for Improved Structural Integrity," *Proc. 4th Int'l Workshop on Structural Integrity of Aging Airplanes,* Atlanta, April 1992, pp. 362-375.

12. Verbruggen, M.L.C.E., "Aramid Reinforced Aluminum Laminates: Adhesion Problems and Environmental Effects," Ph.D. thesis, Department of Aerospace Engineering, Delft University of Technology, Delft, the Netherlands, November 1986.

13. Schijve, J., "Crack Stoppers and ARALL Laminates," Engineering Fracture Mechanics, Vol. 37, No. 2, pp. 405-421, 1990.

14. Pettit, R.G. "ARALL Applications of Large Transport Aircraft," Douglas Aircraft Company Report MDC 91K0007, May 1991.

15. Roebroeks, G.H.J.J., "Towards GLARE: The Development of a Fatigue Insensitive and Damage Tolerant Material," Ph.D. thesis, Department of Aerospace Engineering, Delft University of Technology, Delft, the Netherlands, December 1991.

16. Schijve, J., "Fatigue of Aircraft Materials and Structures," in A. Beukers *et al.*, editors., *Proc. Specialists' Conf. on Fatigue of Aircraft Materials,* Delft University Press, Delft, the Netherlands, October 1992, pp. 113-140.

17. Roebroeks, G.H.J.J., "Fiber Metal Laminates - Recent Developments and Applications, in A. Beukers *et al.*, editors, *Proc. Specialists' Conf. on Fatigue of Aircraft Materials,* Delft University Press, Delft, the Netherlands, October 1992, pp.141-160.

18. Schwarmann, L., N. Ohrloff and T. Beumler, "On the Application of GLARE for Airbus Fuselage Structures, in A. Beukers *et al.*, editors, *Proc. Specialists' Conf. on Fatigue of Aircraft Materials,* Delft University Press, Delft, the Netherlands, October 1992, pp. 191-200.

19. Seegers, J.W.G., "Finite Element Calculations for a Stringer Reinforced Butt Joint," Master's thesis, Delft University of Technology, Department of Aerospace Engineering, Delft, The Netherlands, June 1992.

20. Slagter, W.J., "Flexibility Parameters for a Monolithic Plate with Eccentrically Loaded Pin," *Computers and Structures,* 40, 1991.

21. Müller, R.P.G., "Fatigue Crack Initiation in Riveted Lap Joints and in Pressurized Fuselages, *Proc. SAMPE European Conf.*, Birmingham, England, 1993.

22. Miller, M., K.N. Kaelber and R.E. Worden, "Finite Element Analysis of Pressure Vessel Panels," *Proc. 4th Int. Workshop on Structural Integrity of Aging Airplanes,* Atlanta, March-April 1992, pp. 346-348.

3

Mechanical Testing of Riveted Repairs

3.1 Introduction

"Partial strength produces general weakness."
                                        Sir Robert Seppings, Royal Navy, 1830

This chapter describes the performance of a series of static strength and constant amplitude fatigue tests performed on unstiffened 2024-T3 panels. The panels had milled central 50 mm diameter holes (simulation of removed damaged skin) and riveted one-sided patches. The specimen configuration was shown previously in figure 2.8. It represents a flush skin patch; that is, the patch is mounted inside the fuselage skin.

The specimen configuration and test conditions established the uniaxial finite element model described in chapter 2. Specimen manufacturing conditions were closely controlled. Usually, the only variables were the patch material and thickness.

This close control of conditions admittedly is not feasible with repairs performed in the field. It was implemented to reduce experimental scatter and focus on the effect of patch selection on fatigue life. The manufacturing and test conditions and all exceptions are noted in the following pages.

A few specimens were purposely manufactured with known defects to provide a feeling for the sensitivity of the various patches to common errors made in fuselage structural repair.

The test results show that the soft patching concept explained in the previous chapter improves significantly the fatigue performance and damage tolerance of riveted repairs. Soft patching can be accomplished with lower life cycle costs than with the tapered monolithic aluminum patches used today.

3.2 Specimen Manufacture

Specimens were sheared to final outer dimensions, after which the central cut-out and rivet holes were milled on a numerically controlled milling machine. Countersinking of the rivet holes was performed on a drill press with a conventional countersink tool. Most of the specimens were countersunk in the skins to simulate a flush patch repair. Two specimens were countersunk in the patch to simulate an external repair. Special care was taken to avoid the "knife edge" condition.

Rivets were carefully cold-milled to a "custom" length. The shank extending through the two sheets was equal to 4.8 mm (1.5 times the rivet diameter) +/- 0.1 mm. Riveting was accomplished on the specially designed force controlled riveting machine in the Structures and Materials Laboratory. A riveting force of 8,500 +/- 50 N was adequate to achieve a driven rivet diameter of 4.8 +/- 0.05 mm. This extreme care in riveting followed from the recent results of Müller [1]. His tests showed an elevated fatigue sensitivity of 2024-T3 to rivet shank length and squeezing force.

Some specimens were purposely manufactured with known defects to estimate the effects of typical errors made in the repair process. Two knife edge countersink depths were tested. Separately, a few specimens were riveted with only enough squeeze force to hold the rivets in place (3800 N instead of 8500 N).

3.3 Test Conditions

3.3.1 Static Tests

Static tests were carried out under displacement control on the 100 ton MTS test frame. Displacements were input by hand, resulting in a low but non-constant crosshead rate.

3.3.2 Fatigue Tests

All constant amplitude fatigue tests were performed on a computer-controlled, servo-hydraulically actuated six-ton test frame. Tests were done at room temperature in laboratory air, with a sinusoidal wave shape at a frequency of 10 Hz. Most tests were continued to failure.

The stress ratio R ($\sigma_{min}/\sigma_{max}$) was 0.05. Maximum gross stresses varied from 105 to 140 MPa; however, as the results will show, none of the patch types were tested throughout the stress range. Stress levels for individual patch types were chosen to produce fatigue lives in the range from approximately 150,000 to 600,000 cycles.

It was not the intent of these tests to establish precise "repair fatigue allowables." Rather, the goal was an investigation of the effect of patch selection and load transfer on fatigue quality. Many "real world" variables with strong influence on fatigue life such as riveting quality and operating environment can and do reduce the magnitude of the lives tested here. Thus, these absolute life values cannot be applied directly to operational aircraft.

3.4 Test Results

3.4.1 Static Tests

Two samples were tested statically to failure: a tapered aluminum patch and an untapered GLARE 3 patch. Both failures occurred across the first rivet row in the skin at a stress of 330 MPa.

3.4.2 Fatigue Tests

Figure 3.1 shows the fatigue test results of specimens manufactured within the control specifications outlined in section 3.2. The general "order of merit" of the fatigue tests matched the finite element results exactly. The high stresses predicted by the model in the 1.3 mm untapered patch consistently gave the lowest lives. These were followed in increasing lifetime by the 1.0 mm untapered patch, the tapered patch and the GLARE 3 patch. The location of the countersink (in the skin or in the patch) made no real difference on the findings.

The outcome of the tests was striking: the GLARE 3 patches far outperformed all aluminum patches in number of cycles to fatigue failure at all stress levels tested. For example, at a stress range of 114 MPa, the GLARE patch outlived the untapered patches by a factor of three and exceeded the tapered patch life by a factor of 1.5.

For all specimen types except the untapered 1.3 mm 2024 patch, the results showed very little scatter. This may be attributed to the care taken in specimen manufacturing, especially in the strictly controlled rivet squeeze forces.
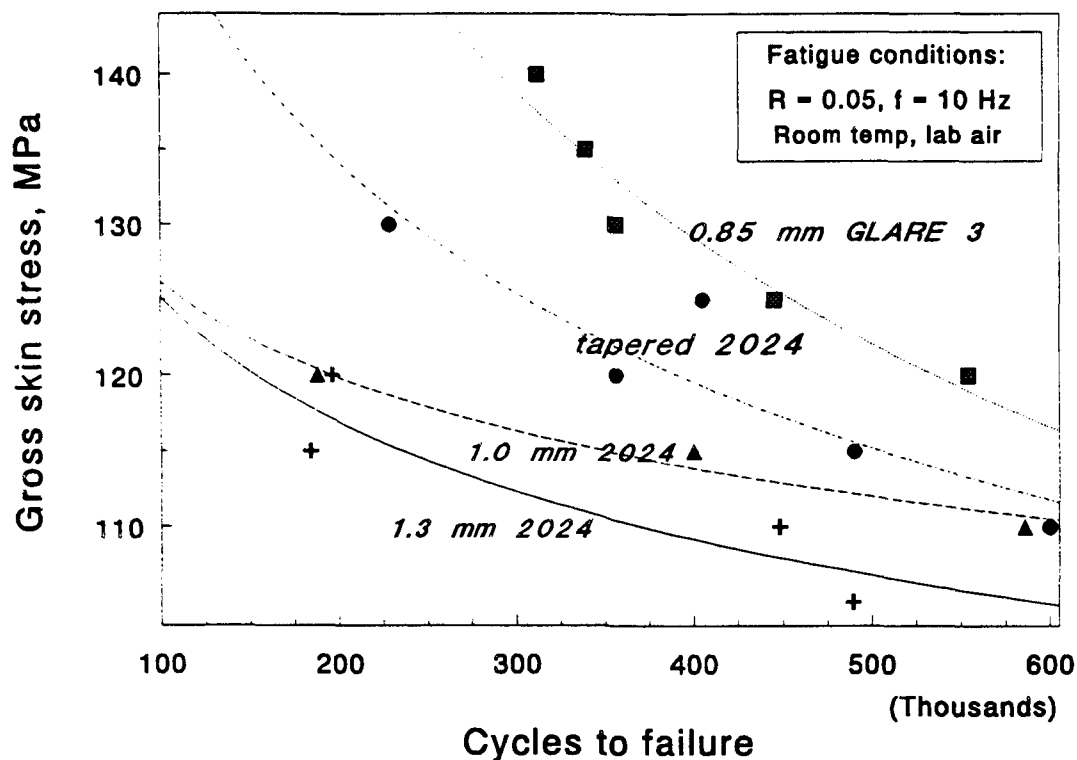
Figure 3.1 Constant amplitude fatigue performance of riveted repairs to 2024-T3 sheets.

3.4.3 Failure Modes

All aluminum patch specimens failed by fatigue of the critical first rivet row in the skin. In most instances where a first crack was observed, cracking initiated in the second rivet hole of the first row. Some exceptions were noted with the tapered patches, where the first crack sometimes initiated from a corner rivet hole. When cracks were observed, failure followed rapidly. In the tapered patch specimen tested at 130 MPa, for example, the first crack was observed visually at 220,000 cycles. Its length was 16 mm. Complete failure was imminent 8,400 cycles later, when the crack had grown to an effective length of 85 mm (including associated rivet holes). The test was halted before final failure.

Skin specimens patched with GLARE 3 showed a different failure mode with their long fatigue life. The first crack would initiate at the cut-out in the skin, then grow quickly until it lay between the nearest two rivets. This was followed by a period of slow crack growth across both sides of the cut-out for more than 100,000 cycles, until the total crack

exceeded the patch width by 10 to 20 millimeters. Final fracture occurred in the skin followed by tensile failure of the GLARE patch.

The crack growth behavior of the GLARE 3 and tapered aluminum patches tested at 130 MPa is illustrated in figure 3.2. Initiation times for the two patch types were similar, although at different locations, as mentioned previously. Many thousands of cycles occurred between initiation and failure in the skin repaired with the GLARE patch.

3.4.4 Effect of Defects

Selected tests were repeated with an additional element added to represent typical mistakes made in repairs. The knife edge condition, which results from too deep a countersink was tested first. Insufficient squeeze force, which can occur when access to the repair is restricted, was tested as well.

3.4.4.1 The Knife Edge Condition. Knife edge countersinking is well-known for its drastic reduction of fatigue lives in riveted joints. According to Niu, the knife edge condition is said to exist when the total depth of the countersink exceeds about two-thirds of the skin thickness [2]. One can expect that the typical quality of riveting found in repairs is poor compared with newly manufactured aircraft. This is because of the relative lack of control of the riveting process during repair.
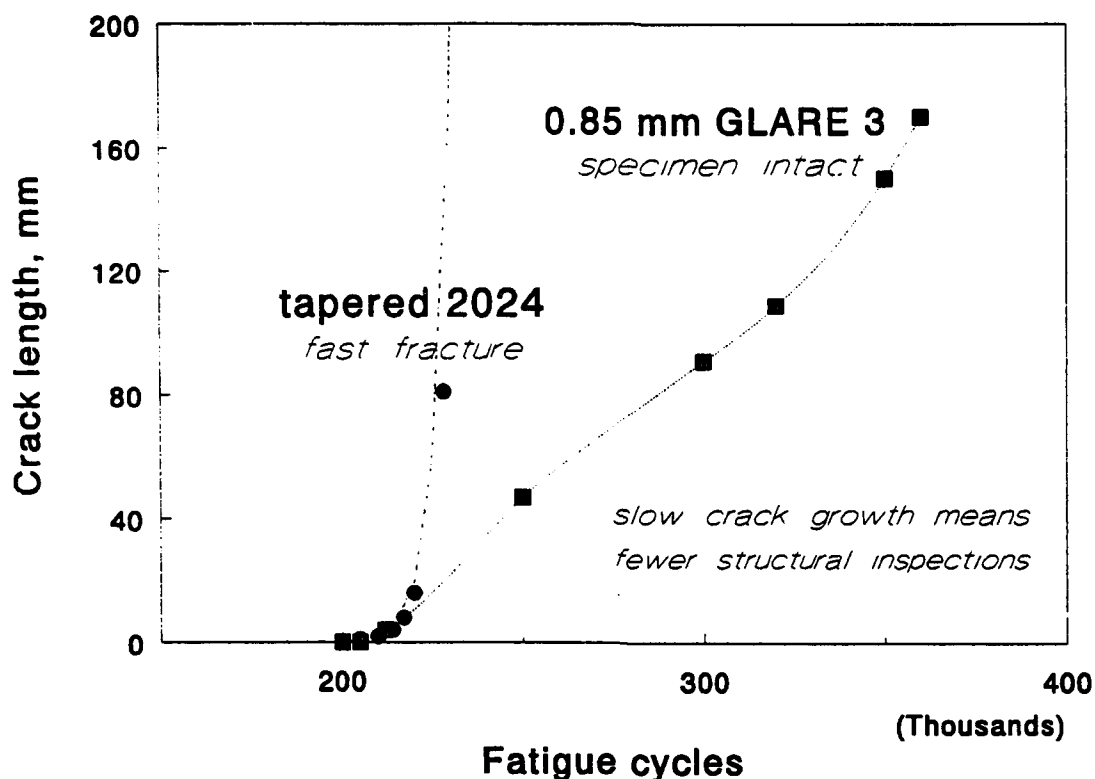
Figure 3.2. Comparison of crack growth behavior of the GLARE 3 and tapered aluminum patches tested in constant amplitude fatigue at 6.5-130 MPa.

In the first series, countersinks were made to approximately 80 percent of the sheet thickness. The countersinks were about half the sheet thickness in the standard specimens. Table 3.1 shows the results.

Table 3.1 Effect of 80% knife edge countersink on riveted repair fatigue lives.

Patch Type	Nominal Sheet Stress, MPa	Fatigue Life of Standard Countersink	Fatigue Life of Knife Edge Countersink	Life Reduction, %
GLARE 3	140	311,000	67,000	78
GLARE 3	130	356,000	293,000	18
Tapered 2024	130	228,000	75,300	67

When the countersink depth was increased to the entire skin thickness, the life reductions were even greater. At 130 MPa, the GLARE 3 specimen failed after 29,400 cycles (a 91 percent reduction). At the same stress level, the tapered patch showed a 92 percent fall, to only 18,100 cycles.

3.4.4.2 Rivet Squeezing Force. Another common defect in riveted repairs is impi operly driven rivets. Table 3.2 illustrates the effect of insufficient squeeze force on the riveting operation on fatigue life. A properly filled rivet hole is necessary for good fatigue performance. "To obtain substantial interference, the rivet must be bucked (driven) squarely. Especially in field repairs where space may be" restricted, rivets are not driven squarely. When this occurs, fatigue lives can be reduced by almost an order of magnitude [3].

Table 3.2. Effect of insufficient squeeze force on riveted repair fatigue lives.

Patch Type	Nominal Sheet Stress, MPa	Cycles to Failure, 8,500 N Squeeze Force	Cycles to Failure, 3,800 N Squeeze Force	Life Reduction %
GLARE 3	130	356,000	44,600	87
Tapered 2024	130	228,000	27,300	88

These specimens were manufactured with 3,800 N of squeeze force, instead of the 8,500 N prescribed in the baseline tests. This resulted in a driven rivet head expansion of only about 10 percent, compared with 50 percent expansion for the baseline specimens. (The intent here was to simulate, in a controlled way, the effect of rivet clinching, which happens when the rivet is not driven squarely.)

The results portray the influence of poor hole filling on fatigue lives. Again, the GLARE 3 patch specimens failed across the first rivet row instead of across the cut-out, as observed in the nominal case. Nonetheless, the GLARE 3 patch repairs continued to outlast the tapered patches.

Figure 3.3 summarizes the effect of defects on the fatigue life of riveted repairs. Although the number of defective samples tested was small, the tendency toward reduced fatigue lives is clear. With equivalent defects, though, the specimens with GLARE patches outlasted those with tapered 2024-T3 patches by an average of 140 percent.
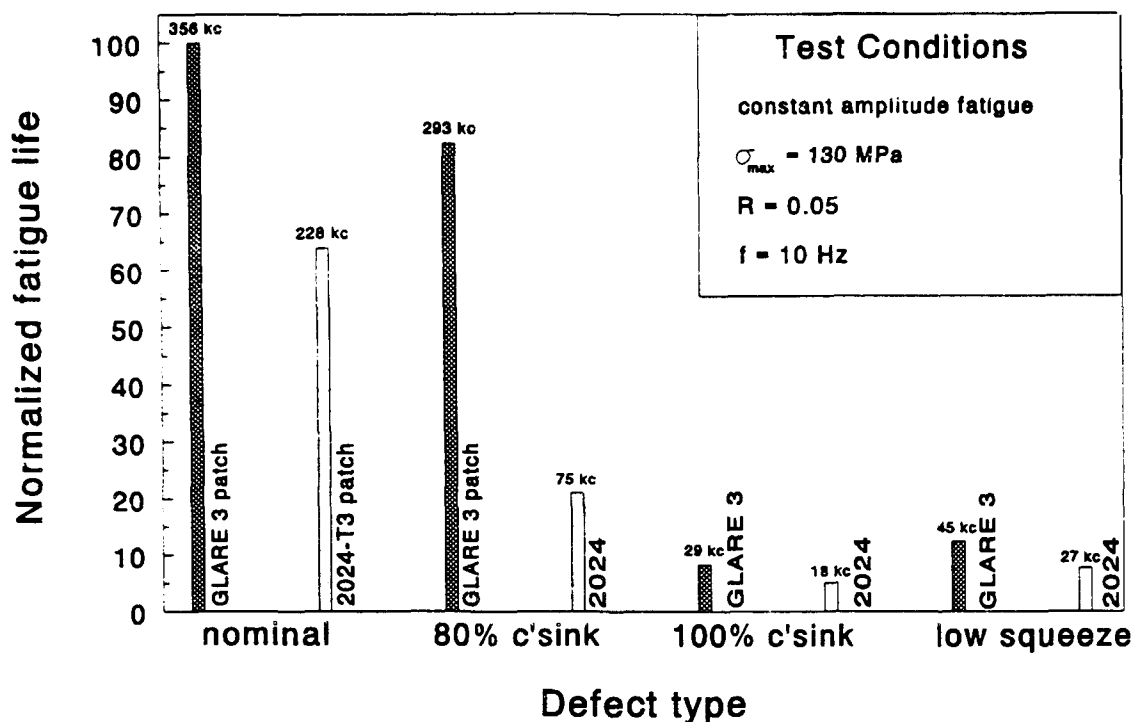
Figure 3.3. Effect of defects on riveted repair fatigue life.
All failures occurred in 2024-T3 sheet.

In addition to the considerable reduction in fatigue lives, a change in failure mode occurred in the defective specimens with GLARE 3 patches. Instead of the damage tolerant mode of cut-out cracking and slow growth observed with the nominally countersunk specimens, both defects shifted the failure location to the first rivet row in the aluminum sheet. This coincided with the area where all the aluminum patch repair specimens failed.

3.5 Discussion

In chapter 2, finite element analysis showed that patch thickness and stiffness played dominant roles in the load redistribution in and around a typical repair configuration. The high stress concentrations at the first rivet row in stiff conventional patches lead to shorter fatigue lives in comparison with the soft GLARE 3 patches.

The fatigue life of 2024-T3 skins repaired with GLARE 3 riveted patches far exceeded any other riveted patch configuration tested. Furthermore, uniaxially loaded 2024-T3 specimens repaired with GLARE 3 patches exhibited a more damage tolerant failure mode (very slow crack growth from the cut-out) than monolithic repair patches. At equivalent stress levels, crack initiation times for tapered 2024 and untapered GLARE 3 were similar. However, skins repaired with the GLARE patch exhibited slow crack growth periods roughly 10 times greater than the tapered patch repairs.

The use of high-strength, moderate-modulus materials like GLARE 3 enables repairs to be made quickly, without the need for thickness tapering. The high strength material allows a thinner patch to be used. This in turn reduces both secondary bending and first row rivet bearing loads, compared with a conventional aluminum patch. The lower overall extensional stiffness of the patch attracts less load into the repair area.

The failure mode experienced with GLARE 3 patches enhances the damage tolerance of *uniaxially loaded* riveted repairs. Cracks grew very slowly from the cut-out. An alternate load path exists through the patch, even when cracks extend well beyond the patch edges. This alternate load path results in a kind of macroscopic crack bridging by the GLARE patch. Crack bridging retards crack growth in the aluminum skin until the skin crack exceeds the width of the patch. This very slow crack growth reduces the need for structural inspections of GLARE patches.

Typical defects found in riveted repairs (poor riveting and knife edge countersinking) reduced the fatigue lives of riveted repairs by factors of up to 10. When these defects occurred in aluminum skins patched with GLARE 3, the crack location changed from across the cut-out to the first rivet row. The GLARE 3 patch repairs retained their better performance compared with the monolithic patches, though. The location of the countersink (in the skin or in the patch) did not affect this performance.

In the analysis of biaxial loading more typically encountered in pressurized fuselages, the corner rivets became more critical with all patch types. However, stresses at the cut-out remained approximately equal to the uniaxial case. A change in failure location to the first rivet row in the aluminum skins is anticipated.

Regardless of failure location, the more favorable load transfer in and around thin GLARE patches should result in the highest fatigue lives possible for a riveted repair.

A simple rule of thumb can be applied in the sub   . GLARE 3 patches for repairing fuselage skins of 2024-T3. Repairers should choose a GLARE 3 patch thickness in the range from 85 to 100 percent of the skin being repaired to assure adequate static strength while maintaining a low patch extensional stiffness. Table 3.3 provides a simple look-up reference applicable to common fuselage skin thicknesses.

Table 3.3. Recommended GLARE 3 Patch Thickness for 2024-T3 Repairs.

Original skin thickness, mm (inches)	GLARE 3 patch thickness, mm (inches)	GLARE 3 patch lay-up (Al sheet thickness)
1.0 (0.040)	0.85 (0.033)	2/1 (0.3)
1.3 (0.050)	1.1 (0.043)	3/2 (0.2)
1.6 (0.063)	1.4 (0.055)	3/2 (0.3)
1.8 (0.070)	1.55 (0.061)	4/3 (0.2)
2.0 (0.080)	1.95 (0.077)	4/3 (0.3)

Elimination of the need for tapering the patch saves a large amount of time and cost from the repair process. The cost comparison in table 3.4 shows that the increased cost of the GLARE material (approximately 10 times the cost per pound of aluminum sheet) has a negligible effect on the finished cost of the repair. In fact, the cost of the additional machining step of tapering approximately equals the premium paid for GLARE. Additional savings for the GLARE repair will result from reduced inspection costs.

Table 3.4. Cost comparison of GLARE 3 and tapered 2024-T3 riveted patch repair.

Category	2024-T3 t = 1.3/0.7 mm	GLARE 3 2/1-0.3 t = 0.85 mm
Material	$ 11	$ 75
Milled taper	51	0
Installation labor*	390	390
Total	$ 452	$ 465

*Includes cutting, drilling, deburring, sealing, riveting, cleaning and inspecting.

Riveted GLARE 3 repairs are best suited for patching of incidental damage and localized corrosion attack of monolithic aluminum fuselages. Conventional corrosion control practices (i.e., "wet" installation of fasteners and fay surface sealing with corrosion inhibiting sealant) should be applied. An even more damage tolerant method known as "crack patching" is better suited for the *in situ* repair of intact cracks in cases widespread fatigue damage. Crack patching is discussed in detail in chapters 5 and 6.

3.6 Summary and Conclusions

Current methods of riveted repair of pressurized aluminum fuselage skins cause fatigue problems for operators. Besides their adverse affect on safety, conventional riveted repairs are accompanied by the unwanted economic burden of increased inspection requirements.

A new concept called "soft patching" has been introduced to improve the fatigue performance of riveted repairs to pressurized aluminum fuselage skins. Soft patching involves the use of thin, untapered patches of the high-strength, low-modulus fiber metal laminate GLARE 3 in place of thick tapered monolithic patches. This reduces load attraction to the repair zone, while diminishing bearing loads on the critical first rivet row and decreasing secondary bending.

Soft patching improves the fatigue life of riveted repairs by 50 to 200 percent over various techniques involving monolithic patches. It simplifies the repair task by eliminating the need for costly, time consuming thickness tapering of patches. Inspection workloads are reduced while safety and damage tolerance are improved at a lower life cycle cost.

References, Chapter 3

1. Müller, R.P.G., "Fatigue Crack Initiation in Riveted Lap Joints and in Pressurized Fuselages," *Proc. SAMPE European Conf.*, Birmingham, England, October 1993.

2. Niu, M. C-Y., "Airframe Structural Design." Hong Kong: Conmilit Press Ltd., 1988.

3. Swift, T., "Repairs to Damage Tolerant Aircraft," *Proc. 2nd Int'l Symp. on Structural Integrity of Aging Airplanes*, Atlanta, Georgia, 20-22 March 1990.

4

Materials and Processes for Bonded Repairs

"I am a parcel of vain strivings tied by a chance bond together."

Henry David Thoreau, *Sic Vita* (1841)

4.1 Introduction

The use of adhesive bonding to join two or more metal parts has been recognized as a structurally efficient, fatigue-resistant method for decades. This chapter introduces the basics of structural adhesive bonding for aluminum aircraft fuselages. Where appropriate, emphasis is given to special processes peculiar to the bonded repairs (as opposed to new manufacturing of aircraft). The following points are discussed, with emphasis on practical aspects:

- history of adhesive bonding (section 4.2),
- adhesion theory (section 4.3),
- design and analysis of bonded repairs (section 4.4),
- surface pretreatments (section 4.5),
- adhesives and curing techniques (section 4.6),
- advanced patch materials(section 4.7), and
- inspection of bonded repairs (section 4.8).

4.2 Background of Adhesive Bonding Technology Development

Successful applications of adhesive bonding in aircraft structures date back to the second World War. De Bruijne, a Dutch chemist working in England during the early 1940s, invented the first "Redux," a phenolic adhesive. The DeHavilland Aircraft Company used Redux to bond plywood spar webs to aluminum spar caps in the Mosquito aircraft, overcoming a critical material shortage.

The Fokker F27 aircraft has had over 30 years of outstanding service experience employing adhesively bonded metal primary structures. However, some aircraft manufacturers continue to view adhesive bonding as black art. They limit bonding to local reinforcements (doublers) and non-critical secondary structures.

The successful development and increasing application of advanced fiber-reinforced organic matrix composite structures has challenged aluminum producers and designers of

metal aircraft. They must take further advantage of the higher structural efficiencies available from the judicious use of adhesively bonded metal structures. Otherwise they face a continual, if gradual, replacement of metal aircraft primary structures with organic composites. The USAF/Douglas/Boeing Primary Adhesively Bonded Structure Technology (PABST) program of the mid-1970s [1] marked a turning point in the perception of bonding.

Since PABST, manufacturers have begun to consider adhesive bonding as more science than art. The development of the highly fatigue-resistant adhesively bonded Aramid Reinforced Aluminum Laminates (ARALL) began at Delft University around 1980. Development of ARALL in the Netherlands and the United States has shown the potential for virtually eliminating fatigue failures from tension-dominated wing structures [2-4]. The first production application of ARALL occurred on the aft cargo door of the Douglas/USAF C-17 military transport [5]. The cargo door has operated successfully in a demanding application, while saving 26 percent of the weight of the original aluminum design. However, the ARALL skins are riveted to their monolithic substructure.

Investigations into fiber metal laminates have continued at Delft, resulting in the glass-reinforced aluminum laminate known as GLARE. GLARE combines the excellent fatigue resistance of ARALL with a higher blunt notch strength [6] and impact resistance [7] than either aramid ARALL or aluminum 2024-T3. GLARE promises real weight savings as a fuselage skin material, especially in fuselage crown areas [8,9]. Adhesively bonded fiber metal laminates show promise for reducing aircraft operating costs through structural weight savings (which cut fuel costs) and reduced structural maintenance expenditures. Most aircraft manufacturers have active GLARE development programs, including Deutsche Airbus in Germany [10], and Douglas and Boeing in the United States. The material is baselined for certain secondary structural applications on the Boeing 777 and has been mentioned as a leading candidate for the upper fuselage skins of the proposed Ultra-High Capacity Aircraft [11].

When faced with the greater structural efficiency of bonding, why then do most aircraft structural repairs done in the world today rely on mechanical fastening? The first reason is the long-lasting perception of poor service experience from the early years of bonded structures and bonded repairs. The chosen adhesive or surface preparation technique often proved inadequate, and bonds simply failed. The negative experience of Boeing with "cold-bonding" adhesives on early model 727, 737 and 747 lap joint doublers is one

example [12-15].   Cold-bonded aluminum patches applied to corrosion-damaged NF-5 vertical stabilizers also experienced durability problems [16].   These and other less widely publicized bonding failures forced researchers back to the laboratory. They seek acceptable combinations of patch materials, adhesives and surface preparations to provide adequate structural repairs with sufficiently long service lives.   Doublers and some skin-to-substructure connections are now reliably bonded in aluminum fuselages, although riveting remains the leading fastening method.   Bonded repairs to primary structure remain uncertified in most cases.

A specialty application of bonding receiving widespread attention is the use of high-stiffness bonded composite patches to repair cracks in aluminum aircraft. Chapters 5 and 6 are devoted to the subject of crack patching analysis and testing, respectively. This process has paid large dividends in specific cases where replacement or conventional repair techniques proved too costly.

A large obstacle to the universal adoption of bonded composite repairs for metal aircraft is their high cost.   The extreme example is that of boron/epoxy, which costs roughly 100 times more than aluminum.   The additional cost of facilities required for present-day bonded repair capability is simply too high for most repairers.   Most structural film adhesives require freezer storage and have a storage life of about six months. Repairers have had a long-standing requirement for economical repair materials with long shelf lives which require simple bonding processes.

Another drawback to the adoption of bonded primary structural repairs is the perception that they take too much time to perform. Scheduled maintenance "down time" on a 747 costs air carriers hundreds of thousands of dollars per day in lost revenues. Unscheduled (emergency) down time costs much more.   Airlines must perform structural repairs of accidental damage quickly, usually in one eight-hour shift, and usually at night. Maintainers may defer more extensive structural repairs (terminating actions) until scheduled overhauls.   However, this comes at a cost of frequent re-inspections of the suspect structure.

Perhaps the most damaging aspect to the general acceptance of bonded repairs is that operators perceive them as requiring too much engineering analysis to be useful.   To overcome this so-called "Ph.D. maintenance syndrome," researchers must develop simple analysis and repair techniques. These techniques must allow the accomplishment of safe,

structurally efficient repairs with a minimum of reference beyond the manufacturer's structural repair manual. Skill levels must be typical of what exists in the aircraft maintenance facilities of major (western) airlines today.

The challenges facing widespread adoption of bonded repairs to metal aircraft primary structures can be summarized as follows:

- repair materials and processes must be durable and reliable.
- repair techniques must be cost-competitive with riveted aluminum repairs.
- repair time should not exceed eight hours, and
- skill levels needed to analyze, perform and inspect bonded repairs should match those available in the industry.

4.3 Adhesion Theory

This section serves only as an introduction to adhesion theory. For a much more in-depth theoretical review, the reader is referred to the excellent work of Kinloch [17]. Another useful book focusing on the practical side of adhesive bonded repair is *Bonded Repair of Aircraft Structures* [18].

Adhesive bonding can be defined as the process of joining two or more materials called *adherends* by a continuous inter-layer of an adhesion-promoting substance (*adhesive*). As opposed to the discrete load transfer accomplished by mechanical fastening, adhesive bonding accomplishes a more uniform load transfer. Furthermore, it does not involve the removal of any of the load-bearing material as is done with riveting.

Wettability is a term describing the action of an adhesive (or adhesive primer) in liquid form on the surface of the adherend. The adhesive must be able to spread evenly over the adherend surface to achieve acceptable bonding quality. In practice, this means the metal adherend must be extremely clean and free of oxides, paints, oils or other contaminants. As will be discussed in section 3.4, good adherend surface preparation is the most important step in the adhesive bonding process.

The adhesive bonding process relies on "the attainment of intimate molecular contact at the adhesive/adherend interface." Good contact across the interface is the first stage in

the formation of strong and stable adhesive joints. "The next stage is the generation of intrinsic adhesion forces across the interface, and the nature and magnitude of such forces are extremely important." The bond must be sufficiently strong and durable to ensure that the interface remains stronger than the adherends throughout its service life [17].

At least five theories covering the mechanisms of adhesion have been proposed in the scientific literature [17,19-23]. The two leading theories are summarized here as they apply to metal bonding.

4.3.1 Adsorption

The widely accepted adsorption theory explains adhesion as the result of interatomic and intermolecular forces acting at the adhesive/adherend interface. In adsorption theory, bonds can be classified as either primary or secondary, which describes their relative strength. Primary bonds can only exist between a metal and an adhesive under a very special set of circumstances and will be discussed further in section 4.5 [17].

The secondary bonds of the adsorption theory are most commonly the weak van der Waals forces. This category also includes hydrogen bonds, which may be two to 10 times stronger than van der Waals forces. In van der Waals forces, the weak electro-negativity differences in dipolar molecules attract each other. According to the adsorption theory, these weak forces produce the adhesive strength, sometimes supplemented by hydrogen bonds. However, for effective bonding, adhesive and adherend must be no more than 1 nm apart. Excellent wetting of the adherend by the adhesive is therefore critical.

Table 4.1 summarizes the different bond types and their typical bond energies. Primary bonds clearly produce higher bond strengths than do secondary bonds. The practical production of such bonds in typical metal bonding, however, is difficult. The expected high values have not been realized, as will be discussed later.

Table 4.1. Bond types and typical bond energies [17].

Type	Bond energy (kJ/mol)
Primary	
ionic	600-1100
covalent	60-700
metallic	110-350
Secondary	
hydrogen	
involving fluorine	up to 40
excluding fluorine	10-25
van der Waals	
permanent dipole-dipole	4-20
dipole-induced dipole	less than 2
dispersion (London)	0.08-40

4.3.2 Mechanical Interlocking

This theory attributes the strength of an adhesive joint to the mechanical keying, or interlocking, of the adhesive into irregularities of the adherend surface, as shown in figure 4.1. Kinloch [17] states that mechanically roughened adherends "do not generally result in a surface topography with cavities suitable for establishing mechanical interlocking with an adhesive." He instead advocates "chemically roughened" (typically anodized) surfaces for good interlocking. However, unpublished work by Oosting at Delft University [24] has established an empirical relationship between surface roughness of mechanically abraded substrates and adhesive strength. Both mechanical and chemical roughening result in the exposure of more surface area to be bonded. This may be the real reason for their apparent improvement in bond strength.

The mechanical interlocking theory has not gained wide acceptance. Moreover, several characteristics of adhesive bonding cannot be explained by mechanical interlocking alone. It cannot, for example, explain the decrease in bond strength that accompanies long-term exposure to a hot, humid environment. However, mechanical surface abrasion does provide the following benefits:
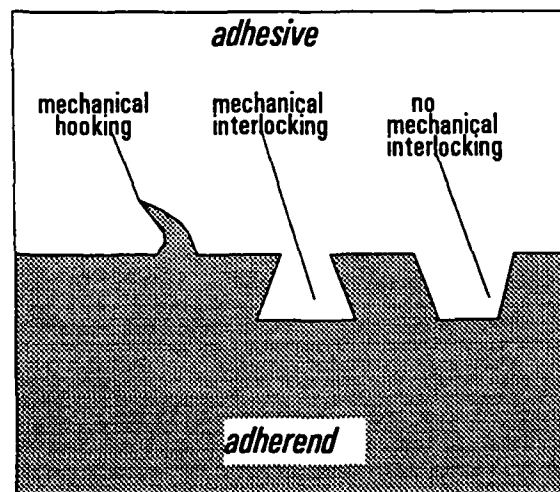
Figure 4.1. Mechanical interlocking.

- removal of contaminants (oxide layers, grease, paint, etc.) and improved wettability,

- increase in the total surface area to be bonded, and

- increase in the energy dissipated in fracture compared to a polished surface.

"Chemically roughened" (i.e., anodized) surfaces will be discussed in detail in section 4.5.

4.4 Design and Analysis of Bonded Repairs

The goal of a properly designed bonded repair is to restore the damaged structure's ultimate load carrying capability. Damage growth should either be arrested o. significantly retarded. The repair must be carried out without causing further damage or creating a new weak link in the structure. In short, the repair allows the structure to fulfill its original intended function.

This section will discuss the mechanics of adhesive bonds. It focuses on the forces acting on the constituents of the bond and presents some simple rules of thumb for adhesive bonded repairs. The discussion is closed with comments on the damage tolerance of flawed bonded repairs.

4.4.1 Forces Acting on an Adhesive Bond

A well-designed adhesive bond transfers loads through shear, not through normal tensile loading of the adhesive. Shear and normal forces make up the basic types of loads acting on adhesive bonds, as shown in figure 4.2. Normal, or mode I loads, occur perpendicular to the plane of the bond. Mode II (shearing) loads act parallel to the bond surface. Combined loads are variously called peel or cleavage forces, but these are primarily terms of convenience. Peeling loads usually refer to the combined shear and tensile loads acting on a thin adherend, while cleavage forces are the result of an offset tensile load.

normal   shear   peel   cleavage
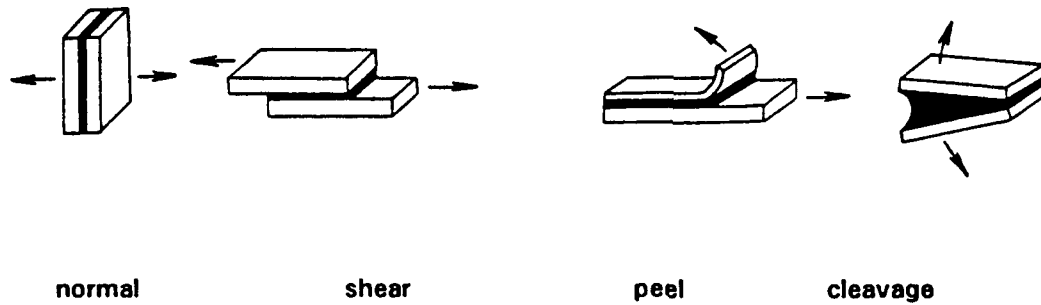
Figure 4.2. Forces acting on an adhesive bond.

Understanding the various loads that can occur in an adhesive joint aids in the proper design of adhesively bonded repairs and in the selection of a good repair adhesive. Many examples of "good" joint design are given in the literature (see figure 4.3). However, the repairer does not always have as much flexibility as the designer of a new structure. For example, while the double lap shear joint is commonly recognized as a far superior lap joint configuration to the single lap, the repairer may be forced to use a single lap configuration. A well-designed joint avoids or minimizes tensile, peel and cleavage loads.

Taking the single-sided lap configuration as typical of a repair joint, one immediately notices similarities with the one-sided riveted patch discussed in the previous chapter. Indeed, as shown in figure 4.4, the offset of the neutral plane induces significant bending moments in the repaired skins at the edges of the patch. This bending results in severe peel forces in the adhesive at the same point where the adhesive is subjected to the highest shear stresses. In reality the highest shear stress occurs very near, but not at the end of, the overlap. Otherwise the free edge of the adhesive would have to sustain a non-zero shear stress, which is impossible. Nonetheless, the stress state described illustrates the need for adhesives with both good shear strength and adequate peel resistance.

Good designs   Poor designs

To reduce out-of-plane
transverse tensile stresses:
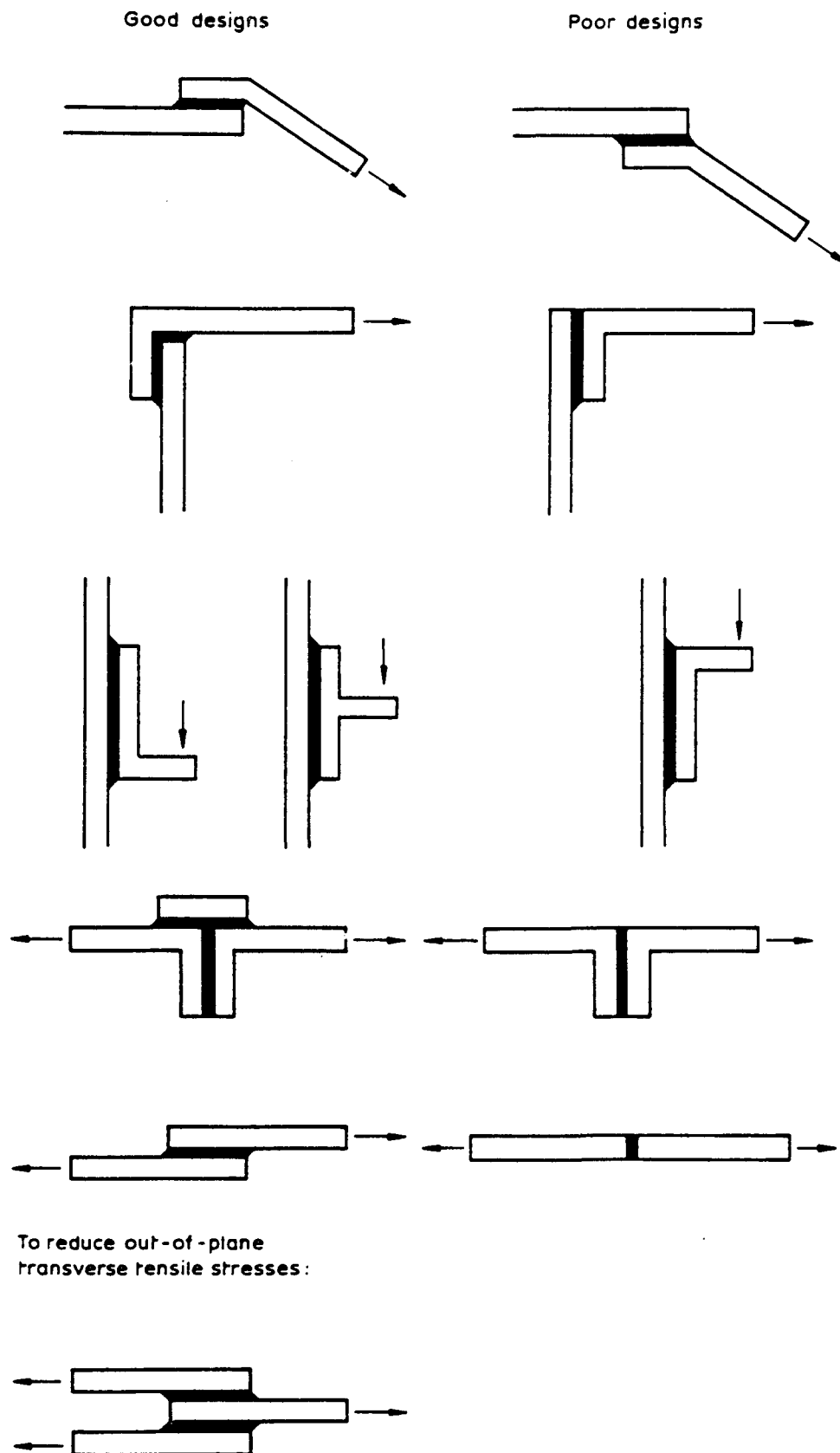
Figure 4.3. Examples of "good" and "poor" joint designs [17].

70
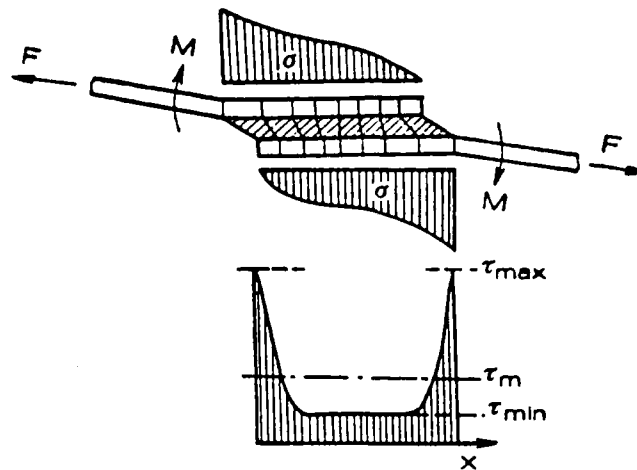
Figure 4.4. Combined bending and non-uniform shear stress distribution
along the bond area of a single lap joint under tensile load [25].

Smart design practices can have real impact on the performance of an adhesively bonded repair. For example, tapering the ends of the patch reduces the bending moments and hence the peel forces. Furthermore, increasing the overlap length reduces the average shear stress in the bond line. A long overlap increases the fracture load of a bonded single lap joint up to a plateau value, as shown in figure 4.5.
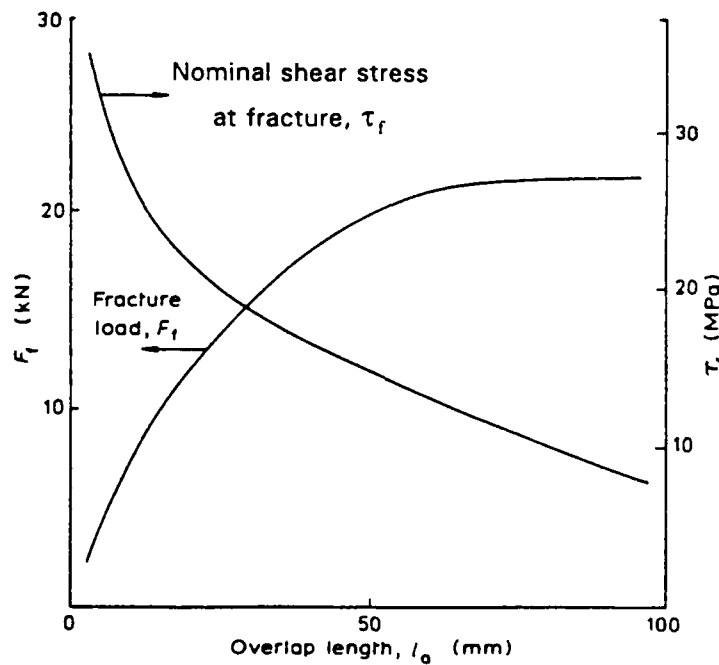
Figure 4.5. Experimentally determined fracture load and stress of bonded modified phenolic
adhesive/aluminum alloy single lap joints; function of overlap length [17].

71

The designer of a bonded repair is cautioned here not to succumb to the temptation of choosing the minimum overlap length suitable to gain sufficient joint strength. A longer overlap than the structurally defined optimum adds long-term durability and damage tolerance of a joint, which will be discussed later.

The thickness of the adhesive bond line also plays an important role in the strength of a bonded joint, as illustrated in figure 4.6. Thicker bond lines rely on the bulk cohesive properties of the adhesive, while thinner bonds take greater advantage of the (stronger) interfacial adhesion forces.
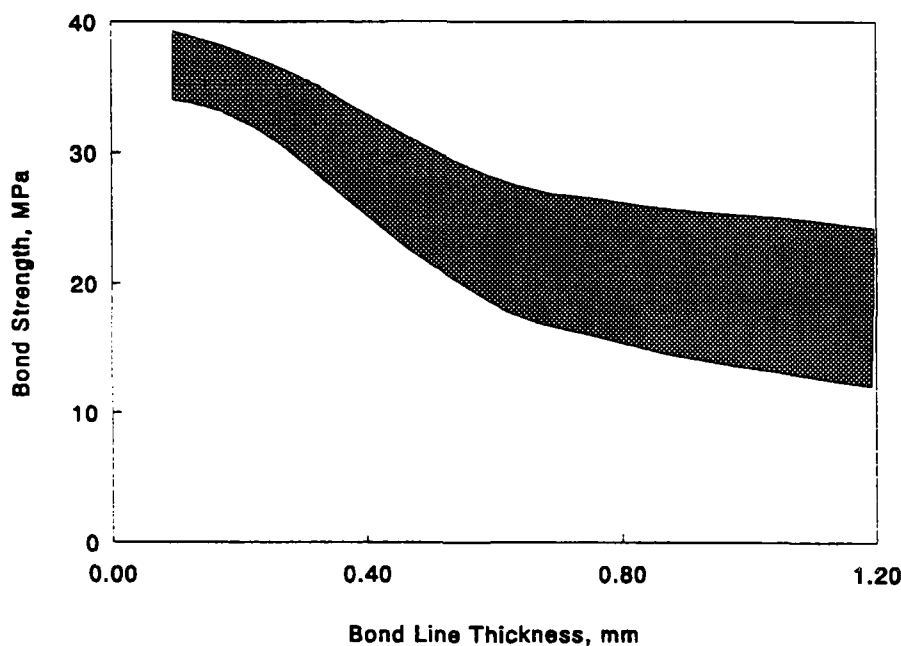
Figure 4.6. Effect of bond line thickness on the shear strength of hot-bonded single lap joints [25].

Analysis of bonded joints was pioneered by Volkerson in 1938. Kinloch [17] presents an English translation of Volkerson's linear elastic method, which considers only the shear forces acting on a joint. Goland and Reissner [26] in 1944 first recognized the significance of eccentricity and its effect on the mechanical performance of adhesive joints. Their method incorporates bending and rotation of the adherends in a linear elastic analysis. This accounts for the significant tensile stresses occurring through the thickness of the adhesive at the ends of a bonded single lap joint.

Many other researchers [27-33] have extended this analysis with both closed-form analytical and finite element techniques to include non-uniform through-the-thickness stress distributions and elastic-plastic adhesive response. However, the Goland and Reissner method gives accurate results as applied to the typical fuselage structure. It is not the intent of this writer to review these competing methods rigorously. Rather, this section presents the important results needed to allow the designer and installer of bonded aircraft structural repairs to proceed with confidence by following certain guidelines. A rigorous calculation of the stresses in the bond line follows in chapter 5.

4.4.2 Design Guides for Bonded Repairs to Aluminum Skins

The PABST program led to a much better understanding of the overall performance of the adhesive bond line [1,13]. In short, the static strength of an adhesive bond is not what determines its overlap length. Rather, the overlap must be long enough to develop a central area of very low adhesive shear stresses. This area acts to anchor the bond to resist creep, further acting as an insurance policy against small areas of poor bonding (porosity, disbonds, etc.). The following general guidelines apply to metal bonded fuselage repairs.

- Choose repair materials to have static load-carrying capability equal to the skins being repaired.

- Use a double lap arrangement whenever practical.

- Use overlap distances of roughly 30 times the base skin thickness for double lap bonded repairs, or 80 times thickness for single lap repairs. This assures that the bond remains at least twice as strong as the underlying structure for skins up to 2.3 mm in thickness. This covers most fuselage skins up to the C-5 Galaxy. It also adds damage tolerance to the bond, as discussed below.

- Taper the thickness of the repair patch at its ends to relieve adhesive peel stresses. The slope of the taper should be about 1:10.

- Make sure a smooth fillet is produced in the bonding process. The fillet helps to reduce the mode I (tensile) stress concentrations that occur at the edge of the overlap.

4.4.3 Damage Tolerance of Bonded Repairs

Hart-Smith presents persuasive arguments that properly designed and installed bonded repairs to fuselage skins can tolerate large flaws without loss of strength and fail-safety [34]. After all, the properly designed bonded repair is much stronger than the adherends. This allows it to avoid acting as "a weak-link fuse in the event of subsequent damage to an adjacent area [13]."

In bonds with the previously prescribed overlap length, large bond flaws do not act to increase adhesive peak stresses; rather, they only shift the location of those peaks. This means that bonded joints with large flaws can be left unrepaired. Smaller flaws exposed to moisture need to be sealed to prevent freeze-thaw cycles from enlarging the defect size.

4.5 Surface Pretreatment

"The prebond surface preparation of metallic adherends is the most critical step in the adhesive bonding process. If not done correctly, all else is for naught."

T. J. Reinhart, *Bonded Repair of Aircraft Structures* (1988)

4.5.1 Production Surface Pretreatments

Aluminum pretreatments that produce a clean surface with a stable oxide film are the key to high adhesive strength and good bond durability. However, before the PABST program, no well-documented scientific basis existed for the evaluation and quality control of pre-bond surface treatments. Some manufacturers, especially Fokker, had success with the chromic acid anodize (CAA) process. However, concerns about the discharge of chromates into the environment should soon end the use of CAA in most of the industrialized world.

The accepted standard is the PABST pretreatment. It involves degreasing the adherends in a solvent, followed by washing in an alkaline solution, deoxidizing (or pickling) in a chromic-sulfuric acid bath, and phosphoric acid anodizing (PAA). The properly anodized surfaces are then air dried, sprayed with an adhesion-promoting, corrosion-inhibiting primer such as BR-127, and oven-cured. The PAA process is "easily controlled, highly reproducible and lacks few critical process variables." The aerospace industry employs it widely [35]. It forms the baseline surface pretreatment process in these discussions.

In a further attempt to reduce environmental damage by eliminating the chromic-sulfuric etching step, Boeing and its subcontractors have recently developed the boric-sulfuric acid anodizing (BSAA) process [27,28]. The process looks quite promising; however, as it is a production process, it will not be considered here.

One drawback to the use of the standard PAA process is the need for submersing the adherend in a tank. This limits its application to off-aircraft bonded repairs (typically removable secondary structures). The development of the Phosphoric Acid Non-Tank Anodizing (PANTA) process by Boeing overcame this limitation. An improvement over PANTA known as PACS (for Phosphoric Acid Containment System) allows easier application and performs equivalently with tank PAA processes [38]. PACS and other non-tank pretreatment processes will be discussed and evaluated in the following section.

4.5.2 Pretreatments for on-Aircraft Repair

Choose "not for a fine glossy surface but such qualities as would wear well."
                                    Oliver Goldsmith, *The Vicar of Wakefield* (1766)

When faced with an on-aircraft repair situation, one has many potential choices for surface preparation. These range from simple surface abrasion to passivating treatments (e.g., Alodine and Pasa Jell) to non-tank anodizing. Researchers in Australia and the United States are investigating methods that involve mechanical abrasion of the two adherend surfaces followed by a wipe with adhesion-promoting silane wetting agents. The silane wipe attempts to create so-called primary bonds between the adherends and the epoxy adhesives commonly used in bonded repair.

Most surface preparation techniques involve the following basic steps:

- degrease and rinse
- deoxidize and rinse
- chemically etch/anodize, rinse and dry
- prime

The adherend must be prepared to produce a clean surface free of oils and other contamination. The surface must be easily wettable to ensure good bond strength and possess a stable oxide layer for long-term durability and corrosion resistance. These conditions must be met reliably with a method that considers the realities of the maintenance environment.

As part of this research project, 23 surface pretreatments were evaluated for peel strength and durability. The evaluated pretreatments were various combinations of mechanical and chemical deoxidizing procedures, passivating or anodizing steps and the selective use of adhesive primers, as shown in table 4.2. Three types of pretreatments were evaluated: Electrochemically produced anodized coatings (tank PAA and PACS), chemical conversion coatings (Alodine 1200 and Pasa Jell 105) and mechanical abrasion. The details are explained in the following paragraphs.

4.5.2.1 Anodizing pretreatment processes. Anodic coatings are "grown" on the bonding surface by passing an electric current through the adherend via a conductive acid medium (in this case, the acid is H_3PO_4). The adherend acts as the anode in an electrochemical

cell, producing a stable, adherent oxide coating of typically 0.1 to 1.0 μm thick. The expected surface morphology of a properly applied phosphoric acid anodic coating is shown schematically in figure 4.7. The surface has a rough, interlocked appearance that has been variously described as "trees" and "antlers."

Table 4.2. Pretreatments evaluated in this program.

Pretreatment Type/ Reporting code	Oxide removal method	Passivating method	Adhesive Primer
Anodizing			
Std PAA EC	Chromic-sulfuric	Tank PAA	EC-3960
SB PAA EC	etch	"	EC-3960
SB PAA	Scotch Brite coarse	"	none
SB PACS	"	PACS	BR-127
BR	"	PACS	none
SB PACS	"		
Deoxidizers/ Conversion Coatings	Scotch Brite + HF	Alodine 1200	EC-3960
SB HF Al EC	Scotch Brite	"	EC-3960
SB Al EC	Scotch Brite + HF	"	silane
SB HF Al Si	Scotch Brite + HF	"	none
SB HF Al	Scotch Brite	"	none
SB Al	Hydrofluoric acid	"	EC-3960
HF Al EC	etch	"	EC-3960
GB HF Al	Grit blast + HF etch	"	none
EC	Grit blast + HF etch	"	EC-3960
GB HF Al	Grit blast		
GB Al EC			
		Pasa Jell 105	EC-3960
	Scotch Brite coarse	"	silane
SB Pasa EC	"	"	none
SB Pasa Si	"	"	EC-3960
SB Pasa	Grit blast	"	none
GB Pasa EC	"		
GB Pasa			
Mechanical only			
SB med	Scotch Brite medium	none	none
SB coarse	Scotch Brite coarse	"	"
GB only	Grit blast	"	"

The standard PAA process has been described extensively in the literature [32,39,40] and will not be reproduced in detail here. One sometimes overlooked by-product of the process is a prodigious amount of hydrogen gas, which must be removed from the bath as it is produced. This can be accomplished quite easily in a tank process by agitating the bath

with air bubbles. However, when non-tank methods such as PACS or PANTA are employed, gas removal must be accomplished by good agitation of the setup and well-planned flow paths.
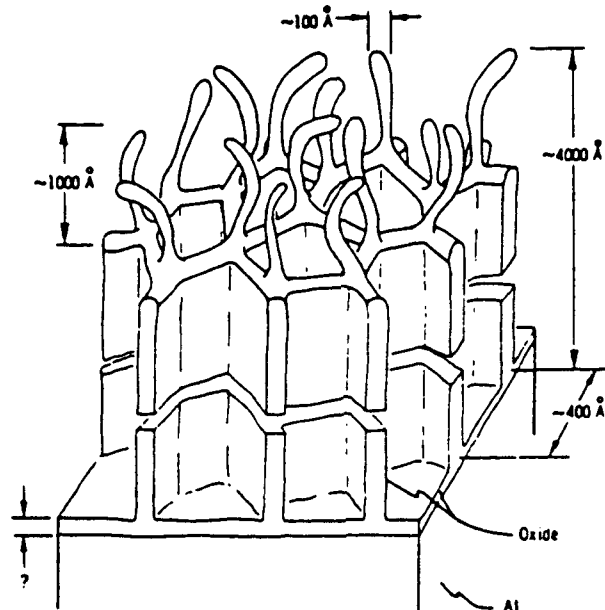
Figure 4.7. Idealized structure of phosphoric acid anodic coating, providing a "chemically roughened" surface and mechanical interlocking. 1000 Angstroms = 0.1 μm [39]

The PACS process was accomplished according to Boeing specifications [38,41]. The goal of the process is to produce a high quality phosphoric anodize layer on the part to be bonded, without removing it from the aircraft.

In the present tests, the PACS treatments were preceded by degreasing the surface with acetone. The degreasing step was followed by mechanically grinding it with a coarse Scotch Brite brush.

4.5.2.2 Deoxidizers and "conversion coatings." The strong deoxidizer hydrofluoric acid (HF) and the proprietary chemical conversion coating products Alodine 1200 and Pasa Jell 105 were considered. The concept behind them is the removal of old oxides and the creation of a uniform thin passive oxide film on the bonding surface. The conversion coatings are mixtures of strong acids that etch the adherend surface. The Alodine and Pasa Jell products also contain chromates as corrosion inhibitors.

4.5.2.3 Mechanical abrasion methods. Grinding and grit blasting have the effect of removing old paint and oxide layers and roughening the surface, increasing the area available for bonding.

4.5.2.4 Adhesive Primers. The primary function of the adhesive primer is to promote good adhesion between the adhesive and the adherend by intimately wetting the adherend surface. Adhesive primers are fundamentally adhesives (about 8-10 percent by weight) that have been thinned down using an organic solvent (about 90 percent by weight). A small amount of coupling agent (0.2 percent) is included.

A secondary but nonetheless important function of primers is their role in inhibiting corrosion within the bond line. This is accomplished by the addition of a small amount of chromates or other corrosion inhibitors to the thinned adhesive. This practice is also undergoing changes to remove unhealthy substances such as heavy metals from the environment. Primers also improve the handling qualities of pretreated sheets, allowing the surfaces to be touched with gloved hands and enabling their safe storage. This removes the need to accomplish a bonding operation in one shift, if desired.

Some primers have been developed to meet the stringent anti-pollution requirements of California. These "low volatile organic compound" primers are often a water-based emulsion [42]. Little is known about their long-term effectiveness.

Primed samples manufactured at Delft and tested in this effort used the 3M primer EC-3960. It was sprayed on the pretreated aluminum surface and allowed to dry at room temperature for 30 minutes. The samples were then dried at 120°C for one hour. In a repair environment, drying can be accomplished with heat lamps or hot air guns. A primer thickness of 6±1 μm was used. One wedge edge sample in this test program was manufactured at Boeing and was primed with American Cyanamid BR-127, similar to EC-3960.

4.5.2.6 Silanes. Early investigations into silane coupling agents began after World War II. In 1947, Witt and co-workers observed that the strength of glass fiber/polyester composites treated with allyltriethoxysilane was doubled compared with fibers treated with ethyltrichlorosilane [43]. More recently, Windecker [35] and others [44,45] have suggested the use of silanes in an aqueous abrasion technique as a replacement for the standard PABST pretreatment for metal adhesive bonding. Results have been inconsistent at best [38,44]. Reports of good durability presented in the literature [45] were based on short-term tests after only a few hours of exposure.

In theory, silanes act as adhesion promoters or coupling agents between organic polymers (adhesives) and metals (adherends). The silane functions by chemisorbing to the surface of the metal, allowing a primary bond to form between the now-modified metal and the adhesive. To achieve this effect, the silane should be applied as a monomolecular layer, but in practice this can be hard to achieve.

Concern exists about the long-term endurance of silane treatments in place of anodization. No stable oxide layer is established with silanes. Plueddemann [43] questioned the durability of the silane-metal interface. Such bonds with "aluminum, for example, are not resistant to hydrolysis." This means that while laboratory-produced silane treatments may result in strong bonds, the durability of such bonds in a hot, humid environment will probably be poor. The presence of multimolecular silane layers can actually expedite the degradation process.

In the current tests, the aminosilane EC-3901 was used. A thin film of primer was applied evenly to the aluminum surface with a moistened cheesecloth. The samples were air dried for three hours before bonding or priming.

4.5.3 Destructive Test Methods

Many standardized tests exist for determining the suitability of pretreatments. One must be careful to select qualification tests that represent the loads in the adhesive in the repair joint. For example, the PABST program showed a significant viscoelastic character in most structural adhesives. Test frequency, thus, is important in characterizing short overlap bonded joint fatigue performance. Low frequency tests cause creep and rupture (short fatigue life) in short overlaps. However, long overlap joints (which are more representative of the actual structure), stabilize creep and give a long fatigue life [13]. Investigators commonly use three tests to qualify adhesives:

- the wedge edge test,
- the floating roller peel test, and
- the lap shear test.

For the results reported in this section, the pretreatment method was the only variable. All specimens were bonded using the epoxy film adhesive AF-163-2K (293 g/m^2). Curing occurred in an autoclave cycle of 120°C for one hour at a pressure of 350 kPa. Although

this is not a realistic cure cycle for repairs, it was chosen to produce a consistently high-quality bond. Suitable non-autoclave cure cycles will be discussed in section 4.6.

4.5.3.1 Wedge edge test (modified ASTM D-3762). Figure 4.8 shows the specimen configuration, modified slightly with thicker adherends and a thicker wedge than the ASTM standard. These changes reduce plastic deformation of the adherends and provide better adhesive discrimination.

The wedge edge test can quickly judge the quality and durability of surface preparation. In the test, a metal wedge is driven into the edge of a bonded specimen. The extension of the resulting crack is monitored over a few hours. If little or no extension of the original crack occurs, the already qualified bonding process is judged acceptable.

$$a_0 = \text{DISTANCE FROM LOAD POINT TO INITIAL CRACK TIP}$$

$$\Delta a = \text{GROWTH DURING EXPOSURE}$$
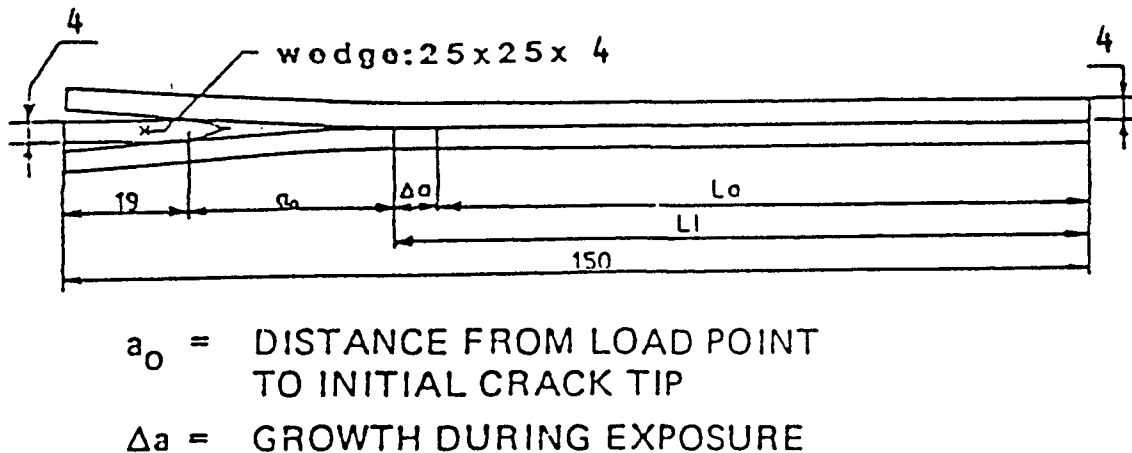
Figure 4.8. Wedge edge test specimen.

Continued exposure to aggressive environments for up to eight weeks (35°C and 99 percent relative humidity in salt spray) gives good discrimination of the overall durability of a particular pretreatment system. Boeing sets a maximum acceptable crack growth of 12.5 mm in 30 days after one week pre-exposure at 49°C in 100 percent humidity [38]. However, hot/wet exposure primarily tests the adhesive in short to moderate duration tests.

The salt spray environment is considered more severe than hot/wet exposure. It is a better discriminator of the corrosion susceptibility of the substrate. Thus, it was chosen for the wedge edge tests. Wedge edge specimens manufactured with the 23 different pretreatments listed already in table 4.2 were subjected to this environment. The resulting crack extension was monitored during the eight weeks of exposure.

4.5.3.2 Floating roller peel test (modified ASTM D-3167). The test setup is shown in figure 4.9. Peel tests performed at Delft typically have a thinner thin adherend and a thicker thick adherend than listed in the ASTM standards. These differences lead to comparatively lower peel values, because less elastic energy is stored in the adherends. The crosshead speed was 100 mm/minute; testing was performed at room temperature.

The floating roller peel test induces loads never intended in a lap joint configuration. Nevertheless, it is a good indicator of the overall quality of the bonding process. An acceptable result is cohesive failure within the adhesive, while adhesive failure at the adhesive/thick adherend interface usually indicates poor surface preparation. It is especially useful in qualifying adhesives for bonded repair, because typical repair configurations induce large peel loads into bond lines, as discussed in section 4.4. A desirable floating roller peel minimum value is approximately 10 N/mm.
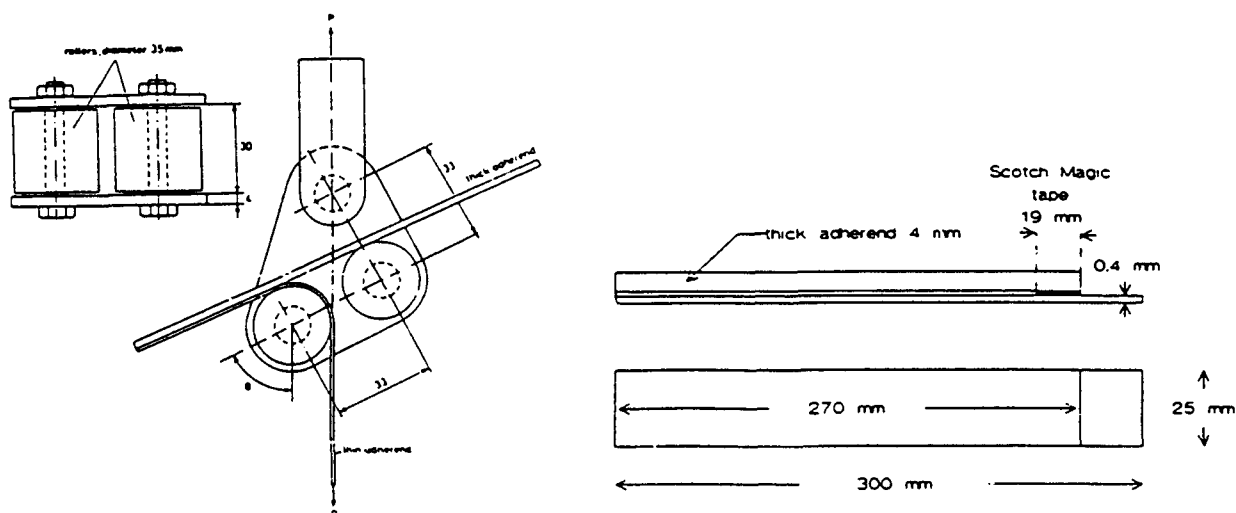
Figure 4.9. Floating roller peel test coupon.

82

4.5.3.3 Lap shear test (modified ASTM D-1002). Figure 4.10 shows the configuration used at Delft. This test typically is performed at room temperature and the highest intended use temperature.
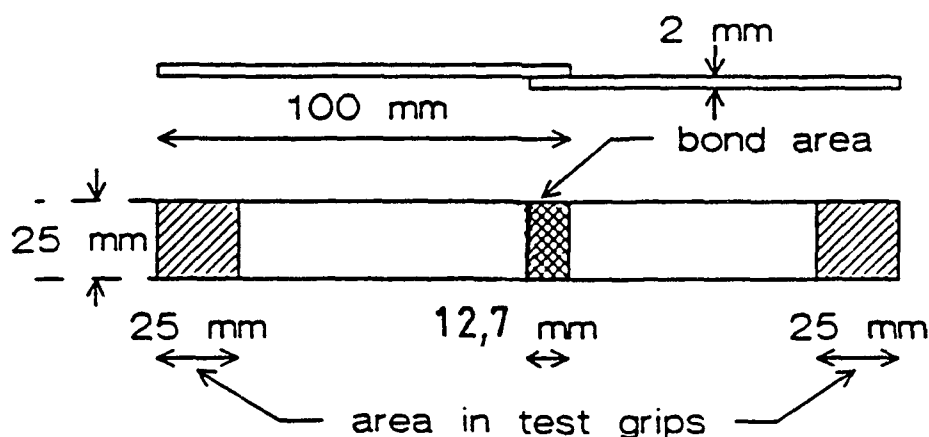
Figure 4.10. Lap shear test coupon.

The lap shear test helps "to assure uniformity in the adhesive product but provides no direct data useful in establishing design allowables for a bonded repair." This is because of the short overlap length, which causes high average shear stresses and significant secondary bending. This causes the adherends to plastically deform at relatively low loads [46].

Hart-Smith, a member of the original PABST team, agrees: He calls the lap shear test "a widely misunderstood source of data that cannot be related to the strength of any joint other than the test coupon itself." [47]   For these reasons it will not be used for surface preparation comparison. The lap shear test will only be used in the adhesive comparison tests presented in section 4.6. In the manufacturing or repair environment, however, it is a useful quality assurance method that can be done easily alongside the production bonded joint.

4.5.4 Test Results

> "You can observe a lot by watching."
>
> Yogi Berra

4.5.4.1 Wedge edge test results. The wedge edge performance of the 23 pretreatments tested is compared in figures 4.11 through 4.13. The specimens were subjected to eight weeks of salt spray exposure at 35°C and 99 percent relative humidity. Each result represents the average of five tests.

In figure 4.11, the results of the 13 unprimed specimens are rank-ordered. Crack extension amounts are reported after one hour and more than 1,300 hours of exposure, respectively. A modification of the standard tank PAA process, where the chromic-sulfuric etch step was replaced by abrasion with Scotch Brite pads, is presented as a benchmark. A short bar (low crack extension) indicates a durable surface preparation. The specimens treated with Alodine 1200 and the PACS process all showed good durability, although they could not match the tank process performance. These were followed in descending order of performance by Pasa Jell 105, amino-silane EC-3901, and non-chemical treatments. The specimens abraded with Scotch Brite alone failed completely after just four days of exposure.
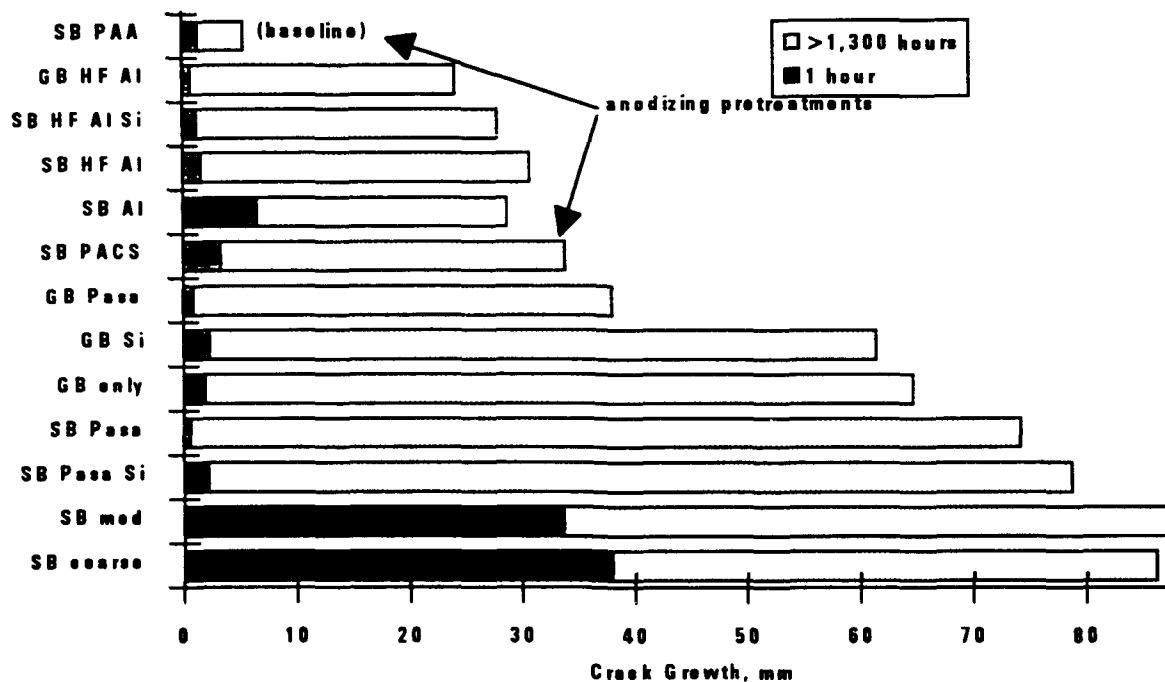
*Figure 4.11   Wedge edge test results, 35°C, 99% relative humidity
salt spray, no primer. Codes after Table 4.2.*

Figure 4.12 presents the outcome of the tests on the 10 primed specimens. The relative rankings stayed approximately the same, with the anodize processes performing best. The addition of the priming step moved the PACS ranking above the Alodine specimens. These usually outperformed Pasa Jell, though the differences were slight. HF etching following mechanical abrasion processes improved the durability only slightly. When either HF etching or mechanical abrasion was used befc the Alodine treatment, the mechanical abrasion techniques gave superior performanc   ˄ worst performance was turned in by the Scotch Brite/Pasa Jell/Primer combination.   oᴛher pretreatments tested except Hydrofluoric/Alodine/Primer approached or exceeded t'   ɩ2.5 mm maximum.
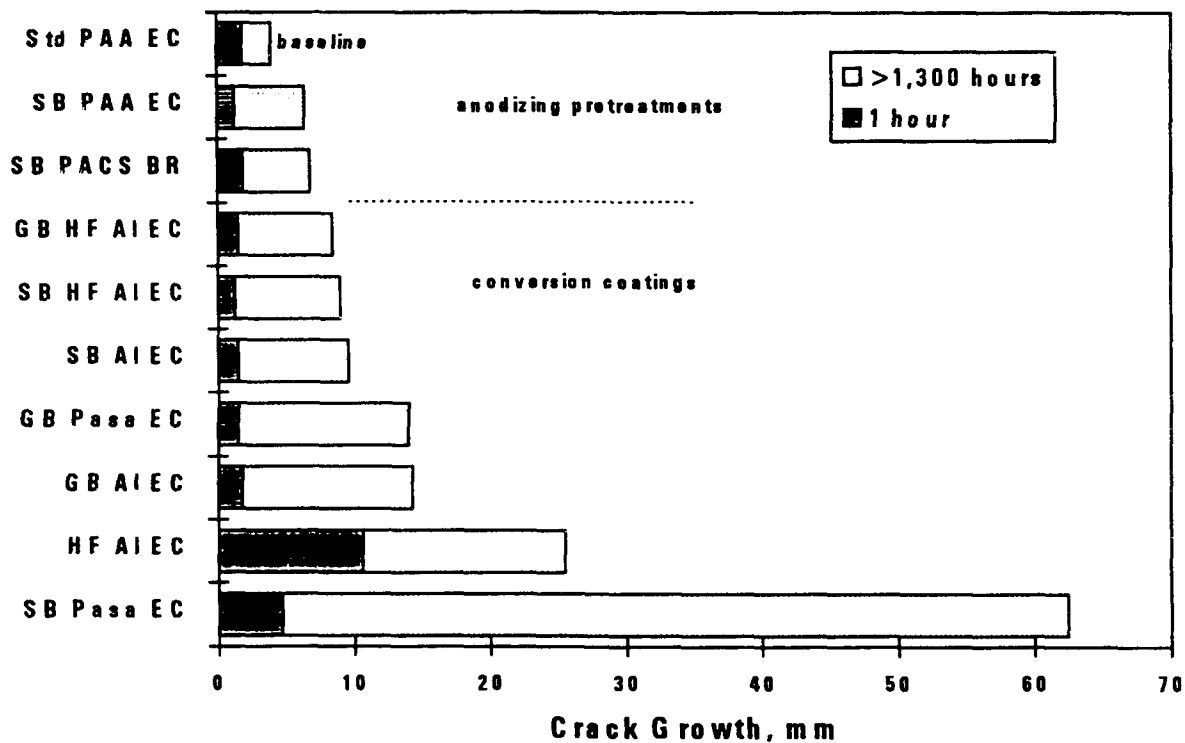
Figure 4.12.   Wedge edge test results,   35°C, 99% relative humidity salt spray,
primed with EC-3960.   Codes after Table 4.2.

When a comparison of the performance of primed versus unprimed specimens is made (figure 4.13), the positive influence of the priming step on durability is unmistakable. Of the non-tank processes, only the Scotch Brite/Pasa Jell combination (worst performance overall) did not exhibit a significant improvement upon priming. The remaining primed specimens exhibited average improvements in long-term durability (measured as reductions in crack growth) of 69 percent.
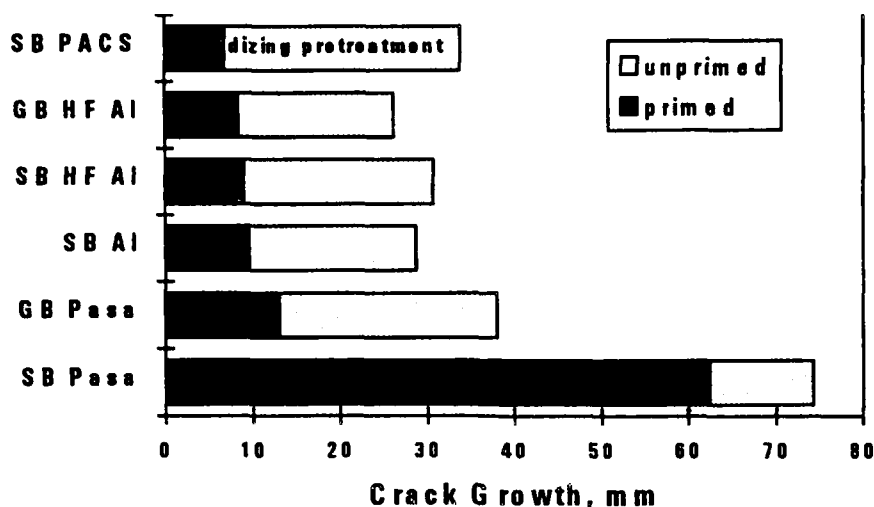
Figure 4.13. Effect of primer on long-term wedge edge test results at 35°C, 99% relative humidity salt spray. Selected non-tank pretreatments shown.

4.5.4.2 Floating Roller Peel Test Results. Based on the results of the wedge edge tests, 13 of the more durable pretreatments were continued to this phase. The average peel strength of the tested pretreatments is shown in figure 4.14. Peel data are presented for two test conditions: at room temperature in lab air and after exposure to 35°C and 99 percent relative humidity for one week.

The data show much better peel results for the anodizing pretreatments (PAA and PACS). However, the priming step has no clear influence on peel values.

Hot/wet exposure caused about 20 percent reduction in peel values. The exception was for specimen pretreated with Scotch Brite/Hydrofluoric Acid Etch/Alodine /Primer, which experienced a 60 percent drop in peel strength.
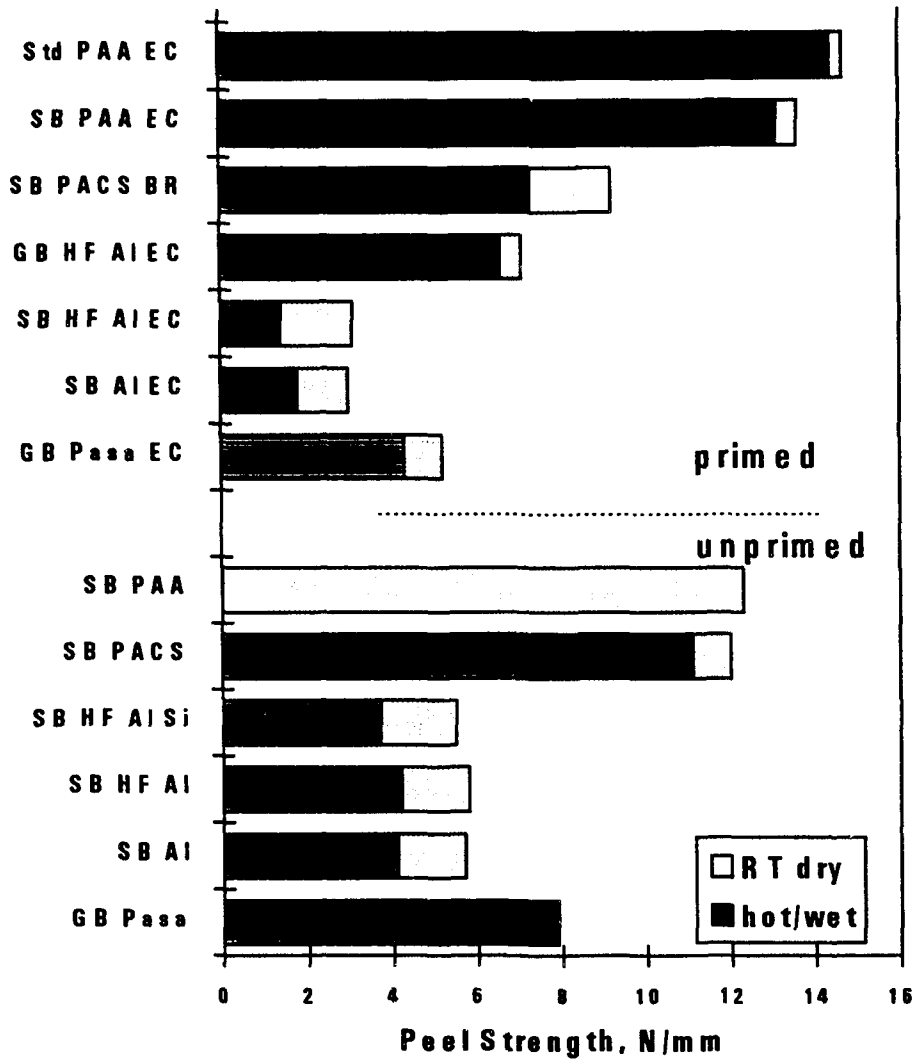
Figure 4.14.   Floating roller peel test results for selected pretreatments.

4.5.5 Discussion

The results show the superiority in durability and peel strength of the anodized and primed pretreatments. PAA and PACS plus adhesive primer were the top two performers in both tests.

In contrast, however, the durability ranking of the two conversion coatings was the opposite of the peel strength results. The Alodine 1200 treatments, which outperformed the Pasa Jell 105 in durability, gave poorer peel results. While promoting good durability,

the Alodine treatment created a thicker, mechanically weaker interface than Pasa Jell surface.

While the addition of a priming step improved the wedge edge durability of most treatments, its effect on peel strength was minimal. In fact, the performance of the PACS specimens primed with BR-127 and the Alodine 1200 specimens primed with EC-3960 was lower than their respective unprimed comparisons. Furthermore, the hot/wet exposure had only limited influence on the results. This could be a function of the short exposure time (one week) or that only the more durable pretreatments were continued to this phase.

The influence of the mechanical abrasion technique can be seen if one compares the grit-blasted (GB) specimens to those subjected to the Scotch Brite (SB) treatment, figures 4.11 through 4.13. The grit-blasted specimens, which gave slightly better wedge edge results, also resulted in higher peel values for otherwise identical pretreatment processes.

The comparison of the adhesive primer EC-3960 to the aminosilane EC-3901 shows that while primer gave better durability, the silane promoted higher peel values. While only one silane treatment passed the durability screen, its peel strength was higher than its primed equivalent, yet well below the desired 10 N/mm.

For bonded repairs to primary structure, the Boeing-developed PACS procedure including the priming step emerges as the clear best choice. It combines excellent durability with the highest peel strength values of any non-tank process. If equipment limitations rule out the PACS procedure, the preferred alternative is the grit blast/HF/Alodine 1200/primer procedure. The grit blast/Pasa Jell 105/primer process is also acceptable.

4.6 Adhesives for Bonded Repair

Many potential repair adhesives exist. Criteria for adhesive selection must consider the operational flight and ground loads and exposure to a wide range of temperatures and humidities. As a minimum, one must bear in mind the following needs:

- adequate long-term durability (as measured by the Delft-modified ASTM D 3762-79 wedge edge test introduced in section 4.5.3.1),

- adequate static shear strength (>25 MPa by the Delft-modified ASTM D 1002-72 lap shear test, see section 4.5.3.3) and peel resistance (>10 N/mm as defined by the Delft-modified ASTM D 3167-76 floating roller peel test, discussed in section 4.5.3.2) at all expected service temperature/humidity combinations,

- fatigue resistance,

- creep resistance,

- low cure temperature (the nearer ambient, the better), and

- curing with vacuum pressure only.

Equally important is the realization that operators perform most repairs with limited equipment. The following adhesive characteristics are highly desirable:

- long storage life (> one year) and limited need for refrigeration,

- ease of handling (good tack and drape for film adhesives),

- long working life at room temperature (four hours or more), and

- limited release of toxic chemicals during repair.

Most western airlines have experience with bonded repair of secondary structures using two-part paste epoxy adhesives. However, the demanding requirements of primary structural repairs will probably force repairers to use higher-performance epoxy film adhesives, which require freezer storage and have only about a six-month shelf life. Some airlines, including KLM, already use rubber-toughened epoxy film adhesives.

In standard autoclave curing processes, the entire component to be bonded is placed inside a vacuum bag. This allows the air in the bag to be evacuated before the curing process

begins. The entire assembly is placed into an autoclave, which can apply high pressures and controlled elevated temperature profiles to the bonded assembly. Proper autoclave curing results in a void-free, strong, durable bond line.

When the part to be bonded cannot be placed in an autoclave, as occurs in most primary structural repairs, one's choice of process parameters is limited. The non-autoclave bonding process is limited to the low pressures achievable with vacuum bags, hydraulic presses or electromagnetic clamps. Heating must be accomplished with electrical resistance blankets, lamps or hot-air blowers, and temperature control of the bonded assembly can be problematic.

This section will discuss recent developments in structural film adhesives for bonded repairs. It includes an evaluation of the suitability of selected new and established aerospace adhesives for use in bonded non-autoclave repair of thin aluminum sheets.

4.6.1 Adhesives for Bonded Repair

An advance in adhesive technology resulted in the availability of structural adhesive films that have long storage lives at room temperature. These films, known as the AF-377 series of 3M Company, have the added benefit of a low curing temperature (96°C vs the standard 120°C for most structural adhesives). A cure temperature below 100°C avoids blowing the core out of moisture-containing hollow structures (e.g., honeycomb) by boiling the entrapped water [48].

The AF-377 series includes both adhesives and prepregs (carbon, glass, or aramid fibers pre-impregnated with adhesive). It was developed primarily for the in-field repair of organic matrix composite structures. The following sections describe three potential repair adhesives considered and the results of a test program carried out to select a suitable metal bond repair adhesive.

4.6.1.1 AF-163-2K/2M. This adhesive was originally included as a benchmark. AF-163-2 is a state-of-the art rubber-toughened epoxy film adhesive used in the autoclave curing of metal-to-metal and honeycomb sandwich bonded structures [49,50]. Toughened adhesives show greater resistance to peeling loads. It was not developed as a "repair

adhesive." Nonetheless, it has been used successfully in bonded repairs [51]. Furthermore, it is well-characterized and commonly available.

4.6.1.2 AF-377-K. This first-generation room temperature storable adhesive was provided for evaluation by the 3M Company. The adhesive could be cured in a vacuum bag at 96°C in two hours, or in one hour at 120°C. The lower cure temperature was considered important in case curing was required in the presence of moisture-containing structure, such as honeycomb.

Early testing performed as a part of this project showed the material to have low peel and shear strengths compared to AF-163-2K. This was attributed to less than optimal cure parameters used in the early tests. Furthermore, the glass fiber carrier resulted in poor durability properties for the adhesive in the wedge edge test. Discussions with 3M indicated a nylon knit carrier should solve the durability problem. Continued evaluations were being planned when the original AF-377 version was superseded by AF-377-2. This was to be available with both mat polyester (-2M) and knit nylon (-2K) carriers. Further assessment of the original formulation AF-377-K was halted at that point.

4.6.1.3 AF-377-2M/2K. According to the manufacturer, the "-2" version was developed to remedy a problem with low resistance to organic solvents in the original version. Unfortunately, this improved fluid resistance was a result of the removal of certain proprietary catalysts from the original formulation. The new formulation requires two hours to cure at 120°C; a 96°C cure now takes six hours.

4.6.2 Non-autoclave Curing Techniques

As discussed earlier, one has a limited choice of curing conditions when faced with a bonded repair. The techniques developed here involved the use of vacuum bags to supply pressure in the bond line. Electrical resistance heat blankets provide the energy required to cure the adhesive. Further information can be found on the subject in the literature [52,53].

Vacuum bagging refers to the sealing of a repair area with heat-resistant plastic films. By evacuating the area to be bonded, the atmosphere provides the pressure required to

accomplish the bonding process. Vacuum bag processes require that the patch and skin contours match well.

Temperature control was achieved with a portable programmable digital controller and some thermocouples placed on the patches. Heat loss to the environment was prevented by placing simple insulating blankets over the bonding assembly.

When repairs are made to complex structures with attached ribs, stringers or spars, a wide variation in temperatures can occur. Over thicker sections, the adhesive may not reach a high enough temperature to cure properly, while the thin sections could be overheated. In real structures, one must employ either multiple heating sources or use available zone-controlled heat blankets. Because of financial limitations, only single-control heat blankets were used in these tests.

Commercially available hot bonding carts usually employ independent controllers for each heat zone used. Variables such as cure temperature, rise time, cure time, etc., can be controlled via a microprocessor in the system. Such units provide alarm functions if deviations occur in the programmed temperature profile or if vacuum pressure is lost. A record of the bond cycle can be printed on paper or stored on floppy disk. A trial run without adhesives is advised for a new situation.

4.6.3 Adhesive Performance Test Results

The following parameters were used based on the recommendations of 3M for vacuum bag curing of AF-163-2K: Use the maximum attainable vacuum pressure (90-95 kPa) for 45 minutes. Heat at a rate of 2.8°C per minute, relaxing the vacuum to 35 kPa at 50°C. Hold at 120°C for one hour, followed by cooling at 3.8°C per minute until vacuum release. The optimum curing parameters for AF-377-2 had not been developed when this series was begun, so an iterative approach was followed in their establishment [54-58].

4.6.3.1 Floating Roller Peel Test. The floating roller peel test, described in section 4.5.3.2, was used to establish cure parameters for AF-377-2 in a two-hour, 120°C cure. For each cure cycle variation, five specimens were tested. Surface preparation consisted of standard tank PAA pretreatments and EC-3960 adhesive primer. All specimens spent 45 minutes at full vacuum (90 kPa) before heating, and had the vacuum pressure lowered when they reached 60. The heating rate, vacuum pressure during cure, and cooling rate

were varied. The goals were to produce an acceptable peel strength with a uniform bond thickness while minimizing voids and bleeding.

The AF-377-2 was tested in two film weights (146 and 293 g/m^2). Furthermore, two carrier types were investigated (nylon knit, -2K, and polyester mat, -2M). The results of an empirical study of bonding variables are shown in table 4.3.

Table 4.3.   Results of cure parameter variations on peel strength of AF-377-2

Adhesive, film weight	Heating rate, °C/minute	Vacuum, kPa above 60°C	Cooling Rate, °C/minute	Peel Strength, N/mm (average)	Comments
AF-163-2K 293 g/m²	2.8	35	3.8	12.2	baseline
AF-377-2K 293 g/m²	2.9	90	2.7	3.6	heavy bleeding, thin bond lines, voids & starvation
	2.7	35	3.0	3.8	moderate bleeding, voids & starvation, cohesive failure
	2.7	10	3.1	3.0	low bleeding, large voids, flat cohesive failure
	5.6	35	5.0	3.0	v. low bleeding, large voids, highest heating rate
	4.0	35	4.5	2.9	low bleeding, large voids, film thickness & strength variation
AF-377-2M 293 g/m² 146 g/m²	4.3	35	5.0	2.9	variation in bond thickness and peel strength near edges
	4.6	35	5.0	5.2	artificially aged/constant thickness, little bleeding, few voids, rough adhesive fracture surface

A problem encountered early in the program involved a large variation in thickness found in the AF-377-2 films. This led to air entrapment during lay-up and excessive voids in the bond lines. When these films were received from 3M, they were tacky. The films progressed naturally to a tack-free brittle state after four to six weeks at room temperature. Frequent handling of the films during their tacky stage probably caused the thickness variations. This problem was overcome by artificially aging the films directly to a

tack-free state upon receipt. Aging was performed in an oven at 65°C for three hours. The long-term effects of such artificial aging on the mechanical properties and storage characteristics of the adhesive are as yet unknown.

The best combination of curing parameters for the AF-377-2 turned out to be a moderately low vacuum pressure at the curing temperature (35 kPa) coupled with high heating and cooling rates (4 to 5°C per minute). These conditions produced more consistent bond line thicknesses, less bleeding, and an acceptable amount of voids.

The higher peel performance of the thinner AF-377-2M (5.2 N/mm for the 146 g/m^2, polyester mat carrier) can be attributed to several factors. The failure surfaces of the thicker films typically showed a flat and featureless cohesive failure in the adhesive near the adhesive/primer interface. However, in the thinner areas of bond lines (typically near the edges of the specimens) the fracture surface followed the carrier film and was much rougher. This was accompanied locally by a higher peel strength. When the thinner film with the mat carrier fractured, the roughness was more pronounced and covered almost 100 percent of the surface.
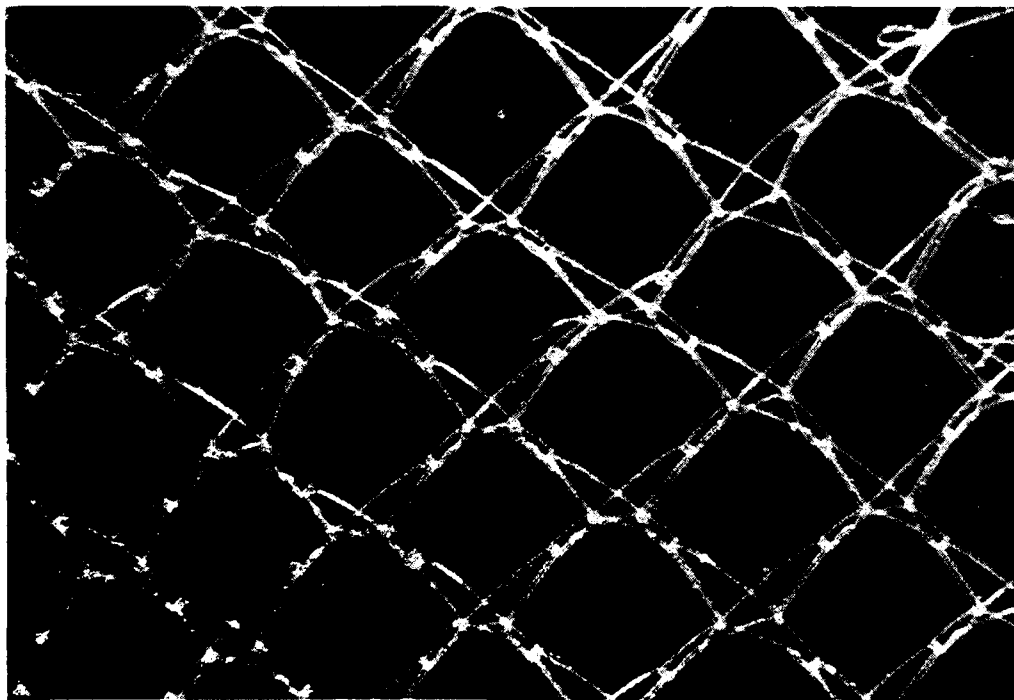
Figure 4.15a. Nylon knit carrier used in AF-377-2K.

The differences in performance can be better explained by examining micrographs of the two carriers, shown in figure 4.15. The nylon knit carrier (4.15a) has larger gaps and presents a low surface area to the adhesive, while the mat carrier (4.15b) shows a random pattern. The mat carrier presents more surfaces on which to bond. Adhesive fractures along the mat carrier require more energy by creating additional fracture surfaces.
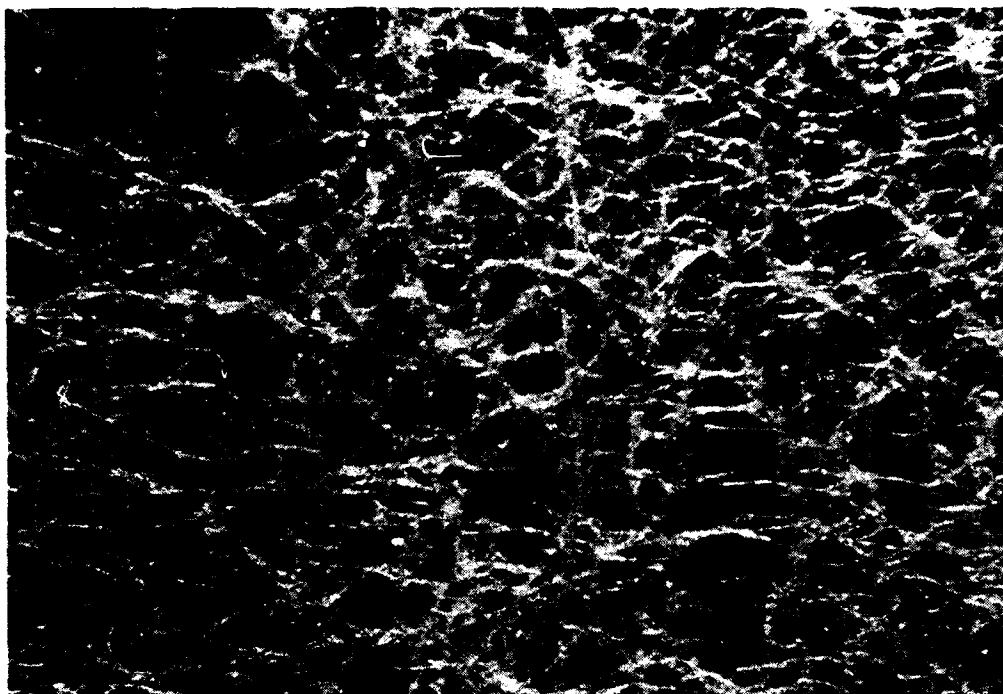
Figure 4.15b. Polyester mat carrier used in AF-377-2M.

Figure 4.16 recapitulates the floating roller peel results, including an AF-163-2K sample made in the autoclave as a further reference. The vacuum-cured AF-377-2M demonstrated peel values less than half those of AF-163-2 cured with vacuum pressure.

All additional tests to AF-377-2 in the following two sections will follow the final cure cycle shown in table 4.3, using AF-377-2M in the 146 g/m^2 film weight. Vacuum-cured and autoclave-cured AF-163-2K, 293 g/m^2, will continue to function as the reference adhesives.
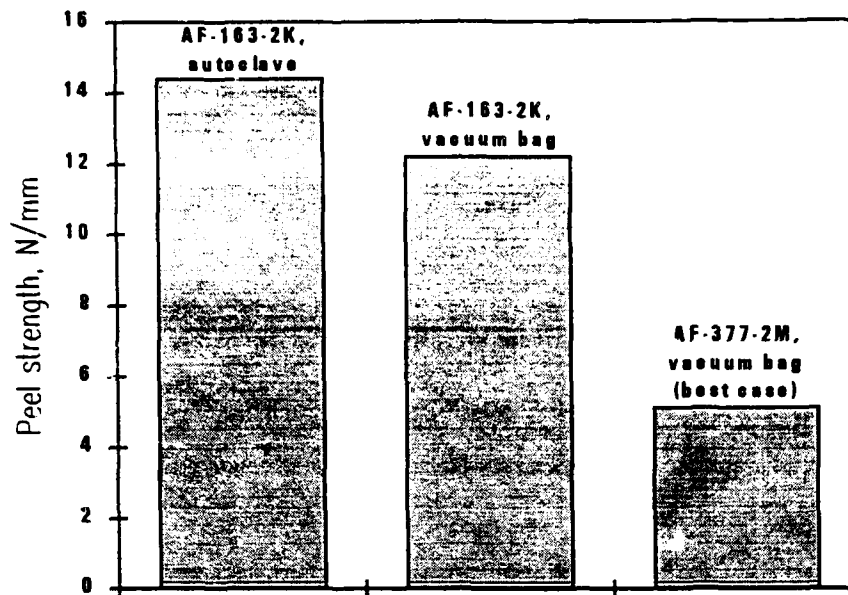
Figure 4.16. Floating roller peel test results.

4.6.3.2 Wedge edge tests. Specimens were prepared as in the previous section. The standard PAA tank processes were followed by EC-3960 primer applied in a thickness ranging from 4.5 to 5.0 µm, according to the appropriate specifications. Instead of the salt fog exposure used to challenge the pretreatments and aluminum substrates in section 4.5, a distilled water environment of 35°C and 99 percent relative humidity was used. (Water is more damaging to epoxy adhesive properties, salt fog is harder on aluminum surfaces.) The specimens were exposed for eight weeks and crack growth was monitored throughout.

Figure 4.17 shows the crack length versus time for the following sample types: AF-163-2K cured both in an autoclave and with a vacuum bag, AF-377-2M cured with a vacuum bag, and the original formulation AF-377-K cured in the vacuum bag. One sees a large difference in performance between the rubber-toughened AF-163 and the more brittle AF-377 series.
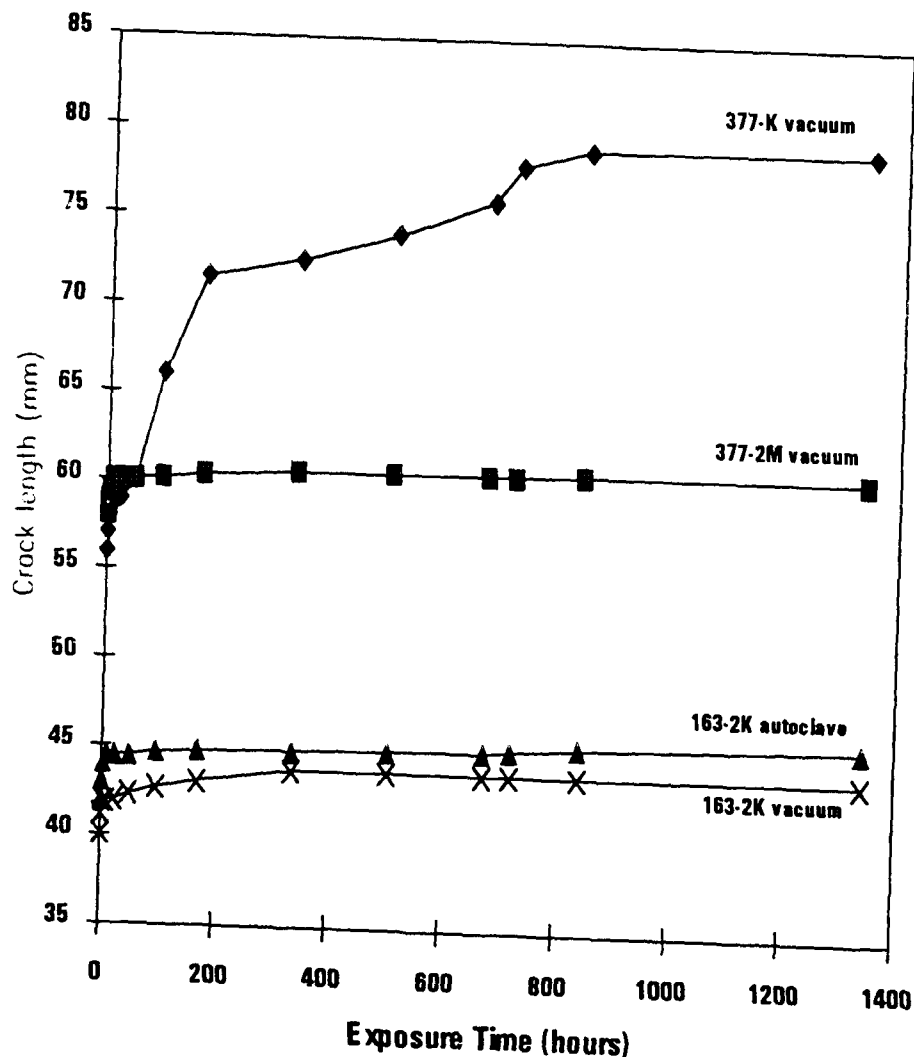
Figure 4.17. Crack length versus time for wedge edge specimens exposed to 35°C, 99% relative humidity.

Apparently the low cure pressure of the vacuum bag cycle has no influence on the durability of AF-163-2K. The large initial crack opening seen with the 377 resins, however, is an indication of the low peel strength of the more brittle adhesives. This is not necessarily a sign of poor durability.

A flat crack extension slope over time may indicate good adhesive durability. However, because of the large initial crack opening displacement of both AF-377 formulations, the remaining crack driving force is smaller.

When crack extension was considered as the durability criterion, only the AF-377-K performed poorly. (Recall that this original formulation used a glass knit carrier, which is

known to cause poor hot/wet performance.) This deficiency ruled out AF-377-K from further consideration. A direct comparison between AF-163 and AF-377-2M is not meaningful.

4.6.3.3 Single lap shear tests. Specimens received the standard PAA pretreatment and EC-3960 adhesive primer before bonding. The same cure parameters chosen for the peel tests were used for the single lap shear specimens. Five specimens were produced of each adhesive.

Testing always resulted in the desired cohesive failure mode. Figure 4.19 presents the average results of the tests. All adhesives showed good performance.
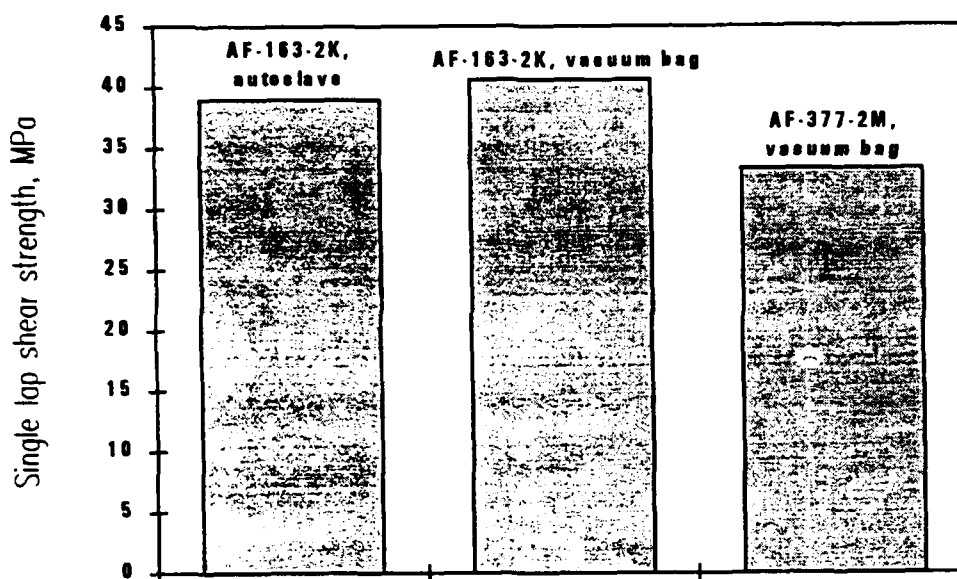
Figure 4.19. Single lap shear test results.

98

4.6.4 Discussion

The techniques demonstrated here show that good quality adhesive bonds can be accomplished outside the autoclave without adding too much complexity to the task of fuselage skin repairs.

Variations in thickness in AF-377 probably resulted from handling the adhesive in its tacky state. Artificial aging of the adhesive is recommended before shipping the adhesive to users. This can improve the quality of the bond by reducing the amount of voids in the bond line.

The mat carrier film version of AF-377 (-2M) gave the best overall performance of the AF-377 formulations tested. Its higher peel strength compared with the knit carrier (2K) can be attributed to the greater creation of new fracture surfaces with the mat formulation. However, its peel strength was still less than half that of AF-163-2K cured with the vacuum bag and heat blanket.

The results of these tests emphasize the need for considering the complete operational environment when choosing an adhesive for bonded repairs. Adhesives used for single-sided bonded repairs to metal fuselage skins will see significant peel loads. While the optimized cure cycle developed for the AF-377-2M showed adequate durability and high lap shear strength, its low peel strength was disappointing.

The ability to store an adhesive at room temperature is highly desirable. However, the low peel strength of the current formulation of AF-377-2 indicates a need for further toughening before it can be recommended as a metal repair adhesive. AF-163-2K will be used for further bonded repairs performed in this research effort.

4.7 Patch Materials

The availability of lightweight, strong, stiff fibers originally developed for use in composite primary structures has led researchers to investigate their application to patching of cracked aluminum aircraft structures. Crack patching exploits the high specific stiffness properties of fibers such as carbon and boron to reinforce cracked aluminum structure. Crack patching works by extending the remaining life of the structure by slowing its rate of crack growth. Table 4.4 [59] compares some important properties of typical composite and metallic repair materials.

Table 4.4. Various materials considered
for bonded patching of aluminum aircraft structures.

Patch Material	Specific Tensile Modulus GPa-cm³/g	Coefficient of Thermal Expansion, $10^{-6}/°C$	Approximate Relative Material Cost
2024-T3 (clad, polished)	26	23	1
R-Glass/Epoxy	20	6.1	1
Aramid/Epoxy	42	-0.8	2
GLARE 2 (3/2)	26	20	5
HM 35 Carbon/Epoxy	120	~-1	16
FT700 Carbon/Epoxy	194	~-1	24
Boron/Epoxy	103	4.5	40

Properties for unidirectional composite prepregs, 60% fiber volume content, except aramid/epoxy, 50% fiber volume content. Composite costs are fibers; prepreg prices are higher. [59]

Aluminum is the most widely used repair material, primarily due to its low cost, ease of use and wide availability. However, it is uncommon as a bonded repair patch material. Maintainers typically use rivets to attach aluminum patches, as was discussed in chapter 2.

Glass fibers are attractive to repairers: They are economical and widely available. Maintainers have employed bonded glass fibers for decades to repair secondary structures such as radomes and control surfaces. Although modern glass fibers have excellent strength and high strain-to-failure (5 percent), glass/epoxy prepregs have specific stiffness lower than aluminum.

GLARE 2 unidirectional fiber metal laminate has the same specific stiffness as aluminum and moderate cost. GLARE is well-known for its exceptional resistance to fatigue [6] and impact [7]. Its outer layer of aluminum acts as a natural environmental barrier. Unlike most composite prepreg materials, GLARE has an unlimited shelf life, and can be plastically deformed.

Aramid/epoxy unidirectional prepregs have about 1.6 times the specific stiffness of aluminum and are available at moderate cost. Aramid fibers are sensitive to moisture pickup from the environment, which has a harmful effect on the mechanical properties of the adhesive bond. (Boeing had well-publicized moisture pickup problems with aramid/epoxy composite control surfaces in the 1980s.) This can be alleviated by bonding a thin protective sheet of aluminum over the composite patch to keep out moisture. (This is in fact a good practice to assure the durability of all bonded composite patches.)

Other factors influencing the use of aramid fibers as a crack patching material are the effect of residual thermal stresses and of the fatigue ratio R ($\sigma_{min}/\sigma_{max}$) on the fibers. Bonding aramid fibers to aluminum above room temperature induces a residual compressive stress in the fibers. Roebroeks [6] found this residual stress contributed to the pullout, microbuckling and final failure of aramid fibers in **ARALL** laminates tested in constant amplitude fatigue at R = 0. This indicates that crack patching of pressurized fuselages with aramid/epoxy patches might be problematic.

Carbon/epoxy prepregs combine high to extremely high specific stiffness with good availability at moderate to high costs. The use of carbon fibers as crack patching materials has achieved varying degrees of success. One limitation to their use is the large galvanic couple between carbon and aluminum. This can cause rapid corrosion of the aluminum. Thin barrier plies of glass fibers between the carbon and aluminum layers can overcome this problem. The extremely high specific stiffness of the newest carbon fibers suggest they may be cost- and weight-competitive with the well-characterized boron/epoxy system.

Boron/epoxy has received perhaps the most attention and application recently as a patch material. It combines one of the highest available specific stiffnesses with none of the galvanic problems suffered by carbon fibers. The major obstacle to its widespread application is its extremely high cost. Boron is expensive because of the enormous amounts of energy required for its manufacture. Moreover, its low annual production is

only 16,000 kg from a sole supplier. The large boron fiber diameter (about 12 times greater than carbon) results in a stiff, "boardy" prepreg that makes forming and working with the prepregs more difficult. This limits boron/epoxy patches to gentler curvatures than carbon/epoxy. As discussed earlier, its major crack patching application has been to extend the life of thick structures whose replacement is too costly.

All fibers considered for use in crack patching have a coefficient of thermal expansion lower than aluminum. This can lead to unfavorable residual tensile stresses in the repaired structure after curing of the patch, which will be analyzed in detail in chapter 5.

4.8 Inspection of Bonded Repairs

> One of the best preserved castles in the Netherlands is Muiderslot, a stone fortress in the middle of the Vecht River. It was built around 1280 for Count Floris V of Holland and Zeeland. It contains a Ridderzaal, or Knights Hall, used in the administration of justice. The Knights Hall contained a limestone table that was used to inspect coins offered in payment of river tolls. The coins were tapped on the table; if the sound was good, the coins were accepted. If the traveler offered counterfeit coins, he ended up in the dungeon beneath the Hall.

The quality assurance of an adhesively bonded repair patch is a challenge. Riveted repairs can be visually inspected and their strength can be reliably predicted based on external condition. However, adhesive bonds can pass all sorts of non-destructive tests and still have little or no bond strength. Inspection methods can be roughly divided into two groups: inspection of the constituents that make up the bonding operation (process control) and inspections performed after the bonding operation has been accomplished.

4.8.1 Process Control

As discussed in previous sections, controlling the surface pretreatment process is the most important step in achieving a high-quality bond. Keys to consistent high-quality bond pretreatments include:

- adequate training of bonding personnel,
- absolute cleanliness in the pretreatment and bonding areas,
- control of the chemicals involved in the pretreatments, and
- surface inspection of the pretreated adherends prior to bonding ("water break" test, anodize and primer layer inspections).

The PABST program showed conclusively that if the adherends fit together before bonding, there was no need to inspect them after bonding, because they were properly bonded. Further, if the pre-bond fit was poor, there was no point in inspecting the bond either---it was unacceptable. Experienced metal bond engineers emphasize that inspecting quality into a product after the fact is the least cost-effective approach for bonded structures. On the contrary, investing in controlling the individual steps (good training, proper surface pretreatments, adequate bond tools and bonding process control) pays much greater dividends [13,60].

4.8.2 Inspection of Adhesive Bonds

Having been duly warned, methods for bond inspections will be discussed nonetheless. A common practice has been the concurrent production of destructive lap shear, peel or wedge edge test specimens with the execution of the bonded repair. The concept here is that if the test specimen performs adequately, the quality of the overall bonding operation is also acceptable. The limitation here is that the tests reveal data only about the static properties of the bond. They give no information about long-term durability.

Non-destructive bond inspections rely on some type of energy put into a bonded structure. For many years, the well-known "coin tap" method has been popular with maintenance personnel for assessing bond integrity. It is highly dependent on operator skill, experience and hearing acuity.

Some semi-automated devices, such as the simple, hand-portable "Woodpecker," are in use at major airline maintenance departments. They operate on a similar pulse-echo principle, sending sonic energy into the part and measuring its reflection. The proven Fokker bond tester uses a resonance-shift principle to detect disbonds [61]. More complex ultrasonic techniques such as A-scan and C-scan are less suitable for field use, because they require a couplant fluid to be placed on the inspected surface. Through-transmission ultrasound is virtually impossible because it requires unhindered access to both sides of the structure. The reader is referred to Krautkramer and Krautkramer [62] and Ensminger [63] for further details.

Once a disbond or other defect is found, the question shifts to what to do with it. Many minor delaminations should simply be left alone. "With a local disbond, testing on the PABST program clearly indicated that adhesive bonds are far more tolerant of flaws and porosity" than was previously believed [13]. A properly designed adhesive bond, much stronger than the adherends, is quite forgiving of small delaminations. Repair of a delamination is typically done by drilling into the delaminated area and injecting repair adhesive. This can result in unintended "sabotage" by inducing corrosion in the bond line. This occurs because moisture is allowed in and the protective anodic layer has been destroyed by drilling [60].

4.9 Summary and Conclusions

The basics of adhesive bonded repairs for aluminum aircraft fuselages have been presented, with emphasis on the practical aspects. Some simple rules of thumb for patch design make it possible for bonded patches to be produced by maintenance personnel.

An extensive evaluation of existing and developmental surface preparation techniques showed the Boeing Phosphoric Acid Containment System (PACS) plus adhesive priming to be the superior in-field pretreatment. It combines excellent durability with the highest peel strength values of any non-tank process. Two non-anodizing treatments gave adequate strength and durability as well. However, the aminosilane EC-3901 was unable to meet either the strength or long-term durability requirements of bonded repairs. It is not recommended for use.

A newly developed epoxy film adhesive with the ability to be stored for long periods at room temperature was investigated. AF-377-2M was evaluated for strength and durability using the high-performance toughened epoxy film AF-163-2K as a comparison. A long shelf life at room temperature is highly beneficial in the maintenance environment. Nevertheless, the low peel strength of the current formulation of AF-377-2 makes it less desirable as a metal repair adhesive. AF-163-2K will be used in further bonded repair research described here.

Experience has shown that consistent high-quality bonding requires investments in adequate training of bonding personnel, attention to detail and cleanliness in the pretreatment and bonding areas, and strict control of pretreatment and bonding processes. While good bond inspection techniques exist and can be used in the field, trying to inspect quality into the bond after the fact is not cost-effective. Further rework of improperly installed bonded repairs frequently does more damage than good.

The following two chapters will delve further into the analytical and practical aspects of bonded repairs.

References, Chapter 4

1. Primary Adhesively Bonded Structure Technology (PABST), General Material Property Data, AFFDL-TR-77-107, Dayton, Ohio, September 1978.

2. Vogelesang, L.B. and J.W. Gunnink, "ARALL: A Materials Challenge for the Next Generation of Aircraft," *Materials and Design*, Vol. 7, No. 6, 1986.

3. Veggel, L. van, "Damage Tolerance Aspects of an Experimental ARALL F27 Lower Wing Panel," presented to the ARALL Laminates Users Conference, Seven Springs, Pennsylvania, 25-28 October 1987.

4. Miller, N., "Structural Improvement of Operational Aircraft, Volume IV, ARALL Evaluation," AFWAL-TR-87-3029, Vol IV, Dayton, Ohio, April 1991.

5. Pettit, R., "Application of ARALL Laminates to the C-17," presented to the AeroMat Conference, Long Beach, California, May 1991.

6. Roebroeks, G.H.J.J., "Towards GLARE: The Development of a Fatigue Insensitive and Damage Tolerant Material," Ph.D. thesis, Delft University of Technology, Faculty of Aerospace Engineering, Delft, the Netherlands, December 1991.

7. Vlot, A., P. Bulters and R. Fredell, "Low and High Velocity Impact Loading on Fiber/Metal Laminates, Carbon/PEEK and Monolithic Aluminum 2024-T3, *Proc. 13th Int'l European SAMPE Conf.*, Hamburg, Germany, 1992, pp. 347-360.

8. Oost, R.C. van, W.J. Slagter, B. van Wimersma, K.J.J.M. Zaal and J.W. Gunnink, "Feasibility Study of the A320 Fuselage Section 13/14 in Aerospace ARALL, Report LRV-07, Delft University of Technology, Faculty of Aerospace Engineering, Delft, the Netherlands, July 1990.

9. Fredell, R. and J. Gunnink, "Fiber Metal Laminates for Improved Structural Integrity," *Proc. Conf. Structural Integrity of Aging Aircraft*, Atlanta, Georgia, March-April, 1992.

10. Schwarmann, L., N. Ohrloff and T. Beumler, "On the Application of GLARE for Airbus Fuselage Structures, in A. Beukers *et al.*, editors, *Proc. Specialists' Conf. on Fatigue of Aircraft Materials*, Delft University Press, Delft, the Netherlands, October 1992, pp. 191-200.

11. "Airbus Studies New Fuselage Composite," *Flight International*, 10 March 1993.

12. "Airframe Makers Use Aging Aircraft Experience to Refine Design Practices," *Aviation Week and Space Technology*, 24 July 1989, pp. 94-95.

13. Hart-Smith, L.J., "Design and Analysis of Bonded Repairs for Metal Aircraft Structures," from *Bonded Repair of Aircraft Structures*, A.A. Baker and R. Jones, editors. Dordrecht, NL: Martinus Nijhoff Publishers, 1988, pp. 31-48.

14. "FAA Proposes Checks for Cracks on 727s," *Aviation Week and Space Technology*, 16 January 1989, p. 63.

15. "Aging Fleet Task Force Boeing 747 Structures Working Group Status Update," 17-19 September 1991.

16. 't Hart, W.G.J. and R.J.H. Wanhill, "Patch Repair of Corroded Aircraft Skin Areas," National Aerospace Laboratory NLR, Amsterdam, NL, 1984.

17. Kinloch, A.J., *Adhesion and Adhesives: Science and Technology*. Chapman and Hall, London, 1987, pp.18-97.

18. Baker, A.A., and R. Jones, editors, *Bonded Repair of Aircraft Structures*. Martinus Nijhoff, Dordrecht, NL, 1988.

19. Deryaguin, B.V. and V.P. Smilga, *Adhesion, Fundamentals and Practice*, McLaren, London, 1969.

20. Voyutski, S.S., Autohesion and Adhesion of High Polymers, John Wiley/Interscience, New York, 1963.

21. Kinloch, A.J., *Durability of Structural Adhesives*, Elsevier, London, 1983.

22. Lieng-Huang, L., in K.L. Mittal and H.R. Anderson, Jr., editors, *Acid Base Interactions: Relevance to Adhesion Science and Technology*, VSP bv, Utrecht, NL, 1991, pp. 3-23.

23. Berger, E.J. in K.L. Mittal and H.R. Anderson, Jr., editors, *Acid Base Interactions: Relevance to Adhesion Science and Technology*, VSP bv, Utrecht, NL, 1991, pp. 207-225.

24. Oosting, R., "Surface Pretreatments," Progress Report, Delft University of Technology, Faculty of Aerospace Engineering, Delft, the Netherlands, September 1991.

25. Semerdjiev, S., *Metal-to-Metal Adhesive Bonding*, Business Books Ltd., London, 1970.

26. Goland, M. and E. Reissner, *J. Appl. Mech.*, **2**, A-17, 1944.

27. Adams, R.D., and N.A. Peppiatt, *J. Strain Anal.*, **8**, 134, 1973.

28. Adams, R.D., and N.A. Peppiatt, *J. Strain Anal.*, **9**,185, 1974.

29. Renton, W.J. and Vinson, J.R., *J. Adhesion*, **7**, 175, 1975

30. Allman, D.J., *Q. J. Mech. Appl. Math.*, **30**, 415, 1977.

31. Renton, W.J. and Vinson, J.R., *J. Appl. Mech.*, **44**,101, 1977.

32. Hart-Smith, L.J., "Further Developments in the Design and Analysis of Adhesively Bonded Structural Joints, Douglas Report Number 6922, Long Beach, California, 1980.

33. Tuttle, M.E., B.M. Barthelemy and H.F. Brinson, *Expt. Techniques,* **8**, 31, 1984.

34. Hart-Smith, L.J., "Effects of Flaws and Porosity on Strength of Adhesive-Bonded Joints," *Proc. 29th SAMPE Symp and Exhib.*, Reno, Nevada, April 1984, pp.840-852.

35. Reinhart, T., "Surface Treatments for Bonded Repairs of Metallic Components," in Baker, A.A., and R. Jones, editors, *Bonded Repair of Aircraft Structures*. Martinus Nijhoff, Dordrecht, NL, 1988, pp.19-30.

36. Wu, P.H., "Implementation of Boric Sulfuric at Boeing Wichita-Replacement for Chromic Acid Anodize," *Proc. 38th Int'l SAMPE Symp.*, Anaheim, California, May 1993, p. 796.

37. Mnich, J. and C. Schoneman, "Sulfuric/Boric Acid Anodizing Status Report--First 22 Months of Operation July 1990-May 1992," *Proc. 38th Int'l SAMPE Symp.*, Anaheim, California, May 1993, pp. 819-833.

38. Thorson, D., "Recent Developments in Surface Preparation for Repair," Proc. 3rd Int'l Conf. Bonded Aircraft Structures Technical Application and Repair Techniques, Metal/Metal Bonding and Advanced Composites, Bremen, Germany, October 1990, pp. 244-260.

39. Wegman, R.F., *Surface Preparation Techniques for Adhesive Bonding*, Noyes Publications, Park Ridge, New Jersey, 1989.

40. Brockman, W. et al., "Adhesion in Bonded Aluminum Joints for Aircraft Constructions," *Int. J. Adhesion and Adhesives*, Vol. 6 No. 3, July 1986, pp.115-143.

41. Knock, K.K., "Structural Repair Bonding," Boeing Document D6-48758, August 1990.

42. Kuhbander, R.J. and J.J. Mazza, "Evaluation of Low VOC Chomated and Non-Chromated Primers for Adhesive Bonding," *Proc. 38th Int'l SAMPE Symp.*, Anaheim, California, May 1993, pp. 785-795.

43. Pluedemann, E.P., *Silane Coupling Agents*, 2nd Edition, Plenum Press, New York, 1991.

44. Kuhbander, R.J. and J.J. Mazza, "Understanding the Australian Silane Surface Treatment," *Proc. 38th Int'l SAMPE Symp.*, Anaheim, California, May 1993, pp. 1225-1234.

45. Baker, A.A., "Crack Patching: Experimental Studies, Practical Applications," in Baker, A.A., and R. Jones, editors, *Bonded Repair of Aircraft Structures*. Martinus Nijhoff, Dordrecht, NL, 1988, pp.121-122.

46. Kelly, L., Introductory Chapter of Baker, A.A., and R. Jones, editors, *Bonded Repair of Aircraft Structures*. Martinus Nijhoff, Dordrecht, NL, 1988, pp. 1-18.

47. Hart-Smith, L.J., "The Bonded Lap-Shear Test Coupon--Useful for Quality Assurance but Dangerously Misleading for Design Data," *Proc. 38th Int'l SAMPE Symp.*, Anaheim, California, May 1993, pp. 239-246.

48. Subrahmanian, K.P., J.W. Davis and B.A. Marteness, "A new low-Temperature Rapid Curing Composite Material for Structural Repair," *Proc. Conf. Bonding and Repair of Composites*, Birmingham, England, July 1989, pp. 101-106.

49. Colucci, F, "3M Aerospace Shows the way," Aerospace Composites and Materials, November-December 1990.

50. Galasso, A. *et al.*, "Aspects of the Fatigue Behaviour of Typical Adhesively Bonded Aircraft Structures," *Proc. 14th ICAF Symposium.*

51. Marsh, G.M., "Repairing Rotor Blades," Aerospace Composites and Materials," 1992.

52. Brown, H., editor, *Composite Repairs*, SAMPE Monograph #1 ,Society for the Advancement of Materials & Processs Engineering, Covina, California, 1985.

53. Hamermesh, C.L., editor, *Composite Repairs*, SAMPE Monograph #2, Society for the Advancement of Materials & Processs Engineering, Covina, California, 1991.

54. "3M Introductory Data: Structural Adhesive Film AF-377-K," 3M Aerospace Materials Department, St. Paul, MN, 1990.

55. "3M Aerospace Technical Data: Structural Adhesive Film AF-163-2," 3M Aerospace Materials Department, St. Paul, MN, Issue No. 1, March 1986.

56. Hoens, R. and R. Fredell, telefax correspondence with Dr. S. Boyd of the 3M Aerospace Materials Department, St. Paul, MN, May-November 1992.

57. McCarvill, W.T., "Prepreg Resins" in *Engineered Materials Handbook, Volume 1: Composites*, ASM International, pp.140-141.

58. Wegman, R.F. and T.R. Tullos, *Handbook of Adhesive Bonded Structural Repair*, Noyes Publications, Park Ridge, New Jersey, 1992.

59. Vermeeren, C.A.J.R., "The Applitaion of Carbon Fibres in ARALL Laminates," Report LR-658, Delft University of Technology, Faculty of Aerospace Engineering, Delft, the Netherlands, September 1991.

60. Hart-Smith, L.J. "How to get the Best Value for Each Dollar Spent Inspecting Composite and Bonded Aircraft Structures," *Proc. 38th Int'l SAMPE Symp.*, Anaheim, California, May 1993, pp. 226-238.

61. Schliekelmann, R.J. "Non-Destructive Testing of Adhesive Bonded Joints," from AGARD-LS-102, Bonded Joints and Preparation for Bonding, Neuilly-Sur-Seine, France, 1979.

62. Krautkramer, J. and H. Krautkramer, *Ultrasonic Testing of Materials*, Springer-Verlag, Berlin, 1990.

63. Ensminger, D., *Ultrasonic Fundamentals: Technology and Applications*, Marcel Dekker, Inc., New York.

5

Analysis of Bonded Crack Patching

5.1 Introduction

"Give me a spirit that on this life's rough sea
Loves t' have his sails filled with a lusty wind,
Even till his sail-yards tremble, his masts crack,
And his rapt ship run on her side so low
That she drinks water, and her keel plows air."

George Chapman,
The Conspiracy of Charles, Duke of Byron (1608)

"Crack patching" refers to the application of adhesively bonded advanced composite materials to the repair of cracked metal structures. Crack patching was first successfully applied to the fracture-critical D6AC steel wing pivot fitting of the General Dynamics F-111 around 1969. The Australian Aeronautical Research Laboratories (ARL) and others have developed this concept further, successfully bonding strong, stiff boron/epoxy or carbon/epoxy composites to cracked thick aircraft structural parts [1-7]. The technique has extended the useful lives of flawed airframes for many years at a reasonable cost. More recently, the United States Air Force has announced plans to reinforce cracked metal longerons on the B-1B using boron/epoxy patches [8]. Federal Express, boron manufacturer Textron and Boeing recently began a cooperative service evaluation of boron/epoxy doublers on the fuselages of two Boeing 747 freighters [9].

Advanced composites can provide high structural efficiency to a repair, and in certain cases they may be the only acceptable choice. Crack patching should be viewed as another specialized tool in the *repertoire* of the damage tolerant repair technician, rather than as a technique to be used every day in all structural repair situations. Crack patching is particularly attractive when replacement of the original cracked structure is exceptionally difficult or expensive, or when replacement parts are unavailable.

This chapter will explain the crack patching analysis developed by Rose and his colleagues. The analysis is expanded further to include the significant thermal effects induced by the large temperature differences between the bonding process and cruise conditions, and the effect of bending induced by a single-sided patch repair is covered.

The entire crack patching analysis package is presented as an interactive computer program suitable for airline maintenance use. The analysis is complemented by a

parametric study comparing various fuselage repair concepts to multiple site damage, in turn validated by coupon and stiffened panel fatigue tests of the most promising concepts in Chapter 6.

5.2 Crack Patching Analysis

5.2.1 Introduction

This section develops the mathematical background necessary for the analysis of crack patching. This will lead to the implementation of a user-friendly computer program in section 5.3 to allow the use of crack patching as a technology in overhaul operations.

The analysis begins with the basic theory developed by Rose. This basic analysis is then expanded to take consider the realities of a bonded repair to cracked pressurized fuselage skins. It will be shown that based on certain realistic simplifying assumptions, the following quantities of interest to the repairer can be determined:

- the change in stiffness in the plate because of the presence of the crack and the bonded repair,
- the reduction in crack tip stress intensity after repair, or patching effectiveness,
- the maximum shear strain in the adhesive, which influences bond durability,
- the maximum tensile stress in the repair patch, and
- the maximum normal stresses in the skin adjacent to the patch, to avoid the introduction of new fatigue cracks.

The analysis is divided into two parts. First, the bonded repair is considered mathematically in place over an uncracked skin. The aim of the first stage is to calculate the stress redistribution in the plate (skin) in the presence of the bonded doubler. In stage two, the crack is introduced into the plate and the crack faces become stress-free. The main concern at that point is to calculate the stress intensity factor in the repaired cracked plate.

5.2.2 The Rose Model

5.2.2.1 Statement of the problem. The Rose model of crack patching is a continuum analysis based on the theory of elasticity. It considers an infinite, center-cracked, isotropic plate with a bonded orthotropic elliptical patch on one side of the plate. The plate is loaded by a remote biaxial stress.

The elliptically shaped reinforcing patch is an efficient shape for transferring load through an adhesive. The ellipse allows an analytical solution. Rectangular patches, preferred in riveted repairs and used in some bonded repairs, result in high peel stresses at the patch corners. This can lead to delamination, which results typically in an elliptically shaped bond remaining intact.

As stated in the introduction, the Rose model divides the analysis into two stages. The first stage considers the redistribution of loads caused by a doubler bonded to an uncracked plate, as shown in figure 5.1a. The doubler will change the stress distribution in the patch. The load-transfer zone at the edge of the doubler is considered small with respect to the patch dimensions.
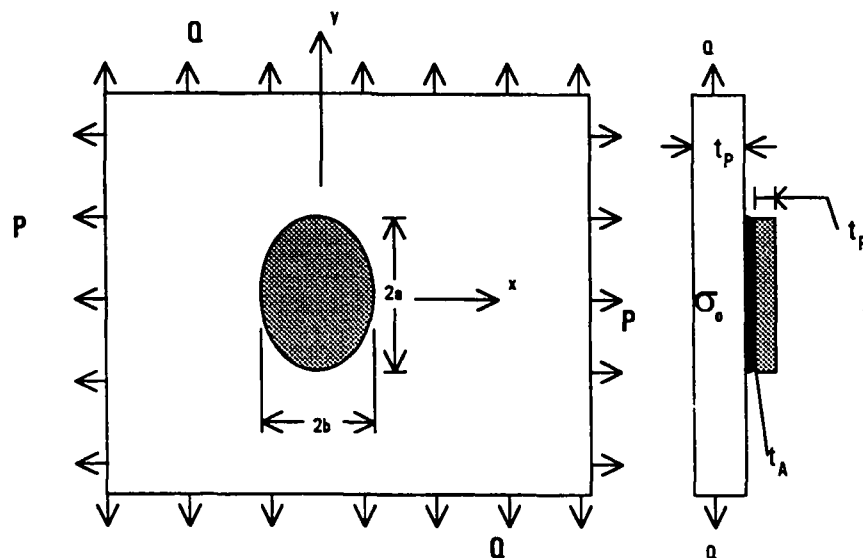
Figure 5.1a. Stage I Configuration Analyzed in Rose Model.
(Bonded patch, no crack, no out-of-plane displacements).

114
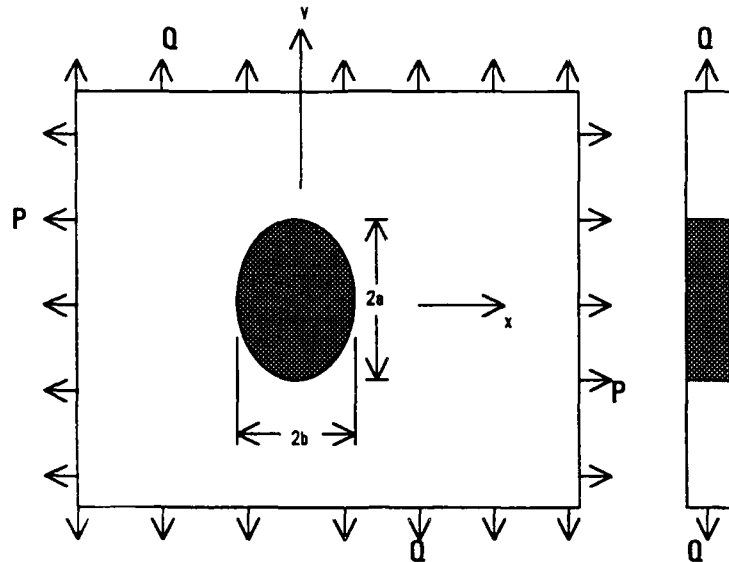
Figure 5.1b. Stage I Configuration Analyzed in Rose Model.
(No crack, equivalent inclusion representing plate and patch.)
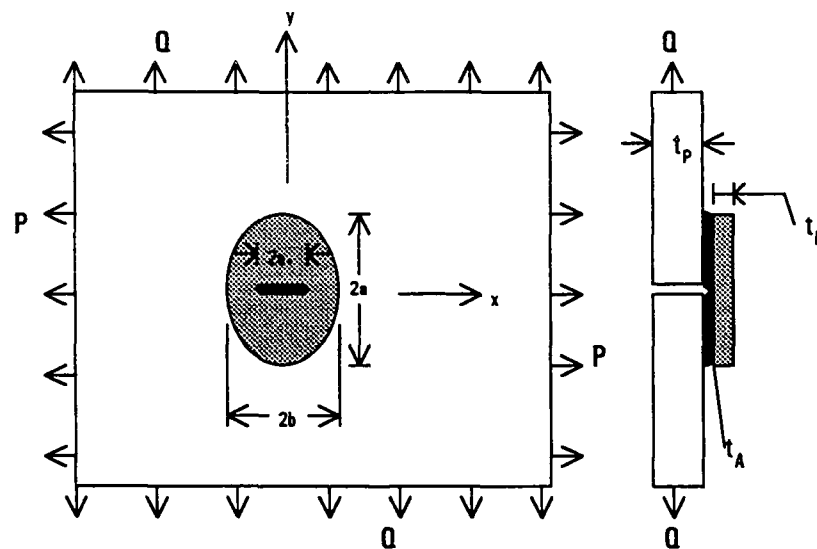
Figure 5.1c. Stage II Bonded Repair Configuration Analyzed in
Rose Model (crack introduced).

To approximate the new stress distribution in the reinforced region, Rose adapted the analogy of a stiff inclusion in the center of an infinite plate, shown in figure 5.1b. The inclusion analogy was first formulated by Muki and Sternberg [10] and expanded by Rose [11]. It ignores that a single-sided patch will induce some bending from eccentricity. However, as the likely repair situation in a fuselage will be on or near stiffening elements,

out-of-plane deformations will be restrained. Thus, secondary bending effects should be absent.

If bending effects can be disregarded and shear load transfer occurs locally at the doubler edge, the model of the equivalent inclusion of figure 5.1b can be adopted. This allows calculation of the global stress distribution in the plate around the patch and in the patched area (or equivalent inclusion). The attractive feature of the model is that an analytical solution is available for an elastic plate with an inclusion with different elastic properties. The solution of Muki and Sternberg [10] applies to orthotropic materials as well, desirable in view of the use of orthotropic composite materials as repair patches.

The effect of an elastic inclusion on the "load flow" is illustrated by the stress trajectories shown in figure 5.2 [14] for a stiff inclusion. This represents the repair problem being considered. The advantage of using an elliptical doubler is that the stress distribution is constant throughout the elliptical inclusion.
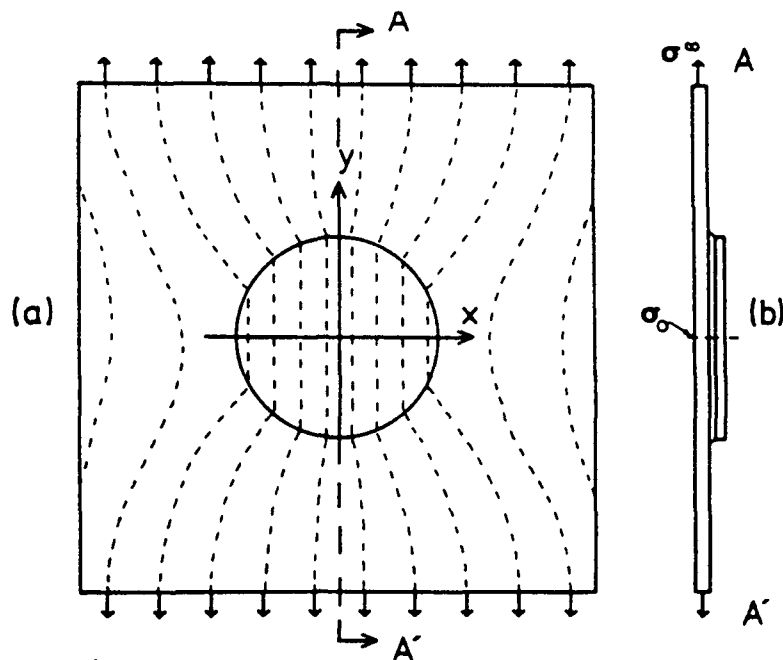
Figure 5.2 Idealized "load flow" into elliptically reinforced region of plate.

In stage II of the analysis, a crack is introduced into the plate; the stresses at the crack face are allowed to relax to zero. The stress distribution changes sharply. Figure 5.1c

shows a cracked infinite plate subjected to remote biaxial stresses denoted P and Q, in the x- and y-directions, respectively. The length of the reinforcement is 2a, the width is 2b. The crack length is represented as $2a_c$.

If the crack is still small, the restraint on crack opening will also be small, because of the low shear stiffness of the adhesive layer. However, if the crack becomes longer, the patch will exert a finite crack closing force.

The primary outputs of stage II are the (repaired) stress intensity factor and the maximum tensile stress in the patch. Throughout the analysis, subscripts will refer to parameters identified with the plate (P), reinforcing patch (R) and adhesive (A). Thus, t_P, t_R and t_A denote the respective thicknesses of the plate, repair patch and adhesive layer, etc.

The Rose analysis is based on the following assumptions:

- All material behavior is linearly elastic, except for limited elastic-plastic deformation in the adhesive layer very near the crack, as discussed in section 5.2.2.2.

- All plate and patch materials are in a state of generalized plane stress. No through-the-thickness variation occurs in the basic analysis.
- The adhesive layer behaves as a linear shear spring. Shear load transfer through the adhesive is discussed in section 5.2.2.2.

- The basic model ignores thermal stresses due to bonding or cruise altitudes. Thermal effects are addressed in section 5.2.5.

- Bending along the crack because of the shift in neutral axis from the one-sided patch is restrained by the substructure. This assumption is considered reasonable, considering the common occurrence of fatigue damage at lap joints, fairing attachment lines, etc., generally riveted to stringers or other longitudinal stiffeners. Expressions describing the bending at the reinforcement boundaries, where such substructure is absent, are derived in section 5.2.6.

5.2.2.2 Load transfer in bonded joints. A brief introduction to the load transfer in bonded joints was given in Chapter 4. In the analysis of crack-patching, two regions of shear load transfer must be distinguished. The first is the zone at the edge of the patch. It must be small compared with overall patch dimensions to allow application of the stage I assumptions. The second load transfer zone is around the crack. Shear stresses are highest in these regions.

Crack patching analysis depends on the length of these two load transfer zones in the bonded repair. The analysis used here is based on the one-dimensional theory of bonded joints developed by Hart-Smith [12]. It is presented in detail in Appendix A, while a summary of major results is given here.

The calculation of the length of the load transfer zones is based on a one-dimensional adhesively bonded single lap joint. The adhesive layer is treated as a shear spring. The *lap joint load transfer length*, $1/\Lambda$, is the principal output, and is expressed as

$$\frac{1}{\Lambda} = \left(\frac{t_A}{G_A}\left[\frac{E_{xP}t_P E_{xR}t_R}{E_{xP}t_P + E_{xR}t_R}\right]\right)^{1/2},\qquad(5\text{-}1)$$

where t_A is the adhesive thickness (mm),

   t_P is the plate thickness (mm),

   t_R is the reinforcement (patch) thickness (mm),

   E_{xP} is the elastic modulus of the plate in the x-direction (GPa),

   E_{xR} is the elastic modulus of the reinforcing patch, x-direction, and

   G_A is the adhesive shear modulus (MPa).

For typical aluminum alloy fuselage skin thicknesses and epoxy film adhesives, this transfer length turns out to be in the range of three to five millimeters. (The rather odd Rose notation of $1/\Lambda$ for a length stems from the fact that it represents a root of a characteristic equation derived later.)

The shear stress in the adhesive is expressed as a function decaying exponentially from the overlap ends, as shown previously in figure 4.4. The analysis for the region around the crack is identical.

5.2.3 Stage I---Inclusion Analysis

The Rose method identifies two means of achieving reductions of the stress intensity factor K. The first reduction comes from the overall effect of the doubler, which diminishes local plate stresses by sharing the load. In stage I, no crack exists in the plate.

As with the previous section, the derivations are presented in Appendix A. The second reduction in K comes from the crack bridging that occurs in stage II, derived in Appendix B.

5.2.3.1 Stresses in the inclusion. The item of highest interest is the plate stress in the region of the doubler. This quantity is given the designation σ_o to be consistent with the Rose derivation. The plate and patch are considered together as an elastically equivalent "inclusion" surrounded by the remainder of the plate. To determine the stress redistribution in the reinforced uncracked plate, the following steps are necessary:

- determination of the elastic constants of the equivalent inclusion,
- determination of the stress in the equivalent inclusion, and
- determination of the load sharing between the plate and reinforcement.

The derivation considers an orthotropic plate under generalized plane stress. After extensive algebra, the elastic constants of the equivalent inclusion (denoted by the subscript I) are as follows:

$$A_{xI} = \frac{A_{xP}t_P + A_{xR}t_R}{t_I},$$
(5-2)

$$A_{yI} = \frac{A_{yP}t_P + A_{yR}t_R}{t_I},$$
(5-3)

$$v_I = \frac{v_P A_{yP} t_P + v_R A_{yR} t_R}{A_{yP}t_P + A_{yR}t_R},$$
(5-4)

$$G_I = \frac{G_P t_P + G_R t_R}{t_I},$$
(5-5)

where

$$A_x = \frac{E_x}{1 - v_{xy}v_{yx}}, \qquad A_y = \frac{E_y}{1 - v_{xy}v_{yx}}$$
(5-6)

and

$$t_I = t_P + t_R.$$

(5-7)

Consider the repair configuration shown in figure 5.1, loaded by the following *remote* biaxial stresses:

$$\sigma_x = P, \qquad \sigma_y = Q, \qquad \tau_{xy} = 0$$

(5-8)

Equilibrium in the inclusion implies:

$$t_I \sigma_{xI} = t_P \sigma_{xP} + t_R \sigma_{xR},$$

(5-9)

Another result of the locally increased stiffness is load attraction to the repaired area. These local increments in stresses are denoted by p and q, in the x-and y-directions, respectively.

The derivations of the equations for the stresses in the plate and patch are presented in Appendix A. The stresses in the equivalent inclusion are represented in final form by:

$$\sigma_{xI} = P + p, \quad \sigma_{yI} = Q + q, \quad \tau_{xy} = 0$$

(5-10)

$$\sigma_{xP} = \sigma_{xI}[1 - \frac{t_R}{t_I}\frac{(A_{xR} - v_I v_R A_{yR})}{E_{xI}}] + \sigma_{yI}\frac{t_R}{t_I}[\frac{v_I}{E_{xI}}A_{xR} - \frac{v_R}{E_{yI}}A_{yR}],$$

(5-11)

Rearrangement of equation 5-9 gives:

$$\sigma_{xR} = \frac{t_I}{t_R}\sigma_{xI} - \frac{t_P}{t_R}\sigma_{xP}$$

(5-12)

Analogous expressions are given for σ_{yP} and σ_{yR} in Appendix A.

5.2.4 Stage II---Introduction of the Crack

In stage II of the analysis, a crack of length $2a_c$ is introduced in the plate along the line $x = 0$. The rigid bond assumption no longer applies, and forces along the crack face are relaxed to zero. The patch is assumed to completely cover the crack in stage II to make possible the calculation of the repaired stress intensity factor K_r.

5.2.4.1 The stress intensity factor in the repaired plate.
Recall that the stage I plate stress σ_{xP} was denoted σ_o to signify the (constant) plate stress in the *uncracked* plate in the inclusion. However, the introduction of the crack in stage II causes the forces in its vicinity to be redistributed. Some of the load is transferred into the patch, while the remainder is redistributed around the crack tips.

For effective crack bridging by the patch to occur, a certain minimum crack length must be reached. Marissen [15] and Roebroeks [16] and co-workers have reported similar phenomena with the fatigue behavior of fiber metal laminates, which might be considered crack-patched from the inside. Fortunately, the required crack length is rather small, about 20 to 60 mm for typical pressurized fuselage skins. (In fiber metal laminates, this minimum crack length is much smaller because of the very thin aluminum sheets used.) Often, the minimum crack size will have been reached or exceeded before inspectors are able to locate it for repair.

The case for the calculation of the repaired stress intensity factor, K_r, for the patched isotropic plate will be developed here. The orthotropic case is presented in Appendix B. To begin, the crack extension force G_f is defined from linear elastic fracture mechanics:

$$G_f = \frac{K^2}{E}$$

(5-13)

This relation can be used to find the boundaries for K between short and long cracks. With short cracks, the influence of the reinforcement can be neglected. The short crack stress intensity factor, denoted by K_u, is:

$$K_u = \sigma_o \sqrt{\pi a_c}$$

(5-14)

which represents an upper bound for K. For longer cracks, K and G_f are limited by the crack-closing influence of the reinforcement. Appendix B presents the derivation resulting in the expression for the crack driving force for long cracks shown below:

$$G_\infty = \frac{t_A}{G_A} \Lambda \sigma_o^2 t_P \qquad\qquad (5\text{-}15)$$

The transition between "short" and "long" cracks can be established by solving for the point where the unpatched value $G_u = G_\infty$. For the isotropic case, this yields a transitional crack length, denoted $a_{c_{trans}}$,

$$a_{c_{trans}} = E_P t_P \frac{t_A}{G_A} \frac{\Lambda}{\pi} \qquad\qquad (5\text{-}16)$$

Thus, for short cracks, the upper bound of K is defined by equation 5-14, while for infinitely long cracks, K is represented by:

$$K_\infty = \sigma_o \sqrt{\pi a_{c_{trans}}} \qquad\qquad (5\text{-}17)$$

An interpolated expression for the "repaired" value K_r can be written as:

$$K_r = \sigma_o \sqrt{\frac{\pi a_{c_{trans}} a_c}{a_{c_{trans}} + a_c}} \qquad\qquad (5\text{-}18)$$

Equations 5-14, 5-17, and 5-18 are summarized graphically in figure 5.3.
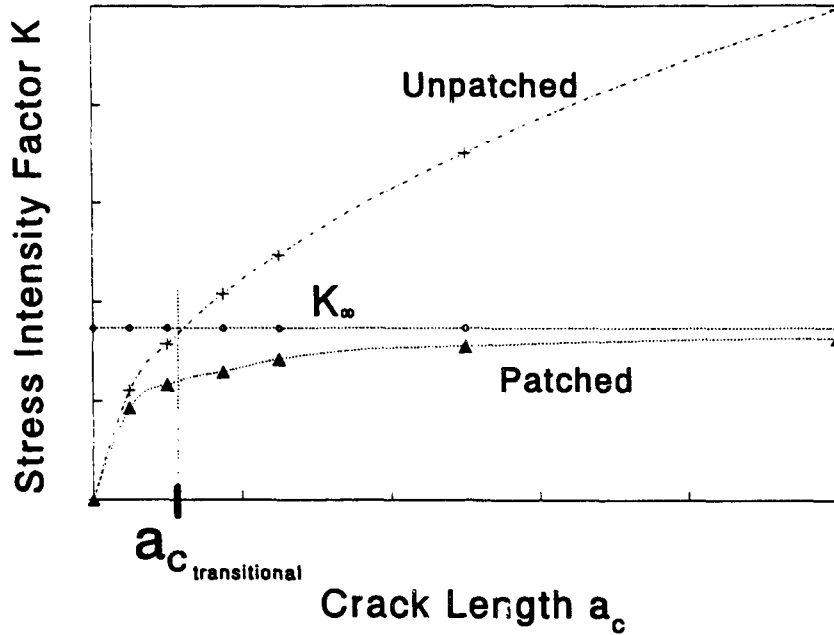
Figure 5.3. Non-dimensional comparison of patched and unpatched K values.

5.2.4.2 Maximum normal stress in the patch. This item is of primary interest in the design of an effective, durable bonded repair. The maximum reinforcement stress occurs at $x = 0$, $y = 0$. A conservative estimate is that the entire load in that area of the inclusion is carried by the patch. (Recall an earlier assumption was that no bending occurs across the crack face because of the presence of a stiffener.) Thus,

$$\sigma_{yR_{max}} \approx \sigma_{yI} \frac{t_P}{t_R} \qquad (5\text{-}19)$$

5.2.4.3 Maximum shear strain in the adhesive. The critical adhesive shear strain occurs at the crack face and at the patch tips if they are not tapered. Using the one-dimensional theory of bonded joints and a two-step elastic-plastic analysis yields:

elastic adhesive behavior: $\sigma_o \Lambda t_P < \tau_{yield}$

Substitution of $x = 0$ into equation 6 in Appendix B allows solution for the maximum shear strain in the adhesive:

$$\gamma_{\max} = \frac{\sigma_o \Lambda t_P}{G_A}$$ (5-20)

plastic adhesive behavior: $\sigma_o \Lambda t_P > \tau_{yield}$

$$\gamma_{\max} = \frac{\tau_{yield}}{2G_A}[1 + (\frac{\sigma_o \Lambda t_P}{\tau_{yield}})^2]$$ (5-21)

In this case, the characteristic crack length $a_{c_{trans}}$ must be modified to [14]:

$$a_{c_{trans}} = \frac{1}{3\pi} \frac{t_A}{G_A} E_x \Lambda t [\frac{\sigma_o \Lambda t_P}{\tau_{yield}}]^2 \cdot [1 + 2(\frac{\sigma_o \Lambda t_P}{\tau_{yield}})^3]$$ (5-22)

The strain behavior described by equations 5-20 and 5-21 is shown in figure 5.4 for some typical structural adhesives. Maximum adhesive shear strain is plotted versus the nominal gross stress in the adherends of a single lap joint. A stiffer adhesive exhibits less strain than a flexible (toughened) adhesive. However, the stiffer adhesive also reaches its yield point at a much lower *adherend* normal stress. This performance influences the choice of an appropriate adhesive for crack patching. While a stiffer adhesive might be preferable from a crack closing standpoint, adhesive strain levels should be kept below the yield point for good long-term durability. These effects will be discussed in greater detail in section 5.4.1.

5.2.4.4 Normal stresses in the plate near the patch. In Chapters 2 and 3, the importance of patch stiffness was discussed as it affected the fatigue life of the riveted repairs. This is also an important factor in bonded repairs: Too much load attraction into the reinforced region will result in high stress concentrations in the plate immediately outside the patch.
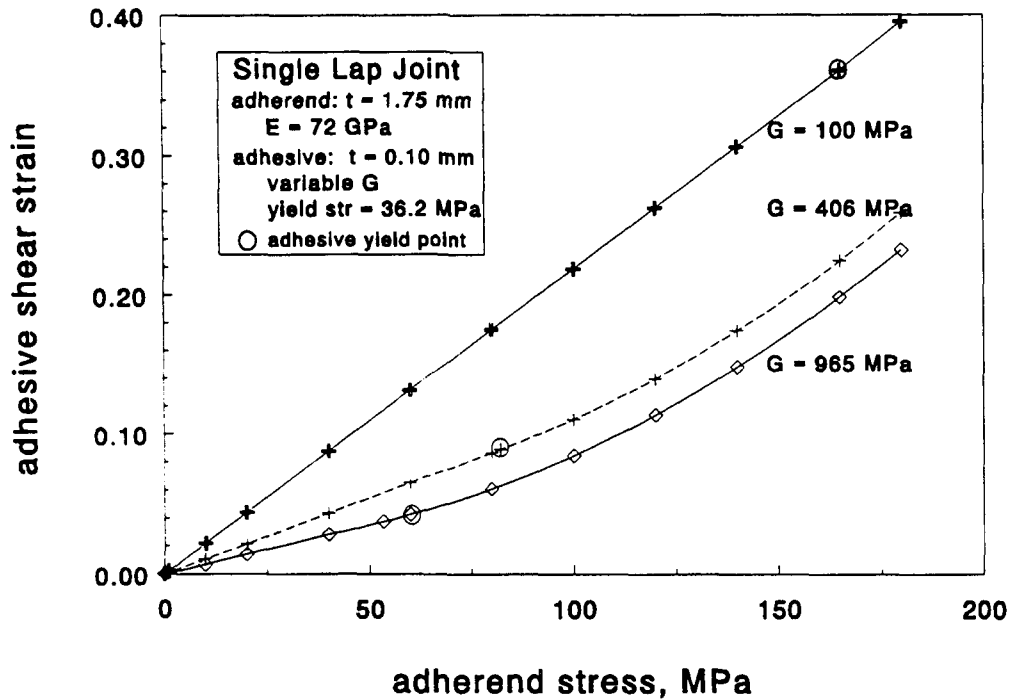
Figure 5.4. Adhesive elastic-plastic peak shear strain behavior as a function of adherend gross stress.

This section considers the edge areas $(x=a^+, y=0)$ and $(x=0, y=b^+)$. By using the output from the stage I analysis performed in section 5.2.3, the stresses in the plate next to the patch can be evaluated.

$(y=a^+, x=0)$

From equilibrium, one can show that the load in the inclusion in the y-direction is carried completely by the plate. Thus,

$$\sigma_{yP} t_P = \sigma_{yI} t_I \tag{5-23}$$

$$\sigma_{yP} = \sigma_{yI} \frac{t_I}{t_P} \tag{5-24}$$

Compatibility of strains at the edge of the patch force:

$$\varepsilon_{xP} = \varepsilon_{xI} \tag{5-25}$$

Substituting into the appropriate elasticity equation yields:

$$\frac{-v_P}{E_{yP}}\sigma_{yP} + \frac{1}{E_{xP}}\sigma_{xP} = \frac{-v_I}{E_{yI}}\sigma_{yI} + \frac{1}{E_{xI}}\sigma_{xI} \qquad (5\text{-}26)$$

Rearranging, substituting equation 5-24 gives:

$$\sigma_{xP} = \sigma_{yI}\left[\, v_P\frac{E_{xP}}{E_{yP}}\frac{t_I}{t_P} - v_I\frac{E_{xP}}{E_{xI}}\,\right] + \sigma_{xI}\frac{E_{xP}}{E_{xI}} \qquad (5\text{-}27)$$

(y = 0, x = b⁺)

Using analogous calculations,

$$\sigma_{yP} = \sigma_{yI}\frac{E_{yP}}{E_{yI}} + \sigma_{xI}\left[\, v_P\frac{E_{yP}}{E_{xP}}\frac{t_I}{t_P} - v_I\frac{E_{yP}}{E_{yI}}\,\right] \qquad (5\text{-}28)$$

$$\sigma_{xP} = \sigma_{xI}\frac{t_I}{t_P} \qquad (5\text{-}29)$$

5.2.5 Thermal Considerations

The use of carbon- and boron-epoxy composites in the repair of aluminum combines materials with large differences in thermal expansion coefficients. However, simple multiplication of the difference in thermal expansion coefficients between patch and plate by the difference between curing and room temperatures overestimates the thermal stress problem. Jones [17] points out that in a typical on-aircraft bonded repair, the surrounding (unheated) structure partially constrains free expansion of the repair area. This results in less severe residual tensile stresses in the aluminum after cooling. However, the Australian work concentrated on the repair of thick and quite stiff structures like fighter aircraft wing structures. In the repair of comparatively flexible fuselage skins, less constraint exists. Furthermore, the skin may deform locally out of plane during heating.

126

This section reviews the thermal effects on crack patching. The temperature changes affecting a bonded patch can be viewed in two steps. When the bonded repair is heated for curing, the surrounding cooler structure acts to constrain free expansion of the plate, while the patch is free to expand. Upon cooling to room temperature, a constant preload exists at the crack tip. Whether this preload is tensile or compressive depends on the relative thermal characteristics of the patch and the constrained plate.

The second thermal step, cooling to approximately -55°C at cruise altitude, allows the entire fuselage to cool equally. When the thermal expansion coefficient of the fuselage is higher than the patch (as with composite patches), the patch acts to open the crack. The effect of this step on crack tip stress intensity factor has been overlooked in previous analyses [1-7, 14, 17]. One study looked at the influence of thermal cycling on the adhesive, but tested only a few cycles and ignored any effects on the crack [18].

This second thermal step is the more important of the two regarding fatigue. With low thermal expansion materials, it imposes an additional *cyclic* tensile stress on the crack tip with every flight. This reduces the effectiveness of crack bridging at the point where flight loads are the highest.

The following simplifying assumptions apply:

- The plate (skin) material is isotropic, resulting in equal thermal characteristics in every direction in the plane of the plate.

- The crack is located midway between two frames and very near a longitudinal stiffening element, as shown in figure 5.5. The frames and stringers outside the heated region act as simple supports, but the stringer adjacent to the crack is neglected in the thermal model. Thermal buckling is ignored.

- The temperature is constant through the thickness of the plate, but varies radially from the center of the patch. Underlying frames and stringers have the same temperature as the adjacent plate.

- All deformations remain in the elastic range of material behavior.

- Plate and patch are in a condition of plane stress.

- Out-of-plane bending in the region of the crack is restrained by the substructure.

- The adhesive acts as a rigid bond.

Section 5.2.5.1 describes the temperature field in the plate. Derivations of the effective coefficient of thermal expansion are given in 5.2.5.2, while section 5.2.5.3 calculates the cumulative residual thermal stresses.

5.2.5.1 Temperature field in the plate. Consider the circular isotropic plate of radius R represented by figure 5.6. The plate is heated to a temperature T_c over a central circular region of radius d by means of a thermostatically controlled heat blanket. The temperature at the edge of the plate will be represented by T_e.
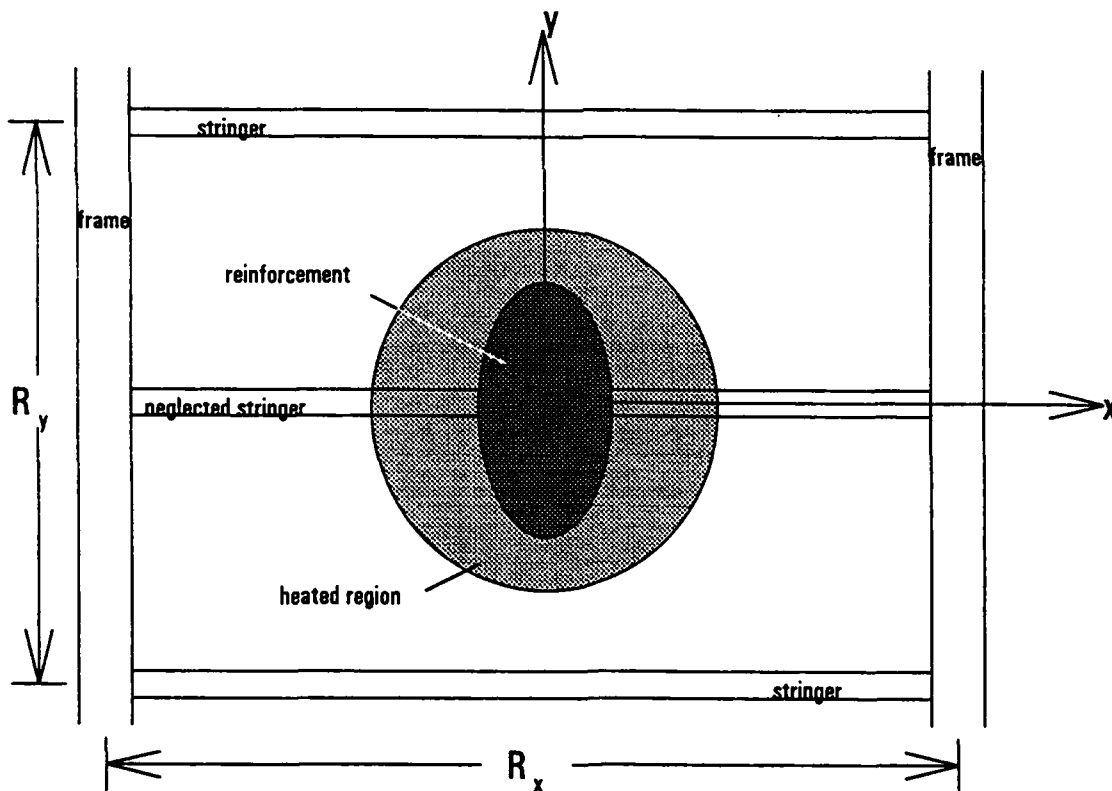
Figure 5.5. Model of local fuselage details for analysis of thermal effects on crack patching.
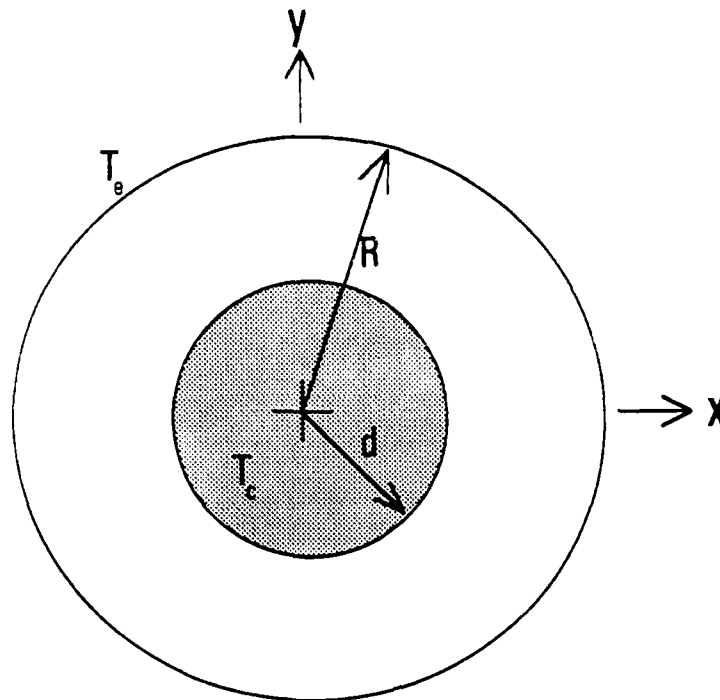
Figure 5.6. Model for calculation of temperature distribution in a circular isotropic patch.

The analysis considers a steady-state temperature field; furthermore, the thermal conductivity of the plate is assumed to be independent of the temperature T. Thus, the temperature field satisfies LaPlace's potential equation [19]:

$$\nabla^2 T = 0 \tag{5-30}$$

Depending on the form of the LaPlace operator, this equation can be written as:

$$\frac{d^2 T}{dr^2} + \frac{n}{r}\frac{dT}{dr} = 0, \tag{5-31}$$

where r denotes the single space coordinate and (n + 1) the number of dimensions involved.

The assumption of constant through-the-thickness temperature in the plate means that n = 1. Thus,

$$\frac{d^2T}{dr^2}+\frac{1}{r}\frac{dT}{dr}=0 \qquad\qquad (5\text{-}32)$$

with boundary conditions $T = T_c$ at $r = d$,

$T = T_e$ at $r = R$.

The solution of equation 5-32 is given as:

$$T = T_e + \frac{[T_c - T_e]\ln(r/R)}{\ln(d/R)}, \qquad R \ge r \ge d.$$

$$(5\text{-}33)$$

$$T = T_c, \qquad\qquad\qquad r \le d.$$

T_e can be determined using the theory of heat transfer through extended surfaces [19]. Consider the configuration of figure 5.7. The outer ring of width dr is treated as a solid body exchanging heat with the media surrounding it. The heat transfer rate $\dot{Q}$ which crosses the outer surface area A is given by:

$$\dot{Q} = hA(r)[T(r) - T_\infty] \qquad\qquad (5\text{-}34)$$

where h is the coefficient of heat transfer (W/m^{2}K),

$A(r)$ is the strip surface area at radius r ($\approx 4\pi r dr$),

$T(r)$ is the temperature of the plate at radius r, and

T_∞ is the temperature of the cooling medium (air).

130
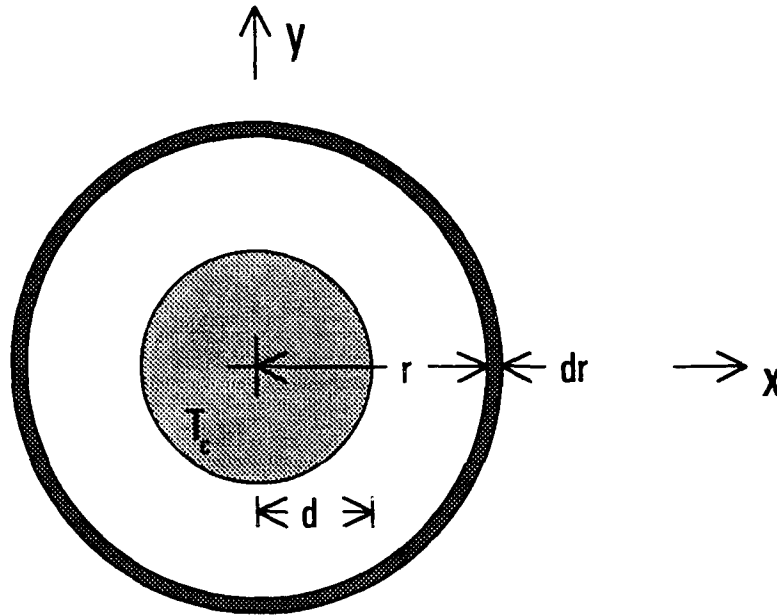
Figure 5.7. Model of heat transfer outward through a differential ring.

The full derivation is presented in Appendix C. The final expression for T_e is

$$T_e = (T_c - T_{ambient})e^{-m(R-d)} + T_{ambient} \qquad (5\text{-}35)$$

where m is a heat transfer constant defined in Appendix C.

The temperature distribution in the plate during the cure cycle is now fully described with equations 5-33 and 5-35. These expressions will be used to develop the effective coefficient of thermal expansion in the following section.

5.2.5.2 *Effective coefficient of thermal expansion.* During the bonding process, the surrounding cooled structure provides restraint to the heated plate. This results in a smaller expansion in the plate than expected. The reinforcement (patch) is able to expand freely. Hence, the use of repair materials with low coefficients of thermal expansion results in smaller than expected static residual stresses at room temperature.

When an aircraft climbs to cruising altitude, its fuselage is cooled uniformly to the ambient temperature (about -55°C at 10,000 meters). The structure surrounding a bonded repair has no constraining influence, and a low expansion patch material shrinks less than the aluminum plate. This induces compression in the patch and imposes a cyclic tensile load on the crack when the pressure differential is loading the fuselage to its highest point.

131

Thus, this so-called second step increases the magnitude of the stress amplitude seen by the crack every flight.

Refer again to figure 5.6. The complete derivation of α_{Peff} is given in Appendix C, which results in the following first-stage temperature drop expression:

$$\alpha_{Peff} = \frac{\alpha_P}{2}(1 + \nu_P)\{1 - \frac{T_e}{T_c} + \frac{d^2}{R^2}(\frac{T_e}{T_c} - 1) - \frac{1 - \frac{T_e}{T_c}}{2\ln(\frac{d}{r})}[\frac{d^2}{R^2} - 1 - \frac{2d^2}{R^2}\ln(\frac{d}{R})]\} \quad (5\text{-}36)$$

The expression for the second-stage drop is understandably simpler because the surrounding structure provides no constraint:

$$\alpha_{Peff} = \alpha_P \quad (5\text{-}37)$$

5.2.5.3 *Calculation of residual thermal stresses.* Determination of the residual thermal stresses involves the analysis of a two-dimensional statically indeterminate structure [20]. Thermal stresses occur as a result of cooling of the (assumed) rigid bond from its stress-free state at the curing temperature. The problem involves three distinct elements, namely:
- the reinforced region of the plate (D in Appendix A),
- the reinforcement (patch), and
- the surrounding matrix (M).

Appendix C presents the derivation in its full detail.

5.2.6 Bending Considerations at the Patch Edge

The assumption was made previously that the substructure would restrain bending at the crack location. However, with a single-sided reinforcement, this assumption is not valid at the edges of the patch. Significant bending occurs away from the frames and stringers, resulting in higher plate stresses in the hoop or y-direction. This analysis will be restricted to that one-dimensional case. The following assumptions apply:

- all deformations are in the elastic range of material response,
- the adhesive bond is rigid,
- the crack is neglected,
- the repair is located midway between two frames over a stringer,
- the remote y-stress causes no out-of-plane bending, and
- plane sections in the reinforced area remain plane in pure bending, consistent with the Bernoulli-Euler bending theory.

Consider the model sketched in figure 5.8. It shows an orthotropic reinforcement bonded to one side of an orthotropic plate over an y-dimension of 2a. Both the reinforcement and the plate are of infinite width. The structure is loaded with the remote stress P in the x-direction.
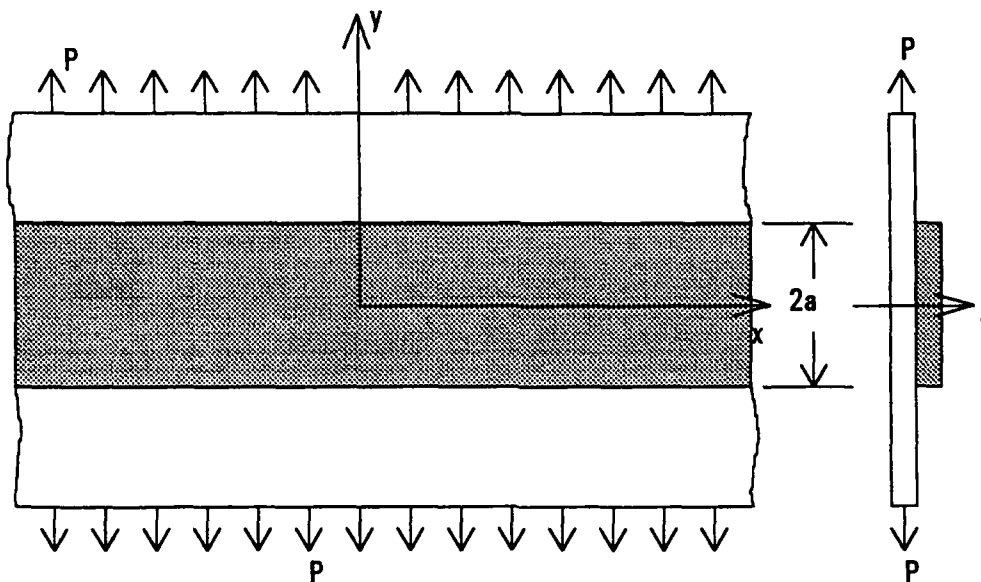
Figure 5.8. View of bending stress model for one-sided bonded reinforcement.

The reinforcement causes a shift in neutral axis that results in secondary bending. This necessitates a separate analysis of the reinforced area (also called the inclusion) and the unreinforced region (surrounding matrix). The full derivation is presented in Appendix D; highlights are given here.

unreinforced region (matrix): neutral axis z = 1/2t_P

$$(E_y I)_m = \frac{E_{yP}}{1 - v_{xyP} v_{yxP}} \int_{-\frac{1}{2}t}^{\frac{1}{2}t} z^2 dz = \frac{E_{yP} t_P^3}{12(1 - v_{xyP} v_{yxP})}$$

(5-38)

inclusion: neutral axis z = z_o

The variable t* denotes the respective reduced thicknesses of the inclusion, plate and patch (reduced = corrected for elastic modulus).

$$t_I^* = \frac{1}{E_{yP}}(E_{yP} t_P + E_{yR} t_R) = t_P + \frac{E_{yR}}{E_{yP}} t_R$$

(5-39a)

$$t_P^* = t_P$$

(5-39b)

$$t_R^* = \frac{E_{yR}}{E_{yP}} t_R$$

(5-39c)

After substitution and reduction, the outcome is

$$z_o = \frac{E_{yP} t_P^2 + E_{yR}[(t_P + t_R)^2 - t_P^2]}{2(E_{yP} t_P + E_{yR} t_R)}$$

(5-40)

Equation 5-40 can be used to calculate the bending stiffness per unit width of the reinforced region.

$$(E_y I)_I = \frac{E_{yP}\{(t_P - z_o)^3 + z_o^3\}}{3(1 - v_{xyP} v_{yxP})} + \frac{E_{yR}\{(t_P - z_o + t_R)^3 - (t_P - z_o)^3\}}{3(1 - v_{xyR} v_{yxR})} \quad (5\text{-}41)$$

Bending moments M_1 and M_2 are applied to the edges of the reinforced area and the surrounding matrix, as shown in figure 5.9.
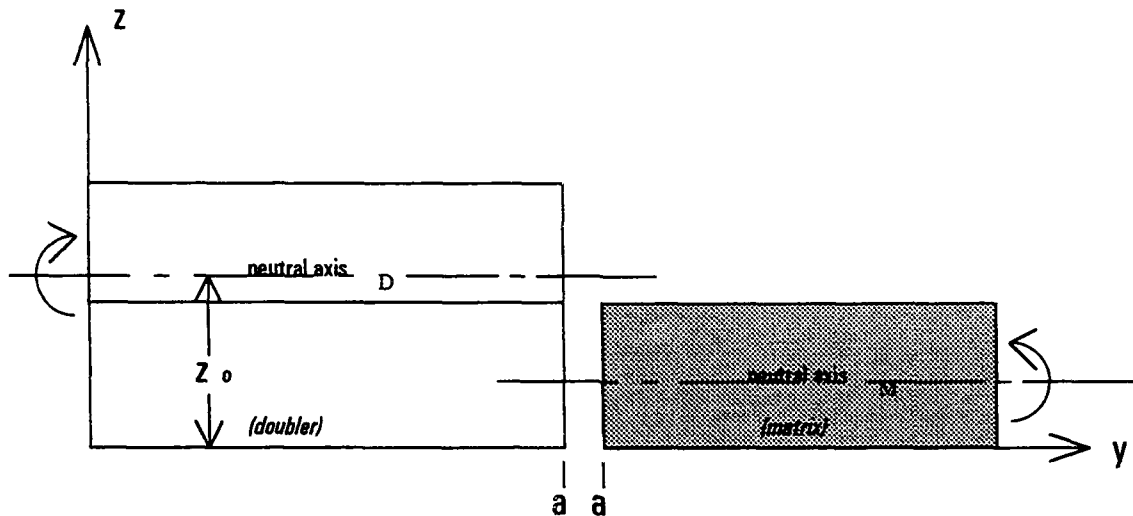
Figure 5.9. Bending moments at the edges of the inclusion and matrix.

The relationship between the bending moment M and the deflection $w(y)$ leads to the following non-linear differential equation:

$$EIw''(y) = P^* t \cdot w(y) = M(y) \quad (5\text{-}42)$$

After much derivation (see Appendix D), the maximum bending stress in the plate at the edge of the reinforced region is:

$$\sigma_{bend_{max}} = \frac{E_{yP} t_P}{2}(z_o - \frac{t_P}{2})\frac{\Phi_I \Phi_M^2 \tanh(\Phi_I a)}{\Phi_M + \Phi_I \tanh(\Phi_I a)} \quad (5\text{-}43)$$

where $\Phi_{I,M}$ are the roots of the of the characteristic equation (5-42) of the inclusion and matrix respectively, and are expressed as:

$$\Phi = \pm \sqrt{\frac{P^* t}{EI}} \qquad\qquad (5\text{-}44)$$

The derivations outlined up to this point form the analytical basis for the crack-patching analysis program described in the following section.

5.3 Crack Patching Analysis Program CALCUREP

5.3.1 Introduction

The derivations in the previous section present quite a computational challenge to the working engineer who wants to analyze a bonded patching repair quickly. Furthermore, the airline maintenance engineer has little knowledge of the design stress levels in the structure he must repair. In the past, this has put the maintainer in a situation of dependence on the manufacturer.

Reliance on the manufacturer for design and analysis of major repairs is both costly and time-consuming. This section describes the development of an alternative: a computer program that performs the crack-patching analysis developed in section 5.2. It allows maintenance engineers with limited knowledge of design stress levels to design and analyze bonded patch repairs quickly. The program is user-friendly, runs on personal computers, and requires short run times (less than five minutes). A user's manual for the program, known as CALCUREP (CALCUlation program for bonded REPairs), is presented in Appendix E.

5.3.2 Required Input

When a repairer finds a crack in a fuselage, he knows where the crack is located, how long it is, and how much (or how little) time is available to design, analyze and install a suitable repair. If the repair is not specified in the Structural Repair Manual, the maintainer must contact the manufacturer for advice. He either may ask for approval of his own repair design, or request a design from the manufacturer. The latter option, obviously, is more expensive and time-consuming.

With CALCUREP, the repairer must specify the following items:

structure to be repaired
- skin (plate) thickness
- skin material
- frame spacing

- stringer spacing
- crack length
- maximum operating altitude
- cabin pressure altitude
- fuselage radius

Specifying the maximum altitude also allows the program to look up the temperature of the standard atmosphere at that altitude. The last two items can be replaced by the detailed stress state of the crack location, if known by the repairer.

repair patch and adhesive

- patch material
- patch dimensions (length, width, thickness)
- adhesive type
- cure temperature
- heating blanket dimensions

The patch dimensions must be specified iteratively by the repair designer. The user's manual (Appendix E) gives general rules of thumb regarding patch dimensions. With these input parameters, the program performs the calculations derived in the previous section. It estimates the far-field stress situation (P and Q in the model) on the simple theory of pressure vessels, which overestimates the skin stresses in a stiffened fuselage.

5.3.3 Program Output

CALCUREP provides the following output:
- the stress intensity factor K_r at the (repaired) crack tip
- the percent reduction in K achieved by the repair
- the maximum normal stress in the patch
- the maximum shear strain in the adhesive
- the bending stresses in the plate at the edge of the patch
- the maximum normal stresses in the plate adjacent to the repair
- thermal effects on all of the above

Furthermore, CALCUREP provides an option to automatically vary one input variable (e.g., patch thickness) and provide the output in the form of a sensitivity analysis. The following section presents the results of a sample calculation.

5.3.4 Sample Calculation

This section describes a typical input/output session with CALCUREP. The upper forward fuselage of an early model of the Boeing 737 is used as a typical multiple site damage case needing repair.

The maintenance engineer is asked for the following data:

structure to be repaired

fuselage radius:	1.8 m
skin (plate) thickness:	0.914 mm
skin material:	2024-T3 aluminum
frame spacing:	508 mm
stringer spacing:	254 mm
crack length:	200 mm (widespread cracking between tear straps)
max. operating altitude:	10 km

repair patches and adhesive

patch materials>	GLARE 2-0.2	GLARE 2-0.3	Boron/epoxy	2024-T3
patch dimensions length*, mm:	104	140	60	160
width, mm:	250	250	250	250
thickness, mm:	0.65	0.85	0.38 (3 plies)	1.0

Patch half-length was chosen to be 80 times the patch thickness.

adhesive type: AF-163-2K epoxy film, t = 0.13 mm

cure temperature: 120°C

heating blanket dimensions: 200 x 200 mm (circular)

The patches are assumed not to be tapered in this example calculation. (Tapering reduces bending at the patch tip and can be done easily with all of the patch materials considered here.) The CALCUREP output, including thermal effects of cruise altitude, is presented below:

	GLARE 2, t = 0.65	GLARE 2, t = 0.85	Boron/epoxy, t = 0.38	2024-T3, t = 1.0
K_r , MPa$\sqrt{m}$	2.1	~0	6.6	not meaningful*
percent reduction in K	96.1	100	88.4	>100*
σ_{max} (patch), MPa	187	156	239	100
γ_{max}	0.020	0.016	0.054	0.028
σ_{max} (load attraction,plate)	122	140	77	168
σ_{max} (bending, plate)+	69	93	50	122
σ_{max} (combined, plate)+	191	233	127	290

*Thermal effects result in crack faces being placed in compression in this case.
+ Can be reduced substantially by tapering patch tips.

The calculations presented here demonstrate that a wide range of patch materials can perform effectively in patching relatively large cracks in pressurized fuselages. Besides effectively reducing the stress intensity factor, other considerations exist. Factors such as acceptably low patch stresses, adhesive shear strains and combined plate stresses at the edge of the patch help guide the repair design. If two-sided patches are used, the bending contribution can be neglected.

Section 5.4.2 discusses what can be considered an acceptable range of outputs for the patch designer.

Patch tapering can be done easily with metal and fiber metal laminate patches on a belt sander or grinder. With composite patches, tapering is realized with ply drop-offs. Tapering reduces the shear strain value in the adhesive at the patch tips and reduces the maximum combined normal stresses in the plate adjacent to the patch. (Neither the effect of the thin outer aluminum environmental barrier recommended for composite patches nor the glass insulating plies for the carbon fiber patches is considered in the calculations.)

5.4 Parametric Studies With CALCUREP

To validate CALCUREP, this section compares the results of sample calculations with published data from the Rose model and other crack patching solutions. The program is used further to perform parametric studies, primarily of the thermal effects of crack patching that have been neglected in the literature. Various crack patching materials are evaluated for crack patching effectiveness.

5.4.1 Comparison with Solutions from the Literature

Several writers have published studies comparing various finite element-based crack patching models [21-23] with the Rose model. These can be used to check the accuracy of CALCUREP.

Figure 5.10, adapted from a detailed finite element analysis in [21], shows a comparison of the crack-bridging efficiency predicted by various elastic models. The parameters of the cracked aluminum plate and the variable-thickness balanced boron epoxy repair patch are given in the figure. Material responses were assumed to be elastic, and thermal effects were ignored.

To consider elastic material behavior only, as did the published models, the CALCUREP input must be modified to include an artificially high adhesive shear yield strength. In this case, CALCUREP matches well with the more complex finite element models from the literature. The maximum difference between CALCUREP and [21] occurs when the repair patch is eight plies thick. Here CALCUREP overestimates the K reduction by no more than five percent. For lower adhesive shear modulus values, the patch effectiveness drops somewhat. This can be understood by considering the adhesive as a shear spring.

The assumption of various authors that the adhesive will behave elastically is questionable, especially when the patch extensional stiffness is small compared with that of the cracked plate. These very thin patches experience large normal strains over the crack and induce large strains in the adhesive as well.

Plate (2024-T3)	Reinforcement (boron/epoxy)	Adhesives
t_P = 2.29 E_P = 71 GPa ν_P = 0.32 crack length = 38.1 mm	E_R = 208 GPa ν_R = 0.1677 length = 152.4 mm width = 50.8 mm	t_A = 0.10 mm G_A = 965 MPa 406 MPa 100 MPa
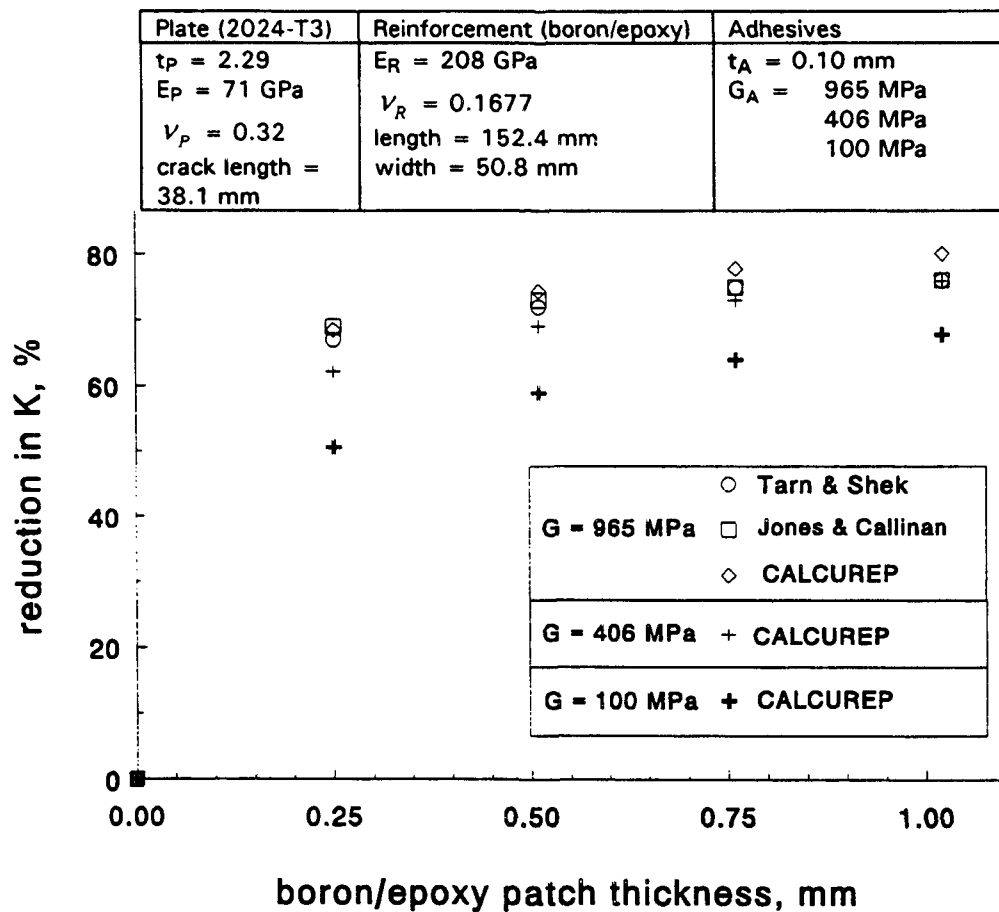
Figure 5.10. *Comparison of reduction in stress intensity factor for various thicknesses of balanced circular boron/epoxy patches bonded to a cracked aluminum sheet.*

The lower two lines in figure 5.11 represent the CALCUREP values when elastic-plastic adhesive behavior is allowed around the crack tip. Two values of adhesive shear modulus (406 MPa, from AF-163-2, and 965 MPa) and the strength of AF-163-2 (τ_{yield} = 36.2 MPa) were used.

The differences between the models are striking. With the elastic model, adhesive shear stresses are able to reach unrealistically high levels, so thin patches appear efficient. However, when patch thicknesses are relatively low, the fiber strains are quite high. This causes early adhesive yielding and delamination, reducing crack-patching effectiveness. This is consistent with the work of Marissen [15] and Roebroeks [16], who found that low fiber/metal ratios resulted in poor crack-bridging efficiency for fiber metal laminates. The elastic results converge with the elastic-plastic model only at higher patch thicknesses

(>0.76 mm, or six plies). At this point, the extensional stiffness of the boron patch approaches that of the plate.

Plate (2024-T3)	Reinforcement (boron/epoxy)	Adhesives
t_P = 2.29 E_P = 71 GPa V_P = 0.32 crack length = 38.1 mm	E_R = 208 GPa V_R = 0.1677 length = 152.4 mm width = 50.8 mm	t_A = 0.10 mm G_A = 965 MPa (elast) G_A = variable (el/pl)
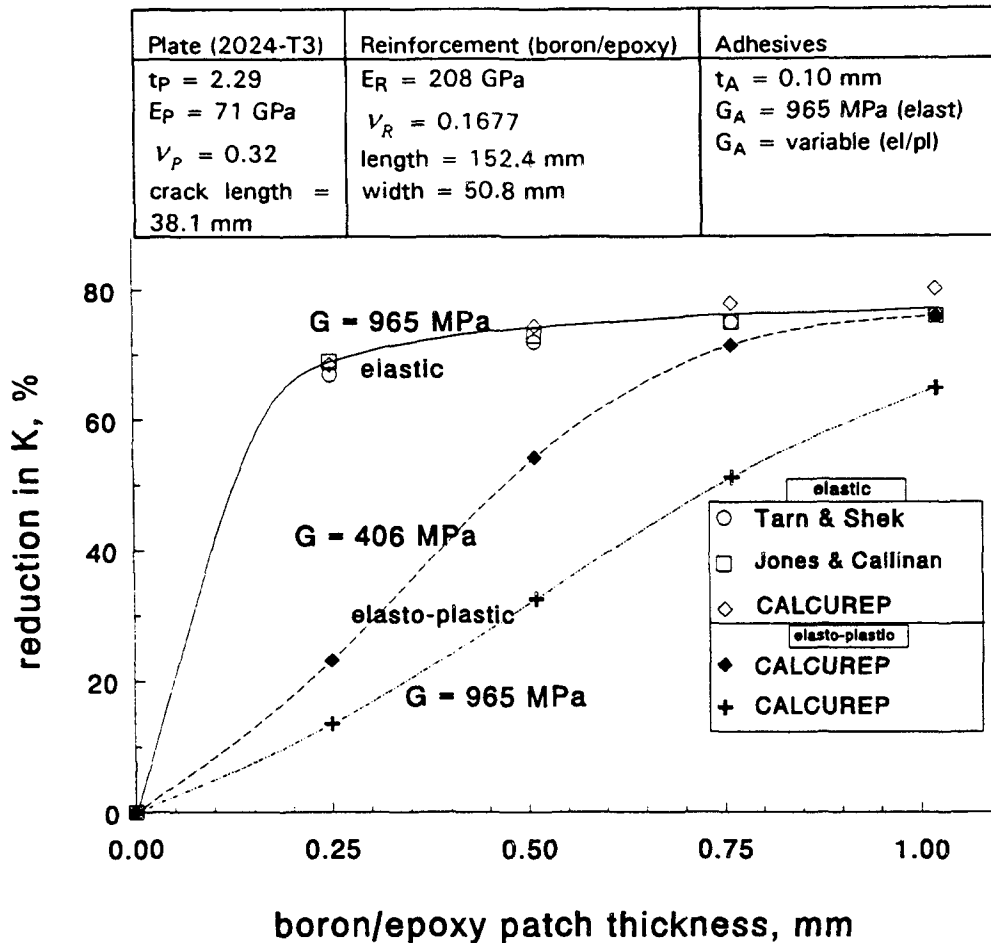
Figure 5.11. Comparison of reduction in stress intensity factor for bonded boron/epoxy patches, elastic and elastic-plastic models of adhesive behavior.

The negative influence of the higher adhesive shear modulus can be understood by again considering the stress-strain behavior of the equal-strength adhesives shown in figure 5.4. A lower adhesive shear modulus could be expected to result in less efficient crack patching (for the elastic models). However, the more flexible adhesive resists yielding to a significantly higher *adherend* stress level. The avoidance of yielding on a large scale can be important in effective crack patching and good patch durability.

The stiffer adhesive is rapidly loaded in shear, resulting in a shorter load-transfer length. However, at moderate plate stress levels, the stiffer adhesive yields. This causes

delamination over a larger area, reducing crack-bridging efficiency compared with the lower modulus (toughened) adhesive.

These results allow sufficient confidence in CALCUREP's basic approach to proceed with additional sensitivity studies outlined in the following sections. The studies assess the thermal problems with various patch materials and the roles of patch geometry and adhesive selection in patching effectiveness. Experimental confirmation of the model's validity will come in Chapter 6.

5.4.2 Comparison of Various Crack-Patching Materials

As mentioned previously, a wide variety of patch materials may perform suitably for crack patching. For the purposes of this analysis, five will be compared:

- the monolithic metals Al 2024-T3 and Ti-6Al-4V,
- the fiber metal laminate GLARE 2, and
- the high-performance composites boron-epoxy and carbon-epoxy SP 500-2.

Selected mechanical properties for the materials are summarized in table 5.1.

Table 5.1. Selected Properties of Patch Materials.

	2024-T3	Ti 6Al-4V	GLARE 2 (3/2)	Boron/epoxy	SP 500-2
E_L (GPa)	72.4	116	65.6	210	186
E_T (GPa)	72.4	116	50.7	25	12
$\alpha_L, 10^{-6}/{}^\circ C$	22.7	7.1	17.9	4.5	-0.9
$\alpha_T, 10^{-6}/{}^\circ C$	22.7	7.1	24.2	20.0	26
$\sigma_{L\,yield}$ (MPa)	303	925	390	1590	2913
ν_L	0.33	0.33	0.33	0.1677	0.31

All modeled repairs use the 3M adhesive AF-163-2 in a 0.13 mm thickness. Its shear modulus is 406 MPa, the shear yield strength is 36.2 MPa.

The fuselage repair configuration corresponds to a case to be tested in Chapter 6. A central crack of 70 mm in a 1.75 mm thick sheet of 7075-T6 is subjected to a remote

biaxial stress field. The stresses result from cabin pressurization (cabin pressure altitude 2800 m, cruising altitude 7625 m). The frames are spaced at 508 mm intervals, while stringers are 200 mm apart. The fuselage radius is 3.6 meters, resulting in a biaxial stress field of σ_{hoop} = 71.3 MPa, σ_{long} = 35.6 MPa.

A single elliptical patch size of 160 mm (long) x 80 mm (wide) will be used for this comparison. The appropriate inputs were made to CALCUREP; results follow in figures 5.12 through 5.18.

Figure 5.12 presents the effectiveness of the various patch materials when thermal considerations are *not* included. As can be expected, very thin high-modulus patches perform adequately. The lower modulus materials require two to three times as much thickness to achieve the same crack-closing effectiveness.
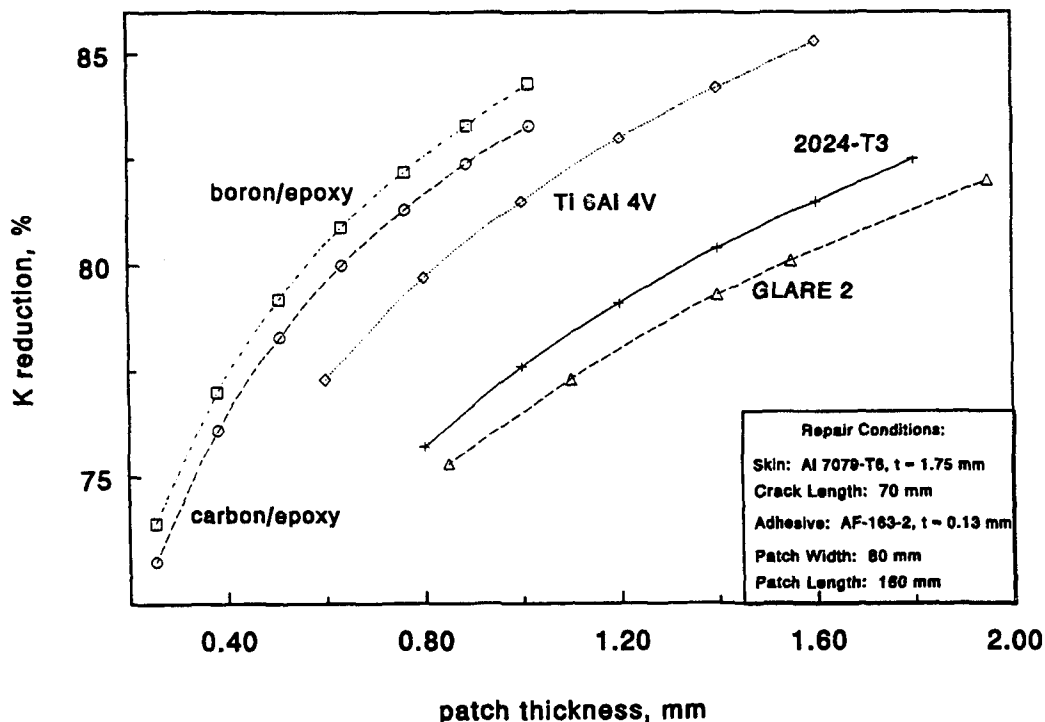
Figure 5.12. Comparison of reduction in stress intensity factor for various bonded patch materials as a function of patch thickness. Thermal effects not included.

When thermal effects of cruise altitude are taken into account, the situation changes drastically, as shown in figure 5.13. The high thermal expansion coefficient materials (2024 and GLARE) perform much more effectively than any thickness of titanium or

composite patches. However, a thicker patch to achieve equivalent extensional stiffness (Et) as the plate being repaired (circled values).

Repair Conditions:
Skin: Al 7079-T6, t = 1.75 mm
Adhesive: AF-163-2, t = 0.13 mm
Crack Length: 70 mm
Patch Width: 80 mm
Patch Length: 160 mm
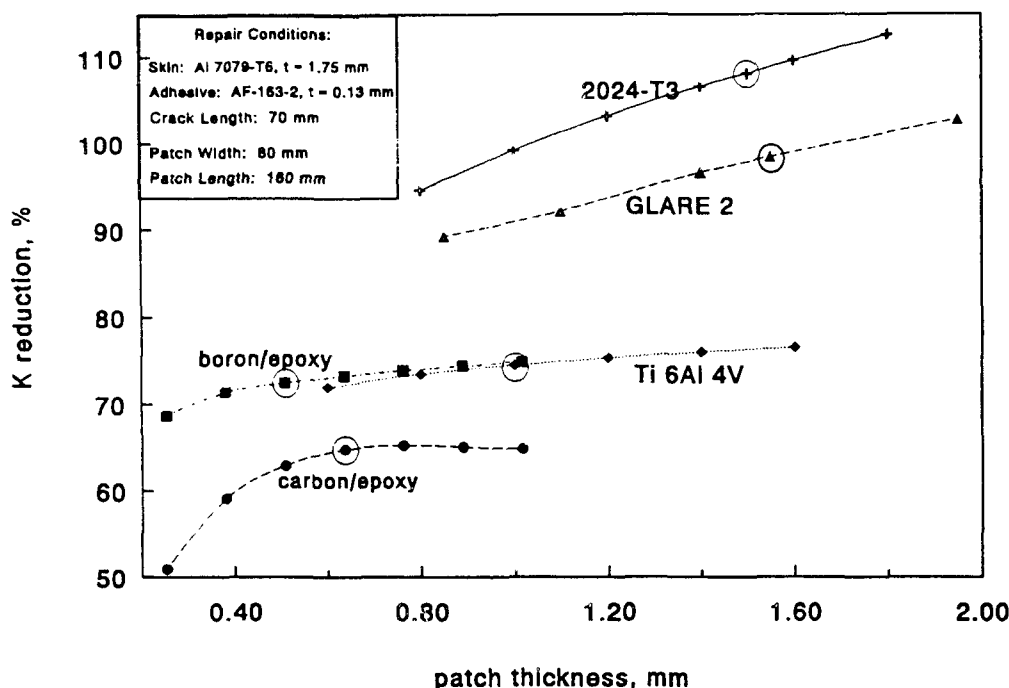
Figure 5.13. Comparison of reduction in stress intensity factor for various bonded patch materials, including thermal effects of cruise. Circles indicate equivalent stiffness patches.

Figure 5.14 presents the crack patching efficiency of only two materials: boron and GLARE 2, both with and without thermal effects. The effectiveness of the GLARE 2 patches is improved when thermal effects are considered. The effect on boron is the opposite: Its relatively low thermal expansion coefficient reduces its effectiveness.

GLARE 2 has a higher effective coefficient of thermal expansion than the stiffened 7075 panel during the 100°C temperature change (from curing to room temperature). The same is true for 2024-T3 patches. GLARE's effective expansion coefficient is smaller than the aluminum fuselage during the cooling from room to cruise temperature. However, the net result with both patch materials is additional tension in the patch and higher crack closing forces. The low thermal expansion materials (boron, carbon and titanium) have effective expansion rates during cure roughly equivalent to the stiffened fuselage, as other writers have pointed out [14,17,23,25,26]. It is the second cooling step that adversely influences the patching effectiveness of boron, carbon and titanium.
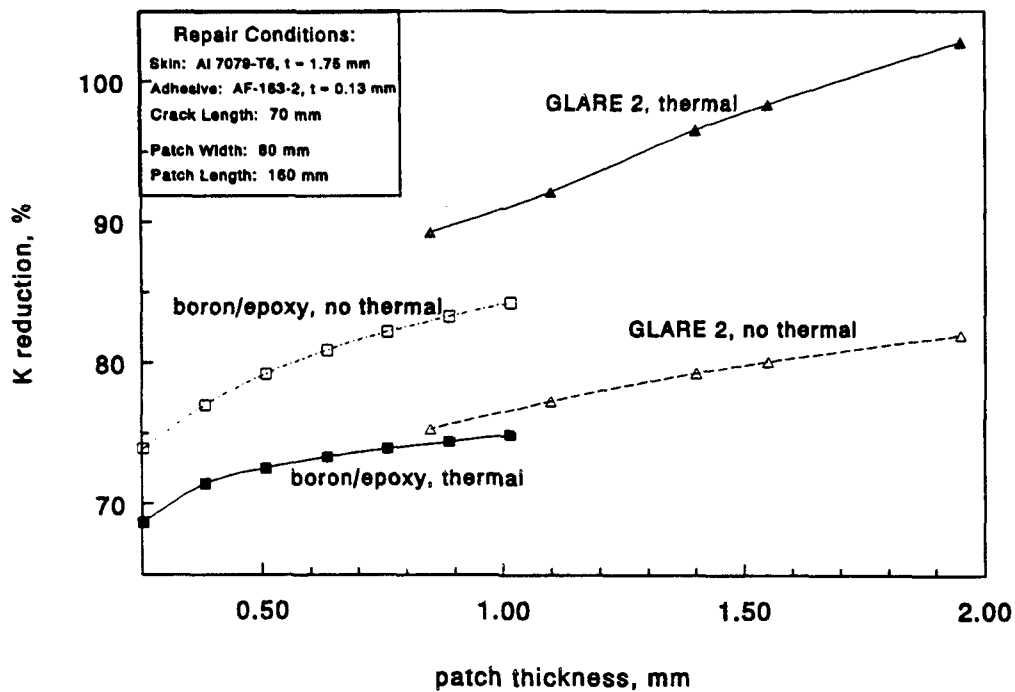
Figure 5.14. Comparison of reduction in stress intensity factor for bonded GLARE 2 and boron/epoxy patches, with and without thermal effects.

Thermal properties affect more than the reduction of K, of course. Equilibrium must be maintained, so the additional crack closing force in the high expansion coefficient materials results in added tension in those patches. Figure 5.15 illustrates.
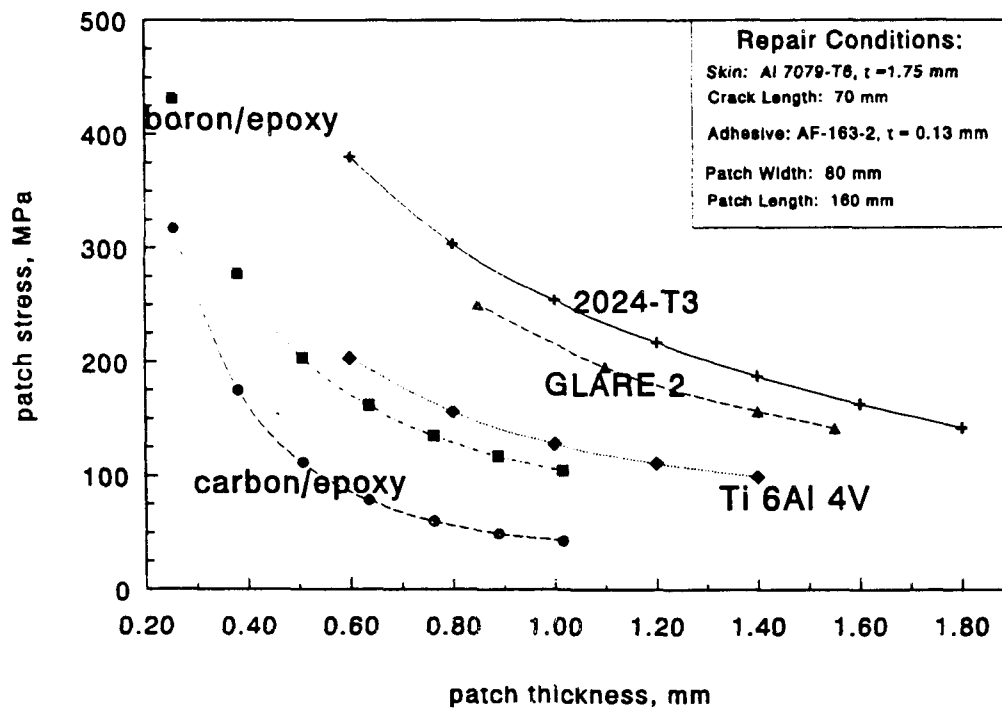
Figure 5.15. Comparison of peak patch stresses for various bonded patch materials, including thermal effects.

The figure shows the thermal expansion coefficient of the patch, *not* its elastic modulus, is most important in determining the maximum normal stress in the patch.

Another important element in patch selection is the stress induced in the plate just outside the patch due to load attraction by the stiff doubler region. Figure 5.16 represents the case of a balanced (two-sided) patch.
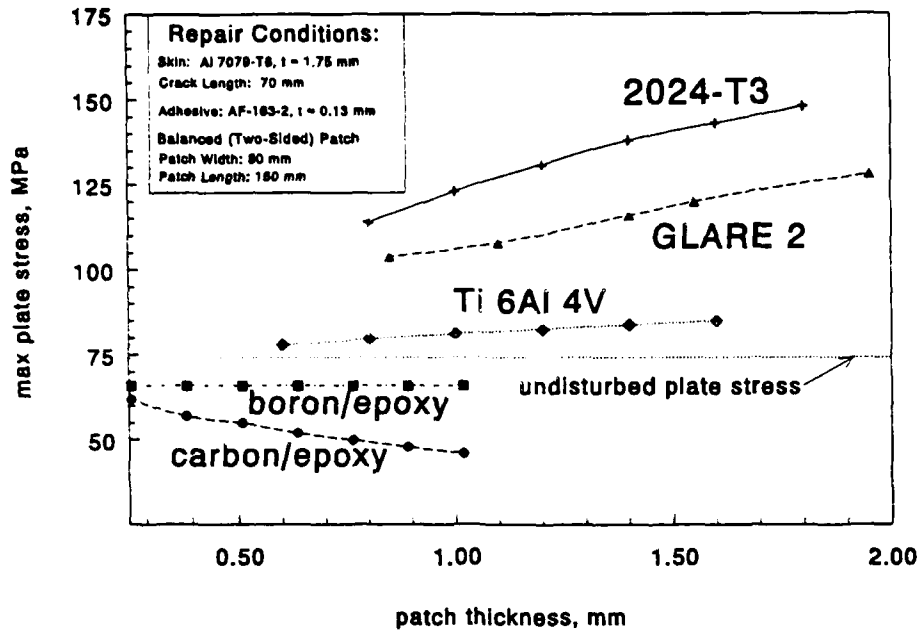
Figure 5.16. Plate peak stresses due to load attraction and thermal effects for bonded two-sided patches. Peak stresses occur just outside the patch edge (x = 0, y = a+).

When conditions force repairers to use one-sided patches, significant bending occurs in the plate at the top edge of the patch. This is especially pronounced with the thicker metal and metal laminate patches, as can be seen in figure 5.17.
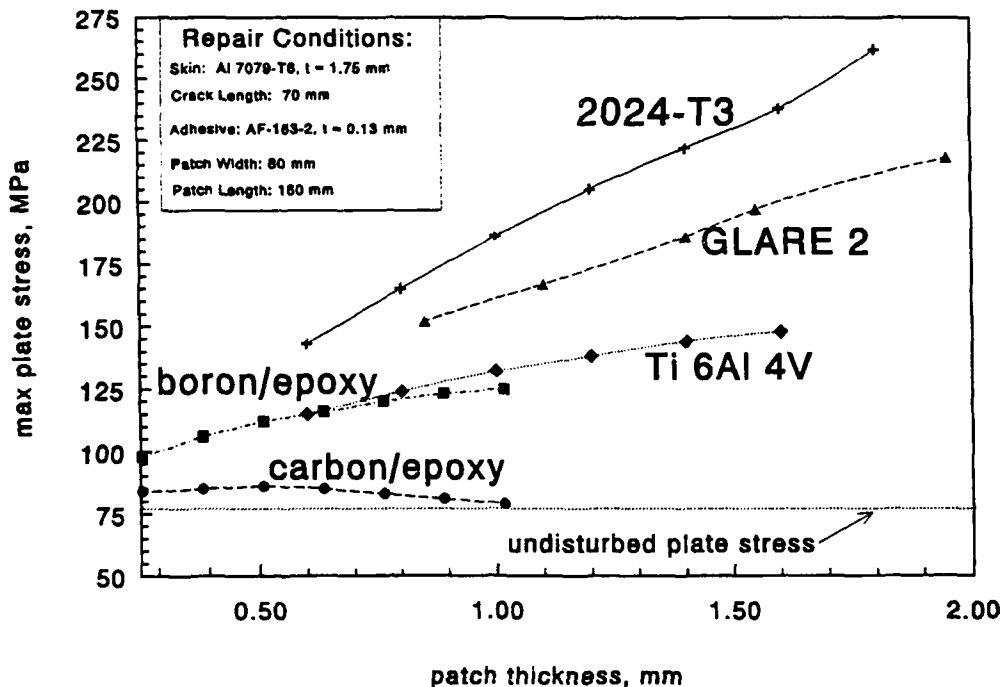
Figure 5.17. Combined (load attraction plus bending plus thermal) stresses in the plate just outside the patch edge for various bonded one-sided patches (at x = 0, y = a+).

149

The high plate stresses that occur at the top of the patch as a result of the thicker patches are a potential source of new fatigue damage. The bending stresses can be alleviated somewhat by tapering the edges of the patches. (This is also possible with the other patches, but is hardly necessary from a bending stress point of view.) Tapering or ply dropping also reduces peel forces in the adhesive at the patch tips.

Figure 5.18 illustrates the effect of tapering the 2024 and GLARE patch tips to 0.5 mm thickness. Tapering the patch tips reduces the peak plate stresses by up to 33 percent for the thickest patches. The (untapered) boron/epoxy curve is included as a reference.

The analysis of tapering involves running CALCUREP twice: first with the higher thickness of the untapered patch, and second with the lower thickness of the tapered area. The user must manually combine the overall output from first run (except for bending stresses) with the bending stress output from the second (tapered) run. Later versions of the program will do this automatically.

Of course, tapering cannot be performed over the crack. This is where the maximum adhesive shear strain occurs. Figure 5.19 compares the peak shear strains for the various patch configurations.
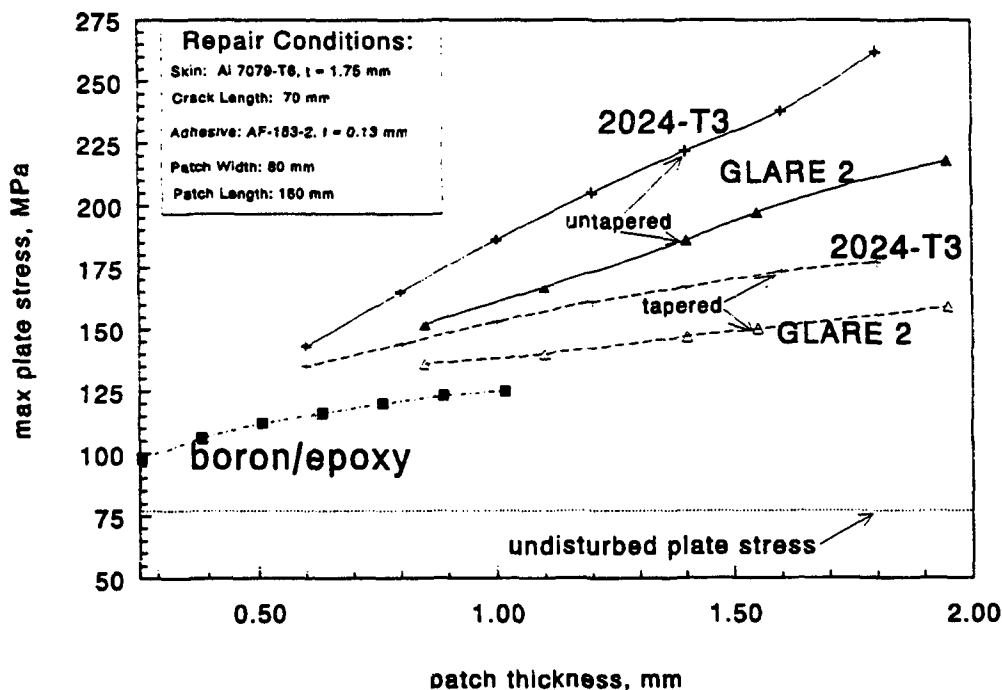
Figure 5.18. Effect of thickness tapering on combined (load attraction plus bending plus thermal) stresses in the plate just outside the patch edge for tapered bonded one-sided patches.
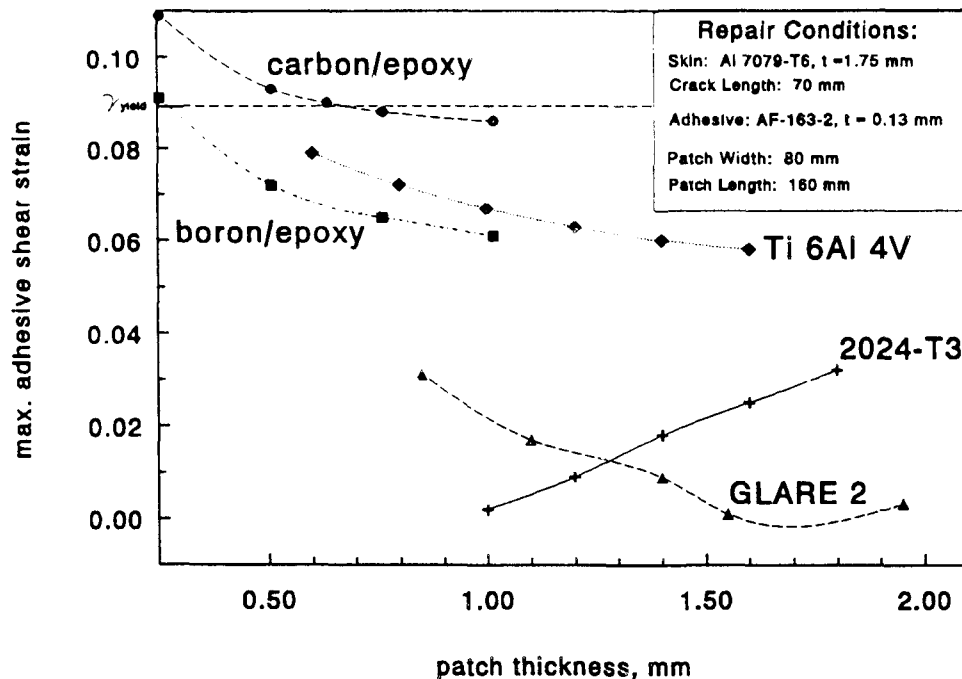
Figure 5.19. Maximum adhesive shear strains over crack, including thermal effects.

The shear strains are highest in the carbon-epoxy patches, followed closely by the titanium and boron-epoxy. In all three, the maximum strain values are near the measured yield strain of AF-163-2, 8.9 percent. This may be attributed to the large mismatches between both thermal expansion and elastic modulus properties compared with the aluminum skin being repaired. In the 2024 and GLARE patches, the shear strains are considerably lower.

Discussion. The preceding plots show that high elastic modulus in not the only parameter to consider in choosing a crack patching material. Figure 5.13 shows that all materials evaluated did an adequate job in reducing cyclic stress intensity factor. However, the very stiff composite patches and titanium under performed both GLARE 2 and 2024-T3. Only carbon/epoxy and the thinnest boron/epoxy patches (two plies, or 0.26 mm) gave K reductions of less than 70 percent.

Interestingly, above a certain thickness level, added composite plies were found to have no influence on crack patching effectiveness. The coefficient of thermal expansion of the patch material does as much to determine K reduction as does elastic modulus.

Both GLARE 2 and 2024-T3 have higher *effective* coefficients of thermal expansion than the stiffened 7075 panel during the 100°C cooling from curing to room temperature). This results in a static compressive preload on the crack, which must be overcome before crack opening and fatigue crack growth can occur.

In contrast, the low thermal expansion materials (boron, carbon and titanium) have effective expansion rates during cure that are equivalent to the stiffened fuselage. What little static residual tensile load may exist at the crack after curing does not contribute to fatigue. However, upon cooling from ambient to cruise temperature, the surrounding structure no longer constrains the patched area. The entire fuselage exterior cools (and shrinks) equally.

This second temperature step, which occurs every flight, causes a reduction of patching effectiveness for the low expansion coefficient materials. Now, the boron, carbon and titanium patches act to prop the crack slightly open. The low temperature of cruise altitude is reached when the highest pressure difference exists in the fuselage, resulting in higher cyclic stresses on the crack for boron, carbon and titanium patches.

Figure 5.15 shows the maximum normal stresses in the various patches. Design stresses should be kept below half the patch yield stress, or 150 MPa for 2024-T3 (1.8 mm patch) and below 195 MPa for GLARE 2 (1.1 mm patch). The other materials have such high strengths that patch failure in not a realistic concern.

For two-sided patches, bending is eliminated and plate stresses just outside the patch remain low, as seen in figure 5.16. Fatigue crack initiation in the plate at the edge of the patch is unlikely without an additional stress concentration such as a rivet hole. If a stress concentration of twice nominal or less is set as a reasonable maximum, all of the considered patches appear acceptable.

When one-sided tapered patches are considered (figure 5.18), again, the composite and titanium patches have no problems. Taking the stress concentration of two as a guide, the total thickness of the GLARE 2 patches must be limited to 1.55 mm or less. By the same standard, the 2024 patch cannot exceed 0.8 mm thickness. This effectively eliminates 2024-T3 from consideration as a one-sided patch.

The maximum adhesive shear strain is critical for good bond durability. Peak shear strains should be kept to less than half the adhesive shear yield strain. Figure 5.19 shows the adhesive shear strain levels are highest for the titanium and composite patch materials. The thinner carbon patches actually exceed the shear yield strain of the adhesive. The large mismatches between plate and patch in both elastic moduli and coefficients of thermal expansion cause these high shear strains. Only the GLARE and 2024 patches have acceptably low shear strain values.

Two comments are appropriate here: First, the adhesive shear modulus has a large influence on shear stress, but shear modulus is not nearly as constant in adhesives as it is in metals. This analysis used the room temperature G_A value given by 3M for AF-163-2. Elastomeric materials like toughened epoxies get stiffer as the temperature drops, so the values given in figure 5.19 could be *un*conservative for the cruise condition. Second, adhesive thickness also has a large influence on shear strain. Both effects will be investigated further in section 5.4.4.

Table 5.2 summarizes the important results from the previous discussion. If the repairer chooses a one-sided patch, only a tapered GLARE 2 patch of 1.1 to 1.55 mm thickness meets all the criteria. For two-sided patching, the choice expands to GLARE 2 ($t_{min} = 1.1$ mm) and 2024-T3 ($t_{min} = 1.8$ mm). High adhesive shear stresses proved to be the universal disqualifier for the titanium, carbon and boron patches. Poor K reduction in the carbon/epoxy patches was also problematic.

Table 5.2. Summary of parametric study of five crack-patching materials.

Parameter	boron/epoxy	carbon/epoxy	Ti 6Al 4V	2024-T3	GLARE 2
K reduction > 70%	$t_{min} = 0.38$	X	OK	OK	OK
$\sigma_{max}(patch) \leq \dfrac{\sigma_{yield}}{2}$	OK	OK	OK	$t_{min} = 1.8$	$t_{min} = 1.1$
$\sigma_{max}(plate) \leq 2\sigma_o{}^*$	OK	OK	OK	$t_{max} = 0.8^*$	$t_{max} = 1.55^*$
$\gamma_{max}(adhesive) \leq \dfrac{\gamma_{yield}}{2}$	X	X	X	OK	OK
acceptable patch total thickness, mm	X	X	X	$t_{min} = 1.8^{**}$	$1.1 \leq t \leq 1.55^*$

*Maximum thickness applies to tapered one-sided patches only.
**Only two-sided patches acceptable.
X Unacceptable, outside of limits.

5.4.3 Influence of Patch Geometry on Effectiveness

For the following sensitivity study, only balanced (two-sided) GLARE 2 patches will be considered. Elliptical patches will be used to repair a central crack in a 1.75 mm thick 7079-T6 stiffened fuselage panel. Two patch thicknesses were used: 1.3 and 1.7 mm. Variables included patch length and width, and the crack length. Because of the initial assumptions on which CALCUREP is based, crack lengths had to be chosen less than or equal to the width of the patch. The major outputs consid   ie reduction in K, the maximum adhesive shear strain, and the effects on plate stresses outside the patch.

5.4.3.1 Influence of a/b ratio. The crack length was held constant at 70 mm, and the patch width was 80 mm. Hart-Smith's rule of 30 times patch thickness for overlap length suggests a/b values (patch length/width) of 1.0 and 1.3, respectively, for the 1.3 and 1.7 mm patch thicknesses. The range of a/b ratios modeled was from 0.75 to 2.0. Table 5.3 summarizes the output.

Table 5.3. Effect of patch a/b ratio on various CALCUREP parameters.

Patch t, mm	a/b	K reduction, %	γ_{max} (adhesive)	$\sigma_{max}(plate), MPa$
1.3	0.75	100	.0004	104
	1.00	100	.0014	107
	1.25	99	.0032	109
	1.50	98	.0049	112
	1.75	98	.0057	115
	2.00	97	.0082	118
1.7	1.00	105	.0011	114
	1.50	104	.0032	121
	2.00	102	.0056	127

Longer patches resulted in small changes in the predicted values. K reductions dropped slightly for higher a/b ratios, but always remained above 97 percent. Maximum adhesive shear strains remained below 1 percent in all cases, but were lowest for the lowest a/b ratios. Longer patches also attracted slightly more load into the plate, but stresses remained reasonably low.

5.4.3.2 Influence of crack length/patch width ratio. If cracks are much shorter than the width of the patch, less patching effectiveness can be expected, as was discussed previously. However, for detectable crack lengths (say, 5 mm or longer), the important question for the repairer becomes by how much to overlap the crack tip.

Crack lengths ranging from 10 to 80 mm were analyzed with the two patch thicknesses. Patch length was constant at 160 mm, patch widths ranged from 80 to 140 mm ($1.14 < a/b < 2.0$). Table 5.4 presents the results.

The results show the crack length/patch width ratio has a minimal influence on patch effectiveness. Calculated adhesive shear strains and plate maximum stresses are almost independent of the crack length.

Table 5.4. Effect of crack length/patch width ratio on various CALCUREP parameters.

Patch, crack	a_c/b	K reduction, %	γ_{max} (adhesive)	$\sigma_{max}(plate), MPa$
$t = 1.3$ mm a/b $=2.0$	0.125	93	.0082	118
	0.25	95	"	"
	0.50	96	"	"
	0.75	97	"	"
	1.00	97	"	"
$t = 1.7$ mm a/b = 2.0 a_c variable	0.125	>100	.0056	127
	0.25	"	"	"
	0.50	"	"	"
	0.75	"	"	"
	1.00	"	"	"
$a_c = 35$ mm b variable	0.50	>100	.0056	121
	0.58	"	"	123
	0.70	"	"	125
	0.88	"	"	127

The results indicate there is a wide range of GLARE 2 patch geometries resulting in acceptable values of effectiveness. No tangible benefits can be gained by making a patch overlap length longer than the Hart-Smith recommendations. Neither does an excessively wide patch significantly improve patch performance.

5.4.4 Effect of Adhesive Properties and Cure Temperature

Once the patch material and geometry have been chosen, the final variables over which the repair technician has control are the adhesive and the cure temperature. For this parametric analysis, two patch materials were considered: GLARE 2 and boron/epoxy, in thicknesses judged reasonable by the preceding analyses. The fuselage structural configuration requiring repair is similar to that already described. The patch length has been reduced to 60 mm for all patch types, based on the previous section's conclusions. Patch thicknesses shown on the graphs represent the total of the two sides (e.g., a 1.3 mm GLARE patch is two 0.65 mm-thick patches).

5.4.4.1 Effect of adhesive thickness. If shear strains in a given adhesive are higher than desired for good durability, an increase in the thickness of the adhesive layer may reduce strain levels. Figure 5.20 illustrates this point.
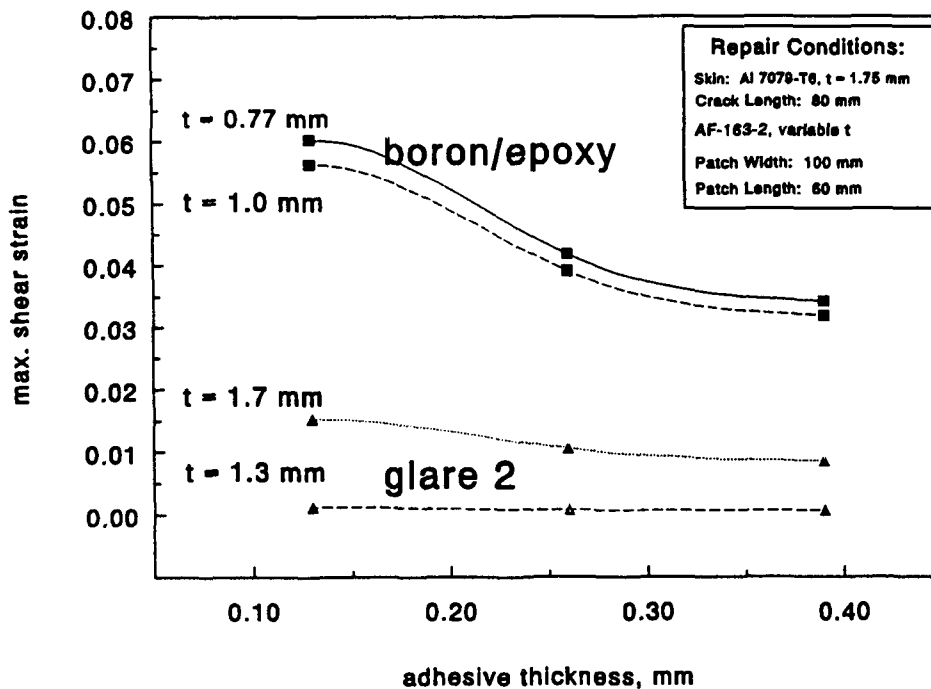
Figure 5.20. The influence of adhesive thickness on maximum adhesive shear strain.

The beneficial effect of a thicker bond line is largest when the mismatch in elastic modulus between the patch and plate is large. Unfortunately, in practice, high quality bond lines thicker than 0.2 mm are difficult to produce. Thicker bond lines add the risk of greater void content. Furthermore, a thicker bond line adds flexibility to the connection between

156

the plate and patch, at the potential cost of a less effective patch. Figure 5.21 illustrates that this flexibility cost is minimal.
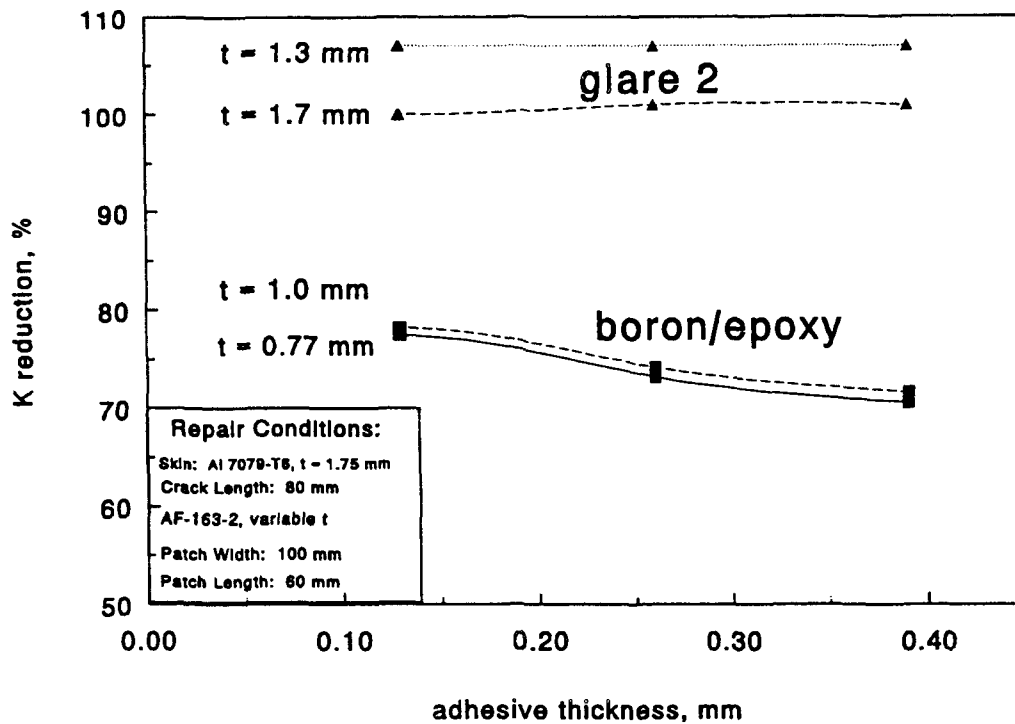
Figure 5.21. Influence of adhesive thickness on crack patching effectiveness.

The choice of adhesive shear modulus is rather limited among toughened epoxy structural adhesives commonly used in bonded repair. Room temperature shear modulus values of 400-500 MPa are common. At the low temperatures of high cruise altitudes, the shear modulus increases by as much as a factor of two.

Figure 5.22 confirms the expectation that as the adhesive becomes stiffer in shear, it experiences lower shear strain values. As expected, this difference is more noticeable with the boron/epoxy patches. With boron, the E mismatch with the aluminum substrate is much greater than in the case of the GLARE patch.

A higher adhesive shear modulus can have a beneficial impact on crack patching effectiveness of high modulus patches, as shown in Figure 5.23. The influence is small, however.
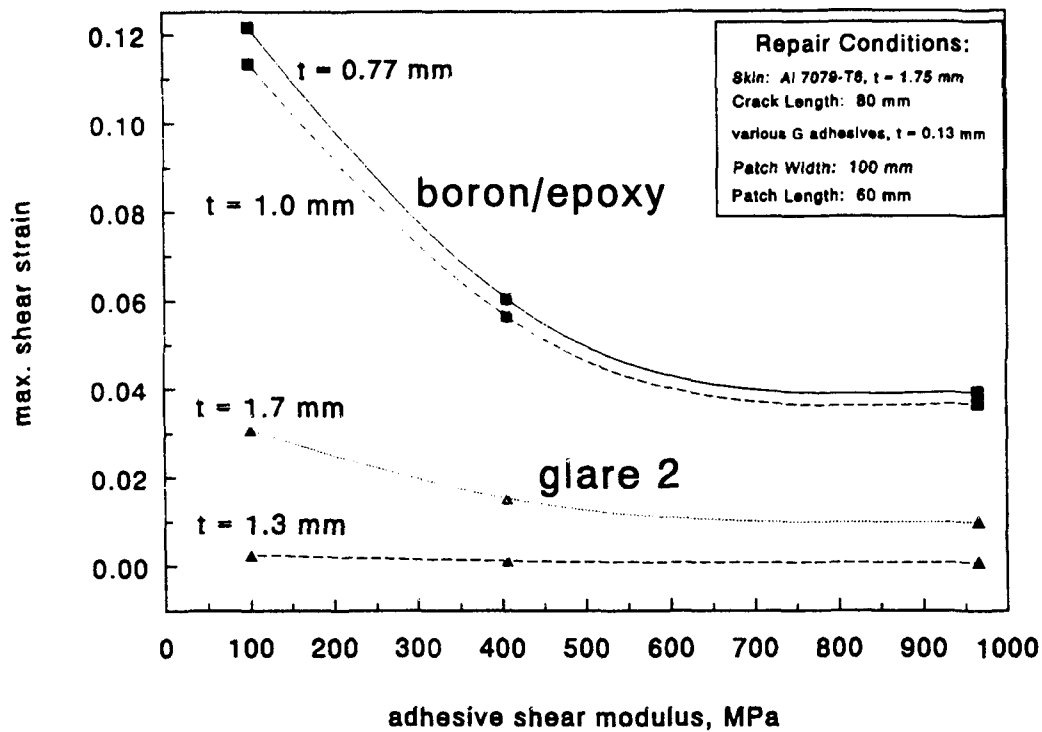
Figure 5.22. The influence of the adhesive shear modulus on maximum adhesive shear strain.
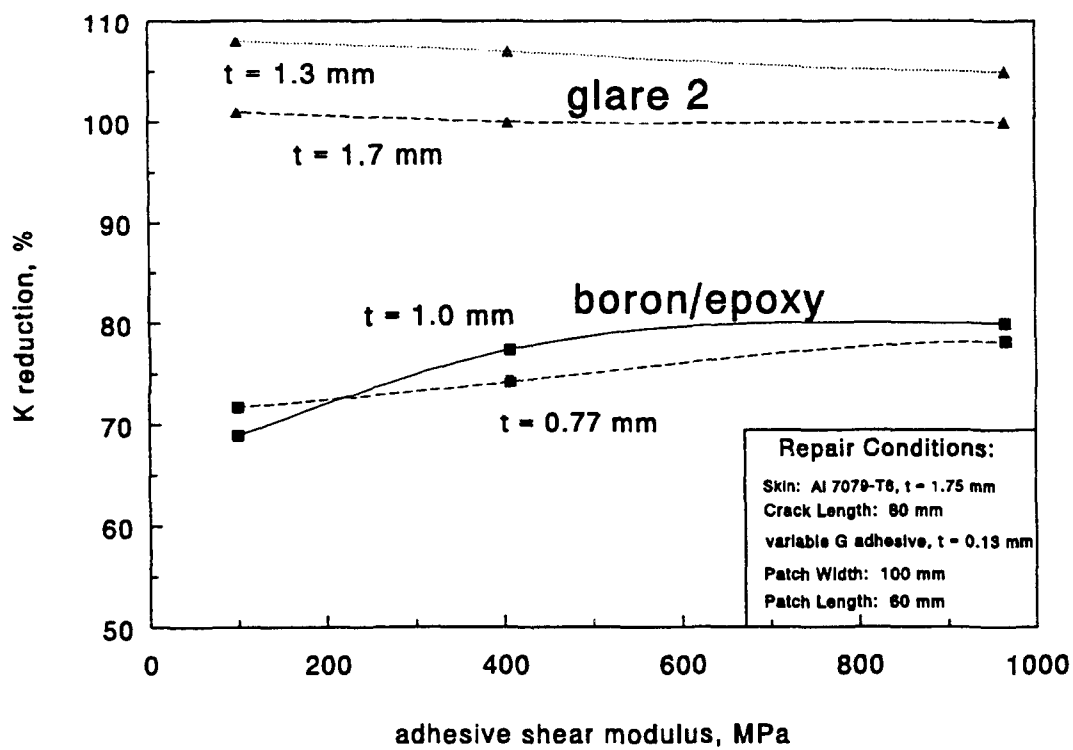
Figure 5.23. The influence of the adhesive shear modulus on crack patching effectiveness.

The final choice available to the repairer is the cure temperature. When repairs are performed on or near structures containing absorbed moisture (e.g., honeycomb), cure temperatures under 100°C are desired. Furthermore, a lower cure temperature can reduce thermal buckling problems. Otherwise, cure temperatures are set by equipment limitations. Temperatures around 120°C are used with toughened epoxies to gain good bonds in reasonable amounts of time.

When materials of different thermal expansion coefficients are bonded, cure temperature can affect residual stress states as well. Baker [24] recommends curing at "the lowest possible temperature" to minimize residual thermal stress. If a patch has a higher effective coefficient of thermal expansion than the substrate, cooling from the cure temperature results in a residual tension in the patch. Also, residual compression exists at the crack tip, which should by itself be beneficial for fatigue crack retardation. If the patch's effective thermal expansion coefficient is lower than the substrate's, a residual tensile load will exist at the crack tip.

Figure 5.24 shows the effect of various cure temperatures on the patching effectiveness of GLARE 2 and boron/epoxy. The GLARE patch benefits from a higher effective expansion because of the restraint on the stiffened fuselage. In the analyzed case, the effective expansion coefficient of the stiffened fuselage is approximately equal to that of boron. Thus, in wide-body fuselage skins, boron neither benefits nor suffers from a change in the cure temperature. The large thermal effects with boron occur in the cooling from room to cruise temperature.

Thermal effects have yet another significant impact on patch selection. The high adhesive shear strains experienced with boron patches cannot be reduced significantly by curing at a lower temperature, as shown in figure 5.25. With GLARE 2, the effect is reversed: A cure temperature of 100 to 120°C actually benefits the bond by reducing adhesive shear strains at operating temperatures.
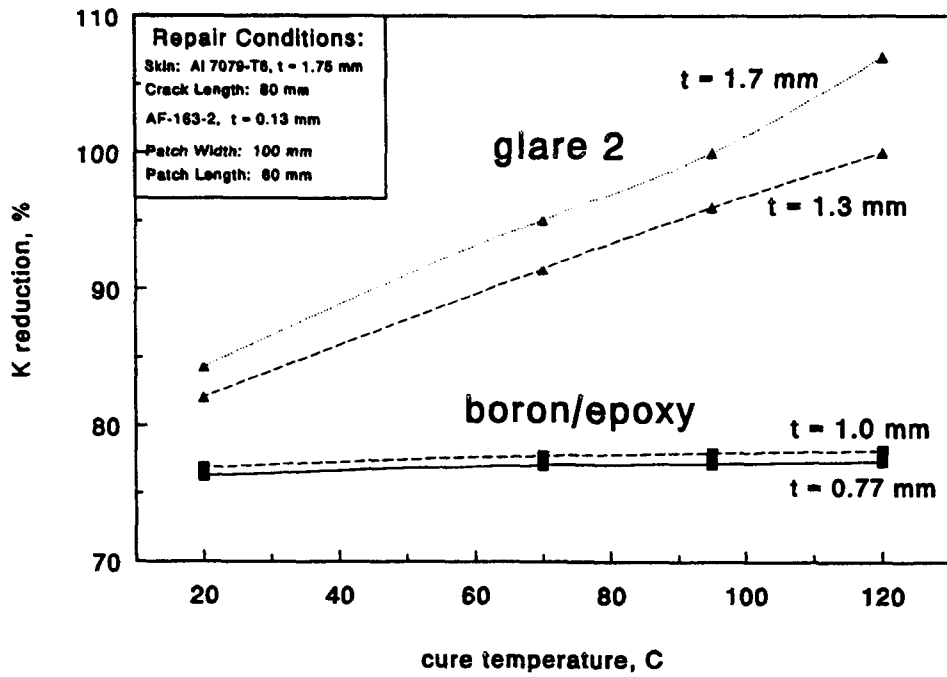
Figure 5.24. The variation in crack patching effectiveness with cure temperature.
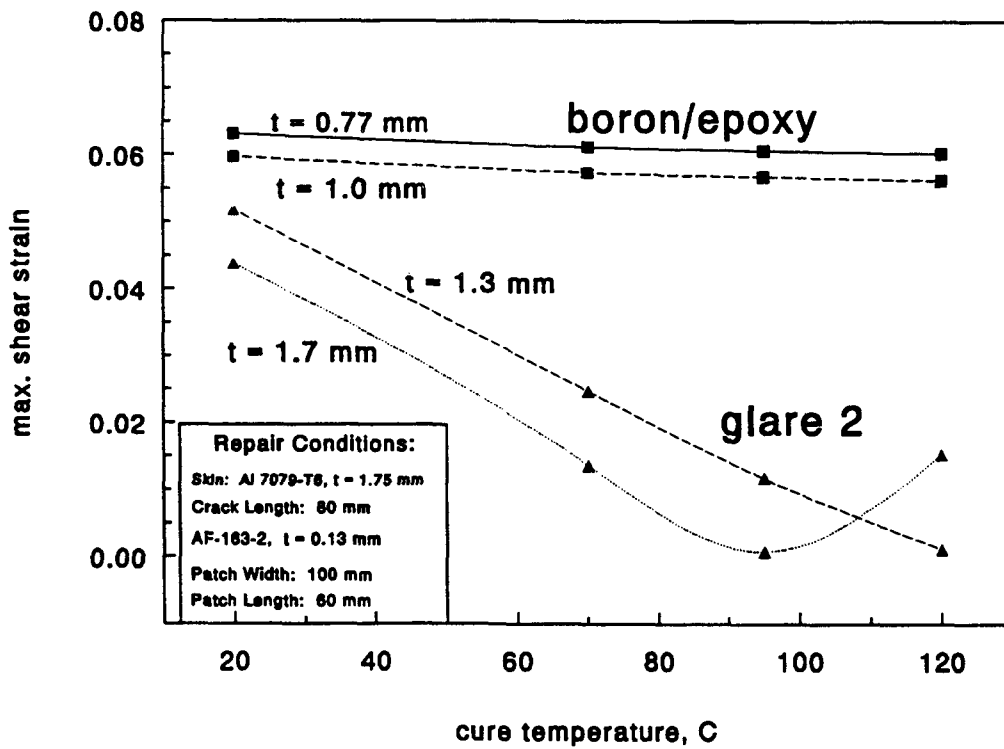
Figure 5.25. The influence of curing temperature on maximum adhesive shear strain.

160

GLARE has a higher effective thermal expansion coefficient than the stiffened aluminum structure during curing. However, when the fuselage is uniformly cooled from room to cruise temperature, the situation is reversed, and GLARE has a lower expansion coefficient than the now-unconstrained aluminum. These two steps cancel each other out, resulting in the low adhesive shear strains calculated here.

5.5 Summary

The Rose model of crack patching has been extended to include thermal effects of cruise altitude and bending stresses induced by one-sided reinforcements. The expanded model was transformed into a user-friendly program suitable for airline maintenance use. This program, called CALCUREP, enables rapid analysis of bonded crack patching repairs on a personal computer. Only limited knowledge of design stresses is necessary.

CALCUREP gives the user the following output:

- the reduction in stress intensity factor of the repaired crack,
- the maximum normal stresses in the patch,
- the maximum adhesive shear strains, and
- the maximum normal stresses in the repaired plate.

An extensive parametric study of various patch materials and configurations was accomplished. The study indicated that the relative effective coefficients of thermal expansion of the patch and the fuselage played the largest roles in determining the performance of the repair. The fiber metal laminate GLARE 2 proved more effective than high elastic modulus composites in reducing the stress intensity factor of a crack in a fuselage.

The use of low thermal expansion coefficient boron or carbon fibers induces high adhesive shear strain levels. These are expected to cause poor long-term durability of such patches on transport fuselages. Monolithic aluminum was an acceptable alternative in two-sided patching situations, though a greater thickness patch was required. The titanium alloy Ti-6Al-4V suffered from similar disadvantages as the composites.

A slight drawback to the use of GLARE and monolithic aluminum patches is the higher stresses that result in the surrounding plate. This problem is most severe when one-sided patches are used. Tapering of the edges of the GLARE patch sufficiently alleviates the high stresses such that new fatigue cracks are not expected. One-sided 2024-T3 patches did not meet all the criteria and thus are not recommended.

Studies of the effect of patch geometry on effectiveness showed that a broad range of patch sizes could perform adequately. Variations in adhesive thickness and shear modulus were shown to have only moderate influences on patch parameters.

Analysis of the effect of cure temperature on patch performance showed that high modulus patch materials like boron, carbon and titanium could not benefit from reduced cure temperatures. Cure temperatures in the range from 100 to 120°C worked best for the GLARE patches.

The net outcome was that GLARE 2 achieves better crack patching effectiveness and lower adhesive shear strains than boron, titanium and carbon patches (low thermal expansion materials). GLARE 2 results in thinner patches and lower plate tensile stresses than monolithic aluminum patches (high thermal expansion coefficient). When two-sided patches are allowed, either GLARE 2 or 2024-T3 is acceptable; however, the GLARE patch is the only acceptable choice for a durable one-sided patch repair.

References, Chapter 5

1. Baker, A.A. *et al.*, "Repair of Mirage III Aircraft Using the BFRP Crack-Patching Technique," *Theoretical and Applied Fracture Mechanics*, 2, 1984, pp.1-15.

2. Baker, A.A., "Fibre Composite Repair of Cracked Metallic Aircraft Components-- Practical and Basic Aspects, *Composites*, 18, Number 4, September 1987, pp.293-307.

3. Jones, R., "Crack Patching: Design Aspects," in *Bonded Repair of Aircraft Structures*, Baker, Jones, editors. Dordrecht: Kluwer Academic Publishers, 1988, pp. 49-76.

4. Jones, R. *et al.*, "Bonded Repair of Multi-Site Damage," from *Structural Integrity of Aging Airplanes*, Atluri, Sampath, Tong, editors. Berlin: Springer Publishing, 1991.

5. Ratwani, M.M., "Development of Bonded Composite Patch Repairs for Crack Metal Structure," *Proc. Int. Workshop on Defense Applications of Advanced Repair Technology for Metal and Composite Structures*, Naval Research Laboratories, Washington, 22-24 July 1981, pp. 370-403.

6. Sandow, F.A. and R.K. Cannon, "Composite Repair of Cracked Aluminum Alloy Aircraft Structure," AFWAL-TR-87-3072, September 1987.

7. 't Hart, W.G.J., and R.J.H. Wanhill, " Patch Repair of Corroded Aircraft Skin Areas," National Aerospace Laboratory NLR, Amsterdam, NL, 1984.

8. "Boron/epoxy Patches to Repair B-1B Longeron Cracking," Aerospace World, *Air Force Magazine*, October 1991, p. 20.

9. Miller, M., *et al.*, "Evaluation of Bonded Boron/Epoxy Doublers for Large Commercial Transport Aircraft, Proc. 5th Int'l Conf. on Structural Integrity of New and Aging Aircraft, Hamburg, Germany, 16-18 June 1993, pp. 255-256.

10. Muki, R. and E. Sternberg, *Int. J. Solids and Structures*, 4, 1968, pp. 75-94.

11. Rose, L.R.F., "An Application of the Inclusion Analogy," *Int. J. Solids and Structures*, 17, 1981, pp. 827-838.

12. Hart-Smith, L.J., "Analysis and Design of Advanced Composite Bonded Joints," NASA CR 2218, 1974.

13. Eshelby, J.D., *Proc. Royal Soc. London*, A241, 1957, pp. 376-396.

14. Rose, L.R.F. "Theoretical Analysis of Crack Patching," in *Bonded Repair of Aircraft Structures*, Baker, Jones, editors. Dordrecht: Kluwer Academic Publishers, 1988, pp. 77-106.

15. Marissen, R., "Fatigue Crack Growth in ARALL," Ph.D. thesis, Department of Aerospace Engineering, Delft University of Technology, Delft, the Netherlands,

16. Roebroeks, G.H.J.J., "Towards GLARE: The Development of a Fatigue Insensitive and Damage Tolerant Material," Ph.D. thesis, Department of Aerospace Engineering, Delft University of Technology, Delft, the Netherlands, December 1991.

17. Rose, L.R.F., "Residual Thermal Stresses," in *Bonded Repair of Aircraft Structures*, Baker, Jones, editors. Dordrecht: Kluwer Academic Publishers, 1988, pp. 90-91.

18. Baker, A.A., G.A. Hawkes and E.J. Lumley, *Proc. 2nd Int. Conf. on Composite Materials,* Toronto, 1978.

19. Grigull, U. and H. Sandner, *Heat Conduction,* Springer-Verlag, Berlin, 1984.

20. Gere, I. and S. Timoshenko, *Mechanics of Materials,* 2nd ed., Boston, 1985, pp 47-131.

21. Tarn, J.Q. and K.L. Shek, "Analysis of Crack Plates with a Bonded Patch," *Engineering Fracture Mechanics,* **40**, (6), pp.1055-1065, 1991.

22. Chu, R.C. and T.C. Ko, "Isoparametric Shear Spring Element Applied to Crack Patching and Instability," *Theoretical and Applied Fracture Mechanics,* **11**, 1989, pp. 93-102.

23. Jones, R., and R.J. Callinan, *J. Structural Mechanics,* **8**, (2), pp.143-149, 1980.

24. Baker, A.A., "Crack Patching: Experimental Studies, Practical Applications," from *Bonded Repair of Aircraft Structures*, Baker, Jones, editors. Dordrecht: Kluwer Academic Publishers, 1988, pp. 107-172.

25. Baker, A.A., M.J. Davis and G.A. Hawkes, paper 4.3, *Proc. 10th Int. Symp. of the Int. Comm. on Aeronautical Fatigue,* 1979.

26. Rose, L.R.F., *Int. J. Fracture,* **18**, pp.135-144, 1982.

6

Mechanical Testing of Crack Patching

"Should the whole frame of Nature round him break,
In ruin and confusion hurled,
He, unconcerned, would hear the mighty crack,
And stand secure amidst a falling world."

Joseph Addison,
Horace, Odes, book III, ode iii [1712]

6.1 Introduction

The previous chapter described analytical techniques for crack patching. Its successful implementation as a repair method for pressurized fuselages requires validation by laboratory testing of patch designs. This section describes the building block testing approach used to verify the predictions described in the previous chapter. These tests demonstrate that crack patching can be adequately described with the analytical techniques that constitute CALCUREP. Crack patching must be shown to be durable: That is, the patches must remain intact for a sufficient number of fatigue cycles without allowing cracks to grow. Furthermore, the damage tolerance of crack patching will be shown by documenting its beneficial effect on (artificial) damage introduced into the repaired structure.

Section 6.2 describes how small flat coupons with central saw cuts were patched and tested in severe constant amplitude fatigue conditions. The successful completion of these coupon tests was followed by durability and damage tolerance tests of a pair of uniaxially loaded saw cut stiffened flat panels. These panels represented as closely as possible a multiple site damage fatigue problem taken from operational service and are described in section 6.3. These results validate the analysis performed by the CALCUREP program and show the value of GLARE 2 in crack patching.

6.2 Coupon Tests of Crack Patching Concepts

6.2.1 Introduction

Several flat unstiffened 7075-T6 coupons were provided with saw cuts to simulate fatigue damage. Most of these coupons were repaired with various bonded patches and fatigued to failure. One repaired specimen was tested statically to failure. The test results were

compared with the predictions of CALCUREP regarding the stress intensity factor of the repair configurations.

6.2.2 Specimen Preparation

All specimens were cut from a 2.0 mm thick sheet of bare (unclad) 7075-T6 to dimensions of 300 by 160 mm. A central saw cut was made in the rolling direction, perpendicular to the load direction. Specimens were degreased, pickled and primed to prepare them for bonding with AF-163-2K adhesive at 120°C in an autoclave.

Nine specimens repaired with two-sided elliptical patches and an unpatched cracked baseline specimen were tested. All repair patches were 60 mm long, as shown in figure 6.1 at right. Patch widths and saw cut lengths were varied. Most patch widths were set equal to the saw cut length to facilitate visual monitoring of any crack growth. The highest stiffness direction in all patches was oriented perpendicular to the saw cut, except G5. This patch was purposely oriented five degrees off the perpendicular to simulate poor installation. Table 6.1 summarizes the specimens.
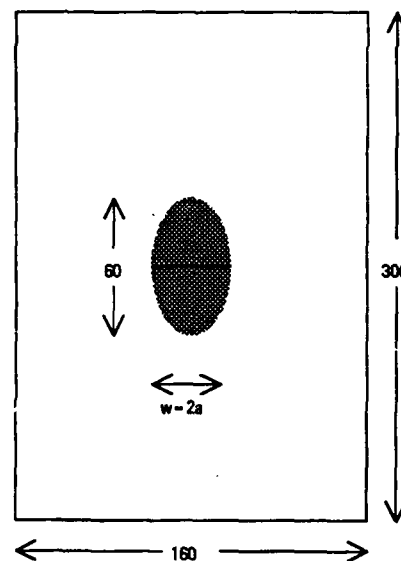
Figure 6.1. Two-sided patch specimen.

Table 6.1. Patch repair coupons.

patch code, type	patch thickness (mm)	$\dfrac{(Et)_{patch}}{(Et)_{skin}}$	patch width (mm)	initial saw cut length (mm)	notes
BL, none	--	0	none	40	baseline
A1, 2024-T3	2 x 1.0	0.97	20	20	
A2, 2024-T3	"	"	40	40	+5 mm cut**
C1, SP500*	2 x 0.25	0.64	40	40	
G1, GLARE 2	2 x 0.85	0.76	20	20	+15 mm cut**
G2, GLARE 2	"	"	40	40	
G3, GLARE 2	"	"	40	30	
G4, GLARE 2	"	"	40	50	
G5, GLARE 2	"	"	20	20	offset 5°, fatigue
GST, GLARE 2	"	"	20	20	static, no fatigue

*Unidirectional SP500 carbon/epoxy tape.
**Fatigue load did not initiate a crack. The saw cut was extended on each side.

6.2.3 Test Conditions

Constant amplitude fatigue tests were carried out on a computer-controlled 6-ton test frame. Specimens were cycled at gross stresses of 6 to 120 MPa at 10 Hz in laboratory air. This stress level is extremely high for 7075-T6, as the unpatched baseline result will show. Most specimens were cycled to failure. However, a few specimens were given extra saw cuts outside the patch when they did not initiate cracks naturally.

6.2.4 Test Results

Figure 6.2 shows the fatigue lives of those tested specimens where the patch completely covered the initial saw cut. The extremely short life of the unpatched specimen (1,462 cycles) attests to the severity of the loading. When no growth occurred on specimens A2 and G1, they received additional cuts to a total length of 50 mm after 175,000 and 100,000 cycles, respectively, so rates could be measured.
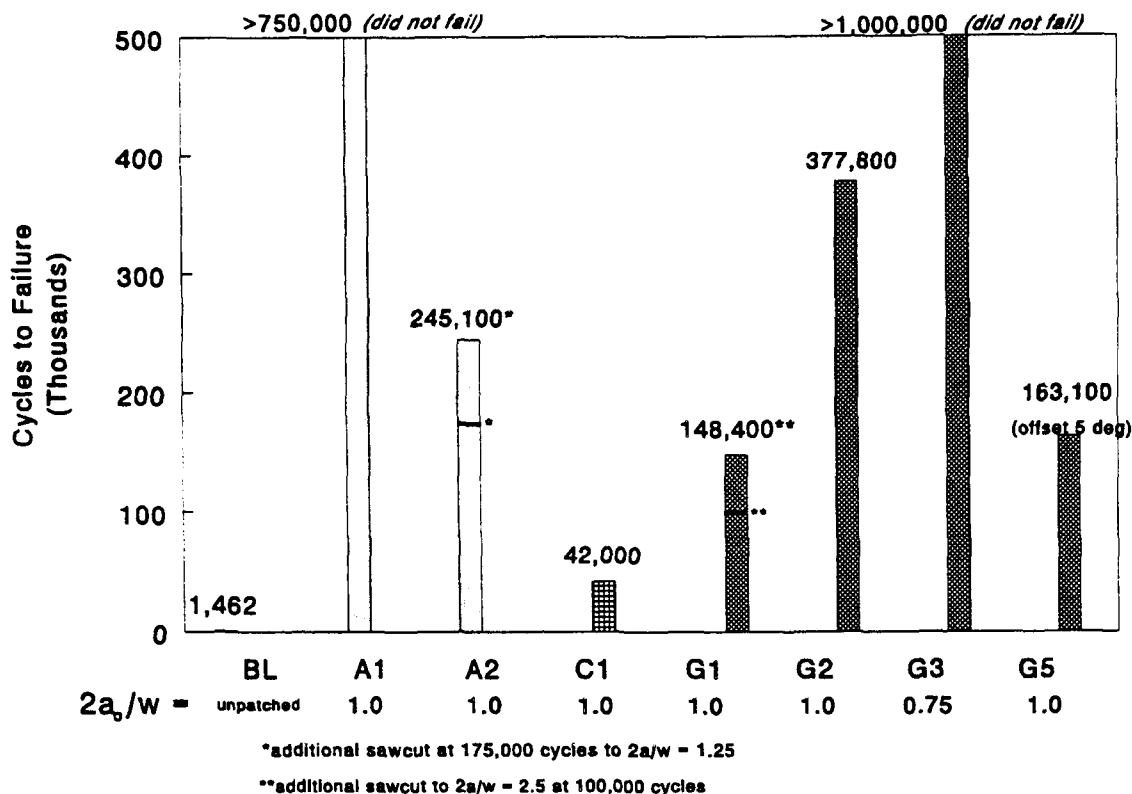
Figure 6.2. Fatigue lives of patched unstiffened 7075-T6 panels.
Constant amplitude fatigue, 6-120 MPa, 10 Hz, lab air.

The results show that even the worst performing patch (SP500 carbon-epoxy) increased the life of the unpatched baseline to 42,000 cycles, i.e., by a factor of nearly 30. Saw cuts under properly bonded 2024 and GLARE 2 patches simply did not re-initiate in 750,000 and 1,000,000 cycles, respectively.

The specimen with the purposely mis-aligned patch (G5) failed after 163,100 cycles. It was the only GLARE patch specimen to experience natural fatigue growth from a fully covered crack. The original saw cut in specimen G4 exceeded the patch width by 25 percent. It failed after only 42,000 cycles.

Two additional 5 mm saw cuts were made in samples A2 and G1 after a limited amount of cycling to provide crack growth data. Without these extra cuts, the samples probably would have resisted re-initiation for extremely long periods. By making the extra cuts, however, comparisons could be made with the CALCUREP-predicted crack growth rates.

Specimens BL, A2, G1, G4 and C1 were monitored closely during crack growth. This provided useful information on crack growth rates. Table 6.2 summarizes the measured crack growth rates of the specimens immediately after re-initiation.

Table 6.2. Measured initial crack growth rates.

specimen	crack length (2a) at re-initiation (mm)	measured initial crack growth rate (μm/cycle)
BL	40	40
A2	50	0.25
C1	30	0.26
G1	50	0.40
G4	40	0.45

The static test specimen, GST, failed at 559 MPa. Failure occurred in the sheet across the saw cut section. The failure was accompanied by simultaneously interlaminar failure of the GLARE patch in the glass/epoxy prepreg. This compares with the published ultimate static strength of 570 MPa for 7075-T6 [1], or a two percent reduction.

6.2.5 Discussion

The results of the coupon tests confirm that a wide variety of patch materials and configurations can give substantial increases in life to saw cut panels. However, some general guidelines can be gleaned from these tests.

Good repair practice involves *choosing a patch width that exceeds the crack* (or saw cut) *length by about a centimeter*. A larger overlap is not necessary, as demonstrated by analysis in the previous chapter, but a small overlap gives a safety margin should crack growth occur. When cracks extend beyond the patch, its beneficial influence is diminished.

Patches should be designed to give a very slow (repaired) crack growth rate. A reasonable goal might be a da/dN value of 0.1 μm per cycle or less, so inspection intervals of the repair can be a long as possible. This crack growth rate value corresponds to a repaired stress intensity factor of approximately 5 $\mathrm{MPa}\sqrt{m}$ for 7075-T6, and roughly 10 $\mathrm{MPa}\sqrt{m}$ for 2024-T3.

The slow crack growth shown by the repair configurations once the cracks had exceeded the patch width indicates this could be a damage tolerant repair method. However, this behavior must be investigated further and confirmed on larger specimens more typical of pressurized fuselage structure.

When cracks were the same length as the patch width, CALCUREP was able to estimate directly the crack tip stress intensity factor. This was true with sample C1, where crack re-initiation and growth occurred naturally from the original saw cut. However, the CALCUREP boundary conditions were violated with sample G4, where the initial saw cut exceeded the patch width. This was the case as well with samples A2 and G1, where additional saw cuts had to be made to achieve crack growth.

To estimate a patched stress intensity factor, the patch was "smeared out" analytically to cover the crack. Thus, the EA of the patch was held constant by increasing its width and reducing its thickness. This allowed the use of CALCUCREP to estimate a K factor after patching. Thermal effects were neglected because they imposed strictly static loads on the saw cut and did not contribute to cyclic stresses.

Using a published da/dN vs. ΔK curve [2], an estimate of the crack growth rate just outside the patch was made. Table 6.3 shows the comparison of measured and calculated crack growth rates for the four patch cases.

Table 6.3. Comparison of crack growth rates, "smearing out" method.

specimen	$2a_0$/patch width	measured initial crack growth rate (μm/cycle)	predicted initial crack growth rate (μm/cycle)	percent difference
A2	50/40	0.20	0.15	25
C1	40/40	0.26	0.30	15
G1	30/20	0.40	0.70	75
G4	50/40	0.45	0.35	22

The differences between the predicted and observed crack growth rates were smallest for sample C1 (15 percent), where the initial saw cut and patch were of equal size. As the ratio of the saw cut length to patch width increased, so did the size of the difference. When the saw cut was 1.5 times the width of the patch, the difference was large (75 percent). The original boundary conditions of CALCUREP should be respected in its employment if accurate results are desired.

Another estimate can be obtained by assuming that the crack opening is fully restrained underneath the patch. The saw cuts beyond the patch edges can then be treated as two separate cracks each with a tip-to-tip length, a^*, of 5 mm. The cyclic stress intensity factor is $\Delta K = \Delta\sigma\sqrt{\pi a^*} = 10.1\, MPa\sqrt{m}$. A graph from Broek [3] for 7075-T6 tested in constant amplitude fatigue, R = 0.05, indicates da/dN = 0.22 μm/cycle for specimen A2 (2024 patch). The less stiff GLARE patches on specimens G1 and G4 gave a higher crack growth rate.

6.3 Patching of Cracked Stiffened Panels

"Our minds thus grow in spots; and like grease spots, the
spots spread. But we let them spread as little as possible: we
keep unaltered as much of our old knowledge, as many of our
old prejudices and beliefs, as we can. We patch and tinker
more than we renew."

William James,
Pragmatism [1907]. Lecture 1

6.3.1 Background

The panel tested in this series represents a stiffened 7079-T6 aluminum fuselage panel
from a large 1960's vintage pressurized transport aircraft suffering from widespread
fatigue damage. The fatigue cracking occurs along a row of rivets where a fairing is
attached to the primary fuselage skin. One of the problems with the repair location is its
tendency to collect water. 7079-T6 is known "to be markedly inferior" compared with the
stress corrosion cracking performance of other high-strength aluminum alloys in alternate
immersion tests in artificial seawater. Thus, the stress intensity factor of a repaired crack
in 7079-T6 operating in an aggressive environment must be kept extremely low ($<$ 5
$MPa\sqrt{m}$) to prevent crack growth [4].

The test panels represented as closely as possible the structural configuration and flight
load conditions leading to this fatigue cracking problem. Two GLARE 2 fiber metal
laminate patch configurations were designed, installed and tested on the two-bay panels
shown in figures 6.3 and 6.4. Each panel had a central 80 mm saw cut to a simulate
fatigue crack that spanned four adjacent rivets and ended at the rivet holes. A single-sided
patch was tested to 100,000 flights (equivalent to 10 lifetimes) at cyclic stress levels
equal to 82 MPa, or 110 percent of the design limit stress in the skin. Fatigue testing was
followed by a static test to the design ultimate stress. In the second panel, a balanced
(two-sided) patch was fatigued for five lifetimes at 110 percent of limit load. Additional
symmetric saw cuts were made in the skin outside the patch. Fatigue testing was
continued for an additional 83,000 cycles to monitor crack growth and demonstrate the
damage tolerance of the design.

173

6.3.2 Panel Design and Manufacture

Figure 6.3 shows a sketch of the test section of the panel. Because of limitations of the test equipment, the 1,200 mm long by 800 mm wide test panel represents approximately an 80 percent scale extensional stiffness (EA) model of the actual aircraft panel. The frame height was maintained at 100 percent of the original design, and the location of the neutral axis was held constant. The extensional stiffness of an additional mid-bay tear strap in the original structure was lumped into the tear straps under the two frames.
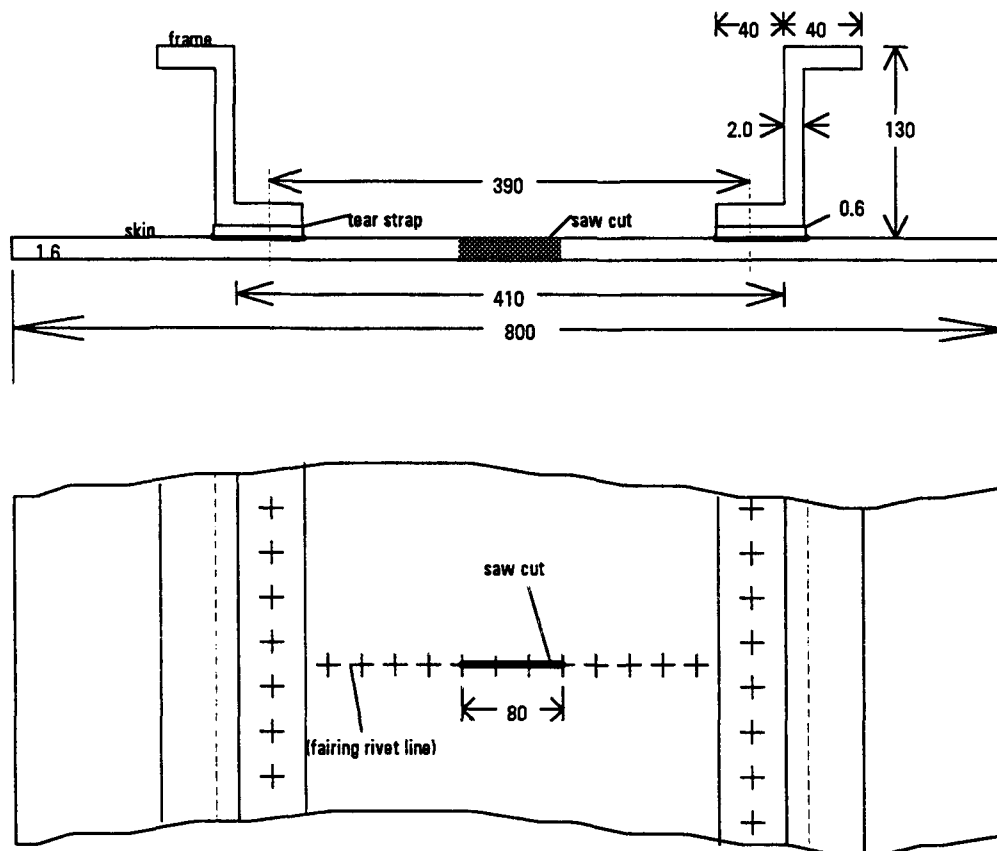
Figure 6.3. Sketch of test section of large 7075-T6 fuselage stiffened panel.
Not to scale. All dimensions mm.

Further compromises were made in manufacturing: because of the unavailability of alloy 7079-T6, 7075-T6 was substituted in its place. 7079-T6 and 7075-T6 have roughly equal fracture toughness values and should give similar fatigue crack growth performance when tested in laboratory air. The original tear straps were bonded titanium alloy; in their place, aluminum alloy tear straps with 50 percent greater cross-sectional areas were substituted to achieve equivalent stiffness. Constant thickness cold-formed z-shaped frames replaced the extruded variable-thickness I-shaped frames of the original design.

174

Two panels were manufactured for testing. Individual sheet parts were sheared to their final dimensions, except the patches. These were rough-cut on a band saw and formed to final dimensions on a belt sander. The tear straps, skin doublers and various other small load introduction parts were alkaline degreased and deoxidized. After bath pretreatment, these smaller items were primed and cured with an epoxy primer to ease handling.

The 1,200 mm long skin panels, too large to fit into the pretreatment tanks, were solvent degreased by hand and abraded with a portable Scotch Brite machine. This was followed by extensive hand-cleaning with clean paper towels dipped in methanol to assure a clean bonding surface. Anodizing was not performed, as this affects only the long-term durability of the bond.

The skin panels, tear straps, skin doublers and GLARE patches (which were supplied with anodized and primed surfaces) were prepared for autoclave bonding by laying them up with AF-163-2 structural epoxy film adhesive. After curing, the bonded assembly was riveted to the frames and load introduction fittings using protruding head 4.8 mm 7050 alloy (E grade) rivets. Riveting quality was kept high by using a force-controlled riveting machine. Rivets were installed on the center line of the specimen to simulate the fairing attachment location. Figure 6.4 shows the final configuration.
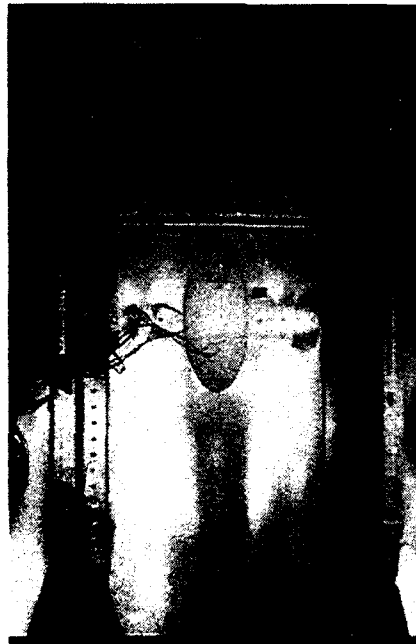
Figure 6.4. Photograph of stiffened test panel.

6.3.3 Patch Selection

Two patch designs were tested: a singled-sided 3/2 lay-up of GLARE 2 (1.4 mm thick) and a balanced pair of 2/1 GLARE 2 sheets with individual thicknesses of 0.85 mm. The width of all patches was set at 100 mm to provide a 10 mm overlap of each saw cut tip. The half-length of the single-sided patch was set at 80 times the thickness, while the half-length of the double-sided patches was set at roughly 35 times their thickness, following the guides discussed in section 4.4.2. Thus, the single-sided patch dimensions were 224 x 100 mm, while the double-sided patches measured 60 x 100 mm.

Elliptical patches were chosen to match the conditions of the analysis. An elliptical patch, besides making calculations much simpler, gives the most efficient load redistribution in a doubler. To produce an accurate elliptical template, the major and minor axes of the patch were simply input into a drawing program on a personal computer and printed.

CALCUREP outputs of the chosen patch configurations are shown in table 6.4. The maximum patch stress occurs over the saw cut, while the maximum plate stress is found just outside the patch tips in the loading direction. It is roughly twice as high as the remote stress in the single-sided patch configuration, a function of bending and load attraction by the stiff inclusion.

The applied stress range (4 to 86 MPa) was set at 110 percent of the design limit load and was based on flight test data supplied by the manufacturer. The patches in this case were bonded in the autoclave (no constraint of "cold" surrounding structure) and tested at room temperature. Thus, the program inputs were adjusted accordingly so thermal stresses were properly compensated. This allowed the measured strains on the specimens to be compared with the calculations.

Table 6.4. CALCUREP input and output for tested repair configurations.

Input Data
Plate material: 7075-T6, t = 1.6 mm Frame spacing: 400 mm Stringer spacing: 10 m Remote uniaxial stress level: 86 MPa Cruise altitude: sea level (room temperature testing) Saw cut length: 80 mm Adhesive: AF-163-2, t = 0.13 mm Cure temperature: 20°C (for calculations only)

Patch Configuration	Single-sided	Double-sided
Material	GLARE 2, 3/2 lay up	GLARE 2, 2/1 lay up
Thickness	1.4 mm	2 x 0.85 = 1.7 mm
Length	224 mm	60 mm
Width	100 mm	100 mm
Tapered?	No	Yes, t_{min} = 0.3 mm

	Output Data	
ΔK reduction, %	84	86
σ_{max}, patch, MPa	130	91
σ_{max}, plate, MPa	185	99

6.3.4 Test Results

6.3.4.1 Panel #1 (single-sided patch). Figure 6.5 shows a detail of the test section and indicates the location of selected strain gages. Stress values converted from measured strains at the nominal skin stress of 86 MPa are displayed in normal type. The three stresses predicted by CALCUREP are shown in italics.

The strain results indicate that CALCUREP is accurate in predicting the combined (load attraction plus bending) stress in the skin with the one-sided patch *(3 percent error)*. The measured stress level is considered excessive from a design durability point of view. However, it was caused by the failure to taper the patch tip before bonding.

One point missed by CALCUREP was the compressive strain experienced by the outer surface of the one-sided patch configuration. This large error stems from the assumption that longitudinal reinforcement at the crack location by a stringer or similar element would

suppress bending. In the tested case, the fairing attachment was omitted and the doubled area was free to deform out of plane. Furthermore, the finite length gage was located in an area of very high strain gradient, while the calculation predicted the stress at an infinitely small point.

Figure 6.5. Measured/predicted stresses in the loading direction, panel #1 (single-sided patch). Parentheses indicate stresses from the back (non-frame) side of the panel. All stresses in MPa. Nominal skin stress = 86 MPa.

Fatigue testing was performed for 100,000 cycles at 3 Hz in room temperature laboratory air. The testing was interrupted regularly for inspection of the panel. Several rivets in the load introduction fittings failed because of excessive bending and were replaced with bolts.

A large crack was found in the skin in the load introduction fitting after 85,000 cycles (more than eight lifetimes of the baseline aircraft). The crack was caused by an error in the detail design of the fitting. Testing was halted temporarily so the crack could be repaired. The load introduction fittings were modified to preclude similar cracks. Fatigue testing was resumed and the panel continued to 100,000 cycles without further incident.

Extensive inspection of the panel showed no fatigue cracking in the test section. The original 80 mm saw cut was visually inspectable and showed no signs of crack initiation. Eddy current scans of the patch showed no sub-surface cracks in the GLARE. Strain gage surveys indicated no measurable change in the structural performance of the panel. As a

final test, the panel was loaded to its estimated design ultimate stress. Neither crack extension nor panel failure occurred, and the patch remained intact.

6.3.4.2 Panel #2 (double-sided patch). All modifications developed for the first panel were made on the second article before testing was begun. Figure 6.6 shows a detail of the test section with the location of selected strain gages. Data from the gages located in the line of the saw cut will be presented later in this section. As with the first panel, stresses converted from the measured strain values at a nominal skin stress of 86 MPa are displayed in normal type. Predicted stresses from CALCUREP are shown in italics.

The strain results from outside the frames indicated that some additional longitudinal bending existed in the panel. As seen in figure 6.6, the skin stresses outside the frame were 92 MPa on the frame side and 79 MPa at the same location on the reverse surface. A significant amount of transverse bending was observed visually in the tests. This probably occurred due to the deletion of the stringers from the test article, which resulted in a relatively flexible panel in the direction transverse to the frames.
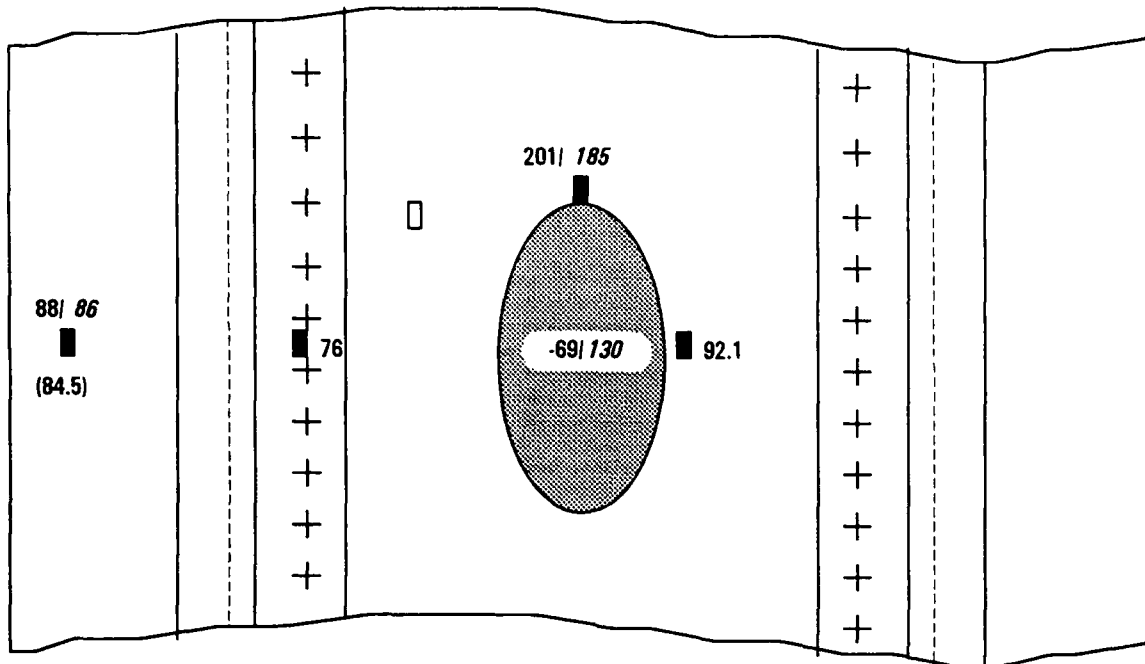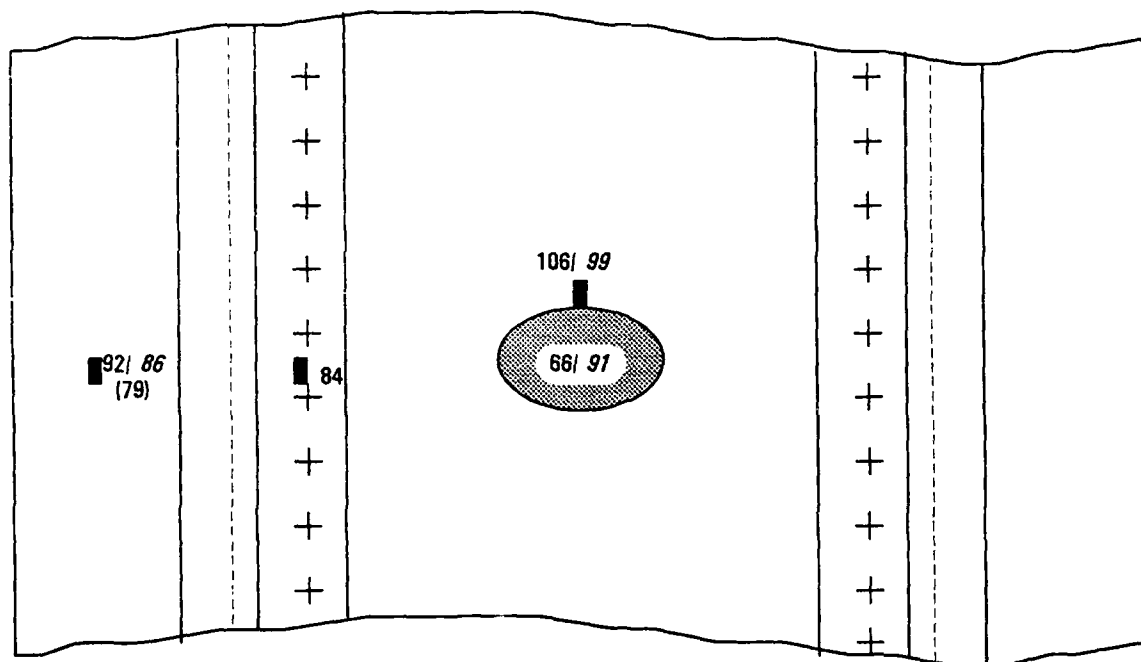

Figure 6.6. Measured/predicted stresses in the loading direction, panel #2 (double-sided patch). Parentheses indicate measured stresses from the back (non-frame) side of the panel. All stresses in MPa. Nominal skin stress = 86 MPa.

179

CALCUREP predicted higher stresses in the patch over the crack than were measured. This could result from at least two potential sources. First, the gage is located in an area of high strain gradient, and is thus averaging strain over the saw cut and areas of lower strain. Second, the model conservatively assumes that all load carried by the inclusion in stage I (uncracked) is carried by the patch in stage II. However, the less stiff cracked inclusion may attract less load. Both sources could lead to a lower measured patch stress than predicted by the model.

The plate stresses at the edge of the patch were roughly half as high (106 MPa) as in the single-sided repair (201 MPa) because of the elimination of bending. The calculations again underestimated these stresses. The error in the two-sided case was seven percent, compared with nine percent for the one-sided patch. These are considered acceptable for experimental strain measurement.

Fatigue cycling was performed at the same skin stress levels as with the first panel. Again, a few rivets in the load introduction fittings failed and were replaced by bolts. No cracking was noted in the test section.

After 50,000 cycles, symmetric 25 mm saw cuts were made in the fairing rivet line at the tips of the patch. These saw cuts were made to test the damage tolerance of the repaired panel. The saw cuts had the effect of creating three cracks with a total tip-to-tip length of 150 mm separated by 15 mm ligaments under the patch tips. An additional strain survey was made before cycling was resumed. Strain surveys were made after significant cracking events throughout damage tolerance testing.

As the new saw cuts lay between two rivets, initiation was rapid, occurring about 2,000 cycles later. Figure 6.7 shows the crack growth behavior. Both cracks grew into the next rivet holes in 8,000 cycles, after 60,000 cumulative cycles. After approximately 29,000 additional cycles, the left crack tip reinitiated, growing in a further 8,500 cycles to the next rivet hole.
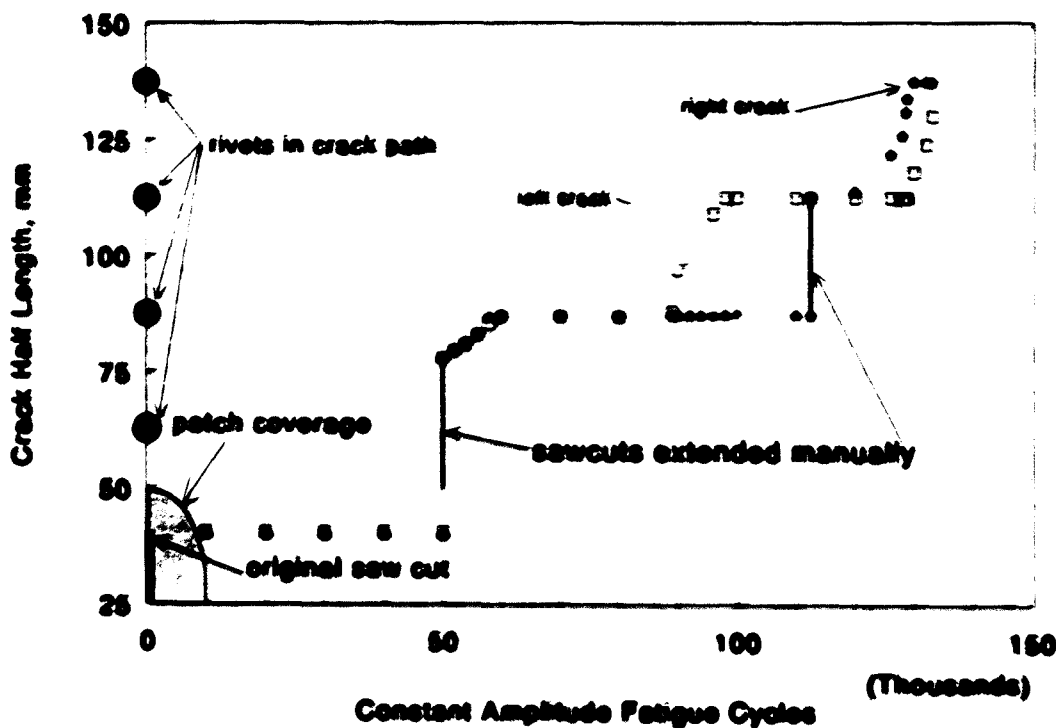
Figure 6.7. Crack growth behavior of panel #2 before and after saw cuts.

Strain gages were placed in the likely crack path on the right side of the patch. To allow for meaningful strain measurements and avoid a seriously unsymmetric test condition, the right crack was extended manually (with an additional saw cut) after 112,500 cycles. This effectively allowed the right crack to "catch up."

At 120,000 cycles, the right crack reinitiated. After 126,000 cycles, a crack was found in the lower frame at a runout of a flange connection strap, away from the test section. The crack tip was stop-drilled and the strap extended three rivets to allow resumption of fatigue testing. A strain survey showed no significant change in load distribution, and cycling was resumed.

After 130,000 cycles, as the right crack tip arrived at the fourth rivet hole in its path, the left crack reinitiated. Fatigue testing was halted after 133,000 cycles as the left crack approached its fourth rivet. The total crack length was 265 mm, one-third of the panel width. Eddy current scans indicated a through-crack in both ligaments under the patch (between the original 80 mm and the 20 mm saw cuts made at 50,000 cycles). Strain

gage data disclosed that the ligaments under the patch tips failed after the third saw cut was made at 112,500 cycles. Eddy current testing confirmed their failure.

The strains in the panel and in the patch increased steadily as the cracks grew. Figure 6.8 shows the large but highly localized influence of crack length on strain distribution. The location of the patch, fairing line rivets, tear strap and frame are included for clarity.
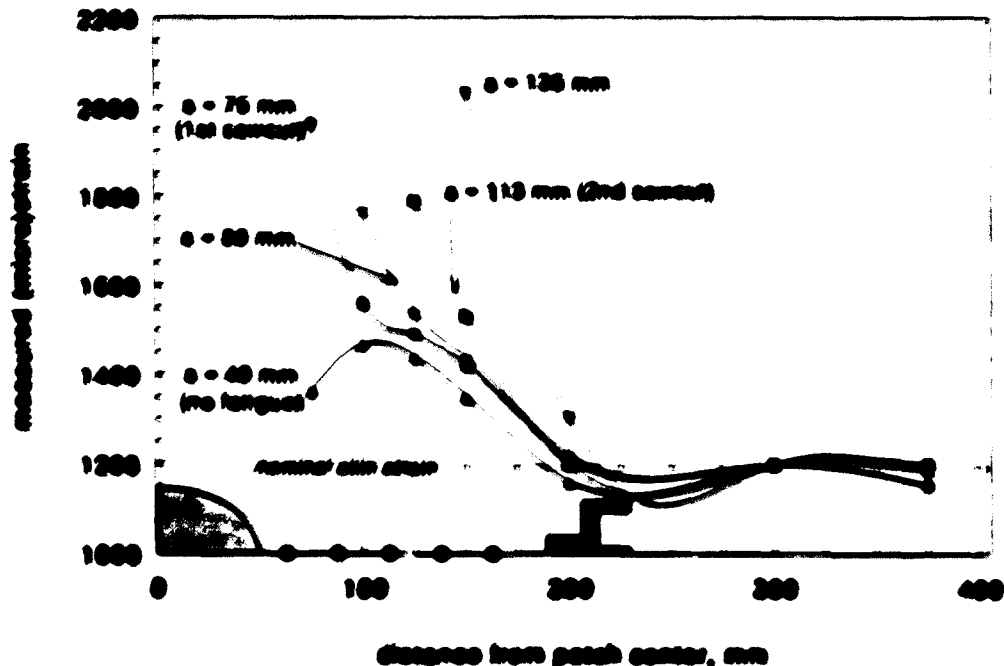
Figure 6.8 *Skin strains in the load direction across the fairing line of panel #2 at various crack lengths.*

Because the patch remained fully intact (no damage was detected after the fatigue test), it implies a large restraint on crack opening. The effective restraint is confirmed by the strain measurements, which show limited increase of the strain, unless the crack tip is close to the gage. Outside the frame, the crack length had a negligible effect on strain readings.

Figure 6.9 shows the details of the strain readings in both the patch and the skin in the area between the frames. (Note the change in scale from the previous figure.) Skin strains are indicated by filled markers, while patch strain markers are unfilled. The strain readings in the patch tip grew extremely large for crack lengths greater than 100 mm. For the longest crack, patch tip strains were more than 2.5 times as high as the strain in the

center of the patch, less than 50 mm away. The patch tip exerted a large restraining force on the crack at over 3,600 microstrain. (In spite of these very high strains, no damage was detected in the GLARE patch after fatigue testing.)
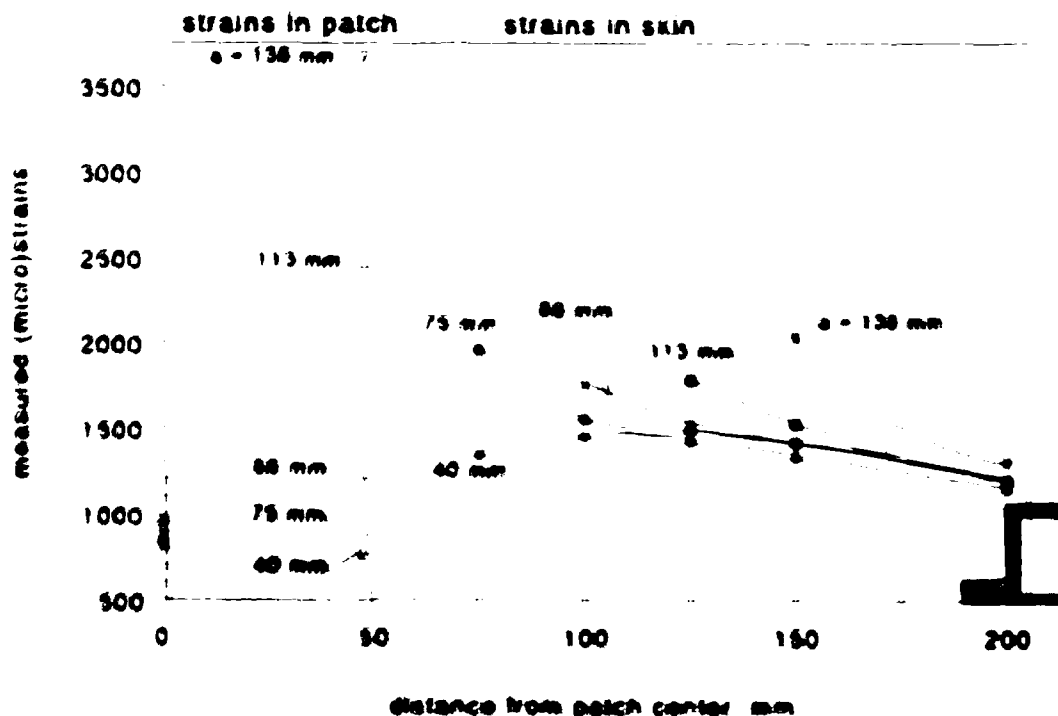
Figure 6 9   Strains in the skin and patch in the central portion of the fairing line of panel #2, various crack lengths. Skin strains are indicated by filled markers, while patch strain markers are unfilled

6.3.5 Discussion

The tests of the large stiffened panels demonstrate the durability and damage tolerance of crack patching with GLARE 2. The patches effectively prevented the large cracks from re initiating from the rivet holes without introducing fatigue or static strength problems into the structure

A noteworthy outcome of the damage tolerance test was the demonstration that the patch influenced cracks that extended beyond the patch. Figure 6 10 shows a detail of the crack growth data presented previously in figure 6 8   (Recall that these cracks grew only after additional saw cuts in the skin extended the damage outside the patched area.) The

crack growth rates between individual rivet holes were approximately constant and are indicated on the figure.
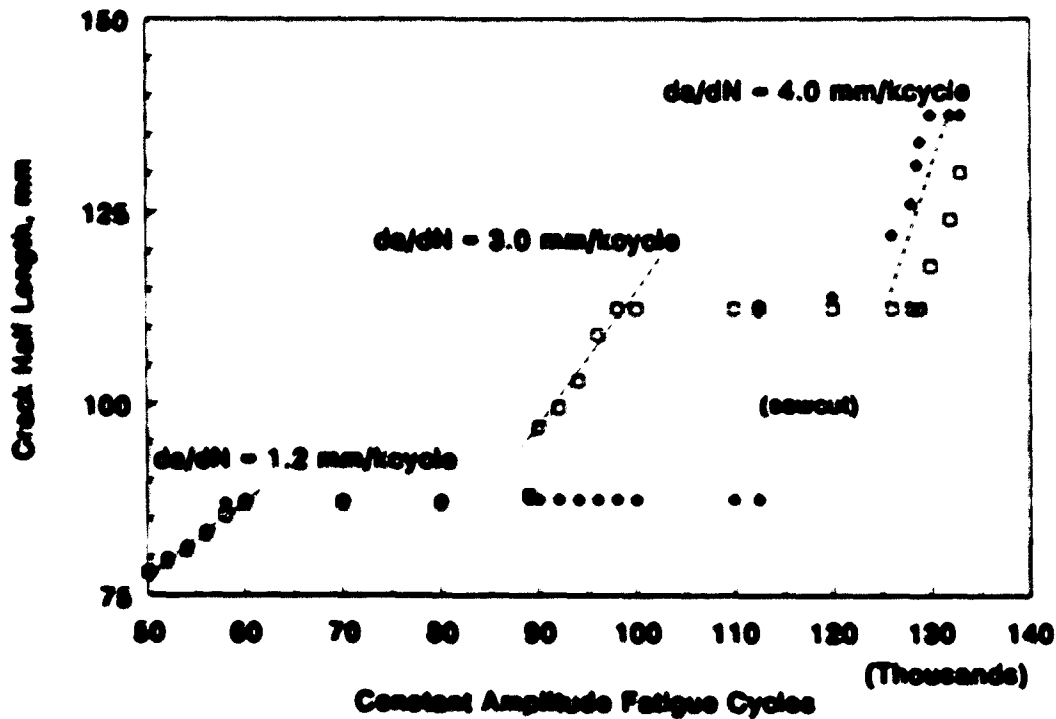
Figure 6.10. Detail of half crack length versus number of fatigue cycles in panel #2.

Calculations of the stress intensity factor of the unpatched crack were performed for various crack lengths representative of the tested panel using the Feddersen solution for a central crack in an *unstiffened* panel under remote loading:

$$\Delta K = \Delta \sigma \sqrt{\pi a} \cdot \sqrt{\sec \pi a / W}. \tag{6-1}$$

where ΔK represents the cyclic stress intensity factor,
   $\Delta \sigma$ is the applied cyclic stress (82 MPa),
   a is the crack half-length, and
   W is the panel width (900 mm).

(The effect of frame and tear straps on ΔK is felt only when the crack approaches very closely.)

Effective stress intensity factors based on the measured crack growth rates were estimated using da/dN vs. ΔK data for 7075-T6 from [3] based on a Dutch NLR test program. Table 6.5 compares the calculated unpatched unstiffened ΔK value with the effective value gleaned from the published crack growth rates.

Table 6.5. Apparent Crack Patching Effectiveness, Long Cracks.

Crack half length, mm	Unpatched ΔK, $MPa\sqrt{m}$	Empirical (patched) ΔK, $MPa\sqrt{m}$	Reduction of ΔK, percent
85	42.4	21	50
110	50.6	26	49
130	56.1	28	50

In this example, the patch exerts a large influence on the crack severity. This is true even when the crack is much larger than the patch. The stress intensity is reduced by 50 percent, which in aluminum alloys corresponds to approximately ten times lower crack growth rate. It is mainly a result of the restraint on crack opening exerted by the intact patch.

An approximation of the restraining effect of the patch can be obtained by considering the patch as an unfailed ligament between two cracks, as illustrated in figure 6.11. The extensional stiffness of the two patches was 97 percent of the uncracked sheet's Et value, so this is a reasonable assumption. It further implies zero crack opening under the patch. The Erdogan solution [5] for two collinear cracks can be expressed as:

$$\Delta K = F \Delta\sigma\sqrt{\pi a} \qquad (6.2)$$

where

$$F = 1 - 0.0017\lambda + 0.1613\lambda^2 - 0.1628\lambda^3 + 0.1560\lambda^4$$

$$\lambda = 2a^* / d$$
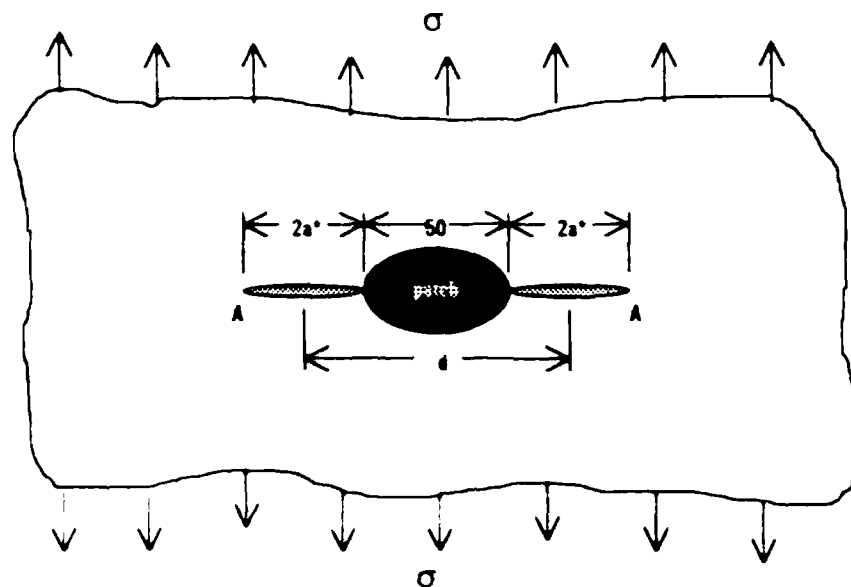
Figure 6.11. Idealization of patched crack as unfailed ligament between
two collinear cracks (after [5,6]).

The Erdogan solution leads to the ΔK values shown in table 6.6.

Table 6.6. Apparent Crack Patching Effectiveness, Long Cracks.

Crack half length, mm	Erdogan ΔK. $MPa\sqrt{m}$	Empirical (patched) ΔK. $MPa\sqrt{m}$	percent difference
85	26	21	24
110	31	26	19
130	35	28	25

The Erdogan solution consistently over-predicts ΔK by an average of 23 percent. A possible reason for this difference is the additional load carried by the frames and tear straps with longer cracks. as shown by figure 6.9. Although the strains are elevated only slightly. the cross-sectional areas of the stiffening elements are large enough to carry a significant additional load.

The high strains placed on the patch emphasizes the need for a high-strength. fatigue-resistant patch material. Monolithic aluminum patches might be problematic in such cases.

When multiple site damage exists ahead of the large patched crack. the rivet holes provide no retardation ahead of the advancing crack tip. Figure 6.12 shows what the crack

growth data from the damage tolerance portion of the test would look like if the retardation periods were removed.
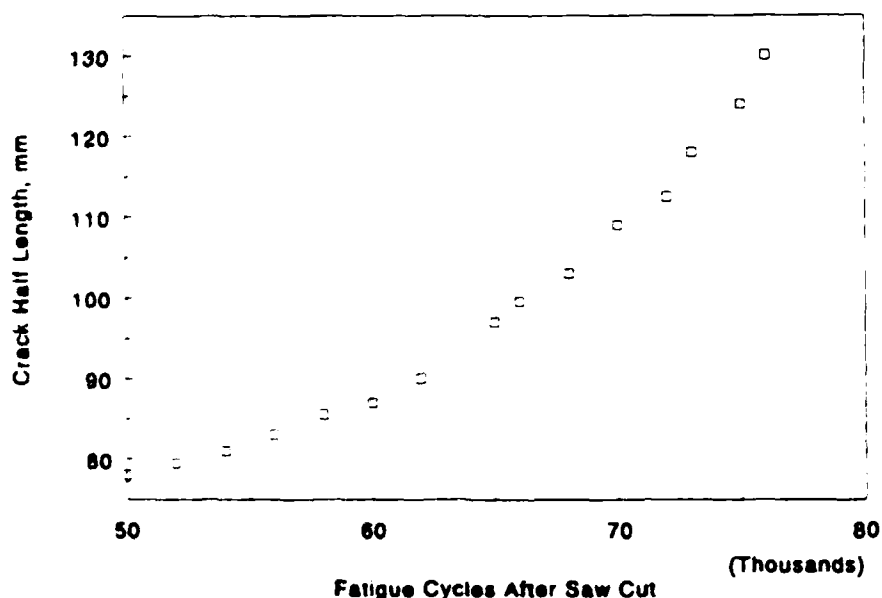
Figure 6. , 2. Hypothetical crack growth curve of two-sided patched crack plus secondary saw cut in presence of multiple site damage.

The curve shows that the useful life of the cracked patched structure (after the second saw cuts) falls sharply. However, the crack growth is still slow. The inspection interval needed to detect the crack could be quite long (say, every 5,000 flights).   without imposing too a large burden on maintenance personnel.

6.4 Summary and Conclusions

The results of static and fatigue tests have been compared with the predictions of CALCUREP in the bonded crack patching of fuselage structures.

Constant amplitude fatigue testing was performed on a series of patched saw cut 7075-T6 coupons. The test results showed:

- A range of bonded patch materials and length/width ratios provides acceptable crack-patching performance. Crack re-initiation from a properly patched panel requires hundreds of thousands of flights or manual extension by saw cuts at typical fuselage stress levels.

- A small overlap (10 mm) of each crack tip by the patch is recommended. Larger overlaps are unnecessary.

187

- Good alignment of orthotropic patches with the crack is necessary for optimum performance. However, small patch misalignments do not completely compromise patch performance.

- The static strength of a properly designed patched saw cut panel approaches the original (uncracked) strength of the panel.

- CALCUREP predicts crack tip stress intensity factors with reasonable accuracy when crack growth occurs at the edge of a patch. When cracks grow larger than the patch, accuracy diminishes quickly.

Two large (1,200 by 800 mm) stiffened panels were constructed and tested to represent a fuselage multiple site damage case taken from service. Advanced fiber metal laminate GLARE 2 patches were applied to 80 mm central saw cuts. Two patch configurations were used to simulate repair access to one and both sides of the fuselage, respectively.

Static strain surveys of the repaired panels revealed that CALCUREP is able to predict the stress state around a bonded two-sided patch repair with good accuracy. With one-sided patches, the predicted stress in the patch was not accurate. This was because the original assumption of the crack location over an intact stringer did not apply with the test configuration. As a result, significant bending occurred in the area of interest. This bending was not accounted for in the model.

Durability (fatigue) testing of the one-sided configuration at high fatigue stress levels showed no crack growth from the saw cut in ten aircraft lifetimes. Later static testing sustained the design ultimate stress of the skin.

The panel with the two-sided patch was fatigued for 50,000 cycles (five aircraft lifetimes) without experiencing any crack growth from the repaired saw cut. Additional saw cuts were then made outside the patch in line with the original damage. Fatigue testing continued for an additional 83,000 cycles while slow crack growth was monitored.

Crack growth measurements correlated with strain data showed that the patch exerted a large restraint on crack opening even when the crack had grown well beyond the patch. The Erdogan fracture mechanics solution for two collinear cracks with an intact ligament was shown to provide a reasonably good prediction of such crack growth behavior. The patch reduced the rate of crack growth of long cracks by a factor of approximately ten compared with the unpatched case.

The panel was retired when the crack reached 260 mm in length. No cracks could be found in the GLARE patch. The slow crack growth proved the damage tolerance of the crack patching concept as applied to stiffened fuselage structures.

References, Chapter 6

1. Hertzberg, R.W., *Deformation and Fracture Mechanics of Engineering Materials*, 3rd edition, John Wiley and sons, New York, 1989, p.21.

2. Paris, P.C., "Fatigue--An Interdisciplinary Approach", *Proc. 10th Sagamore Conf.,* Syracuse University Press, Syracuse, NY, 1964, p.107.

3. Broek, D., *Elementary Engineering Fracture Mechanics,* Leiden, Noordhoff International Publishing, 1974, p. 230.

4. Hertzberg, R.W., *op.cit.,* pp. 410-440.

5. Erdogan, F., "On the Stress Distribution in Plates with Collinear Cuts Under Arbitrary Loads," Proc. 4th U.S. Nat. Congr. Appl. Mech., 1962, pp.547-553.

6. Murakami, Y., *Stress Intensity Factors Handbook,* Pergamon Press, 1987, pp. 194-195.

7

Summary and Conclusions

7.1 Background and Goals of this Research

The Aloha incident was a wake-up call to the aeronautical world. It showed that transport aircraft operators need improved techniques to perform simple, economical, damage tolerant structural repairs to aircraft.

Current repair practices for fuselage structures involve almost exclusive use of riveted repairs. The current practices are in many respects inadequate and lead to fatigue problems. Simple changes to the current riveted repair procedures are needed to improve flight safety without requiring higher skill levels in maintenance or increasing life cycle costs. "Soft patching," the application of the high-strength, moderate-modulus fiber metal laminate GLARE 3 to riveted repairs, was discussed in chapters 2 and 3 as a means of accomplishing these goals.

Chapter 4 focused on bonded repairs, describing recent material and process developments that simplify the method and improve its quality. Chapter 5 presented recent developments in the analysis of bonded "crack patching" repairs. It introduced a user-friendly computer program known as CALCUREP to enable airline maintenance engineers to extend the life of fatigue-damaged fuselage components. Detailed parametric studies showed that GLARE 2 fiber metal laminates are a better choice than expensive, high-stiffness boron-epoxy composites for bonded patching of pressurized fuselage cracks. The results of fatigue and damage tolerance testing of bonded crack patching for fuselage structures were given in Chapter 6.

7.2 Soft Patching for Durable, Damage Tolerant Riveted Repairs

Current methods of riveted repair of pressurized aluminum fuselage skins result in premature fatigue cracking of the repaired skin. The result is increased inspection requirements for operators. Small improvements can be made in riveted repairs by performing time-consuming, expensive thickness tapering of patches (chapters 2 and 3).

- A new concept called "soft patching" has been introduced to improve the durability of riveted repairs. Soft patching of pressurized aluminum fuselage skins uses thin untapered patches of the fiber metal laminate GLARE 3 in place of thick tapered monolithic patches. Soft patching reduces load attraction into the repair area, diminishes bearing loads on the critical first rivet row and decreases secondary bending in the skins.

- Soft patching improves the fatigue life of riveted repairs by up to three times over various techniques involving monolithic patches. It simplifies the repair task by eliminating the need for costly, time consuming thickness tapering of patches. Inspection workloads are reduced while safety and damage tolerance are improved and life cycle costs are diminished.

7.3 Surface Treatments for In-Field Bonded Repairs

The basics of adhesive bonded repairs for aluminum aircraft fuselages have been presented, with emphasis on the practical aspects (chapter 4).

- An extensive evaluation of surface preparation techniques showed the Boeing Phosphoric Acid Containment System (PACS) plus adhesive priming to be the superior aluminum surface preparation for in-field repair. PACS combines excellent durability with the highest peel strength values of any non-immersion pretreatment process.

- A newly developed epoxy film adhesive with the ability to be stored for long periods at room temperature was investigated for potential use in bonded repairs. AF-377-2M was evaluated for strength and durability using the high-performance toughened epoxy film AF-163-2K as a comparison. A long shelf life at room temperature is highly

192

beneficial in the maintenance environment. However, the low peel strength of the current formulation of AF-377-2 makes it less desirable as a metal repair adhesive. The more conventional epoxy film adhesive AF-163-2K was carried over for the remaining bonded repair research performed in this effort.

7.4 Bonded Crack Patching

Crack patching is a technique originally developed to extend the life of cracked thick structures on fighter aircraft. In its original applications, boron/epoxy and carbon/epoxy composites have been used successfully in a variety of *high-value repairs*. Recently, similar boron/epoxy repairs have been proposed for repairing pressurized transport fuselages suffering from multiple site damage. However, the structural and operational characteristics of transport aircraft are sufficiently different from fighters to cause doubt whether direct substitution of the processes will be successful.

Transport fuselages experience high loads at cruise altitudes over 10 km, where temperatures are lowest. The Rose model of crack patching was extended to include thermal effects of cruise altitude and bending stresses in the plate at the tip of one-sided reinforcements (chapter 5).

The expanded Rose model was transformed into a user-friendly program suitable for airline maintenance use. This program, called CALCUREP, enables rapid analysis of bonded crack patching repairs on a personal computer. Only limited knowledge of loads and design stresses is required to carry out preliminary patch designs.

- An extensive parametric study of various patch materials and configurations was performed. It indicated the patch coefficient of thermal expansion was the single most important *parameter in determining the overall effectiveness of a bonded crack patching repair*. The fiber metal laminate GLARE 2 proved more effective than high modulus composites in reducing the stress intensity factor of a crack in a fuselage.

- High modulus, low thermal expansion coefficient patches such as boron and carbon result in very high adhesive shear strain levels. These high shear strains are expected to cause poor long-term durability of such patches. Monolithic aluminum was an acceptable alternative in situations where two-sided patching was possible, though a

thicker patch was required. Titanium alloys suffer from similar thermal expansion drawbacks as the composites.

• The use of one-sided GLARE and monolithic aluminum patches causes relatively high stresses that result in the surrounding plate. Tapering of the edges of the GLARE patch sufficiently alleviates the high stresses such that new fatigue cracks are not expected. However, even tapered one-sided 2024-T3 patches cause unacceptably high plate stresses and thus are not recommended for fuselage skin repair.

• Studies of the effect of patch geometry on effectiveness showed that a broad range of elliptical patch sizes perform adequately. Variations in adhesive thickness and shear modulus were shown to have only minor influences on patch parameters.

• Analysis of the effect of cure temperature on patch performance showed that high modulus patch materials like boron, carbon and titanium could not benefit from reduced cure temperatures. Cure temperatures in the range from 100 to 120°C gave the best effectiveness for the GLARE patches.

The results of static and fatigue tests have been compared with the predictions of CALCUREP in the bonded crack patching of fuselage structures (chapter 6). Constant amplitude fatigue testing was performed on a series of patched saw cut 7075-T6 coupons. The test results showed:

• A range of bonded patch materials and length/width ratios provides acceptable crack-patching performance. A small overlap (10 mm) of each crack tip by the patch is recommended. Crack re-initiation from a properly patched panel requires hundreds of thousands of flights at typical fuselage stress levels.

• The static strength of a properly designed patched saw cut panel approaches the original (uncracked) strength of the panel.

• CALCUREP predicts crack tip stress intensity factors with reasonable accuracy when crack growth occurs at the edge of a patch. When cracks grow larger than the patch, accuracy diminishes quickly. In such cases, the Erdogan solution for two collinear cracks is quite suitable.

Two large stiffened panels were constructed and tested to represent a fuselage multiple site damage case taken from service. Advanced fiber metal laminate GLARE 2 patches were applied to 80 mm central saw cuts. Two patch configurations were used to simulate repair access to one and both sides of the fuselage, respectively.

- CALCUREP is able to predict the stress state around a bonded two-sided patch repair with reasonable accuracy. With one-sided patches, the predicted stress in the patch was not accurate. This was because the original assumption of the crack location over an intact stringer did not apply to the tested configuration. As a result, significant bending occurred in the area of interest that was not modeled.

- Durability testing of the one-sided configuration at high fatigue stress levels showed no crack growth from the saw cut in ten aircraft lifetimes. Subsequent static testing sustained the design ultimate stress of the skin.

- Damage tolerance testing of a stiffened panel showed a two-sided patch could withstand large artificial damage (saw cuts) outside the patch. Fatigue testing demonstrated slow, stable crack growth behavior and verified the damage tolerance of the crack patching concept as applied to stiffened fuselage structures.

7.5 Recommendations for Further Research

The present research has clearly revealed the advantages of soft patching as a damage tolerant fuselage repair technique leading to durable restorations of structural integrity. These favorable results were confirmed by analysis and testing, which led to a good understanding of the variables involved. At the same time, simple techniques were developed for the practical application of soft patching.

The experience with soft patching should be extended in an experimental and analytical program to cover a wider variety of structural configurations. For example, the crown section and window belt should be considered, along with a larger variation of loading cases (e.g. biaxial loading and curved panels). Results from barrel tests (simulated fuselages) would be most worthwhile.

For *bonded crack patching repairs*, the computer program CALCUREP can be improved and expanded to include directly the influence of thickness tapering on load attraction and bending at the edge of the patch. Buckling induced by local heating during cure should be investigated to establish maximum allowable cure temperatures.

Finally, an investigation into crack patching effectiveness on multiple short cracks in riveted fuselage lap joints (the multiple site damage problem) should be carried out.

Samenvatting (Dutch Summary)

De luchtvaartmaatschappijen hebben betere technieken nodig om eenvoudige en 'schade toelaatbare' reparaties uit te voeren. Vooral de ongelukken met de 747 van Japan Air Lines en de 737 van Aloha Airlines hebben dit duidelijk gemaakt. Momenteel worden bij de reparaties van rompconstructies bijna uitsluitend klinkverbindingen toegepast. De huidige praktijken zijn in veel opzichten onvoldoende veilig en kunnen leiden tot vermoeiingsproblemen.

Er zijn eenvoudige wijzigingen nodig in de huidige procedure voor geklonken reparaties, waardoor de vliegveiligheid verhoogd kan worden, zonder dat dit onderhouds-vaardigheden van een hoger niveau of toenemende kosten met zich meebrengt. Dit concept, bekend als *"soft patching"*, maakt gebruik van het vezel-metaal laminaat GLARE-3 in geklonken reparaties. GLARE-3 heeft een hoge sterkte en een relatief lage elasticiteitsmodulus, waardoor het materiaal uitmate geschikt is voor deze toepassing. *Soft patching* reduceert de doorleiding van de belasting in het gerepareerde gebied, verlaagt de belasting op de kritieke eerste klinknagelrij en vermindert de secundaire buiging in de huid. Als gevolg hiervan neemt de levensduur van geklonken reparaties toe, tot drie maal de waarde voor monolitisch reparatiemateriaal. Het vereenvoudigt het reparatiewerk doordat het arbeidsintensieve afschuinen van de randen van de *patches* niet meer nodig is. De duur van de inspectiewerkzaamheden kan worden verminderd, terwijl de veiligheid- en schadetolerantie groter worden en de totale kosten afnemen.

Het tweede deel van dit proefschrift richt zich op geavanceerde gelijmde reparaties, en beschrijft recente ontwikkelingen in materialen en processen die de reparatie vereenvoudigen en de kwaliteit verhogen. Dit deel behandelt verder de recente ontwikkelingen in de spanningsanalyse van gelijmde *"crack patching"* reparaties. *Crack patching* is een techniek die oorspronkelijk is ontwikkeld om de levensduur van gescheurde dikwandige constructies van jachtvliegtuigen te vergroten. Oorspronkelijk werden boron-epoxy en koolstof-epoxy composieten succesvol gebruikt in verscheidene reparaties van zwaarbelaste constructies. Dit proefschrift beschrijft nieuwe analyse-methodes, waaronder een gebruikersvriendelijk computerprogramma onder de naam CALCUREP. Deze methodes moeten de onderhoudsingenieur in staat stellen om op een eenvoudige en goedkope manier de levensduur van rompcomponenten met vermoeiingsschade te verlengen.

Gedetailleerde parametrische studies hebben aangetoond dat GLARE-2 vezel-metaal laminaten als patch-materiaal geschikter zijn dan de dure, hoge-stijfheid boron-epoxy composieten. Een van de oorzaken hiervan is het feit dat door de lage temperatuur op kruishoogte de thermische uitzettingscoëfficiënt van het patchmateriaal een belangrijke factor is bij de materiaalkeuze. De resultaten die werden berekend met het CALCUREP computermodel werden vergeleken met testresultaten van proefstukken die gescheurde rompconstructies simuleerden. Het blijkt dat CALCUREP in staat is om de spannings-verdeling rond een reparatie accuraat te berekenen.

Curriculum Vitae

Robert Fredell was born 10 May 1960 in Sacramento, California. After graduating from high school in 1978 as a Presidential Scholar and National Merit Scholar, he entered Oklahoma State University in Stillwater, Oklahoma, where he studied Mechanical and Aerospace Engineering and participated in the Air Force Reserve Officer's Training Corps. He graduated with a Bachelor of Science degree in Mechanical Engineering (Aerospace Option) and was commissioned a Regular Officer in the United States Air Force in December, 1982.

As a Second Lieutenant, he earned a Master of Science degree in Mechanical Engineering at Oklahoma State in 1983, under the sponsorship of the Air Force Institute of Technology. In 1984, he was transferred to Wright-Patterson Air Force Base, Ohio, where he worked as a corrosion engineer at the Air Force Acquisition Logistics Center on various aircraft systems including the C-17 and the Advanced Tactical Fighter (now the YF-22). As a First Lieutenant, he worked as a project engineer in the Air Force Flight Dynamics Laboratory, directing the application of advanced metallic structures to the solution of durability problems on the F-111 and A-10 aircraft.

After promotion to Captain, the author was assigned to the Air Force Materials Laboratory, where he co-developed and managed a program with the Northrop Corporation that flew several hundred advanced composite parts on operational USAF F-5 and T-38 aircraft. In 1988, he was transferred to the United States Air Force Academy in Colorado Springs, Colorado. There he served as an Instructor and later an Assistant Professor in the Department of Engineering Mechanics.

In 1991, he moved to Delft, the Netherlands, to begin his doctoral studies under the sponsorship of the Air Force Institute of Technology. There he joined the Fiber Metal Laminates project of the Production and Materials group within the Faculty of Aerospace Engineering. After completion of his dissertation, he rejoined the Department of Engineering Mechanics at the U.S. Air Force Academy as an Assistant Professor.

The author is married to the former Kristine Elizabeth Oppermann of Colorado Springs. In his free time, he enjoys traveling, reading and downhill skiing.

A

Analysis of Crack Patching:
Fundamentals of Adhesive Joints
Stage I of the Rose Model

This section develops the mathematical background necessary for the analysis of crack patching. The analysis used here is based the one-dimensional theory of bonded joints developed by Hart-Smith [1], and proceeds to stage I of the model developed by Rose.

The analysis is divided into two parts. In this appendix, a bonded doubler is considered mathematically in place over an uncracked skin. The aim of the first stage is to calculate the stress redistribution in the plate (skin) in the presence of the bonded doubler. In stage two (appendix B), the crack is introduced into the plate and the crack faces become stress-free. The main concern at that point is to calculate the stress intensity factor in the repaired cracked plate.

The Rose model of crack patching is a continuum analysis based on theory of elasticity. It considers an infinite, center-cracked, orthotropic plate with a bonded orthotropic elliptical patch on one side of the plate. The plate is loaded by a remote biaxial stress.

The elliptically shaped reinforcing patch is an efficient shape for transferring load through an adhesive. The ellipse greatly simplifies the elastic analysis. Rectangular patches, preferred in riveted repairs and used in some bonded repairs, result in high peel stresses at the patch corners. This can lead to delamination, which results typically in an elliptically shaped bond remaining intact.

As stated previously, the model divides the analysis into two stages. The first stage considers the redistribution of loads caused by a doubler bonded to an uncracked plate. The adhesive bond is assumed to be rigid; that is, no relative displacement happens between the plate and the reinforcement. The load-transfer zone is small with respect to

the patch, and the reinforced region is treated as a stiff inclusion in center of an infinite plate. This stage makes use of the inclusion analogy first formulated by Muki and Sternberg [2] to calculate the redistribution of stresses in the plate.

Figure A.1 shows a cracked infinite plate subjected to remote biaxial stresses denoted P and Q, in the x- and y-directions, respectively. The length of the reinforcement is 2a, the width is 2b. The crack length is represented as $2a_c$.
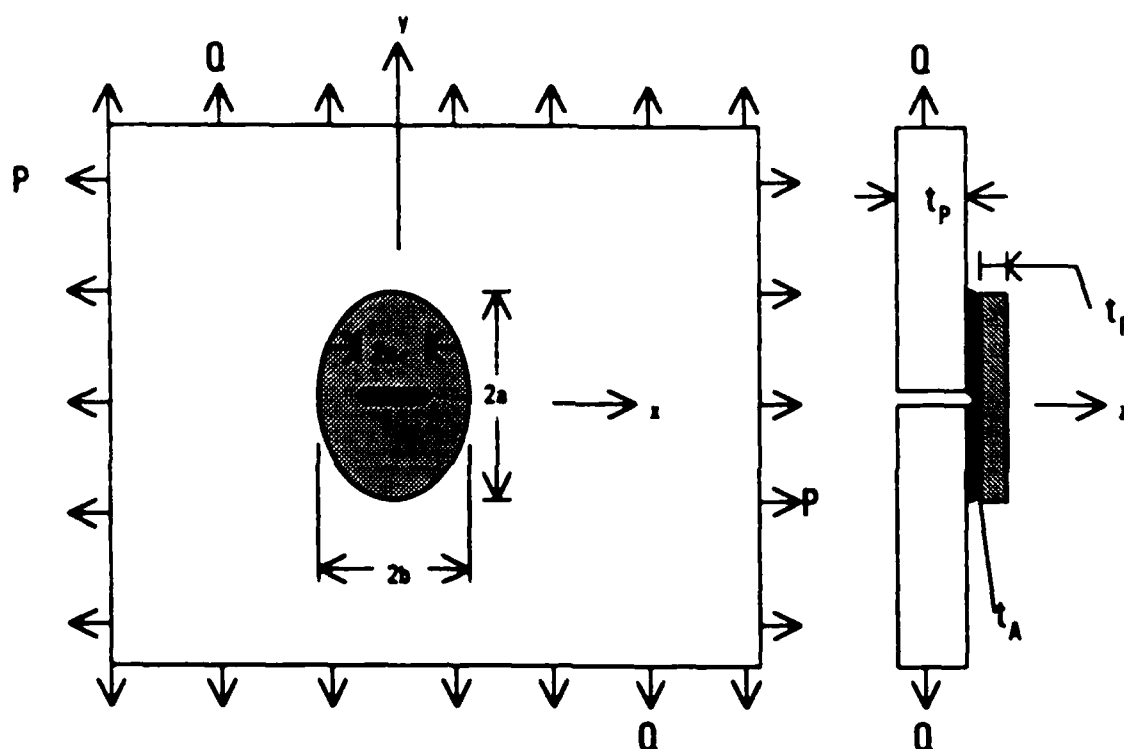
Figure A.1. Bonded Repair Configuration Analyzed in Rose Model.

Most fatigue cracks in pressurized fuselages occur as a result of first principal stress, which corresponds to the x- or hoop direction in the model. The y-direction is parallel to the longerons.

Throughout the analysis, subscripts will refer to parameters identified with the plate (P), reinforcing patch (R) and adhesive (A). Thus, t_P, t_R and t_A denote the respective thicknesses of the plate, repair patch and adhesive layer, etc.

The analysis is based on the following assumptions:

- All material behavior is linearly elastic, except for limited elastic-plastic deformation in the adhesive layer restricted to an area very near the crack, as discussed in section 5.2.2.2. Hooke's law applies to the analysis.

- All plate and patch materials are in a state of generalized plane stress. No through-the-thickness variation occurs in the basic analysis.

- The adhesive layer behaves as a linear shear spring. Shear load transfer through the adhesive is discussed in section 5.2.2.2.

- The basic model ignores thermal stresses due to bonding or cruise altitudes. Thermal effects are addressed in section 5.2.5.

- Bending along the crack because of the shift in neutral axis from the one-sided patch is restrained by the substructure. This assumption is considered reasonable, considering the common occurrence of fatigue damage at lap joints, fairing attach lines, etc., which are generally riveted to longerons or other longitudinal stiffeners. Expressions describing the bending at the reinforcement boundaries, where such substructure is absent, are derived in section 5.2.6.

Load Transfer in Bonded Joints A brief introduction to the load transfer in bonded joints was given in chapter four. In the analysis of crack-patching, two regions of shear load transfer must be distinguished. The first is the zone at the edge of the patch. It must be relatively small compared with overall patch dimensions to allow valid application of the rigid bond assumption in stage I. This zone is easily made non-critical in practice by tapering the patch to relieve bending in the plate and reduce peel and shear stresses in the adhesive. The second and more critical load transfer zone is around the crack. Thickness tapering is impossible here; consequently, shear stresses are highest in this region.

The calculation of the load-transfer zones can be reduced to the solution of an ordinary differential equation. Consider the one-dimensional bonded single lap joint shown in figure A.2. It shows semi-infinite strips of unit width with extensional stiffnesses $E_{yP}t_P$, $E_{yR}t_R$.
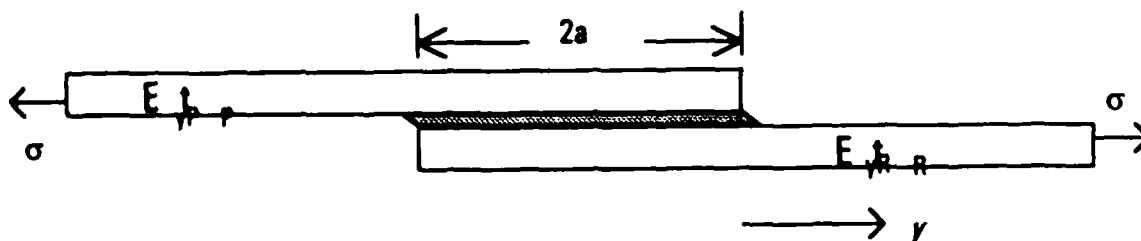
Figure A.2. bonded single lap joint configuration.

In one-dimensional lap joint theory, variation of stress and displacement in the y-direction are ignored [3].

Let $F(x,y)$ denote the shear traction per unit area exerted by the adhesive layer on the reinforcement at the point (x,y). This surface traction can be replaced by a body force distributed uniformly across the thickness of each adherend. The adhesive layer will induce equal and opposite shear tractions to the adjoining plate and reinforcement. From the corresponding body forces, $-F/t_P$ and F/t_R respectively, the differential equation of equilibrium can be derived:

$$\sigma'_{yP} = \frac{F_y}{t_P} \qquad \text{(A-1a)}$$

$$\sigma'_{yR} = \frac{F_y}{t_R} \qquad \text{(A-1b)}$$

The adhesive layer is modeled as a shear spring, resulting in a shear traction per unit length of:

$$F_y = \frac{G_A}{t_A} [v_{yP} - v_{yR}] \qquad \text{(A-2)}$$

where G_A is the elastic shear modulus of the adhesive,

t_A is the adhesive thickness layer, and

$v_{yP,yR}$ are the respective displacements of the plate and reinforcement (patch) in the y direction.

Hooke's law for a one-dimensional orthotropic elastic strip yields the following relationships for the normal stress σ_y:

$$\sigma_{yP} = E_{yP} v'_{yP} \qquad \text{(A-3a)}$$

$$\sigma_{yR} = E_{yR} v'_{yR} \qquad \text{(A-3b)}$$

where E_{yP}, E_{yR} are the respective elastic moduli in the x direction.

Differentiating (A-2) twice with respect to y and substituting from (A-3) leads to

$$F_y'' = \frac{G_A}{t_A} [\frac{\sigma_{yP}'}{E_{yP}} - \frac{\sigma_{yR}'}{E_{yR}}]$$
(A-4)

Substituting from (A-1), one arrives at

$$F_y'' = \frac{G_A}{t_A} [\frac{F_y}{E_{yP} t_P} + \frac{F_y}{E_{yR} t_R}]$$
(A-5)

which can be rewritten as the differential equation

$$F_y'' - \Lambda^2 F_y = 0$$
(A-6)

where

$$\Lambda^2 = \frac{G_A}{t_A} [\frac{1}{E_{yP} t_P} + \frac{1}{E_{yR} t_R}]$$
(A-7)

Equation A-6 is a second order linear homogeneous differential equation with constant coefficients. Its solution take the form of $F_y = e^{ry}$. Its roots are real and unequal:

$$r^2 = \Lambda^-$$
(A-8a)

$$r = \pm \Lambda$$
(A-8b)

The general solution of A-6 is of the form:

$$F_y = c_1 e^{\Lambda y} + c_2 e^{-\Lambda y}$$
(A-9)

The constants must be solved for using the boundary conditions. The first case considered will be at the edge of the patch (y = a, x = 0).

Figure A.3 shows the configuration of an infinite strip with extensional stiffness $E_{yP} t_P$ reinforced with a strip of length 2a and extensional stiffness $E_{yR} t_R$. Both have unit width.
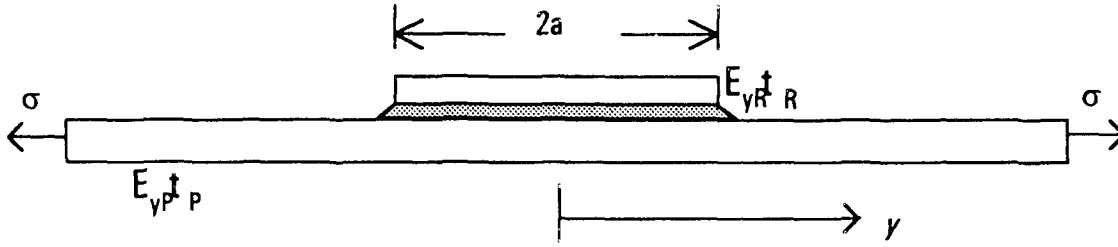
Figure A.3. Model for load transfer at edge of bonded patch.

Because of symmetry, F_y is odd in y [4]. At the edges of the patch, the stresses in the patch are zero. Using (A-2) and (A-3), and the boundary condition that $F_y(y) = -F_y(-y)$, the following is true:

$$F_y'(y = \pm a) = \frac{G_A}{t_A}\frac{\sigma_{yP}}{E_{yP}}$$

(A-10)

where σ_{yP} denotes the remote unidirectional stress in the y direction. Looking at equation A-9 and the first boundary condition, one sees that $C_1 = -C_2 (= C)$.

Thus:

$$F_y = C(e^{\Lambda y} - e^{-\Lambda y})$$

(A-11)

Application of the second boundary condition enables the solution of C:

$$F_y'(y = a) = C\Lambda(e^{\Lambda a} + e^{-\Lambda a})$$

$$\Rightarrow C = \frac{G_A}{t_A}\frac{1}{\Lambda(e^{\Lambda a} + e^{-\Lambda a})}\frac{\sigma_{yP}}{E_{yP}}$$

(A-12)

The general solution of equation A-6 is thus:

$$F_y = \frac{G_A}{t_A}\frac{\sigma_{yP}}{E_{yP}}\frac{e^{\Lambda y} - e^{-\Lambda y}}{\Lambda(e^{\Lambda a} + e^{-\Lambda a})} = \frac{G_A}{t_A}\frac{\sigma_{yP}}{E_{yP}}\frac{1}{\Lambda}\frac{sinh(\Lambda y)}{cosh(\Lambda y)}$$

(A-13)

Equation A-13 indicates that the shear stress in the adhesive can be expressed as a function decaying exponentially from the overlap ends. (The analysis for the region around the crack, presented in Appendix B, is identical.)

A-6

where $1/\Lambda$ is known as the *lap joint load transfer length*

$$\frac{1}{\Lambda} = (\frac{t_A}{G_A} [\frac{E_{yP} t_P E_{yR} t_R}{E_{yP} t_P + E_{yR} t_R}])^{1/2} \qquad\qquad \text{(A-14)}$$

For typical aluminum alloy fuselage skin thicknesses and epoxy film adhesives, this transfer length turns out to be in the range of three to five millimeters. An assumption of the analysis is that the load transfer effectively occurs over the load transfer length $1/\Lambda$, which must be small with respect to the overall patch dimensions to allow valid use of the rigid bond assumption in stage I of the Rose model.

Stage I---Inclusion Analysis The Rose method [5,6] identifies two means of achieving reductions of the stress intensity factor K. The first reduction comes from the overall effect of the doubler, which diminishes local plate stresses by sharing the load. In stage I, no crack exists in the plate, and adhesive bonds are assumed to be rigid.

The item of highest interest is the plate stress in the region of the doubler, σ_o. To determine the stress redistribution in the reinforced uncracked plate, the following steps are necessary:

- determination of the elastic constants of the equivalent inclusion,
- determination of the stress in the equivalent inclusion, and
- determination of the load sharing between the plate and reinforcement.

Figure A.4 shows a sketch of the orthotropic uncracked plate of thickness t_P under consideration. A reinforcement of thickness t_R is rigidly bonded to the plate. Out-of-plane bending caused by the eccentricity of the patch is ignored. By considering a two-dimensional idealization of the problem, stresses and displacements can be determined by using the equations of generalized plane stress.
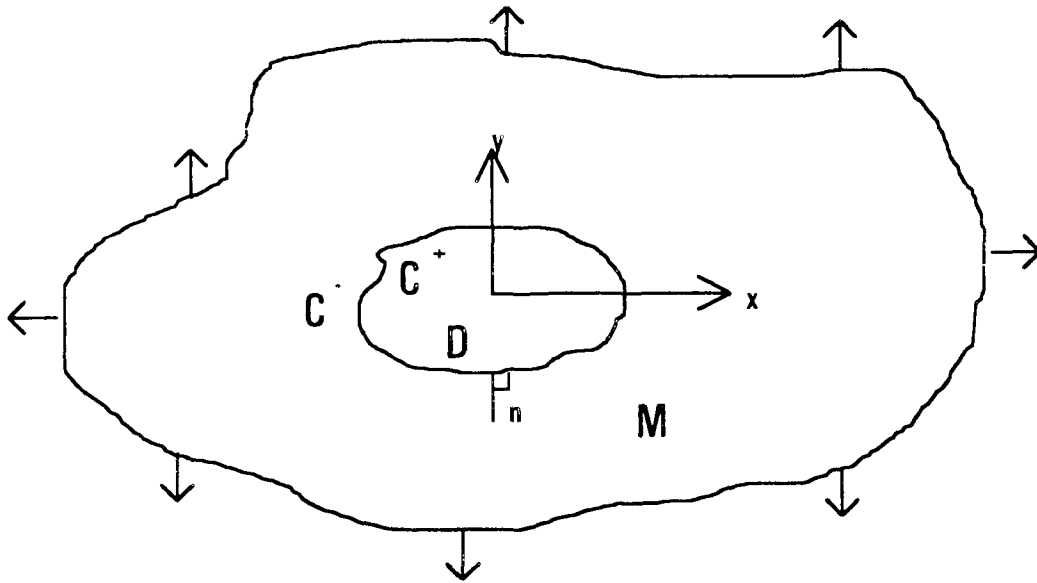
Figure A.4. Inclusion analogy model of patched uncracked plate.

A separate system of notation will be introduced to keep consistency with the literature. *D* denotes the area covered by the reinforcement, called the *inclusion,* bounded by the curve *C.* The region outside the reinforcement is called the *matrix* (denoted *M). C⁺* and *C⁻* indicate the direction of approach to the boundary, as noted in the figure. The normal to *C* is called *n.*

The components of stress and displacement are indicated using the subscripts x and y. Repeated subscripts indicate a summation, while a comma denotes partial differentiation with respect to the subscript following the comma. The sub- and superscripts R and I indicate the reinforcing patch and inclusion, respectively, while P indicates the plate.

The inclusion analogy is based on the concept that the reinforced region *D* can be replaced by an elastically equivalent inclusion I without altering the stress or displacement conditions in the matrix M.

The following assumptions apply:

- the adhesive layer transmits shear load by exerting equal and opposite shear tractions on the adjoining plate and reinforcement,

- the shear tractions are replaced by body forces having the same resultant force, which is distributed uniformly through the thickness, and

- the theory of generalized plane stress will be used to determine average stresses.

Let F(x,y) represent the shear traction per unit area at the point (x,y). Replacement of the shear tractions with body forces leads to $-F/t_P$ and F/t_R in the plate and reinforcement, respectively. The equilibrium equations are:

$$\sigma_{xy,x}^P(D) = \frac{F_y}{t_P} \qquad \text{(A-15a)}$$

$$\sigma_{xy,x}^R(D) = \frac{F_y}{t_P} \qquad \text{(A-15b)}$$

The original reinforced region D is now replaced by a hypothetical inclusion of thickness t_I having the same shape *D* and boundary *C* of the original patch. The inclusion assumes the individual load-bearing duties of the original plate and reinforcing patch. Thus,

$$t_I \sigma_{xy}^I(D) = t_P \sigma_{xy}^P(D) + t_R \sigma_{xy}^R(D) \qquad \text{(A-16)}$$

Differentiation of A-16 with respect to x and substitution into A-15 yields:

$$t_I \sigma_{xy,x}^I = t_P \sigma_{xy,x}^P(D) + t_R \sigma_{xy,x}^R(D) \qquad \text{(A-17)}$$
$$= F_y - F_y = 0$$

So,

$$\sigma_{xy,x}^I(D) = 0 \qquad \text{(A-18)}$$

and equilibrium is satisfied, as no unreacted body forces are acting within the hypothetical inclusion. The inclusion stresses are the result of the tractions T_y acting on the boundary *C*:

$$T_y^I(C) = t_I \sigma_{y,x}^I(C^+) n_x \qquad \text{(A-19)}$$

The inclusion must satisfy certain boundary conditions that follow from compatibility to validate the analogy:

$$T_y^I(C) = -t_P \sigma_{y,x}(C^-) n_x$$

$$\qquad \text{(A-20)}$$

$$v^I(C^+) = v^P(C^-)$$

That is, for the inclusion analogy to be true, step changes in the displacement **v** and the tractions **T** cannot occur at the boundary *C*. If the above boundary conditions are met, the reinforced area can truly be called an inclusion with distinct constitutive properties from the matrix.

To satisfy the first condition, an appropriate thickness value t_I must be chosen such that continuity of tractions exists. This will be explained further on the following pages. The second boundary condition (displacements) is satisfied by the rigid bond assumption. From this, it follows that the displacement field remains constant:

$$v^I(D) = v^P(D) = v^R(D) \qquad \text{(A-21)}$$

Thus, the inclusion analogy can be used in crack patching analysis. What remains is the derivation of the elastic constants of the equivalent inclusion. In the following section, the superscripts P, R, and I will revert to subscripts.

Elastic constants of the equivalent inclusion Consider an orthotropic plate under generalized plane stress [7]. An orthotropic plate has three planes of elastic symmetry with respect to an orthogonal coordinate system, greatly reducing the complexity of the stress-strain relationships. The assumption of plane stress, which ignores through-the-thickness stress variations, further simplifies the analysis. Four independent elastic coefficients remain: the principal Young's moduli E_x and E_y, the major Poisson's ratio $\nu(= \nu_{xy} = \nu_{yx})$, and the shear modulus G ($= G_{xy} = G_{yx}$) . The stress-strain equations for an orthotropic plate under generalized plane stress take the form:

$$\begin{bmatrix} \sigma_x \\ \sigma_y \\ \tau_{xy} \end{bmatrix} = \begin{bmatrix} A_x & \nu A_y & 0 \\ \nu A_x & A_y & 0 \\ 0 & 0 & 2G \end{bmatrix} \begin{bmatrix} \varepsilon_x \\ \varepsilon_y \\ \gamma_{xy} \end{bmatrix} \qquad \text{(A-22)}$$

where

$$A_x = \frac{E_x}{1 - v_{xy} v_{yx}}, A_y = \frac{E_y}{1 - v_{xy} v_{yx}}$$

(A-23)

Equations A-22 and A-23 apply to both an orthotropic plate and reinforcement. From symmetry, one can conclude:

$$\frac{v_{xy}}{E_x} = \frac{v_{yx}}{E_y}$$

(A-24)

Determination of the elastic constants of the *inclusion follows from substitution into* equation A-16. With respect to σ_x:

$$\sigma_{xI} t_I = \sigma_{xP} t_P + \sigma_{xR} t_R$$

(A-25)

Substitution into the stress-strain relationship of equation A-22 yields:

$$A_{xI} t_I \varepsilon_{xI} + v_I A_{yI} t_I \varepsilon_{yI} = A_{xP} t_P \varepsilon_{xP} + v_P A_{yP} t_P \varepsilon_{yP} + A_{xR} t_R \varepsilon_{xR} + v_R A_{yR} t_R \varepsilon_{yR}$$ (A-26)

The rigid bond assumption causes all strains to be equal at a given (x,y). Hence,

$$A_{xI} t_I \varepsilon_x + v_I A_{yI} t_I \varepsilon_y = A_{xP} t_P \varepsilon_x + v_P A_{yP} t_P \varepsilon_y + A_{xR} t_R \varepsilon_x + v_R A_{yR} t_R \varepsilon_y$$

(A-27)

Equation A-27 must be true for any ε_x and ε_y. Consider $\varepsilon_x = 0$:

$$v_I A_{yI} t_I = v_P A_{yP} t_P + v_R A_{yR} t_R$$

(A-28)

$$v_I = \frac{v_P A_{yP} t_P + v_R A_{yR} t_R}{A_{yI} t_I}$$

(A-29)

For $\varepsilon_y = 0$, the solution procedure is similar:

$$A_{xI} = \frac{A_{xP} t_P + A_{xR} t_R}{t_I}$$

(A-30)

Equation A-16 can be considered with respect to σ_y:

$$\sigma_{yI} t_I = \sigma_{yP} t_P + \sigma_{yR} t_R \qquad \text{(A-31)}$$

Substituting the stress-strain relationship from equation (A-22) with the rigid bond assumption yields the equation:

$$A_{yI} t_I (v_I \varepsilon_x + \varepsilon_y) = A_{yP} t_P (v_P \varepsilon_x + \varepsilon_y) + A_{yR} t_R (v_R \varepsilon_x + \varepsilon_y) \qquad \text{(A-32)}$$

Setting ε_x to zero,

$$A_{yI} = \frac{A_{yP} t_P + A_{yR} t_R}{t_I} \qquad \text{(A-33)}$$

Substitution of A-33 into A-29 gives:

$$v_I = \frac{v_P A_{yP} t_P + v_R A_{yR} t_R}{A_{yP} t_P + A_{yR} t_R} \qquad \text{(A-34)}$$

Consider equation A-16 with respect to τ_{xy}:

$$\tau_{xyI} t_I = \tau_{xyP} t_P + \tau_{xyR} t_R \qquad \text{(A-35)}$$

Consistent with the preceding calculations,

$$2 G_I \gamma_{xy} t_I = 2 G_P \gamma_{xy} t_P + 2 G_R \gamma_{xy} t_R$$

simplifying gives

$$G_I = \frac{G_P t_P + G_R t_R}{t_I} \qquad \text{(A-36)}$$

The elastic constants of the equivalent inclusion are summarized in Table A.1.

Table A.1. Elastic constants of the equivalent inclusion.

$$A_{xI} = \frac{A_{xP} t_P + A_{xR} t_R}{t_I} \qquad (A\text{-}30)$$

$$A_{yI} = \frac{A_{yP} t_P + A_{yR} t_R}{t_I} \qquad (A\text{-}33)$$

$$v_I = \frac{v_P A_{yP} t_P + v_R A_{yR} t_R}{A_{yP} t_P + A_{yR} t_R} \qquad (A\text{-}34)$$

$$G_I = \frac{G_P t_P + G_R t_R}{t_I} \qquad (A\text{-}36)$$

The stress in the equivalent inclusion These stresses can be determined analytically (that is, without resulting to finite element calculations) only in the case of simple reinforcement shapes and load distributions. Consider again the repair configuration shown in figure A.1, loaded by the following remote biaxial stresses:

$$\sigma_x = P, \qquad \sigma_y = Q, \qquad \tau_{xy} = 0 \qquad (A\text{-}37)$$

The elliptical shape greatly simplifies the calculation of the stress in the inclusion. This shape allows the continued assumption of a state of uniform plane stress [8]. Figure A.5 (from [5]) shows a sketch of the load flow into and around the reinforced region. (Recall from chapters two and three that a uniaxial remote stress can lead to a locally biaxial stress field due to the change in stiffness.)
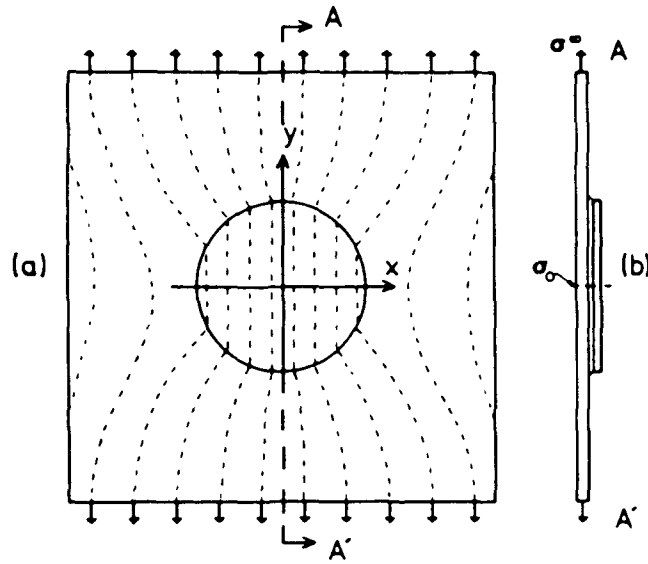
Figure A.5. Idealized "load flow" into elliptically reinforced region of plate.

Let the stress in the inclusion be described by:

$$\sigma_{xI} = P + p, \sigma_{yI} = Q + q, \tau_{xy} = 0 \qquad (A\text{-}38)$$

where p and q denote additional stresses relative to the remote biaxial stresses as a result of load attraction into the stiffer inclusion. Shear stresses are zero as a result of the biaxial tension external loading and because of symmetry in the repair. Lekhnitskii's theory of the inclusion problem [9] leads to a set of linear equations for p and q. However, it also restricts the types of plate material that can be considered. In this derivation, the plate material will be limited to isotropic materials. From [9], the characteristic equation becomes:

$$\lambda^4 + [\frac{E_{xP}}{G_P} - 2\nu]\lambda^2 + \frac{E_x}{E_y} = 0 \qquad (A\text{-}39)$$

Now,

$$Det = [\frac{E_{xP}}{G_P} - 2\nu]^2 - 4\frac{E_{xP}}{E_{yP}} > 0 \quad only\ if\ [\frac{E_{xP}}{G_P} - 2\nu]^2 > 4\frac{E_{xP}}{E_{yP}} \qquad (A\text{-}40)$$

So, $\lambda^2 = \dfrac{-[\dfrac{E_{xP}}{G_P} - 2\nu] \pm \sqrt{Det}}{2}$ $if: Det > 0$

This implies that the first-stage analysis is valid only for plate material meeting the condition:

$$[\frac{E_{xP}}{G_P} - 2v]^2 > 4\frac{E_{xP}}{E_{yP}} \qquad \text{(A-41)}$$

The more general case of an orthotropic plate is discussed first. The above relations will generally hold for an orthotropic plate and will result in two pairs of imaginary and unequal roots $\pm i\alpha$ and $\pm i\beta$ with $\alpha > \beta$. Using Lekhnitskii's theory [9], one finds the following set of linear equations:

$$[\frac{b}{a}\frac{\alpha+\beta}{E_{xP}} + \frac{1}{E_{xI}}]p - [\frac{\alpha\beta - v_P}{E_{xP}} + \frac{v_I}{E_{xI}}]q = [\frac{1}{E_{xP}} - \frac{1}{E_{xI}}]P - [\frac{v_P}{E_{xP}} - \frac{v_I}{E_{xI}}]Q$$

$$\text{(A-42)}$$

$$-[\frac{1}{\alpha\beta E_{yP}} - \frac{v_P}{E_{xP}} + \frac{v_I}{E_{xI}}]p + [\frac{a}{b}\frac{\alpha+\beta}{\alpha\beta E_{yP}} + \frac{1}{E_{yI}}]q = -[\frac{v_P}{E_{xP}} - \frac{v_I}{E_{xI}}]P + [\frac{1}{E_{yP}} - \frac{1}{E_{yI}}]Q$$

For an isotropic plate, the following relationship is true:

$$G = \frac{E}{2(1+v)} \qquad \text{(A-43)}$$

(where $E_x = E_y = E$ and $v_{xy} = v_{yx} = v$)

Substitution into the characteristic equation A-40 gives

$$\lambda^4 + [2(1+v) - 2v]\lambda^2 + 1 = 0$$
$$\lambda^4 + 2\lambda^2 + 1 = 0$$
$$Det = (4-4) = 0$$

which gives double roots at $\pm i$. Allowing the roots $\alpha = \beta = 1$ [10] and substituting into equation A-42 for an orthotropic plate yields the following relationships

$$[\frac{b}{a}\frac{2}{E_{xP}} + \frac{1}{E_{xI}}]p - [\frac{1-v_P}{E_{xP}} + \frac{v_I}{E_{xI}}]q = [\frac{1}{E_{xP}} - \frac{1}{E_{xI}}]P - [\frac{v_P}{E_{xP}} - \frac{v_I}{E_{xI}}]Q$$

$$\text{(A-44)}$$

$$-[\frac{1}{E_{yP}} - \frac{v_P}{E_{xP}} + \frac{v_I}{E_{xI}}]p + [\frac{a}{b}\frac{2}{E_{yP}} + \frac{1}{E_{yI}}]q = -[\frac{v_P}{E_{xP}} - \frac{v_I}{E_{xI}}]P + [\frac{1}{E_{yP}} - \frac{1}{E_{yI}}]Q$$

to allow the calculation of the additional stresses p and q due to load attraction by the stiff inclusion. The total stresses in the inclusion were given in equation A-38.

Stress redistribution in the plate and reinforcement The final step in the stage I analysis is the determination of the load-sharing arrangement between the plate and the reinforcing patch. The calculation of the remaining plate stress σ_{xP} at the prospective crack location follows from equation A-16:

$$t_I \sigma_{xI} = t_P \sigma_{xP} + t_R \sigma_{xR}. \tag{A-45}$$

Substitution of the stress-strain relationships from equation A-22 yields

$$t_P \sigma_{xP} = t_I \sigma_{xI} - [A_{xR}\varepsilon_x + v_R A_{yR}\varepsilon_y]t_R \tag{A-46}$$

Taking the inverse of equations A-22 with respect to the inclusion parameters allows solution for the strains:

$$\begin{bmatrix} \varepsilon_x \\ \varepsilon_y \\ \varepsilon_z \end{bmatrix} = \begin{bmatrix} \dfrac{1}{E_{xI}} & \dfrac{-v_I}{E_{yI}} & 0 \\ \dfrac{-v_I}{E_{xI}} & \dfrac{1}{E_{yI}} & 0 \\ 0 & 0 & \dfrac{1}{2G_I} \end{bmatrix} \begin{bmatrix} \sigma_x \\ \sigma_y \\ \sigma_z \end{bmatrix} \tag{A-47}$$

Substitution yields

$$\sigma_{xP} = \sigma_{xI}[1 - \frac{t_R}{t_I}\frac{(A_{xR} - v_I v_R A_{yR})}{E_{xI}}] + \sigma_{yI}\frac{t_R}{t_I}[\frac{v_I}{E_{xI}}A_{xR} - \frac{v_R}{E_{yI}}A_{yR}]. \tag{A-48}$$

Rearranging equation A-45 gives:

$$\sigma_{xR} = \frac{t_I}{t_R}\sigma_{xI} - \frac{t_P}{t_R}\sigma_{xP} \tag{A-49}$$

Analogous to the preceding calculations, one can derive the expressions for stresses in the y direction:

$$\sigma_{yP} = \sigma_{xI} \frac{t_R}{t_I} \frac{A_{yR}}{E_{xI}} [v_I - v_R] + \sigma_{yI} [1 - A_{yR} \frac{t_R}{t_I} (\frac{1}{E_{yI}} - \frac{v_I v_R}{E_{xI}})] \qquad \text{(A-50)}$$

$$\sigma_{yR} = \frac{t_I}{t_R} \sigma_{yI} - \frac{t_P}{t_R} \sigma_{yP} \qquad \text{(A-51)}$$

References, Appendix A

1. Hart-Smith, L.J., "Analysis and Design of Advanced Composite Bonded Joints," NASA CR 2218, 1974.

2. Muki, R. and E. Sternberg, *Int. J. Solids and Structures*, 4, 1968, pp. 75-94.

3. Sneddon, I.N., *Adhesion*, D.D. Eley, editor, Oxford University Press, 1961.

4. Boyce, W.E. and R.C. DiPrima, *Elementary Differential Equations and Boundary Value Problems*, 4th edition, J. Wiley & Sons, New York, 1986, pp. 540-548.

5. Rose, L.R.F. "Theoretical Analysis of Crack Patching," in *Bonded Repair of Aircraft Structures*, Baker, Jones, editors. Dordrecht: Kluwer Academic Publishers, 1988, pp. 77-106.

6. Rose, L.R.F., "An Application of the Inclusion Analogy," *Int. J. Solids and Structures*, 17, 1981, pp. 827-838.

7. Gere, I. and S. Timoshenko, *Mechanics of Materials,* 2nd ed., Boston, 1985, pp 47-131.

8. Eshelby, J.D., *Proc. Royal Soc. London*, A241, 1957, pp. 376-396.

9. Lekhnitskii, S.G., *Theory of Elasticity of an Anisotropic Elastic Body*, Holden-Day, San Francisco, 1963, Chapter 3, Section 25.

10. Muskhelishvili, N.I., *Some Basic Problems of the Mathematical Theory of Elasticity,* Section 82, Noorhof, Groningen, the Netherlands, 1953.

B

Stage II Analysis of Crack Patching
Introduction of the Crack

In stage II, a crack is introduced into the plate and the stresses at the crack face are allowed to relax to zero. At this point, the rigid bond assumption must be abandoned to allow crack opening displacement. Primary focus is placed on the load transfer and the stresses in the immediate vicinity of the crack. The patch and plate are considered to be of infinite extent; crack opening restraint is considered independent of the size of the reinforcement. The primary outputs of stage II are the (repaired) stress intensity factor and the maximum tensile stress in the patch.

Figure B.1 shows a cracked infinite plate subjected to remote biaxial stresses denoted P and Q, in the x- and y-directions, respectively. The length of the reinforcement is 2a, the width is 2b. The crack length is represented as $2a_c$.

Most fatigue cracks in pressurized fuselages occur as a result of first principal stress, which corresponds to the x or hoop direction in the model. The y-direction is parallel to the longerons.

Throughout the analysis, subscripts will refer to parameters identified with the plate (P), reinforcing patch (R) and adhesive (A). Thus, t_P, t_R and t_A denote the respective thicknesses of the plate, repair patch and adhesive layer, etc.
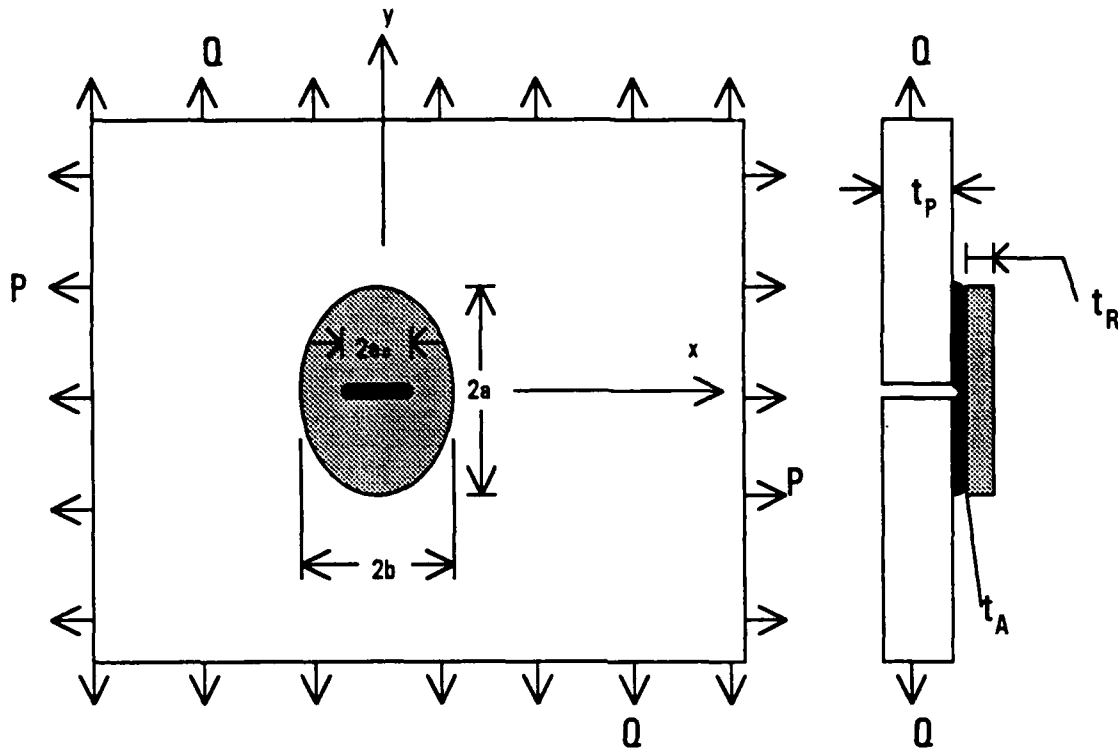
Figure B.1. Bonded Repair Configuration Analyzed in Rose Model.

The analysis is based on the following assumptions:

- All material behavior is linearly elastic, except for limited elastic-plastic deformation in the adhesive layer restricted to an area very near the crack, as discussed in section 5.2.2.2. Hooke's law applies to the analysis.

- All plate and patch materials are in a state of generalized plane stress. No through-the-thickness variation occurs in the basic analysis.

- The adhesive layer behaves as a linear shear spring. Shear load transfer through the adhesive is discussed in section 5.2.2.2.

- The basic model ignores thermal stresses due to bonding or cruise altitudes. Thermal effects are addressed in section 5.2.5.

- Bending in the vicinity of the crack because of the shift in neutral axis from the one-sided patch is restrained by the substructure. This assumption is considered reasonable, considering the common occurrence of fatigue damage at lap joints, fairing attach lines, etc., which are generally riveted to longerons or other longitudinal stiffeners. Expressions describing the bending at the reinforcement boundaries, where such substructure is absent, are derived in Appendix D.

Stage II---Introduction of the Crack This stage of the analysis introduces a crack of length $2a_c$ in the plate along the line y = 0. The rigid bond assumption no longer applies, and forces along the crack face are relaxed to zero. The plate *and the patch* are assumed to be of infinite extent in stage II to make possible the calculation of the repaired stress intensity factor K_r.

Load Transfer Around the Crack The second and more critical load transfer zone is around the crack. Thickness tapering is impossible here; consequently, shear stresses are highest in this region. The analysis used here is based the one-dimensional theory of bonded joints developed by Hart-Smith [1]. Appendix A presented a detailed analysis of the load transfer at the edges of the patch; to set up the stage II analysis of Rose, the analysis is continued here.

The calculation of the length of the load transfer zones is based on a one-dimensional adhesively bonded single lap joint. The adhesive layer is treated as a shear spring. The *lap joint load transfer length*, $1/\Lambda$, is the principal output, and was expressed in Appendix A as

$$\frac{1}{\Lambda} = (\frac{t_A}{G_A}[\frac{E_{yP}t_P E_{yR}t_R}{E_{yP}t_P + E_{yR}t_R}])^{1/2} \qquad \text{(B-1)}$$

Figure B.2 shows the one-dimensional model on which the calculations are based. An infinite strip doubler of unit width is bonded to two semi-infinite strips of the unit-width plate. The ends of the plate share the point x = 0.
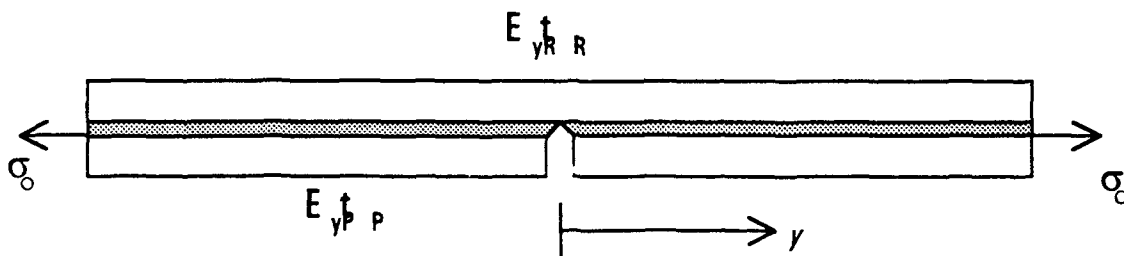
Figure B.2. One-dimensional strip model of load transfer around the crack.

σ_o represents the normal stress in the reinforced plate resulting from the first stage analysis of the Rose model, as discussed in Appendix A. Introduction of the crack causes

B-3

the stress along the crack face to relax to zero. This requires an imaginary stress $-\sigma_o$ to neutralize the original stress. The reinforcement must develop additional tensile stress to compensate. Thus, neglecting bending, over the crack,

$$\sigma_{yR} = \sigma_o \frac{(t_P + t_R)}{t_R} \tag{B-2}$$

Using these relationships and equation A-1, one can calculate the first derivatives of the respective displacements. Substituting into the first derivative of equation A-2 yields the first boundary condition for F_y:

$$F_y'(y = 0) = \frac{G_A}{t_A} \left[\frac{-\sigma_o}{E_{yP}} - \frac{\sigma_o t_P}{E_{yR} t_R} \right]$$

$$= -\sigma_o t_P \frac{G_A}{t_A} \left[\frac{1}{E_{yP} t_P} + \frac{1}{E_{yR} t_R} \right]$$

$$= -\sigma_o t_P \Lambda^2 \tag{B-3}$$

The second boundary condition states that the shear traction will be zero at infinity:

$$F_y(y \to \pm\infty) = 0 \tag{B-4}$$

Inserting B-4 into equation A-9 yields $C_1 = C_2 = 0$, resulting in the following equation:

$$F_y = Ce^{-\Lambda|y|} \tag{B-5}$$

which automatically satisfies the second boundary condition. The first boundary condition helps to solve for C:

$$F_y'(y = 0) = -\Lambda C = -\sigma_o t_P \Lambda^2$$

$$\Rightarrow C = \sigma_o t_P \Lambda \tag{B-6}$$

Hence:

$$F_y = \sigma_o t_P \Lambda e^{-\Lambda|y|} \tag{B-7}$$

Thus, if tapering is not performed, the load transfer lengths and shear traction distribution are identical at the patch tip and the crack face.

The Stress Intensity Factor in the Repaired Plate The introduction of the crack causes the forces in its vicinity to be redistributed. Some of the load is transferred into the patch, while the remainder is redistributed around the crack tips.

For effective crack bridging by the patch to occur, a certain minimum crack length must be reached. A certain amount of controlled delamination between the patch and the plate in the vicinity of the crack tip is necessary to develop fully the desired restraint of crack opening. Fortunately, the required crack length (Ω/π) is rather small, on the order of 20 to 60 mm for typical pressurized fuselage skins. In many cases, the minimum crack size will have been reached or exceeded before inspectors are able to locate it for repair.

The case for the calculation of the repaired stress intensity factor K_r for the patched orthotropic plate is developed here. To begin, the crack extension force G_f is defined from linear elastic fracture mechanics for the orthotropic case:

$$G_f = \frac{K^2}{\sqrt{2E_{xP}E_{yP}}} \cdot \sqrt{\left(\frac{E_{xP}}{E_{yP}}\right)^{1/2} + \frac{E_{yP}(E_{xP} - 2\nu_P)}{2G_PE_{xP}}} \qquad \text{(B-8)}$$

This relation can be used to find the boundaries for the stress intensity factor K. As with the isotropic case, for short cracks, no reduction occurs, so the short crack stress intensity factor, denoted by K_u, is:

$$K_u = \sigma_o\sqrt{\pi a_c} \qquad \text{(B-9)}$$

which represents an upper bound for K. For longer cracks, K and G_f are limited by the crack-closing influence of the reinforcement. An expression for the limiting value of the crack extension force $G_{f\infty}$ relies on the assumption that plate and patch are of infinite extent. The crack extension force is defined by:

$$G_{f\infty} = \frac{\partial W}{2t_P\partial a_c} \qquad \textit{per crack face} \qquad \text{(B-10)}$$

$$G_{f\infty} = \partial W \qquad \text{per unit thickness} \tag{B-11}$$
$$\text{per unit crack length for each crack face}$$

The differential quantity ∂W represents the work performed by allowing the plate stress σ_o to relax to zero at the crack faces. ∂W is calculated by multiplying σ_o by the relative displacement between the plate and reinforcing patch at the crack location. Thus,

$$G_{f\infty} = \sigma_o(u_{yP} - u_{yR}) = \sigma_o u_{yrel} \tag{B-12}$$

From equation B-7, at the crack location $(y = 0^{\pm})$:

$$F_y(y = 0^{\pm}) = \Lambda \sigma_o t_P \tag{B-13}$$

Substitution into equation A-2 yields:

$$u_{rel} = \frac{t_A}{G_A} \Lambda \sigma_o t_P \tag{B-14}$$

From equation B-12, one finds an expression for the crack extension force for long cracks:

$$G_{f\infty} = \frac{t_A}{G_A} \Lambda \sigma_o^2 t_P \tag{B-15}$$

The isotropic case of the transition between short and long cracks was developed in Chapter 5. For the orthotropic case, the transition crack length is expressed as:

$$a_{c_{trans}} = \frac{\Lambda t_P}{\pi C_o} \frac{t_A}{G_A} \tag{B-16}$$

where

$$C_o = \frac{1}{\sqrt{2 E_{xP} E_{yP}}} \sqrt{\left(\frac{E_{xP}}{E_{yP}}\right)^{1/2} + \frac{E_{yP}(E_{xP} - 2\nu_P G_P)}{2 G_P E_{xP}}} \tag{B-17}$$

Maximum Shear Strain in the Adhesive Introduction of the crack alter the stress fields in the plate, reinforcing patch and adhesive from the states calculated in stage I (appendix A). Theses changes are restricted to the small zone around the crack, resulting in the

maximum adhesive shear strain occurring adjacent to the crack. This is particularly true if the patch is tapered in any way.

The analysis allows for plastic adhesive behavior in the zone around the crack. However, the elastic case is developed first.

- *elastic adhesive case:* $\sigma_o \Lambda t_P < \tau_{yield}$

Substitution of $x = 0$ into equation B-7 allows solution for the maximum shear strain in the adhesive:

$$F_{y_{max}} = \sigma_o t_P \Lambda = G_A \gamma_{max} \tag{B-18}$$

$$\gamma_{max} = \frac{\sigma_o \Lambda t_P}{G_A} \tag{B-19}$$

- *elastic-plastic adhesive case:* $\sigma_o \Lambda t_P > \tau_{yield}$

$$\gamma_{max} = \frac{\tau_{yield}}{2G_A}[1 + (\frac{\sigma_o \Lambda t_P}{\tau_{yield}})^2] \tag{B-20}$$

In this case, the characteristic crack length $a_{c_{trans}}$ must be modified to [2]:

$$a_{c_{trans}} = \frac{1}{3\pi} \frac{t_A}{G_A} E_x \Lambda t [\frac{\sigma_o \Lambda t_P}{\tau_{yield}}]^2 \cdot [1 + 2(\frac{\sigma_o \Lambda t_P}{\tau_{yield}})^3] \tag{B-21}$$

Maximum Normal Stress in the Patch The maximum reinforcement stress occurs at $x = 0$, $y = 0$. A conservative estimate is that the entire load in that area of the inclusion is carried by the patch. (Recall an earlier assumption was that no bending occurs across the crack face because of the presence of a stiffener.) Thus,

$$\sigma_{yR_{max}} \approx \sigma_{yI} \frac{t_P}{t_R} \tag{B-22}$$

The Stresses in the Plate Adjacent to the Patch   One important factor in repairing a structure is to avoid creating new fatigue or static strength problems. Thus, the analysis of crack patching must consider the stress state in the skin just outside the patch edges.

patch tip (y = a⁺, x = 0)

From equilibrium, one can show that the load in the inclusion in the y-direction is carried completely by the plate. Thus,

$$\sigma_{yP} t_P = \sigma_{yI} t_I \tag{B-23}$$

$$\sigma_{yP} = \sigma_{yI} \frac{t_I}{t_P} \tag{B-24}$$

Compatibility of strains at the edge of the patch force:

$$\varepsilon_{xP} = \varepsilon_{xI} \tag{B-25}$$

Substituting into the appropriate elasticity equation yields:

$$\frac{-\nu_P}{E_{yP}} \sigma_{yP} + \frac{1}{E_{xP}} \sigma_{xP} = \frac{-\nu_I}{E_{yI}} \sigma_{yI} + \frac{1}{E_{xI}} \sigma_{xI} \tag{B-26}$$

Rearranging, substituting equation B-24 gives:

$$\sigma_{xP} = \sigma_{yI} \left[\nu_P \frac{E_{xP}}{E_{yP}} \frac{t_I}{t_P} - \nu_I \frac{E_{xP}}{E_{yI}} \right] + \sigma_{xI} \frac{E_{xP}}{E_{xI}} \tag{B-27}$$

patch flank *(y = 0, x = b⁺)*

Using analogous calculations,

$$\sigma_{yP} = \sigma_{yI}\frac{E_{yP}}{E_{yI}} + \sigma_{xI}\left[\,\nu_P\,\frac{E_{yP}}{E_{xP}}\frac{t_I}{t_P} - \nu_I\,\frac{E_{yP}}{E_{yI}}\right] \quad \text{(B-28)}$$

$$\sigma_{xP} = \sigma_{xI}\frac{t_I}{t_P} \quad\quad\quad\quad \text{(B-29)}$$

References, Appendix B

1. Hart-Smith, L.J., "Analysis and Design of Advanced Composite Bonded Joints," NASA CR 2218, 1974.

2. Rose, L.R.F. "Theoretical Analysis of Crack Patching," in *Bonded Repair of Aircraft Structures*, Baker, Jones, editors. Dordrecht: Kluwer Academic Publishers, 1988, pp. 77-106.

C

Analysis of Crack Patching: Thermal Considerations

This appendix reviews the thermal effects on crack patching. The temperature changes affecting a bonded patch to a pressurized fuselage can be viewed in two steps. When the bonded repairs are heated for curing, the surrounding cooler structure partially constrains free expansion of the plate. Upon cooling to room temperature, a constant tensile preload exists on the crack tip. This preload can be either tensile or compressive, depending on the relative coefficients of thermal expansion of the patch and constrained plate.

The second step, cooling to approximately -55°C at cruise altitudes around 10,000 meters, does not involve any constraint, because the entire fuselage cools equally. This second step is the more important of the two regarding fatigue, for it imposes an additional *cyclic* tensile stress on the crack tip with every flight.

The following simplifying assumptions apply:

- The plate (skin) material is isotropic, resulting in equal thermal characteristics in every direction in the plane of the plate.

- The crack is located midway between two frames and very near a longitudinal stiffening element, as shown in figure C.1. The frames and stringers outside the heated region act as simple supports, but the stringer adjacent to the crack is neglected in the thermal model. Thermal buckling is ignored.

- The temperature is constant through the thickness of the plate, but varies radially from the center of the patch. Underlying frames and stringers have the same temperature as the adjacent plate.

- All deformations remain in the elastic range of material behavior.

- Plate and patch are in a condition of plane stress.

- Out-of-plane bending in the region of the crack is restrained by the substructure.

- The adhesive acts as a rigid bond.
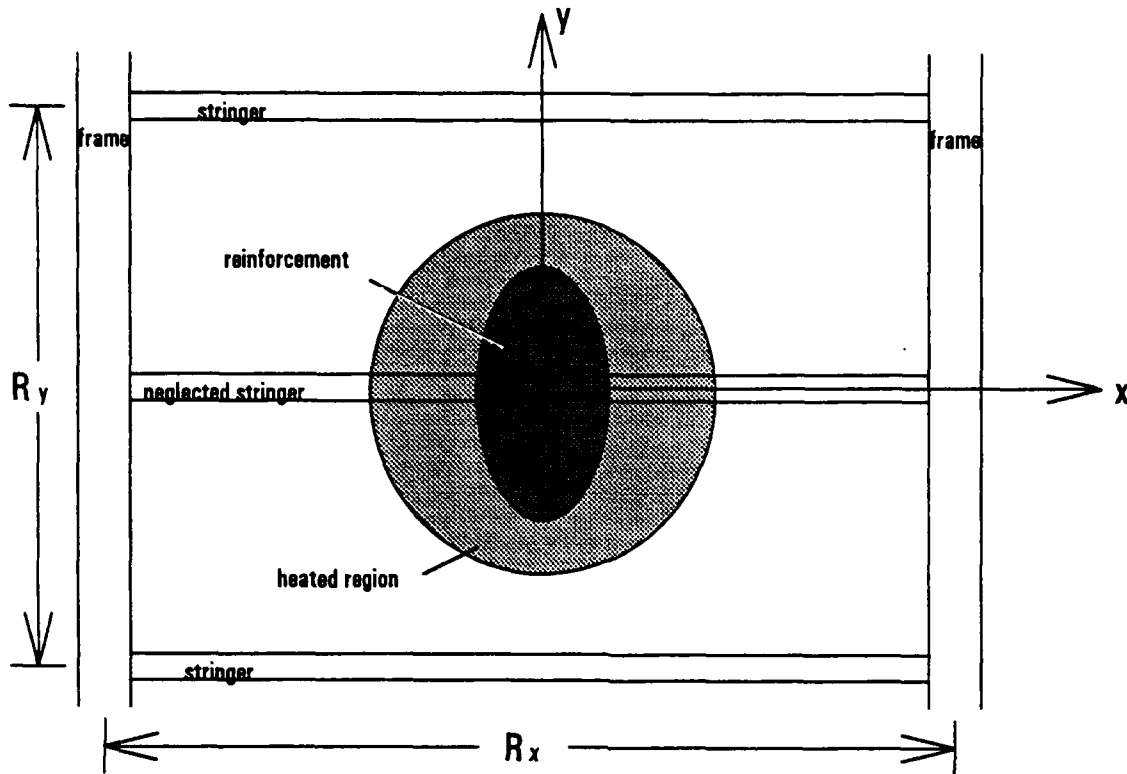
Figure C.1. Model of local fuselage details for analysis of thermal effects on crack patching.

Temperature Field in the Plate Consider the circular isotropic plate of radius R represented by figure C.2. The plate is heated to a steady-state temperature T_c over a central circular region of radius d by means of a thermostatically controlled heat blanket. The temperature at the edge of the plate will be represented by T_e.
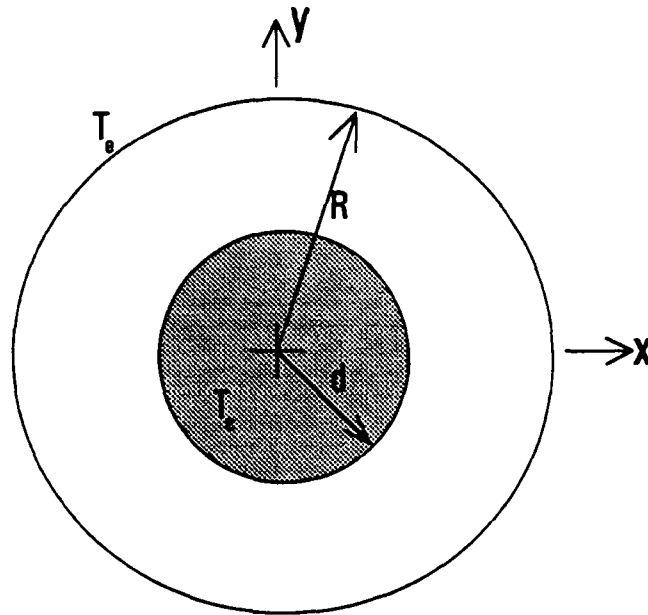
Figure C.2. Model for calculation of temperature distribution in a circular isotropic patch.

The thermal conductivity of the plate is assumed to be independent of the temperature T. Thus, the temperature field satisfies LaPlace's potential equation [1]:

$$\nabla^2 T = 0 \qquad\qquad (C\text{-}1)$$

Depending on the form of the LaPlace operator, this equation can be written as:

$$\frac{d^2 T}{dr^2} + \frac{n}{r}\frac{dT}{dr} = 0, \qquad\qquad (C\text{-}2)$$

where r denotes the single space coordinate and (n + 1) the number of dimensions involved.

The assumption of constant through-the-thickness temperature in the plate means that n = 1. Thus,

$$\frac{d^2 T}{dr^2} + \frac{1}{r}\frac{dT}{dr} = 0 \qquad\qquad (C\text{-}3)$$

with *boundary conditions* $T = T_c$ at $r = d$, $T = T_e$ at $r = R$.

The solution of equation C-3 is:

$$T = T_e + \frac{[T_c - T_e]\ln(r/R)}{\ln(d/R)}, \qquad R \geq r \geq d. \qquad \text{(C-4a)}$$

$$T = T_c, \qquad\qquad r \leq d. \qquad \text{(C-4b)}$$

T_e can be determined using the theory of heat transfer through extended surfaces [1]. Consider the configuration of figure C.3. The outer ring of width dr is treated as a solid body exchanging heat with the media surrounding it. The heat transfer rate $\dot{Q}$ which crosses the outer surface area A is given by:

$$\dot{Q} = hA(r)[T(r) - T_\infty] \qquad \text{(C-5)}$$

where h is the coefficient of heat transfer (W/m²K),

$A(r)$ is the strip surface area at radius r ($\approx 4\pi r dr$),

$T(r)$ is the temperature of the plate at radius r, and

T_∞ is the temperature of the cooling medium (air).
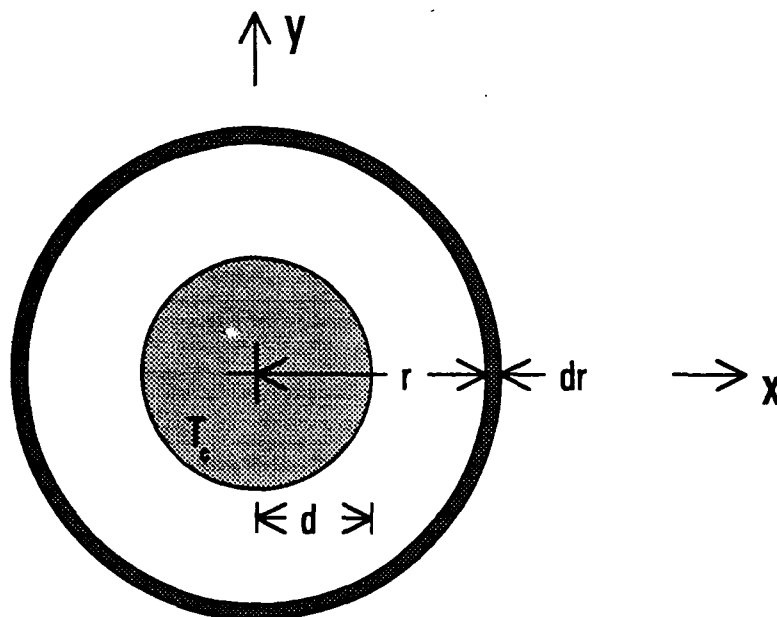
Figure C.3. Model of heat transfer outward through a differential ring.

The decrease in the radial heat transfer rate must be equal to the heat transfer rate at the circumference $u(r)$. For a circular ring dr at radius r:

$$\dot{Q}(r) - \dot{Q}(r + dr) = h[T(r) - T_\infty]u\,dr \qquad \text{(C-6)}$$

where

$$u = 2(2\pi r + t_p) \approx 4\pi r \qquad \text{(C-7)}$$

Using a Taylor series expansion yields

$$\dot{Q}(r + dr) = \dot{Q}(r) + \frac{d\dot{Q}}{dr}dr \qquad \text{(C-8)}$$

and the Biot-Fourier law of conduction gives

$$\dot{Q} = -kf\frac{dT}{dr} \qquad \text{(C-9)}$$

where k = *thermal conductivity [W/m K]*
f = *strip cross-sectional area* = $2\pi r t_p$

Substituting into equation C-3 gives the following differential equation:

$$\frac{d^2 T}{dr^2} = \frac{hu}{kf}(T - T_\infty) = m^2(T - T_\infty) \qquad \text{(C-10)}$$

A particular solution of the non-homogeneous problem exists when $T = T_\infty$. The solution of the homogeneous equation has the form $C_1 e^{mr} + C_2 e^{-mr}$. The general solution is

$$T = C_1 e^{mr} + C_2 e^{-mr} + T_\infty \qquad \text{(C-11)}$$

As $r \rightarrow \infty, T = T_\infty$:

$$T = C_1 e^{mr} + T_\infty = 0 \Rightarrow C_1 = 0$$

At r = d,

$$T = C_2 e^{-md} + T_\infty = T_c \Rightarrow C_2 = e^{md}(T_c - T_\infty)$$

Thus, equation C-11 has the form

$$T = (T_c - T_\infty)e^{-m(r-d)} + T_\infty \qquad \text{(C-12)}$$

Equation C-12 makes possible the calculation of T_e, which is necessary to establish the temperature field. Firs· determination of the constant m is required:

$$m^2 = \frac{hu}{kf} = \frac{h}{k}\frac{4\pi r + 2t_P}{2\pi r t_P} = \frac{h}{k}\left(\frac{2}{t_P} + \frac{1}{\pi r}\right) \approx \frac{2h}{kt_P} \qquad \text{(C-13)}$$

For aluminum alloys, k = 238 W/m K. For the film coefficient h, a natural convection by air is assumed with h = 10 W/m² K. Substituting these values into equation C-13 yields

$$m^2 \approx \frac{0.084}{t_P} \approx \frac{1}{12t_P}$$

$$m \approx \sqrt{\frac{1}{12t_P}} \qquad \text{(C-14)}$$

The final expression for T_e becomes (when $T_\infty = T_{ambient}$)

$$T_e = (T_c - T_{ambient})e^{-m(R-d)} + T_{ambient} \qquad \text{(C-15)}$$

The temperature distribution in the plate during the cure cycle is now fully described with equations C-4 and C-15. These expressions will be used to develop the effective coefficient of thermal expansion in the following section.

Effective Coefficier: of Thermal Expansion During the bonding process, the surrounding cooled structure provides restraint to the heated plate. This results in a smaller expansion in the plate than the unconstrained case. However, the reinforcement (patch) is still able to expand freely. Hence, the use of repair materials with relatively low coefficients of thermal expansion results in smaller than expected residual stresses at room temperature.

These stresses are (usually) compressive in the repair patch and tensile in the aluminum plate.

When a transport aircraft climbs to cruising altitude, its fuselage is cooled uniformly to the ambient temperature (about -55°C at 10,000 meters). The structure surrounding a bonded repair has no constraining influence, and a low expansion patch material shrinks less than the aluminum plate. This induces additional compression in the patch and imposes a tensile load on the crack at the same time that the pressure differential is loading the fuselage to its highest point. Thus, this so-called second step increases the magnitude of the stress amplitude seen by the crack every flight.

Refer to figure C.4. A state of generalized plane stress with zero body forces is assumed. Because of symmetry of deformation the net shear stresses will also be zero.
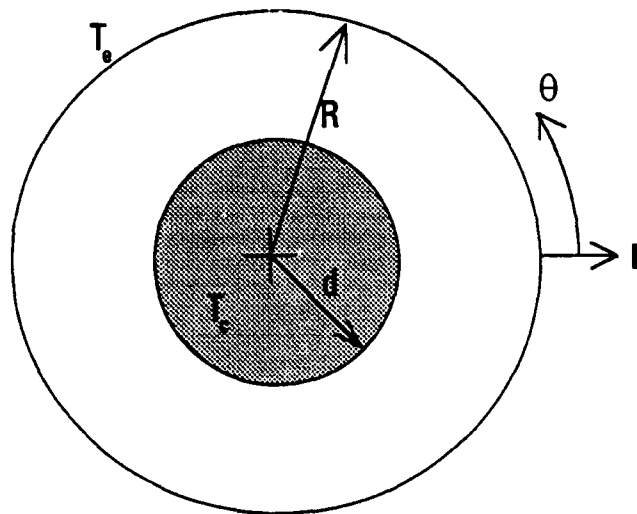
Figure C.4. Polar coordinate model for calculation of effective thermal expansion coefficient.

The single polar coordinate equilibrium equation is

$$\frac{d\sigma_{rP}}{dr} + \frac{\sigma_{rP} - \sigma_{\theta P}}{r} = 0$$

(C-16)

The isotropic stress-strain relationships for plane stress require some modification to account for the strain due to thermal expansion of the plate [2].

$$\varepsilon_{rP} = \frac{1}{E_P}(\sigma_{rP} - v\sigma_{\theta P}) + \alpha_P \Delta T$$

(C-17a)

$$\varepsilon_{\theta P} = \frac{1}{E_P}(\sigma_{\theta P} - v\sigma_{rP}) + \alpha_P \Delta T \qquad \text{(C-17b)}$$

where ΔT is the change from the cure temperature to the temperature of interest.

Solving for the stress components of equations C-17 gives

$$\sigma_{rP} = \frac{E_P}{1 - v^2}[\varepsilon_{rP} + v\varepsilon_{\theta P} - (1 + v)\alpha_P \Delta T] \qquad \text{(C-18a)}$$

$$\sigma_{\theta P} = \frac{E_P}{1 - v^2}[\varepsilon_{\theta P} + v\varepsilon_{rP} - (1 + v)\alpha_P \Delta T] \qquad \text{(C-18b)}$$

Substitution of these values into equation C-16 yields

$$r\frac{d}{dr}(\varepsilon_{rP} + v\varepsilon_{\theta P}) + (\varepsilon_{rP} - \varepsilon_{\theta P})(1 - v)\alpha_P r\frac{dT}{dr} = (1 + v)\alpha_P r\frac{dT}{dr} \qquad \text{(C-19)}$$

Let u denote the displacement in the radial direction. For the thin circular disk, the following can be written:

$$\varepsilon_{rP} = \frac{du}{dr} \text{ and } \varepsilon_{\theta P} = \frac{u}{r} \qquad \text{(C-20)}$$

Substitution into equation C-19 yields

$$\frac{d}{dr}[\frac{1}{r}\frac{d(ru)}{dr}] = (1 + v)\alpha\frac{dT}{dR} \qquad \text{(C-21)}$$

Solving equation C-21 yields

$$\frac{1}{r}\frac{d(ru)}{dr} = (1 + v)\alpha_P \Delta T + C_1$$

$$\frac{d(ru)}{dr} = r(1 + v)\alpha_P \Delta T + C_1 r$$

$$ru = (1+v)\alpha_P \left(\int^r r\Delta T dr + \frac{1}{2}C_1 r^2 + C_2 \right)$$

Let $\frac{1}{2}C_1 = C_1$. Hence,

$$u = (1+v)\alpha_P \frac{1}{r}\int_0^r r\Delta T dr + C_1 r + \frac{C_2}{r} \qquad \text{(C-22)}$$

Evaluating boundary conditions allows solution of the constants in C-22:

$u = 0$ at $r = 0$:

$$u(r=0) = (1+v)\alpha_P \lim_{r\to 0}\frac{1}{r}r\left(\int_0^r R\Delta T dr + \lim_{r\to 0}\frac{C_2}{r}\right)$$

In the heated region, T is constant, so

$$\lim_{r\to 0}\frac{1}{r}\int_0^r R\Delta T dr+ = \lim_{r\to 0}\frac{1}{2}r\Delta T = 0 \quad \text{Hence, } C_2 = 0.$$

$u = 0$ at $r = R$:

$$u(r=R) = (1+v)\alpha_P \lim_{r\to 0}\frac{1}{R}\int_0^R r\Delta T dr + C_1 R = 0 \quad \text{Thus,}$$

$$C_1 = -(1+v)\alpha_P \frac{1}{R^2}\int_0^R r\Delta T dr$$

The final form of C-22 becomes

$$u = \frac{\alpha(1+v)}{R}\left(\frac{R}{r}\int_0^r r\Delta T dr - \frac{r}{R}\int_0^R r\Delta T dr\right) \qquad \text{(C-23)}$$

The expression for the strain becomes:

$$\varepsilon_r = \frac{du}{dr} = \frac{\alpha(1+v)}{R}\left(R\Delta T - \frac{R}{r^2}\int r\Delta T dr - \frac{1}{R}\int_0^R \Delta T dr\right) \qquad \text{(C-24)}$$

which gives an effective coefficient of thermal expansion α_{eff} in the heated region of:

$$\alpha_{eff} = \frac{\alpha_P(1+v)}{RT_c}\left(RT_c - \frac{R}{r^2}\int_0^r r\Delta T dr - \frac{1}{R}\int_0^R \frac{1}{r\Delta T dr}\right) \qquad \text{(C-25)}$$

The integrals in equation C-25 can be solved using the temperature distribution given in equations C-4:

$$\int_{e}^{d} r T_c \, dr = T_c \int_{o}^{d} r \, dr = T_c \left[\tfrac{1}{2} r^2 \right]_0^d = \tfrac{1}{2} T_c d^2$$

$$\int_{o}^{R} r \Delta T \, dr = \int_{e}^{d} r T_c \, dr + \int_{d}^{R} \left(r T_e + \frac{R(T_c - T_e) \ln(\tfrac{r}{R})}{\ln(\tfrac{d}{R})} \right) dr$$

$$= \tfrac{1}{2} T_c d^2 + T_e \int_{d}^{R} r \, dr + \frac{(T_c - T_e) \ln(\tfrac{r}{R})}{\ln(\tfrac{d}{R})} \int_{d}^{R} r \ln(\tfrac{r}{R}) dr$$

$$= \tfrac{1}{2} T_c d^2 + T_e \left[\tfrac{1}{2} r^2 \right]_d^R + \frac{(T_c - T_e)}{\ln(\tfrac{d}{R})} \int_{d}^{R} \tfrac{1}{2} \ln(\tfrac{r}{R}) dr^2$$

$$= \tfrac{1}{2} T_c d^2 + \tfrac{1}{2} T_e (R^2 - d^2) + \frac{(T_c - T_e)}{\ln(\tfrac{d}{R})} \left(\left[\tfrac{1}{2} r^2 \ln(\tfrac{r}{R}) \right]_d^R - \int_{d}^{R} r^2 d \ln(\tfrac{r}{R}) \right)$$

$$= \tfrac{1}{2} T_c d^2 + \tfrac{1}{2} T_e (R^2 - d^2) + \frac{(T_c - T_e)}{\ln(\tfrac{d}{R})} \left(\left[\tfrac{1}{2} r^2 \ln(\tfrac{r}{R}) \right]_d^R - \int_{d}^{R} \tfrac{1}{2} r^2 \tfrac{1}{r} dr \right)$$

$$= \tfrac{1}{2} T_c d^2 + \tfrac{1}{2} T_e (R^2 - d^2) + \frac{(T_c - T_e)}{\ln(\tfrac{d}{R})} \left(\left[\tfrac{1}{2} r^2 \ln(\tfrac{r}{R}) \right]_d^R - \left[\tfrac{1}{4} r^2 \right]_d^R \right)$$

$$= \tfrac{1}{2} T_c d^2 + \tfrac{1}{2} T_e (R^2 - d^2) + \frac{(T_c - T_e)}{\ln(\tfrac{d}{R})} \left(-\tfrac{1}{2} d^2 \ln(\tfrac{d}{R}) - \tfrac{1}{4} R^2 + \tfrac{1}{4} d^2 \right)$$

Substitution into equation C-25 gives the following relationship:

$$\alpha_{P_{eff}} = \frac{\alpha_P}{2}(1 + v_P)\left\{ 1 - \frac{T_e}{T_c} + \frac{d^2}{R^2}\left(\frac{T_e}{T_c} - 1\right) - \frac{1 - \frac{T_e}{T_c}}{2\ln(\frac{d}{r})}\left[\frac{d^2}{R^2} - 1 - \frac{2d^2}{R^2}\ln(\frac{d}{R})\right] \right\} \qquad \text{(C-26)}$$

This derivation was based on the polar coordinate system shown in figure C.4. However, one must consider separate effective thermal expansion coefficients for the x- and y-directions to make use of the derivations in the other appendices. This is accomplished by substituting $T_e = T_x$, $d = d_x$ and $R = R_x$ for the x-direction and $T_e = T_y$, $d = d_y$ and $R = R_y$ for the y-direction. Hence,

$$\alpha_{P_{eff_x}} = \frac{\alpha_P}{2}(1 + v)\left\{ 1 - \frac{T_x}{T_c} + \frac{d_x^2}{R_x^2}\left(\frac{T_x}{T_c} - 1\right) - \frac{1 - \frac{T_x}{T_c}}{2\ln(\frac{d_x}{R_x})}\left[\frac{d_x^2}{R_x^2} - 1 - \frac{2d_x^2}{R_x^2}\ln(\frac{d_x}{R_x})\right] \right\} \qquad \text{(C-27)}$$

$$\alpha_{P_{eff_y}} = \frac{\alpha_P}{2}(1+\upsilon)\{1 - \frac{T_y}{T_c} + \frac{d_y^{\ 2}}{R_x^{\ 2}}(\frac{T_y}{T_c}-1) - \frac{1-\frac{T_y}{T_c}}{2\ln(\frac{d_y}{R_y})}[\frac{d_y^{\ 2}}{R_y^{\ 2}}-1-\frac{2d_y^{\ 2}}{R_y^{\ 2}}\ln(\frac{d_y}{R_y})]\} \quad \text{(C-28)}$$

Equations C-27 and 28 apply to the cure cycle only, because of the constraint that exists in the surrounding structure. The expression for the second-stage drop is understandably simpler, because the surrounding structure provides no constraint:

$$\alpha_{P_{eff_x}} = \alpha_{P_{eff_y}} = \alpha_P \quad \text{(C-29)}$$

Calculation of Residual Thermal Stresses   Determination of the residual thermal stresses involves the analysis of a two-dimensional statically indeterminate structure [3]. Thermal stresses occur as a result of cooling of the (assumed) rigid bond from its stress-free state at the curing temperature. The problem involves three distinct elements, namely:

- the reinforced region of the plate (D in Appendix A),
- the reinforcement (patch), and
- the surrounding matrix (M).

The situation at the cure temperature is considered first. At this temperature, all three members undergo a volume change expressed by the displacement of the boundary *C*. As mentioned previously, buckling of the skin from thermal effects is not considered. A rigid bond between the patch and the reinforced region of the plate is assumed to exist. However, upon cooling, the three elements will try to return to their original dimensions. This is prevented by the rigid bond, which induces thermal stresses.

Thermal stresses that result from the cooling from cure to room temperature are static stresses. However, the thermal stresses that occur when the structure is cooled (or heated) by flight conditions have a cyclic nature.

The three elements are assumed to be separated from each other in the following derivations. A combination of loads applied to the three members must satisfy the boundary conditions resulting from the rigid-bond assumption, equilibrium and compatibility.

The patch and the reinforced portion of the plate are considered first. The members want to experience the following displacements on cooling (positive outward):

region D   x direction: $\delta = -\alpha_{Peff_x} \Delta Ta$ (C-30a)

              y direction: $\delta = -\alpha_{Peff_y} \Delta Tb$ (C-30b)

patch   x direction: $\delta = -\alpha_{R_x} \Delta Ta$ (C-31a)

              y direction: $\delta = -\alpha_{R_y} \Delta Tb$ (C-31b)

Loads per unit length of magnitude P_1 are applied to the edges of the patch and the reinforced plate region to satisfy the rigid-bond assumption. The individual stress-strain relations are:

reinforced isotropic plate $\varepsilon_{xP} = \dfrac{1}{E_{xP}t_P}[P_{1xP} - v_P P_{1yP}]$ (C-32a)

$\varepsilon_{yP} = \dfrac{1}{E_{yP}t_P}[P_{1yP} - v_P P_{1yP}]$ (C-32b)

orthotropic reinforcement $\varepsilon_{xR} = \dfrac{1}{E_{xR}t_R}[P_{1xR} - v_R P_{1yR}]$ (C-33a)

$\varepsilon_{yR} = \dfrac{-v_R P_{1xR}}{E_{xR}t_R} + \dfrac{P_{1yR}}{E_{yR}t_R}$ (C-33b)

Equilibrium conditions require that:

$P_{1xP} = -P_{1xR}$ (C-34a)

$P_{1yP} = -P_{1yR}$ (C-34b)

The rigid-bond assumption results in equal strains in the x and y directions. Equations C-30 through C-34 result in the following:

$$P_{1xP}\left(\frac{1}{E_{xP}t_P} + \frac{1}{E_{xR}t_R}\right) - P_{1yP}\left(\frac{v_P}{E_{xP}t_P} + \frac{v_R}{E_{xR}t_R}\right) = [\alpha_{Peff_x} - \alpha_{R_x}]\Delta T \qquad \text{(C-35a)}$$

$$-P_{1xP}\left(\frac{\nu_P}{E_{xP}t_P}+\frac{\nu_R}{E_{xR}t_R}\right)+P_{1yP}\left(\frac{1}{E_{xP}t_P}+\frac{1}{E_{yR}t_R}\right)=\left[\alpha_{Peff_y}-\alpha_{R_y}\right]\Delta T \qquad \text{(C-35b)}$$

Let:

$$B_1=\frac{1}{E_{xP}t_P}+\frac{1}{E_{xR}t_R}$$

$$B_2=\frac{\nu_P}{E_{xP}t_P}+\frac{\nu_R}{E_{xR}t_R}$$

$$B_3=\frac{1}{E_{xP}t_P}+\frac{1}{E_{yR}t_R} \qquad \text{(C-36)}$$

$$B_4=(\alpha_{Peff_x}-\alpha_{R_x})\Delta T$$

$$B_5=(\alpha_{Peff_y}-\alpha_{R_y})\Delta T$$

Solving the set of linear equations C-35 yields:

$$P_{1yP}=\frac{B_5+\dfrac{B_2 B_4}{B_1}}{B_3-\dfrac{B_2^{\,2}}{B_1}} \qquad \text{(C-37)}$$

$$P_{1xP}=P_{1yP}\frac{B_2}{B_1}+\frac{B_4}{B_1} \qquad \text{(C-38)}$$

The next phase takes the surrounding matrix *M* into consideration. The patch and reinforced skin area *D* are considered one (inclusion) with internal loads P₁. As before, consideration is give to the unrestrained displacements of the inclusion and the matrix as a result of cooling with respect to the boundary *C* The unrestrained displacements follow from equations C-35:

inclusion

x direction: $\delta = -\alpha_{P_{eff_x}}\Delta Ta + \dfrac{a}{E_{xP}t_P}[P_{1x} - v_P P_{1y}]$ (C-39a)

y direction: $\delta = -\alpha_{P_{eff_y}}\Delta Tb + \dfrac{b}{E_{xP}t_P}[P_{1y} - v P_{1x}]$ (C-39b)

surrounding matrix

x direction: $\delta = -\alpha_{P_{eff_x}}\Delta Ta$ (C-40a)

y direction: $\delta = -\alpha_{P_{eff_y}}\Delta Tb$ (C-40b)

Compatibility requires displacements to be equal. Loads per unit length of P_2 are applied to the edges of the inclusion and the (inner) edges of the surrounding matrix. The reaction of the members to external forces will be discussed in the following paragraphs.

Inclusion (I). In the inclusion, stress and displacement are taken positive outward. The load applied to the edges of the inclusion is shared by the reinforcing patch and plate. The resulting displacements *u* and *v* (corresponding to the x and y directions, respectively) are equal:

$$P_{2xP_I} = \frac{E_{xP}t_P}{1 - v_P{}^2}\left(\frac{u}{a} + v_P\frac{v}{b}\right)$$ (C-41a)

$$P_{2yP_I} = \frac{E_{xP}t_P}{1 - v_P{}^2}\left(v_P\frac{u}{a} + \frac{v}{b}\right)$$ (C-41b)

$$P_{2xRI} = \frac{t_R}{1 - v_{xyR}v_{yxR}}\left(E_{xR}\frac{u}{a} + v_R E_{yR}\frac{v}{b}\right)$$ (C-42a)

$$P_{2yR_I} = \frac{t_R}{1 - v_{xyR}v_{yxR}}\left(v_R E_{yR}\frac{u}{a} + E_{yR}\frac{v}{b}\right)$$ (C-42b)

The total applied load is represented by:

$$\sum P_{2x_I} = P_{2xP_I} + P_{2xR_I} \tag{C-43a}$$

$$\sum P_{2y_I} = P_{2yP_I} + P_{2yR_I} \tag{C-43b}$$

Hence,

$$\sum P_{2x_I} = \frac{u}{a}\left(\frac{E_{xP}t_P}{1-v_P^2} + \frac{E_{xR}t_R}{1-v_{xyR}v_{yxR}}\right) + \frac{v}{b}\left(\frac{E_{xP}t_P v_P}{1-v_P^2} + \frac{E_{yR}t_R v_R}{1-v_{xyR}v_{yxR}}\right) \tag{C-44a}$$

$$\sum P_{2y_I} = \frac{u}{a}\left(\frac{E_{xP}t_P v_P}{1-v_P^2} + \frac{E_{yR}v_R t_R}{1-v_{xyR}v_{yxR}}\right) + \frac{v}{b}\left(\frac{E_{xP}t_P}{1-v_P^2} + \frac{E_{yR}t_R}{1-v_{xyR}v_{yxR}}\right) \tag{C-44b}$$

Expressions for the displacements u and v can be derived as functions of the total loads applied at the edges of the inclusion:

$$\frac{v}{b} = \frac{\sum P_{2x_I}}{C_2} - \frac{\left(\sum P_{2y_I} - \sum P_{2x_I}\frac{C_3}{C_2}\right)\frac{C_1}{C_2}}{C_2 - \frac{C_1 C_3}{C_2}} \tag{C-45}$$

$$\frac{u}{a} = \frac{\left(\sum P_{2y_I} - \sum P_{2x_I}\frac{C_3}{C_2}\right)}{C_2 - \frac{C_1 C_3}{C_2}} \tag{C-46}$$

where:

$$C_1 = \frac{E_{xP}t_P}{1-v_P^2} + \frac{E_{xR}t_R}{1-v_{xyR}v_{yxR}} \tag{C-47a}$$

$$C_2 = \frac{E_{xP}t_P v_P}{1-v_P^2} + \frac{E_{yR}t_R v_R}{1-v_{xyR}v_{yxR}} \tag{C-47b}$$

$$C_3 = \frac{E_{xP}t_P}{1-v_P^2} + \frac{E_{yR}t_R}{1-v_{xyR}v_{yxR}} \tag{C-47c}$$

Surrounding matrix (M). Consider a circular plate of radius R with a central circular hole of radius a. The hole is loaded by P (positive inward). The outer edges of the plate are simply supported. A polar coordinate system is used. The equilibrium equation is as follows:

$$\frac{d\sigma_r}{dr} + \frac{\sigma_r - \sigma_\theta}{r} = 0 \qquad (C\text{-}48)$$

The stress-strain relationships are:

$$\sigma_r = \frac{E_{xP}}{1 - \nu_P^2}\left(\frac{du}{dr} + \nu_P\frac{u}{r}\right) \qquad (C\text{-}49a)$$

$$\sigma_\theta = \frac{E_{xP}}{1 - \nu_P^2}\left(\frac{u}{r} + \nu_P\frac{du}{dr}\right) \qquad (C\text{-}49b)$$

where u denotes radial displacement (positive outward).

Substitution of equations C-49 into C-48 gives the following differential equation:

$$\frac{d}{dr}\left(\frac{1}{r}\frac{d(ru)}{dr}\right) = 0 \qquad (C\text{-}50)$$

This yields:

$$\frac{1}{r}\frac{d(ru)}{dr} = C1$$

$$\frac{d}{dr}(ru) = C1r$$

$$ru = \int_a^r C1rdr + C2$$

$$ru = [\tfrac{1}{2}C1r^2]_a^r + C2$$

$$ru = \tfrac{1}{2}C1(r^2 - a^2) + C2$$

$$u = \tfrac{1}{2}C1(r - \tfrac{a^2}{r}) + C2/r$$

$$(let\ \tfrac{1}{2}C1 = C1)$$

$$u = C1r(1 - \tfrac{a^2}{r^2}) + C2/r \quad (r \geq a)$$

The unknown constants can be determined by applying the boundary conditions.

$$u = 0 \quad @ \quad r = R \tag{C-51}$$

$$\sigma_r = 0 \quad @ \quad r = a \tag{C-52}$$

This yields:

$$C1 = \frac{P(1 - v_P{}^2)}{E_{xP} t_P} \cdot \frac{1}{[2 + (1 - v_P)(\frac{R^2}{a^2} - 1)]} \tag{C-53a}$$

$$C2 = -\frac{P(1 - v_P{}^2)}{E_{xP} t_P} \cdot \frac{R^2 - a^2}{[2 + (1 - v_P)(\frac{R^2}{a^2} - 1)]} \tag{C-53b}$$

At the inner edge, *r* = *a*, the following displacement occurs:

$$u = -\frac{Pa(1 - v_P{}^2)}{E_{xP} t_P} \cdot \frac{\frac{R^2}{a^2} - 1}{[2 + (1 - v_P)(\frac{R^2}{a^2} - 1)]} \tag{C-54}$$

The reaction of a circular plate with a circular hole to a force P is described by equation C-54. Recall the repair configuration. Application of equation C-54 in the x and y directions allows one to determine the reaction to loads P_2 at the inner edge of the surrounding matrix, if one assumes the polar model represents the Cartesian coordinate system used in the original model. This leads to:

$$u_x = -\frac{P_{2x_M} a(1 - v_P{}^2)}{E_{xP} t_P} \cdot \frac{\frac{R_x{}^2}{a^2} - 1}{[2 + (1 - v_P)(\frac{R_x{}^2}{a^2} - 1)]} \tag{C-55}$$

$$u_y = -\frac{P_{2y_M} b(1 - v_P{}^2)}{E_{xP} t_P} \cdot \frac{\frac{R_y{}^2}{b^2} - 1}{[2 + (1 - v_P)(\frac{R_y{}^2}{b^2} - 1)]} \tag{C-56}$$

This completes the calculation of displacements in the inclusion and matrix due to the loads P_2 at the boundary *C*. The number of variables can be reduced by noting that equilibrium requires

$$\sum P_{2x_I} = P_{2x_M} = P_{2x} \tag{C-57a}$$

$$\sum P_{2y_I} = P_{2y_M} = P_{2y} \tag{C-57b}$$

The unrestrained displacements of the inclusion and surrounding matrix follow from equations C-39 and C-40. The displacements resulting from external loads appear in equations C-45 and C-46 (inclusion) and C-55 and C-56 (matrix). Compatibility forces that equal displacements must exist in both directions.

x direction:

$$-\alpha_{xeff} a\Delta T + \frac{a}{E_{xP}t_P}(P_{1x} - \nu_P P_{1y}) + u = -\alpha_{xeff} a\Delta T + u_x$$

$$\frac{u}{a}E_{xP}t_P + (P_{1x} - \nu_P P_{1y}) = P_{2x}(1 - \nu_P^2)\left(\frac{1 - \dfrac{R_x^2}{a^2}}{(1 + \nu_P)(1 - \nu_P)\dfrac{R_x^2}{a^2}}\right)$$

$$P_{2x} = \frac{(1 + \nu_P) + (1 - \nu_P)\dfrac{R_x^2}{a^2}}{(1 - \nu_P^2)\left(1 - \dfrac{R_x^2}{a^2}\right)}\left(\frac{u}{a}E_{xP}t_P + (P_{1x} - \nu_P P_{1y})\right)$$

Let

$$D_1 = \frac{(1 + \nu_P) + (1 - \nu_P)\dfrac{R_x^2}{a^2}}{(1 - \nu_P^2)\left(1 - \dfrac{R_x^2}{a^2}\right)} \tag{C-58}$$

Thus

$$P_{2x} = D_1\left(\frac{u}{a}E_{xP}t_P + (P_{1x} - \nu_P P_{1y})\right) \tag{C-59}$$

y direction:

Analogous to the x direction, one finds:

$$P_{2y} = D_2\left(\frac{v}{b}E_{xP}t_P + (P_{1y} - \nu_P P_{1x})\right) \tag{C-60}$$

where

$$D_2 = \frac{(1+\nu_P)+(1-\nu_P)\dfrac{R_y{}^2}{b^2}}{(1-\nu_P{}^2)\left(1-\dfrac{R_y{}^2}{b^2}\right)}$$

(C-61)

u and v remain functions of the applied loads P_2. Substitution of the expression for u and v, equations C-45 and C-46, into C-58 and C-60 gives:

$$P_{2x} = D_1[\left(P_{2y} - P_{2x}\frac{C_3}{C_2}\right)F_1 + F_2]$$

(C-62)

$$P_{2y} = D_2[\frac{P_{2x}}{C_2}E_{xP}t_P - \left(P_{2y} - P_{2x}\frac{C_3}{C_2}\right)\frac{C_1}{C_2}F_1 + F_3]$$

(C-63)

where

$$F_1 = \frac{E_{xP}t_P}{C_2 - \frac{C_1 C_3}{C_2}}$$

(C-64a)

$$F_2 = P_{1x} - \nu_P P_{1y}$$

(C-64b)

$$F_3 = P_{1y} - \nu_P P_{1x}$$

(C-64c)

Equations C-62 and C-63 form a set of linear equations. Solving them yields the following relationships for the loads P_2:

$$P_{2x} = \frac{D_1}{1+D_1 F_1 \frac{C_3}{C_2}}\left(\frac{K_1}{K_0}F_1 + F_2\right)$$

(C-65)

$$P_{2y} = \frac{K_1}{K_0}$$

(C-66)

where:

$$K_0 = 1 - D_2 H_1 F_1 E_{xP}t_P + D_2 F_1 \frac{C_1}{C_2} - D_2 H_1 F_1{}^2 \frac{C_1 C_3}{C_2}$$

(C-67a)

$$K_1 = D_2[H_1 F_2 E_{xP} t_P + H_1 F_1 F_2 \frac{C_1 C_3}{C_2} + F_3]$$ (C-67b)

$$H_1 = \frac{D_1}{C_2 + D_1 F_1 C_3}$$ (C-67c)

Substitution of the calculated loads P_2 into equations C-45 and C-46 allows solution of the inclusion displacements. These can be used to solve for the loads per unit length in the plate and patch with equations C-41 and C-42. These loads are complementary to the previously discussed internal loads P_1. Linear superposition of the total thermal loads, divided by respective thicknesses, yields the following thermal stresses:

thermal stresses in the plate:

$$\sigma_{x,thermal_P} = \frac{P_{1x} + P_{2x}}{t_P}$$ (C-68a)

$$\sigma_{y,thermal_P} = \frac{P_{1y} + P_{2y}}{t_P}$$ (C-68b)

thermal stresses in the patch:

$$\sigma_{x,thermal_R} = \frac{-P_{1x} + P_{2x}}{t_R}$$ (C-69a)

$$\sigma_{y,thermal_R} = \frac{-P_{1y} + P_{2y}}{t_R}$$ (C-69b)

References, Appendix C

1. Grigull, U. and H. Sandner, *Heat Conduction,* Springer-Verlag, Berlin, 1984.

2. Timoshenko, S. and Goodier, J.N., *Theory of Elasticity,* 2nd edition, McGraw-Hill, New York, 1951.

3. Gere and Timoshenko, *Mechanics of Materials,* 2nd edition, PWS-Kent Publishing, Boston, 1984.

D

Analysis of Crack Patching: Bending Considerations

The assumption was made previously that no bending would occur at the crack location because of restraint provided by the substructure. However, in the case of a single-sided reinforcement, considerable bending stress exist at the edges of the patch. Significant bending occurs away from the frames and longerons, resulting in substantially higher stresses in the plate in the hoop or x-direction. This analysis will be restricted to that one-dimensional case. The following assumptions apply [1]:

- all deformations are in the elastic range of material response,
- the adhesive bond is rigid,
- the crack is neglected,
- the repair is located midway between two frames over a longeron,
- the remote y-stress causes no out-of-plane bending, and
- plane sections in the reinforced area remain plane in pure bending, consistent with the Bernoulli-Euler bending theory.

Consider the model sketched in figure D.1. It shows an orthotropic reinforcement bonded to one side of an orthotropic plate over an x-dimension of 2a. Both the reinforcement and the plate are of infinite width. The structure is loaded with the remote stress P in the x-direction.
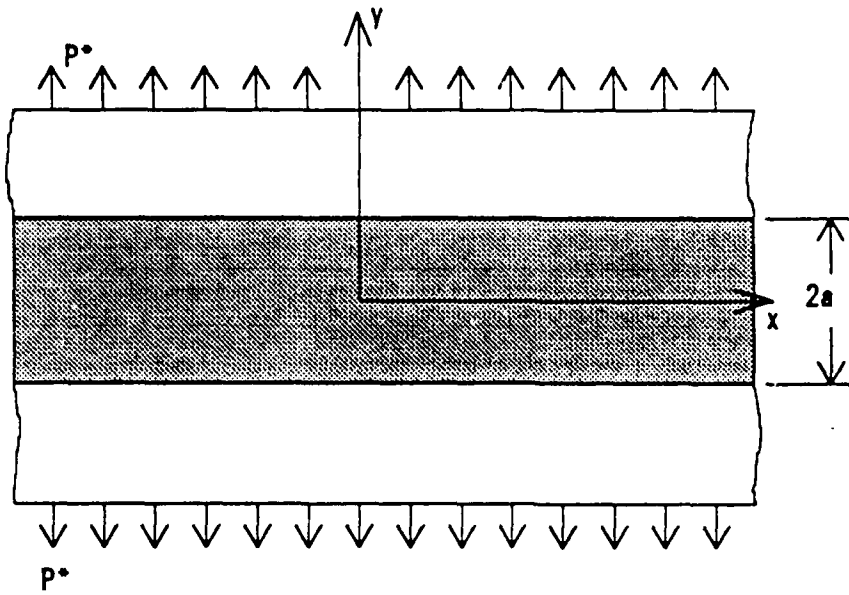
Figure D.1. View of bending stress model for one-sided bonded reinforcement.

The reinforcement causes a shift in neutral axis that results in secondary bending. This necessitates a separate analysis of the reinforced area (also called the inclusion) and the unreinforced region (surrounding matrix).

unreinforced region (matrix): neutral axis $z = 1/2t_P$

$$(E_y I)_m = \frac{E_{yP}}{1 - v_{xyP} v_{yxP}} \int_{-1/2t}^{1/2t} z^2 dz \; \frac{E_{yP} t_P^3}{12(1 - v_{xyP} v_{yxP})} \tag{D-1}$$

inclusion: neutral axis $z = z_o$

$$z_o = \frac{1}{t_I^*} \left[\int_0^{t_P} z dt_P^* + \int_{t_P}^{t_P + t_R} z dt_R^* \right] \tag{D-2}$$

The variable t^* denotes the respective reduced thicknesses of the inclusion, plate and patch (reduced = corrected for elastic modulus).

$$t_I^* = \frac{1}{E_{yP}}(E_{yP}t_P + E_{yR}t_R) = t_P + \frac{E_{yR}}{E_{yP}}t_R \qquad \text{(D-3a)}$$

$$t_P^* = t_P \qquad \text{(D-3b)}$$

$$t_R^* = \frac{E_{yR}}{E_{yP}}t_R \qquad \text{(D-3c)}$$

Substitution and reduction yields

$$z_o = \frac{1}{t_P + \dfrac{E_{yR}}{E_{yP}}}\left[\frac{E_{yR}}{E_{yP}}\int_0^{t_P} z\,dz + \frac{E_{yR}}{E_{yP}}\int_{t_P}^{t_P+t_R} z\,dz\right]$$

$$z_o = \frac{1}{E_{yP}t_P + E_{yR}t_R}\{E_{yP}[\tfrac{1}{2}z^2]_0^{t_P} + E_{yR}[\tfrac{1}{2}z^2]_{t_P}^{t_P+t_R}\}$$

$$z_o = \frac{E_{yP}t_P{}^2 + E_{yR}[(t_P+t_R)^2 - t_P^2]}{2(E_{yP}t_P + E_{yR}t_R)} \qquad \text{(D-4)}$$

Equation D-4 can be used to calculate the bending stiffness per unit width of the reinforced region.

$$(E_yI)_I = \frac{E_{yP}}{1-\nu_{xyP}\nu_{yxP}}\int_{-z_o}^{t_P-z_o} z^2\,dz + \frac{E_{yR}}{1-\nu_{xyR}\nu_{yxR}}\int_{t_P-z_o}^{t_P-z_o+t_R} z^2\,dz$$

$$(E_yI)_I = \frac{E_{yP}\{(t_P-z_o)^3 + z_o^3\}}{3(1-\nu_{xyP}\nu_{yxP})} + \frac{E_{yR}\{(t_P-z_o+t_R)^3 - (t_P-z_o)^3\}}{3(1-\nu_{xyR}\nu_{yxR})} \qquad \text{(D-5)}$$

Bending moments M_1 and M_2 are applied to the edges of the reinforce area and the surrounding matrix, as shown in figure D.2.
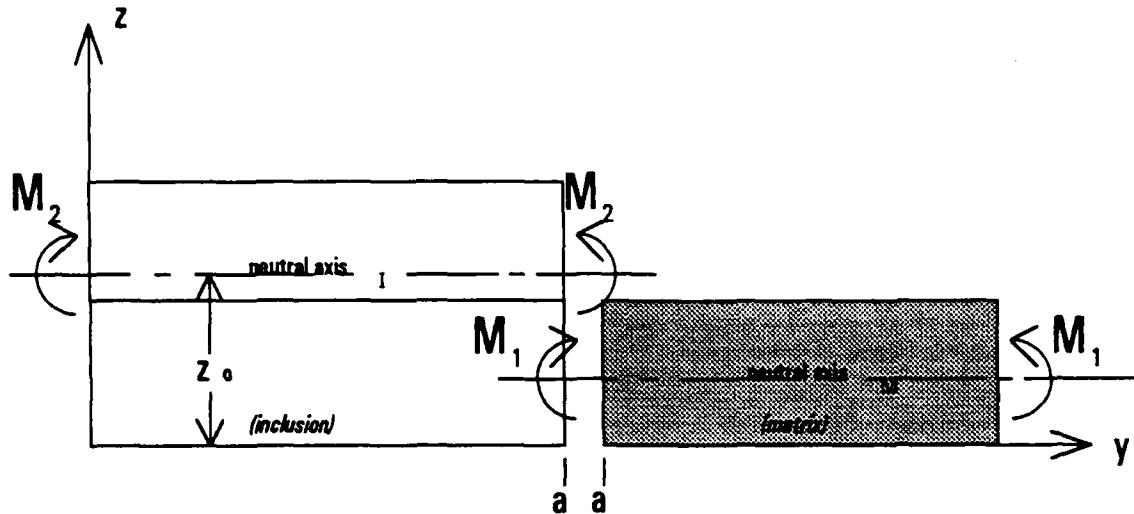
Figure D.2. Bending moments at the edges of the inclusion and matrix.

The relationship between the bending moment M and the deflection $w(y)$ leads to the following non-linear differential equation:

$$EIw''(y) = P^* t \cdot w(y) = M(y) \qquad \text{(D-6)}$$

where $w(y)$ is the displacement in the z (out of plane) direction at a point y.

The boundary conditions of equation D-6 are set by the symmetry and equilibrium of the inclusion and the surrounding matrix:

$$w_m(y \to \infty) = 0 \qquad \text{(D-7a)}$$

$$w_I'(y = 0) = 0 \qquad \text{(D-7b)}$$

$$w_m(y = a) = \frac{M_1}{P^* t_P} \qquad \text{(D-7c)}$$

$$w_I(y = \infty) = 0 \qquad \text{(D-7d)}$$

Equation D-6 is a homogeneous differential equation with constant coefficients. Its general solution has the form:

$$w(y) = C_1 e^{r_1 y} + C_2 e^{r_2 y} \tag{D-8}$$

where r_1, r_2 are the roots of the characteristic equation.

The displacement $w(y)$ can be expressed in terms of the bending moments M_1 and M_2 at $y = a$. Once again, the inclusion and matrix are treated separately.

unreinforced region (matrix)

The roots of the characteristic equation can be expressed as

$$r_{1,2} = \pm \Phi_M = \pm \sqrt{\frac{P^* t_P}{(EI)_M}} \qquad \text{(let } y = y\text{-}a\text{)} \tag{D-9a}$$

$$w(y \to \infty) = C_1 e^{\Phi_M (y-a)} = 0 \quad \therefore C_1 = 0 \tag{D-9b}$$

$$w(y = a) = C_2 e^0 = \frac{M_1}{P^* t_P} = C_2 \tag{D-9c}$$

$$w(a < y < \infty) = \frac{M_1}{P^* t_P} e^{-\Phi_M (x-a)} \tag{D-9d}$$

inclusion

The roots of the characteristic equation can be expressed as

$$r_{1,2} = \pm \Phi_I = \pm \sqrt{\frac{P^* t_I}{(EI)_I}} \tag{D-10a}$$

$$w'(y = 0) = \Phi_I (C_1 - C_2) = 0 \quad \therefore C_1 = C_2 \tag{D-10b}$$

$$w(y = a) = C_1 [e^{\Phi_I a} + e^{-\Phi_I a}] = \frac{M_2}{P * t_I} \qquad \text{(D-10c)}$$

$$w(0 \leq y < a) = \frac{M_2}{P * t_I} \frac{cosh(\Phi_I x)}{cosh(\Phi_I a)} \qquad \text{(D-10d)}$$

The bending moments can be calculated by considering compatibility between the inclusion and the surrounding matrix:

$$w_I(a) - w_M(a) = z_o - \tfrac{1}{2} t_I \qquad \text{(D-11a)}$$

$$w_I'(a) = w_M'(a) \qquad \text{(D-11a)}$$

Substitution of equations D-9 and D-10 into D-11a yields:

$$\frac{M_2}{P * t_P} - \frac{M_1}{P * t_P} = z_o - \tfrac{1}{2} t_P \qquad \text{(D-12)}$$

Equation D-11b yields

$$\frac{M_2}{P * t_P} \Phi_I \tanh(\Phi_I a) = -\frac{M_1}{P * t_P} \Phi_M \qquad \text{(D-13)}$$

Rearranging equation D-12 and substituting into D-13 yields;

$$\frac{M_1}{P * t_P} = \frac{-(z_o - \tfrac{1}{2} t_P) \Phi_I \tanh(\Phi_I a)}{\Phi_M + \Phi_I \tanh(\Phi_I a)} \qquad \text{(D-14)}$$

$$\frac{M_2}{P * t_P} = \frac{(z_o - \tfrac{1}{2} t_P) \Phi_M}{\Phi_M + \Phi_I \tanh(\Phi_I a)} \qquad \text{(D-15)}$$

D-6

The bending stress distribution in the plate at the edge of the patch is:

$$\sigma_{bend}(z) = E_{yP}(\tfrac{1}{2}t - z)w''_M(y = a)$$

$$= E_{yP}(\tfrac{1}{2}t_P - z)\frac{M_1}{P * t_P}\Phi_M{}^2$$

$$= E_{yP}(z - \tfrac{1}{2}t_P)(z_o - \tfrac{1}{2}t_P)\frac{\Phi_I \Phi_M{}^2 \tanh(\Phi_I a)}{\Phi_M + \Phi_I \tanh(\Phi_I a)} \qquad \text{(D-16)}$$

The maximum bending stress in the plate occurs at the edge of the reinforced region at the upper surface $z = t_P$ and is represented by:

$$\sigma_{bend_{max}} = \frac{E_{yP}t_P}{2}(z_o - \tfrac{1}{2}t_P)\frac{\Phi_I \Phi_M{}^2 \tanh(\Phi_I a)}{\Phi_M + \Phi_I \tanh(\Phi_I a)} \qquad \text{(D-17)}$$

Reference, Appendix D

1. Gere, I. and S. Timoshenko, *Mechanics of Materials,* 2nd ed., Boston, 1985, pp 47-131.

E

CALCUREP User's Manual

Introduction

Crack patching is the adhesive bonding of advanced composite materials to repair cracked metal aircraft structures. Crack patching was first successfully applied to the fracture-critical D6AC steel wing pivot fitting of the General Dynamics F-111. Researchers in Australia and others have developed this concept further, bonding strong, stiff boron or carbon epoxy composites to cracked aircraft structures with good results. The technique has extended the useful lives of flawed airframes for many years at a reasonable cost. More recently, the United States Air Force has announced plans to use boron/epoxy to reinforce cracked structures on the B-1B and the F-16.

Advanced composites are usually the lightest way to repair a structure. Crack patching is another specialized tool for the structural repair technician. It probably isn't a technique that will be used every day in all structural repair situations. Crack patching is particularly attractive when replacement of the original cracked structure is exceptionally difficult or expensive, or when replacement parts are unavailable.

An excellent reference that fully explains the theory of crack patching is *Bonded Repair of Aircraft Structures.* The book was edited by Alan Baker and Rhys Jones, two pioneers in crack patching. (Dordrecht, the Netherlands: Kluwer Academic Publishers, 1988) In addition to crack patching theory, it also covers the important materials and processes information necessary for good adhesive bonding.

This appendix serves to guide users of the crack patching analysis program CALCUREP. CALCUREP was developed at the Faculty of Aerospace Engineering of Delft University of Technology, the Netherlands. The entire crack patching analysis package is presented in a

user-friendly interactive computer program suitable for airline maintenance use. The program calculates the following quantities of interest to the repairer:

* the reduction in crack tip stress intensity after repair,
* the maximum shear strain in the adhesive,
* the maximum tensile stress in the repair patch, and
* the change in stiffness in the fuselage skin because of the presence of the crack and the bonded repair.

To use CALCUREP, you need a personal computer that runs DOS. A 386 SX or faster PC will shorten the calculation times, but CALCUREP will run on older PCs as well. It takes up 825 kilobytes of memory on your hard disk.

CALCUREP is based on a mathematical model developed by L.R.F. Rose, which in turn is based on four theories: *elasticity theory, fracture mechanics*, the *theory of bonded joints* and the *theory of heat transfer.* Each theory will be briefly introduced as it applies to the calculations.

Elasticity theory means that the loads placed on the crack patching materials won't be loaded so highly that they permanently deform, or yield. When materials behave elastically, they return to the same position or length they had before they were loaded.

Fracture mechanics includes the study of how cracks grow in metals and other structural materials. The stresses in a material at a crack tip can be very high, and they get higher as the crack gets longer. A quantity known as the *stress intensity factor*, K, measures how strong the crack-opening forces are. The whole point of crack patching is to reduce K so cracks grow slowly or not at all. Figure 1 shows a sketch comparing K for an unpatched crack with a patched crack.

You can see that the longer an *unpatched* crack grows, the higher K gets. If K gets too high, the material will fracture. With a properly designed bonded patch, K reaches a limiting value, no matter how long the crack gets. A well-designed patch will keep K so low that the crack grows very slowly. This allows long inspection intervals for the repair.

If you know the K value of the repaired crack and the type of cracked material, you can use the table provided later to predict the crack growth rates. Knowing the crack growth rate lets you set inspection intervals.
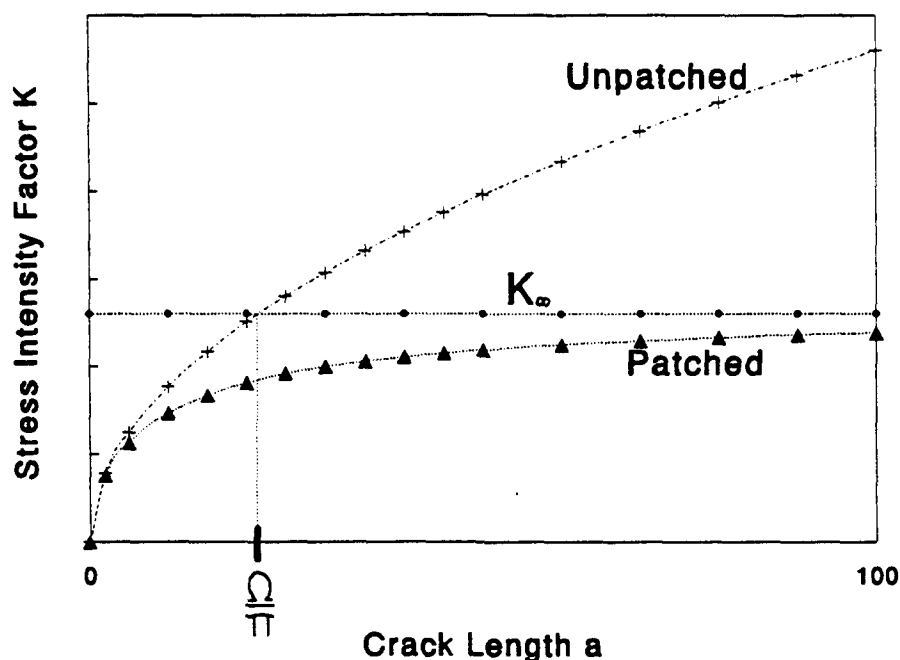
Figure 1. Non-dimensional comparison of patched and unpatched K values.

Using the *theory of bonded joints* allows you to calculate the way load is transferred in and out of the bonded patch. With a bonded joint, the adhesive at the edges of the patch (and the crack) does most of the work. The rest of the bond acts as an anchor to make sure the bond is long-lasting.

The use of carbon- and boron-epoxy composites in the repair of aluminum combines materials with large differences in thermal expansion coefficients. The *theory of heat transfer* lets you calculate the stresses in the bonded repair area that result from these large differences. In CALCUREP, the program assumes you'll heat a small area around the patch for bonding. Most of the aircraft will stay at room temperature. Figure 2 illustrates this idea.

During the bonding process, the surrounding cooled structure restrains the heated fuselage skin. This restraint limits the thermal expansion of the skin, but the patch is able to expand freely. Composite patch materials have low coefficients of thermal expansion. This means that thermal stresses at room temperature are small, but when the fuselage gets very cold at high altitudes, thermal stresses can become very large.
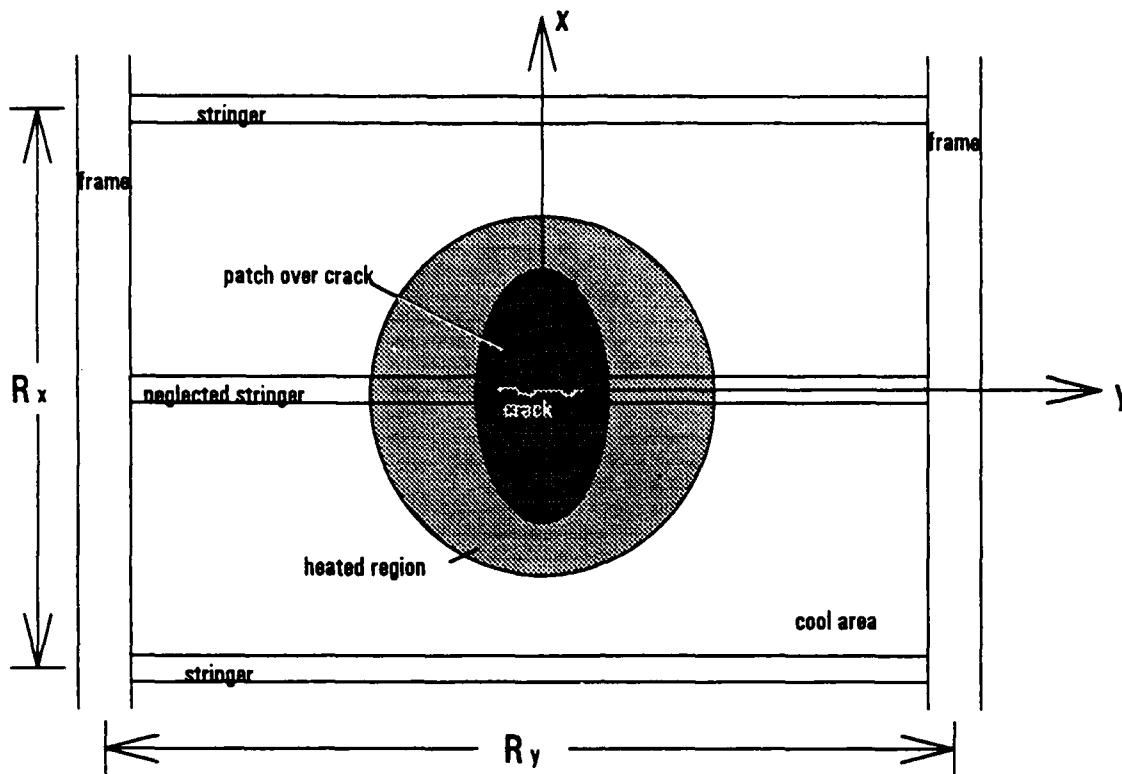
Figure 2. Model of local fuselage details for analysis of thermal effects on crack patching.

When an aircraft climbs to cruising altitude, its fuselage is cooled uniformly to the surrounding air temperature (about -55°C at 10,000 meters). The structure surrounding the bonded repair has no constraining influence, and a low expansion patch material shrinks less than the aluminum fuselage skin. This puts the patch in compression and tries to open the crack, the opposite of what you want. The stresses in the fuselage are at their highest point. This can reduce the effectiveness of composite patches like boron/epoxy and carbon/epoxy.

The Rose model does its calculations in two steps. In stage one, the calculations ignore the crack in the fuselage. This lets the computer calculate what's happening in the skin next to the patch and in the adhesive layer near the patch edge.

The second stage of the Rose model looks very closely at the skin, patch and adhesive around the crack. In the second step, the computer calculates what forces are acting to keep the crack from growing.

The next section will explain the analysis program CALCUREP. A detailed example is given of a calculation. This is followed by some rules of thumb for preliminary design and patch material selection.

Crack Patching Analysis Program CALCUREP

This section describes the computer program CALCUREP that performs crack-patching analysis. It allows maintenance engineers with limited knowledge of fuselage design stress levels to design and analyze bonded patch repairs. The program is user-friendly, runs on desk-top personal computers, and requires short run times (less than five minutes).

A repairer knows where a crack is located and how long it is. He also knows how much (or how little) time is available to design, analyze and install a suitable repair. If the repair is not specified in the Structural Repair Manual, the maintainer must contact the manufacturer to find out what to do. He may ask the manufacturer for approval of his own repair design, or request a design from the manufacturer. Asking the manufacturer for a repair design is more expensive and takes more time.

With CALCUREP, the repairer must specify the following items:

structure to be repaired
- skin thickness
- skin material
- frame spacing
- stringer spacing
- crack length
- maximum operating altitude
- cabin pressure altitude
- fuselage radius

(If you know the detailed stress state at the crack location, the last two items aren't needed.)

repair patch and adhesive
- patch material
- patch dimensions (length, width, thickness)
- adhesive type
- cure temperature
- heating blanket dimensions

With these input parameters, the program calculates the properties of the repair. It estimates the far-field stress situation on the simple theory of pressure vessels, which slightly *over*estimates the skin stresses in a stiffened fuselage. (This keeps you on the safe side.)

Program Output

CALCUREP provides the following output:

- the stress intensity factor K_r at the (repaired) crack tip
- the percent reduction in K achieved by the repair
- the *maximum normal stress* in the patch
- the maximum shear strain in the adhesive
- the maximum normal stresses in the fuselage skin adjacent to the repair
- thermal effects on all of the above
- bending stresses in the fuselage skin at the edge of the patch

CALCUREP provides an option to vary one input variable (for example, patch thickness) and provide the output in the form of a sensitivity analysis. The following section presents the results of a sample calculation.

Sample Calculation

This section describes a typical input/output session with CALCUREP. The upper forward fuselage of an early model of the Boeing 737 is used as a typical fuselage multiple site damage case needing repair.

Once you have installed the program on your hard disk in the subdirectory CALCUREP, log in to it from DOS:

- Change directory to \CALCUREP\.
- Type **barn**, press ENTER.
- Type your password, press ENTER.
- Choose the type of introduction graphics (y/n).
- Enter on which drive you want to store your data.

The data input and the results of the program can be stored in a separate output file. These output files can be created with the help of the **file manager**. A list of existing

output files is displayed on the monitor in the subdirectory you're using. The following menu is presented at the bottom of the screen.

[F1] New File

Press the F1-key to create a new output file. You will be asked to enter the new file name. This file name is limited to eight characters (without extension) and must have the extension "*.pas*". The file name you type in is checked for uniqueness and composition (length and extension). If you give an improper file name, the program asks you to try again. Type in "737xampl.pas" and press return. You cannot overwrite an existing file.

[F2] Exit to DOS

Use this option to copy, rename or delete output files within DOS. Every change you make to a file in DOS must also be carried out in the master file **listfile.pas**. For example, if you want to delete a file, you also must delete it in listfile.pas with a DOS text editor.

[F3] Help

Information on the use of the file manager is displayed in the message window. Use the PgDn-key for more help or to end the help item.

[F4] Buffer File

The existing file **buffer.pas** is overwritten with the data input and the results of the current session. The buffer file is a temporary file for program output.

data input plate

This section allows you to describe the structure being repaired. You can go through this section by simple, no-value menus. A choice is made by entering the appropriate number. The program automatically replies by displaying the corresponding serial menu.

The alternative option at the end of the list enables you to insert non-standard material data by answering specific questions for both cases.

Enter the following data:

- skin material: 2024-T3 aluminum
- skin thickness: 0.914 mm *(you must put the zero first!)*

The program displays a full numeric presentation of the chosen plate material. A menu appears at the bottom of the screen with the following options:

[F1] Continue

Press the F1-key to move on to the next section of the program.

[F2] Repeat

Press the F2-key to repeat the corresponding part of the program.

[F3] Change Screen Data

Press the F3-key to change the data in the presentation on the screen.
Note: The F3 option cannot be used to alter the nature of the material (from isotropic to orthotropic).

The first value in the presentation is highlighted. Use the space bar to "highlight" your way through the list. Upon arrival at the value(s) to be altered, you simply enter the new values. You must use the space bar to leave this mode and return to the original menu. If you enter a value the computer can't read (for example .05 instead of 0.05), the computer won't accept your input. If this occurs, re-enter the data and continue.

data input reinforcement (patch)

Here, you select the repair patch material. This section of the program is similar to the data input of the plate material.

Input the following data for the repair patch. (You will have to do each configuration on a separate run.)

Patch material	*Thickness, mm*	*Lay-up*
Fiber metal laminate GLARE 2	0.85	2/1-0.3
Composite Boron/epoxy	0.38	3 plies
Monolithic 2024-T3	1.00	not applicable

data input adhesive

You select the adhesive to be used for bonding. This section is similar to the data input of the plate and the patch. If you're using an adhesive not shown on the menu, you must enter new data for the alternative adhesive.

Make the following inputs:

> adhesive type: AF-163-2K epoxy film, $t = 0.25$ *mm*
> cure temperature: 120°C

material data input presentation

The repair materials you have selected will be summarized on the monitor. You are offered the possibility to repeat the complete repair material data input.

configuration data input

The computer will ask you simple questions about patch dimensions, airplane geometry, cruise conditions, repair tools and the type of loading. To decrease input variables, the program again uses simple menus.

- patch length (perpendicular to the crack, use 160 times the patch thickness)
  - GLARE 2: 140 mm
  - Boron/epoxy: 60 mm
  - 2024-T3: 160 mm
- patch width (parallel to the crack, use the crack length plus 50 mm): 250 mm
- crack (half) length: 100 mm *(long crack between tear straps)*
- heating blanket dimensions: 380 x 380 mm (square)
- frame distance: 508 mm
- stringer distance: 254 mm
- type of loading: 2) remote biaxial stress field *due to internal pressure*
- cruise altitude: 10000 m *(no commas in numeric inputs!)*
- pressure vessel stress situation: typical biaxial stress field due to pressure
- cabin altitude: 2500 m

data presentation

The program shows a complete display of the repair configuration at the end of data input. At the bottom of the screen, you'll find the menu with the following items:

[F1] Calculate

This option ends the data input procedure and starts calculating using the chosen repair configuration.

[F2] Repeat

Pressing the F2-key will restart the entire data input for the patch repair configuration.

[F3] Change Screen Data

Data in the presentation on the screen can be changed (see data input plate).

[F4] Automatic

This option is very useful to investigate the crack-patching problem numerically. It offers the possibility to change the value of one input variable automatically (for example, the thickness of the patch) and see the effect on the typical crack-patching properties.

Pressing the F4-key presents a menu from which the input variable can be chosen. The program displays the variable in question with the original value, highlighted. You will now be asked for the final value and the interval (size of steps between the original and final values). The following menu is presented:

[F1] Calculate

The F1-key starts the calculation.

[F2] Change Screen Data

Data on the screen can be changed (see data input plate).

At this stage we must distinguish between the non-automatic calculation (F1) and the automatic calculation (F4).

1. non-automatic calculation

The option **Calculate** (F1) at the previous section displays and writes the results on the screen and to the output file, respectively.

results

The results on the monitor are divided over five pages:

page 1: Normal loading stresses

- remote stress and load-attraction of the inclusion.
- stage I and II analysis.

page 2: Thermal stresses

- situation at cruise altitude and sea level, based on the temperatures in the so-called "standard atmosphere."
- stage I analysis.

page 3: Total stresses

- normal loading stresses + thermal stresses.
- stage I and II analysis.

page 4: Plate stresses at the edges of the patch

- with and without thermal influences.
- stage I analysis.

page 5: Bending stresses at the top edge of the patch (x-direction).

- with and without thermal influences.
- stage I analysis.

Use the PgDn, PgUp and End-key to turn over the pages or to end this section of the program.

The following menu appears at the bottom of the screen:

[F1] Restart CALCUREP

This option closes the file you have been working on and lets you start again on a completely new configuration. *You should carefully consider using* [F2] *before pressing this key.*

[F2] Change Single Variable

This option allows you to change the value of one or more input variables without re-running the entire program input.

Pressing the F2-key presents a list of input variables. Entering the appropriate number enables you to change the corresponding value of the variable in question. This can be repeated until the number **0** (no more changes) is inserted. The program starts calculating automatically.

[F3] Quit

Exit to DOS.

2. automatic calculation

The option of automatic calculation does not display the results on the screen. All the results are written to the output file.

The following menu is displayed on the screen:

[F1] Make Plot

This option plots the results of the automatic calculation on 10 different pages.

page 1:	Normal loading stresses.
page 2:	Thermal stresses.
page 3:	Total stresses.
page 4:	K-factors.
page 5:	Reduction in K-factor.
page 6:	Maximum adhesive shear strains.
page 7:	Maximum reinforcement stresses.

page 8:   Plate edge stresses (without thermal stress).
page 9:   Plate edge stresses (with thermal stresses).
page 10:   Bending stresses in the plate at the top edge of the patch.

Again, the PgDn, PgUp, and End-keys are used to turn over the pages or to end this section of the program. The Print Option offers you the possibility to make a hard copy on the on-line printer.

[F2] Restart CALCUREP

[F3] Quit

Exit to DOS.

After making the various inputs, you will be able to assemble an overall picture of the patched crack. The data are summarized in the following table as a sample output. All output includes thermal effects. *Note that these data are arranged differently from what you will see on the computer screen, for clarity.*

CALCUREP Sample Output

Property	GLARE 2, t = 0.85 mm	Boron/epoxy, t = 0.38 mm	2024-T3, t = 1.0 mm
K_r, MPa	0	6.6	<0
% reduction in K	100	88	>100
Max patch stress, MPa	156	239	100
Max adhesive shear strain	0.016	0.054	0.028
Plate stress, MPa (load attraction)	140	77	168
Plate stress, MPa (bending) +	93	50	122
Plate stress, MPa (combined) +	233	127	290

*Thermal effects result in crack faces being placed in compression in this case.
+Can be reduced by tapering patch tips.*

This means a wide range of patch materials can do a good job in patching large cracks in pressurized fuselages. The patch must reduce the stress intensity factor. For a good patch, you need low patch stresses and low adhesive shear strains so the patch lasts a

long time. Combined fuselage skin stresses at the edge of the patch can't be so high that a new fatigue crack starts in the skin there. The following section gives some general guidelines for designing bonded patches.

Design Guidelines for Crack Patching

1. <u>Repaired Stress Intensity Factor</u>. You should aim for a stress intensity factor low enough so the crack grows slowly, so you don't have to inspect it every flight. Research has shown that a certain K value for a particular material gives a predictable crack growth rate. The table below shows a range of reasonable values.

Repaired K values needed to get various crack growth rates.

skin material	1 mm in 10,000 cycles	1 mm in 1,000 cycles
2024-T3	$\approx 10 MPa\sqrt{m}$	$\approx 20 MPa\sqrt{m}$
7075-T6	$\approx 4 MPa\sqrt{m}$	$\approx 11 MPa\sqrt{m}$

Cracks in 7075-T6 grow faster than in 2024-T3. You have to do a better job of crack patching with 7075 to get equal crack growth rates. This value, plus the maximum stress in the patch, help you choose the *minimum thickness of the patch*.

2. <u>Maximum Stress in the Patch</u>. This value depends on the yield strength of the patch material you're using. A good guide is to stay at or below one-half the yield strength of the patch. This gives you a safety margin so the patch can still take the ultimate design load and not yield. The yield strengths and recommended maximum patch stresses for some possible patch materials are shown below.

Strength of Various Patch Materials.

	2024-T3	Ti 6Al-4V	GLARE 2 (3/2)	Boron/epoxy
Yield Stress (MPa)	303	925	390	1590
Recommended Patch Design Stress (MPa)	151	462	195	795

The table shows that a large difference exists in the yield strengths of candidate crack patch materials. Use this value to help choose the *minimum thickness of your patch*.

3. <u>Maximum Shear Strain in the Adhesive</u>. This depends on the yield strain of the adhesive used for the bond. A good aerospace quality rubber-toughened epoxy like AF-163-2 has a yield strain in shear of about 0.09. Stay *below half the yield strain,* (or 0.045 for AF-163-2) of the adhesive to make sure the bond lasts a long time.

4. <u>Maximum Stress in the Plate (Skin) Around the Patch</u>. This number is a complex combination of load attraction into the repair, bending and thermal effects. To calculate this number, you must take the maximum plate stress value (thermal influences included) from data page 4. Then add it to the maximum bending stress value from data page 5 (thermal stresses included). The *total* of these two values is what's important, and the current version of CALCUREP doesn't add them for you.

You can reduce combined fuselage skin stresses easily by tapering the patch at its edges. Tapering of metal and fiber metal laminate patches can be done on a belt sander or grinder. With composite patches, tapering is done with ply drop-offs. Tapering also reduces the shear strains in the adhesive at the patch tips. This is good for patch *durability.*

If you do taper the patches, calculating the maximum plate stress is a bit more complicated. You have to do the normal calculations for the patch that you intend to install to get the value for plate stresses at the edge of the patch. Then you have to do the calculation again with the minimum thickness of the (tapered) edge to get the value for the plate bending stresses at the patch edge. Add these two values together to get the combined plate stresses.

Summary

CALCUREP presents a simple, user-friendly method to perform preliminary analysis of crack patching designs using the proven Rose model. It gives the structural repair engineer a tool to reduce costs and down time by quickly and easily calculating the items of interest in a bonded patch repair.

CALCUREP cannot, however, replace the function of the aircraft manufacturer in the approval of repairs not covered by the Structural Repair Manual.

The program is still in a developmental stage. If you would like to receive a copy of the executable file, or if you have any comments or suggestions about how to improve CALCUREP, please contact:

> Captain Robert Fredell, USAF
> Department of Engineering Mechanics
> 2354 Fairchild Hall, Suite 6H2
> USAF Academy, CO 80840-6240
> USA